Alma Mater Studiorum – Università di Bologna

DOTTORATO DI RICERCA IN

CHIMICA

Ciclo XXXII

Settore Concorsuale: 03/A2

Settore Scientifico Disciplinare: CHIM/02

A multi-methodological approach for the study of polymorphism in organic pigments and pharmaceuticals

Presentata da: Arianna Rivalta

Coordinatore Dottorato   **Supervisore**

Prof.ssa Domenica Tonelli   **Prof.ssa Elisabetta Venuti**

Co- Supervisore

Prof. Raffaele Guido Della Valle

Esame finale anno 2020

Abstract

The study of polymorphism has an important role in several fields of materials science, with applications in organic semiconductors and pharmaceutics, because structural differences lead to different physico-chemical properties of the system.

This PhD work was dedicated to the investigation of polymorphism in Indigo, Thioindigo and Quinacridone, as case studies among the organic pigments employed as semiconductors, and in Paracetamol, Phenytoin and Nabumetone, chosen among some commonly used Active Pharmaceutical Ingredients (API).

The aim of the research was to improve the understanding on the structures of bulk crystals and thin films, adopting Raman spectroscopy as the method of choice, while resorting to other experimental techniques to complement the gathered information. Different crystalline polymorphs, in fact, may be conveniently distinguished by their Raman spectra in the region of the lattice phonons (10-150 cm-1), the frequencies of which, probing the inter-molecular interactions, are very sensitive to even slight modifications in the molecular packing.

In particular, we have used Confocal Raman Microscopy, which is a powerful, yet simple, technique for the investigation of crystal polymorphism in organic and inorganic materials, being capable of monitoring physical modifications, chemical transformations and phase inhomogeneities in crystal domains at the micrometre scale. In this way, we have investigated bulk crystals and thin film samples obtained with a variety of crystal growth and deposition techniques. Pure polymorphs and samples with phase mixing were found and fully characterized.

Raman spectroscopy was complemented mainly by X-ray Diffraction (XRD) measurements for bulk crystals and by Atomic Force Microscope (AFM), Grazing Incidence X-ray Diffraction (GIXD) and Transmission Electron Microscopy (TEM) for thin films. Structures and phonons of the investigated polymorphs were computed by DFT methods, and the comparison between theoretical and experimental results was used to assess the relative stability of the polymorphs and to assist the spectroscopic investigation. The Raman measurements were thus found to be able to clarify ambiguities in the phase assignments which otherwise the other methods were unable to solve.

Table of contents

Acronyms

AFM	Atomic Force Microscopy
API	Active Pharmaceutical Ingredient
BAMS	Bar-Assisted Meniscus Shearing
CCD	Charge Coupled Device
CIF	Crystallographic Information File
CSD	Cambridge Structural Database
CSP	Crystal Structure Prediction
DFT-vdw	Density Functional Theory with van der Waals corrections
DSC	Differential Scanning Calorimetry
EPO	European Patent Office
FDA	Food and Drug Administration
GIXD	Grazing Incidence X-ray Diffraction
MBE	Molecular Beam Epitaxy
NSAID	Nonsteroidal Anti-Inflammatory Drug
PET	Polyethylene Terephthalate
PVD	Physical Vapor Deposition
PVT	Physical Vapor Transport
PXRD	Powder X-Ray Diffraction
QCM	Quartz Crystal Micro-balance
SIP	Surface Induced Polymorph
SSNMR	Solid-State Nuclear Magnetic Resonance
SVA	Solvent Vapor Annealing
TEM	Transmission Electron Microscopy
TGA	Thermogravimetry Analysis
UHV	Ultra-High Vacuum
XRD	X-Ray Diffraction

Chapter 1

1. General introduction

Definition of polymorphism

The term polymorphism (from the Greek πολυ "many" and μορφή "form", so "to have many forms") is used in several disciplines. In crystallography it appeared for the first time in the early 1800s to identify and classify the possible different crystal structures of the arsenate and phosphate salts.

With the aim of obtaining a general definition, Walter McCrone (1965) worked on the statement and its relative exceptions, still valid today, defining a polymorph as a "solid crystalline phase of a given compound resulting from the possibility of at least two different arrangements of the molecules of that compound in the solid-state ". [1], [2]

Since molecules can be highly flexible, polymorphs can exist as a consequence of a different arrangements in the primitive cell of the molecules with either the same or different conformations. This distinction gives rise to the phenomena of packing and conformational polymorphism, respectively.

In terms of thermodynamics, there are two types of polymorphic behaviour named enantiotropic and monotropic. Figure 1.1a represents the free energies and the transition enthalpies of a polymorphic pair as a function of temperature in an enantiotropic situation. Here, the transition temperature between the two polymorphs (t.p. $_{II/I}$) lies below their melting points and therefore the phenomenological manifestation is that there can be a reversible transition from one phase to another without going through the gas or liquid phase. Figure 1.1b represents instead a monotropic situation: there is no transition point below the melting points of the two polymorphs and therefore the two phases are not interconvertible. [3], [4]

A reliable criterion to identify a system as polymorphic could be that its different crystal structures must be all attributable to the same liquid, or gaseous, state.
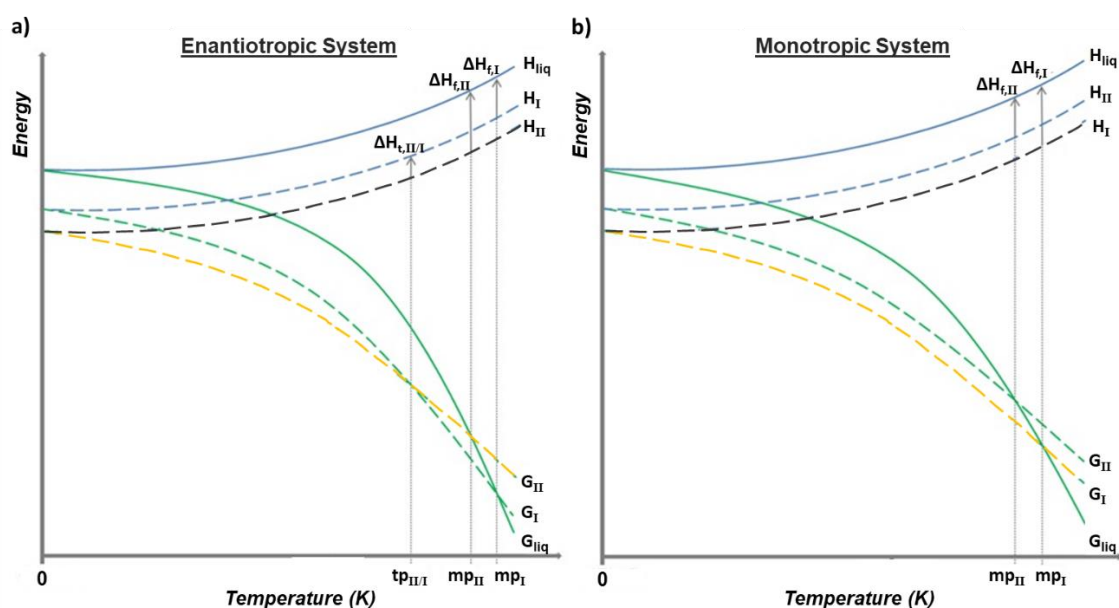
Figure 1.1: The illustration is a diagram of a dimorphic system where G is the Gibbs free energy and H is the enthalpy. The Roman numerals indicate the two polymorphs; m.p. is the melting point and t.p.$_{II/I}$ is the transition point between the two polymorphs, in which form II is the stable form below the transition point.

Also different tautomers (or isomers, diastereoisomers, zwitterions etc) of a molecule can give different crystalline forms with distinct melting points and in principle be comparable to polymorphs. However, the classification depends on the time scale considered. [5] Indeed, only crystals of tautomers which rapidly interconvert at melting point (or in solution) will be classified as polymorphous, while those with slower interconversion kinetics will be classified as chemically distinct compounds. It is evident that in this definition there is a strong component of subjectivity and ambiguity, also because both the equilibrium composition and the velocity of this process depend on the temperature of the experiment.

Based on the above considerations, there are still different opinions on the more correct definition of the polymorphism, however the initial formulation of McCrone certainly remains for the moment the most satisfying.

When discussing the definition of the term polymorphism, it is necessary to clarify the difference between polymorphism and allotropy. The term allotropy (from the Greek ἄλλος "other" and τρόπος "manner, form", so "to have other forms") [2] defines the property of some chemical elements to exist in different forms, in the same physical state,

called allotropes. Coined by Jöns Jacob Berzelius, this name identifies, specifically, the structure of the chemical bond that exists between the same type of atoms. In other words, when the atoms of the element are bonded together in a different manner, they give origin to allotropes. Commonly allotropy refers to pure elements in the solid-state, while polymorphism generally concerns the compounds. Perhaps the most known example, among the elements displaying allotropic phases, is carbon that exists in graphite, diamond, graphene, fullerene and nanotubes forms. It is easy to perceive how much the properties can differ from an allotropic phase to another. Exactly as for allotropic forms, different polymorphs of a compound can exhibit important differences in thermodynamic and mechanical chemical-physical characteristics. [1]

Another phenomenon worth mentioning is the so-called pseudo-polymorphism. This also was defined by McCrone in 1965, [2] and occurs when different crystal structures differ either in the nature or stoichiometry of the solvent molecules included in the lattice. Although this definition has also opened a debate about the exact distinction among the terms pseudo-polymorph, co-crystal and solvate, the point has been widely clarified by Bernstein. [5], [6] Following this author, when more than one chemical species is involved in the formation of a crystalline phase, different names are adopted for the phase, depending on the physical state and the nature of one of the components at room temperature. In particular: if all the components are found to be pure in the solid-state at room temperature (RT), the phase will be classified as co-crystal; if at least one of the components instead is found as liquid, the phase will be classified as solvate. Recently there has been a growing interest in solvates. [7]

Somehow, the boundary between pseudo-polymorphism and polymorphism it is rather labile, because often solvent and compound form a chemical structure of supra-molecular nature with specific properties. Modifying the stoichiometric ratio between the two it is possible to cause the collapse of the structure from ordered to amorphous, or even generate a new stable or metastable structure, in relation to the type and strength of the interaction among the species involved as well as a complex set of thermodynamic and kinetic parameters.

In the broader definition of the polymorphism of a compound, it is common practise to includes not only its different crystalline forms of a compound, but also hydrates and solvates with different solvents, or finally, amorphous phases and non-crystalline condensates. The different cases are shown in Figure 1.2.
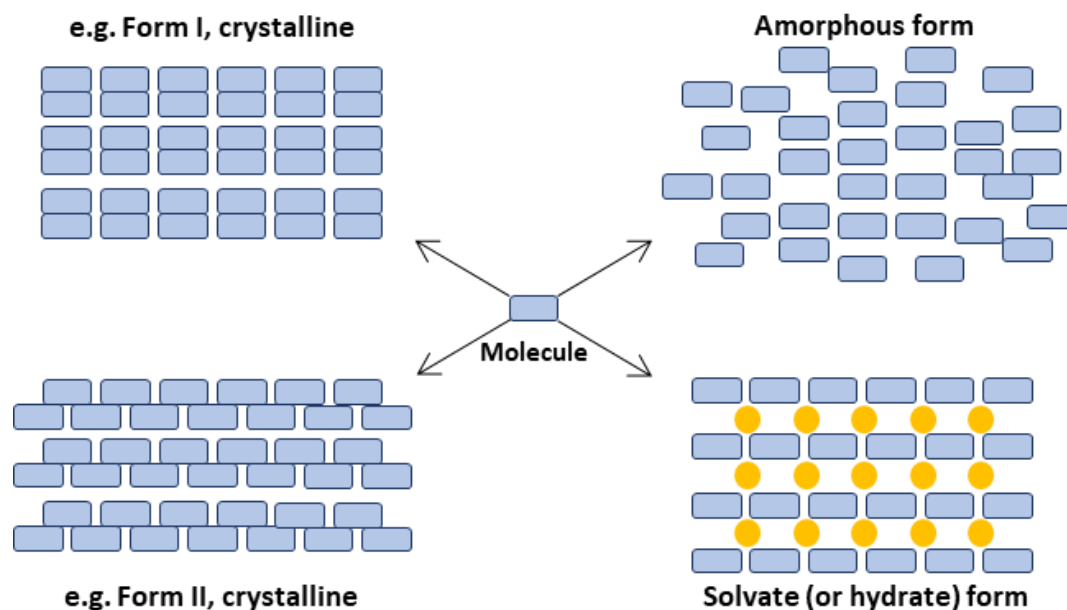
Figure 1.2: The illustration shows some examples of possible polymorphs and solvates of a compound.

A phenomenon which is not widely recognized but often occurs during the crystallization of systems displaying polymorphism, is that of the so-called concomitant crystallization, which is the appearance, in the same conditions of temperature and pressure, of more than one structure. The phenomenon is relevant for two reason specifically: i) from a scientific point of view, experiments that simultaneously yield crystals of different polymorphs offer structural and thermodynamic information, which are not available if only one phase crystallizes, ii) from a commercial perspective, process conditions which cause a concomitant crystallization must be avoided since they lead to materials that do not meet prescribed specifications. In theory, it is possible to define experimentally for any compound solvent, temperature, rate of evaporation or cooling, and other conditions under which a material will crystallize in a given form, [4], [8] namely the occurrence domain. [9] These conditions exist for every compound, but they are rarely

fully known, and besides they are not necessarily unique for a given substance or, in the present context, polymorph. In regions in which there is overlap of occurrence domains, two or more polymorphs may thus crystallize under essentially identical conditions, leading to the phenomenon of the concomitant polymorphs. The combination of thermodynamic and kinetic factors, and their interplay in the crystallization processes is in fact the event that makes concomitant crystallization possible. [4]

An interesting but very frustrating phenomenon linked to polymorphism is the possible elusiveness, or "disappearance" of the polymorph itself. It is common opinion that an authentic crystalline form should be reproducible, even if the selection of the right experimental conditions can take time and effort. However, it may happen and there are many examples in the literature that a previously prepared form becomes elusive and does not appear anymore after obtaining the most stable one. A phenomenon which is widely reported in the literature. Despite a possible explanation for this is that the environment becomes contaminated by small "micro-seeds" of the most stable polymorph, [5] but it is not yet clear what role nucleation exactly plays in the process and, subsequently, in the disappearance of the polymorph. [10]

Polymorphism in organic materials

The increasing interest of crystal engineering in the development of new functional materials has raised attention to the phenomenon of polymorphism in organic compounds. In fact, large and flexible molecules, kept together by weak non-directional forces, are expected to exhibit many alternative packing arrangements, with small differences in structure and energy, leading to polymorphism. For this reason, this phenomenon is very common in organic materials. [11]

Despite its long-standing interest as a subject of investigation, polymorphism in molecular crystals remains one of the most fascinating phenomena of solid-state chemistry. As a matter of fact, it is a challenge to the very concept of being able to design a crystalline solid with a-priori defined structure (and therefore properties) based on the chemical knowledge of its molecular components. This is the realm of "crystal engineering", defined in 1988 by Gautam Desiraju [12] as "the understanding of

intermolecular interactions in the context of crystal packing and the utilization of such understanding in the design of new solids with desired physical and chemical properties".

At the present, the process of regulating onset and evolution of a specific solid form is still relatively random and in many cases the outcome of the crystal growth is more the result of mere chance rather than planning. On the other hand, the possibility of exerting a control is of the highest importance because, as mentioned above, polymorphism has the prerogative to drastically influence mechanical, physical and chemical properties of the material, such as solubility, bioavailability, hygroscopicity, chemical stability, hardness, thermal and electrical conductivity. [13] For instance, even small differences in the structure may affect the narrow band structure of organic semiconductors.

It is therefore evident how polymorphism is a crucial issue for all the applications that involves structured organic materials. Even though the system is otherwise chemically pure, concomitant polymorphism may easily yield phase mixing, and thus constitute an intrinsic source of disorder with detrimental effects on charge transport, bioavailability and other key properties. [11], [14], [15] To this purpose, a detailed study of the polymorphism, the so-called polymorph screening, is required. This implies the search of different crystalline, solvates and amorphous phase, together with relationships (enantiotropic and/or monotropic) among them.

Polymorph screening usually requires the combined use of different techniques. The main one is the X-ray Diffraction (XRD), which provides a knowledge of stereo-geometry and distribution of molecules in the crystal. A variety of microscopy techiniques, together with Differential Scanning Calorimetry (DSC), Thermogravimetry (TGA), Raman and Infrared (IR) spectroscopy and Solid-State Nuclear Magnetic Resonance (SSNMR), are all precious for the structural characterization and at the study of the phase diagram of the substance. Among the variables of the system that influence or determine the crystallization process, there are temperature, pressure, solvents from which the solid phase precipitates, as well as conditions like permanence of a solid phase in a controlled atmosphere of the solvent vapor and mechanical stress produced by

grinding. The most effective way to proceed is to evaluate the effect on the different phases by varying and analysing one variable at a time.

The results are often unexpected and the consequent picture is complex, giving reason again to McCrone [2] who, in his study of polymorphism, wrote this famous sentence:

"It is at least this author's opinion that every compound has different polymorphic forms and that, in general, the number of forms known for each compound is proportional to the time and money spent in research on that compound."

Surface mediated polymorph

More and more frequently, many different applications (e.g. devices for organic electronics or plasters for pharmaceutics) employ crystalline thin films. These are obtained by growths at the solid interfaces of a variety of different substrates, spanning from silicon oxides to polymers, composite materials, or even paper.

The materials crystallizing in these conditions often display forms different from those observed in the bulk, [16]–[18] which can be grouped under the broad definition of "surface mediated structures" and have been often called surface induced (SIP) in the current literature. The mechanisms through which the substrate may tune the phase nucleation and the role of kinetics factors have been studied, [17], [19] but often not fully clarified. The surface can act as a template for molecular deposition [20] or, even more interestingly, the subtle interplay of weak interactions at the interface may lead to fully new molecular arrangements, [17], [18] unknown in the bulk, and for these we adopt here the denomination "surface selected". Sometimes, however, the effect of the interface is to stabilize forms otherwise metastable in the conditions of growth, and in this case the expression "surface stabilized" is adequate. [21] Finally, the definition thin film (TF), or better surface induced structure, should apply to those we consider distorted bulk structures, based on their similarity with their parent bulk structure, as a result of the substrate perturbation affecting the growth in the first monolayer.

Such forms are frequently observed in films for organic electronics and can determine the electric properties of the system. [22], [23] Probably the most famous

example is still the physical vapor deposition of the organic semiconductor Pentacene on silicon oxide substrates, for which the expression "thin film phase" was first introduced to describe the structure appearing in the first monolayer. [20], [22] Macroscopic free-standing single crystals of this very phase are not accessible, as surface interactions are required for its existence. However, upon subsequent layer growth, an increasing and independently growing portion of the bulk phase is formed, while the nucleation of the surface phase is confined to less than 100 nm from the substrate. [24]

In the pharmaceutical field, instead, scarce data exist on the formation of these forms, but the application of solid surfaces as nucleation or crystallization mediators is a highly promising emerging alternative to assist the formulation of new drugs. [25], [26] Although numerous literature studies show that growth alterations occur in the proximity of a surface (as will be extensively discussed in this thesis), in most cases only the already known polymorphs were observed. However, this might be due to the fact that most of these studies lacked the experimental tools necessary to unambiguously identify the presence and the nature of surface mediated structures.

A full structural characterization is still a challenging task and several methods have to be employed to solve the structure of thin films. Atomic Force Microscopy (AFM) measurements can be performed to identify morphology alterations that, in some case, can help the investigation. Another common technique is the Grazing Incidence X-ray Diffraction (GIXD), together with electron diffraction, but unfortunately they provide a limited number of Bragg reflections due to weak diffraction, small scattering volumes, high aspect ratio or defects. This suggests to exploit the synergy of computational tools and complementary experimental techniques to gather information on the film characteristics.

To tackle this problem in the present thesis, we have used confocal Raman spectroscopy and sample mapping in the region of lattice phonons. [11] This method has proved to be fast, non-destructive and *in situ*, both for crystal structure recognition and phase mixing in domains at the micrometre scale and can be extended from bulk crystals to thin films on technologically substrates and also to working electronic devices. [27]

1.1.   Aim of the thesis

As discussed previously, crystal engineering still represents an open challenge in the development of the physical chemistry of the solid-state. In recent years, extensive theoretical work was directed toward identifying and predicting new polymorphic forms, in particular of organic molecules, for compounds with various applications. [28] In fact, the fascinating idea of using polymorph control and morphology alteration to produce a material with specific proprieties, plays an important role in several fields of materials science. This PhD work, in particular, focused on organic compounds with applications such as semiconductors and pharmaceutics.

The aim of the thesis was to improve the understanding on the crystal structures in films, adopting Raman spectroscopy as the method of choice, while resorting to other experimental techniques to complement the gathered information.

For all the studied systems, similar approaches have basically guided the investigation. Various methods of growth have been adopted to grow single crystal of the compounds, with the aim of obtaining different polymorphs in the bulk (if they existed) to be characterized structurally and spectroscopically. Such a procedure makes possible to associate each crystal form to a measured Raman spectrum, which extends from the region of lattice phonons to the intra-molecular modes. Solid-state density functional calculations combined with van der Waals (DFT-vdw) corrections have been applied by the research group to estimate the relative energies of the various polymorphic modifications, and to validate and confirm the spectral assignments.

Once the situation with the bulk state of a given system has been clarified, investigation has moved to films. Methods of preparation have been selected either following the literature or guided by the physical-chemical properties identified in the study of the bulk. Among the deposition methods, drop casting, spin coating, dip coating, bar-assisted meniscus shearing (BAMS) and Physical Vapor Deposition (PVD) were employed depending mainly on the solubility and the volatility of the studied compound. Instead, regarding the techniques used for characterization in addition to Raman, we made also use of X-ray, IR and Fluorescence spectroscopy for bulk investigation, while

Atomic Force Microscope (AFM), Grazing Incidence X-ray Diffraction (GIXD) and Transmission Electron Microscopy (TEM) for thin films.

1.2.   Organization of the thesis

The thesis is organized as follows. In the second chapter the main employed techniques are described. The investigation regarding organic semiconductor compounds is illustrated in chapter 3. We first explain, in a short introduction, devices and the role of polymorphism in this field, in particular its effects on films. In the following, the studied systems are described: Indigo, Thioindigo and Quinacridone. The polymorphism of pharmaceutics is the content of chapter 4. This is organized as the previous chapter, therefore there is first an introduction on the important role of the phenomenon in this field. In the following, our results for the Paracetamol, Phenytoin and Nabumetone systems are described.

Finally, general conclusions can be found in chapter 5.

Chapter 2

2. Instruments, crystal growth and film deposition

In this chapter we describe the experimental setup of the instrument mainly used in this work (other employed set ups will be discussed in the chapters that follow), together with the methods for crystal growth and films deposition.

2.1.   Raman spectroscopy

A Raman instrument is composed by:

- Monochromatic excitation light source;
- Sample focusing system;
- Filter to separate the Raman scattered light from the Rayleigh signal;
- Multiple dispersion stage (one or more diffraction gratings);
- Detector;
- Data analysis system.

The excitation light is selected to maximize the Raman signal, which is intrinsically weak and for this reason a laser source is needed. An important factor that determines the choice of the excitation wavelength is the occurrence of fluorescence emission from the sample, which may overlap with Raman bands. To avoid this phenomenon, sources with excitation energies lower than the electronic transitions of the system under examination are generally used. Our available sources were either in the visible region, in particular from Argon ion lasers (commonly used in the green/blue region of the visible spectrum) and a Kripton ion laser, with strong emission in the red/yellow, or in the near infrared such as diode lasers (≈ 800 nm). Taking into account that the Raman intensity is proportional to the fourth power of the frequency of the radiation, in the ideal situation, the lowest laser wavelength that is not absorbed should be selected, also limiting other processes such as the degradation of the sample by thermal or photochemical effect.

In order to collect high quality Raman spectra, it also necessary to filter the Rayleigh component of the scattering. Notch or long-pass optical filters are typically used

for this purpose, but a very effective way is to use a triple-grating monochromator in subtractive mode to isolate the desired signal. [29] This allows observing also Raman shifts in the terahertz range, while holographic filters typically reflect some of the low frequency bands in addition to the unshifted laser light. However, new volume holographic filters are becoming very common and performing. In fact, recent advances in glass technology allows the design of low scattering, and very narrow bandwidth gratings that gives 50% transmission at positions less than 3.5 cm^{-1} from the central filter position.

The signal detectors called Charge-Coupled Devices (CCD) have been a big innovation in Raman spectroscopy, as compared to previous detectors they present a lower noise with higher quantum efficiency. The latest models on the market have exceptional performance, with a signal-to-noise ratio of about one photoelectron/pixel/hour.

Their operation is based on the collection of charges photogenerated by the sensitive surface of the detector on a series of pixels. The charge is accumulated in each pixel and, upon reading, sequentially transported in an output amplifier. The sensitive elements can be arranged in both one-dimensional and two-dimensional matrices, with a high number of pixels. The quantum efficiency peak covers the entire spectral range normally used in Raman. Among the many advantages offered by these detectors, as compared to the photomultipliers used in the past, such a configuration not only allows to acquire spectra simultaneously at all wavelengths of interest, but also from different areas of the samples.

2.1.1. Spectroscopy of molecular solids

Raman spectroscopy can be used to provide chemical information, both qualitatively and quantitatively, ranging from the identification of functional groups of a molecular structure up to more complex applications in materials science. [30], [31]

For the purposes of this thesis, we apply it to get information on organic molecular solids. These are crystals in which molecules retain their chemical identity, because

intermolecular interactions (arising from hydrogen bonds and Van der Waals forces) are much weaker than the intramolecular ones (covalent bonds). Because of the large difference in the strength of the two kinds of interactions involved, the vibrational modes of the crystals typically span two distinct energy regions: the so called "lattice" modes typically lie at frequencies between 10–150 cm^{-1}, while the "intramolecular" modes are generally found at higher frequencies. The lattice modes are cooperative motions in which the molecules in the unit cells rotate and translate one with respect to the other, as a whole, essentially without deforming. The intramolecular modes, instead, correspond to the vibrational modes of the isolated molecule, combined and slightly perturbated by crystal interactions. For this reason, while the intramolecular modes usually vary very little between different polymorphs, the lattice vibrations strongly depend on the crystallographic packing, and can be used to distinguish between different structures.

As a result, the vibrational spectra in the intramolecular region make possible the identification of the molecular species involved, while those in the intermolecular region allow one to identify the various polymorphs.

Based on its application over the entire energy range of the crystal vibrations, in addition to the use of microscopy techniques and of polarized light for the excitation, the study of polymorphism by Raman spectroscopy can provide:

- Chemical information - from the analysis of the vibrational modes in the intramolecular region; [31]
- Information on the structure and dynamics of the crystal lattice - from the analysis in the intermolecular region; [11], [32]
- Information on molecular order, anisotropy, alignment and organization in crystalline domains - from measurements in polarized light; [11], [33]
- Information on spatial distribution of physical/chemical structural inhomogeneities - by means of Raman mapping with micrometric spatial resolution. [11], [34]

2.1.2. Raman spectrometer configuration

The instrument used in this thesis to record Raman spectra at low wavenumbers (10–150 cm^{-1}) is a confocal micro-Raman spectrometer, Horiba Jobin Yvon T64000, interfaced with an Olympus BX40 microscope and having a CCD detector. The spectrometer has three monochromators, set up in double subtractive + additive configuration, so to achieve an efficient subtraction of the Rayleigh scattering of the excitation light. This configuration (see Figure 2.1) is optimized to acquire the spectra very close to the laser line, down to a $\Delta v \approx 5$ cm^{-1}, thus enabling the detection of the lattice phonon region.
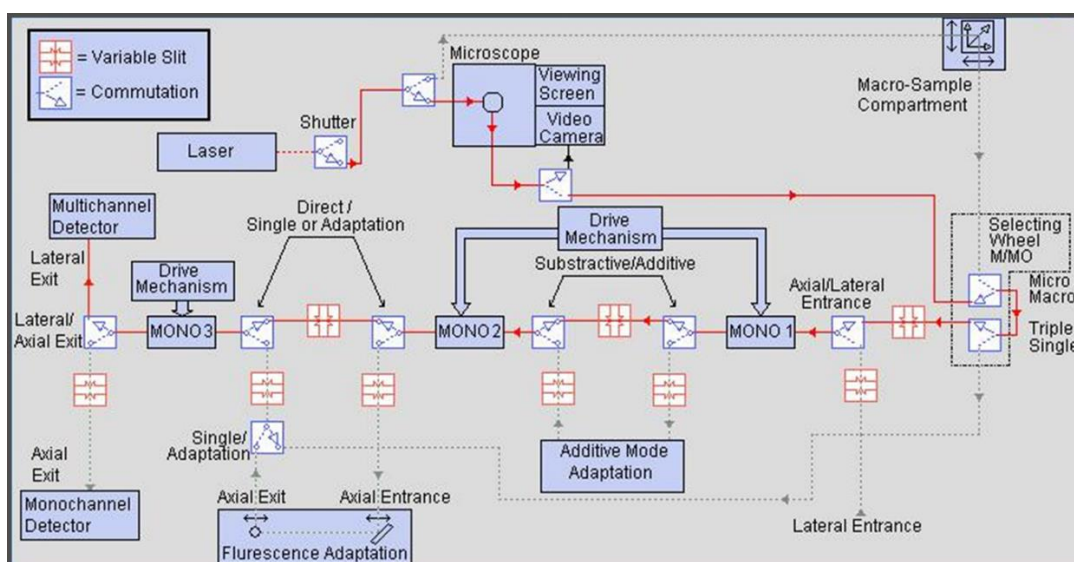
Figure 2.1: Illustration of the Raman T64000 spectrometer (Horiba Jobin-Yvon): triple monochromator in double subtractive configuration + one additive.

The excitation was from the laser lines at 752.5 and 647.1 nm (this with the nominal power of 1 W) of a multiline tunable Kr$^+$ gas laser. The incoming power was reduced by means of neutral filters, selecting their optical density in each experiment to prevent sample damage, while the actual power focused on the sample was kept anyway lower than 1 mW (estimated power density 2500 W/cm^2).

A further advantage of the instrument is the possibility of working in confocality, because of the coupling with the Olympus optical microscope. This is equipped with 100x,

50x, 20x, 10x and 6.3x objectives, which allow for a spatial resolution below 1 micron and a theoretical field depth ranging from about 7 to 900 μm (see Table 2.1).

The effect of the confocal configuration (illustrated in Figure 2.2), which uses a pinhole, is that the microscope is highly efficient at rejecting out of focus scattered light and the image comes from a thin section of the sample. This gives the possibility of a discrimination along the Z axis (vertical resolution along the thickness of the sample), in addition to the discrimination in the XY plane.
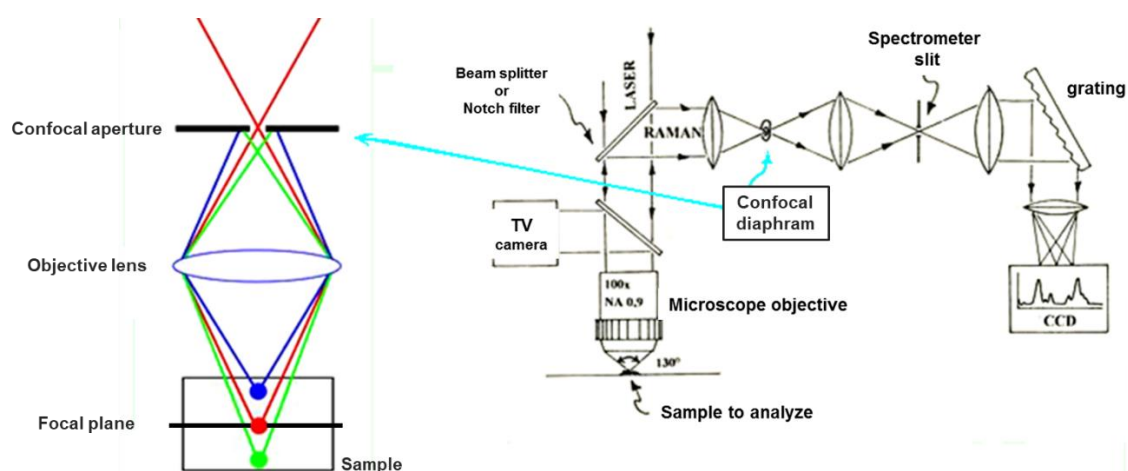
Figure 2.2: Optical scheme of a confocal microscope and the effect of confocal diaphragm on the depth of field. The scattering is collected exclusively from the focal plane (red trace).

Raman spectra in the 100–2000 cm^{-1} wavenumber range were often recorded on a single grating spectrometer, the Renishaw system 1000, equipped with a notch filter and coupled to a Leica DM LM microscope. The spectrometer is equipped with 50x, 20x and 5x objectives and allows for a nominal spatial resolution lower than 2 μm in XZ and 4 mm in Z when the 50x objective is used. Both the 785 nm wavelength of a diode laser (with a nominal power of 500 mW) and the 514.5 nm line of an Ar$^+$ gas laser (with an output power of around 25 mW) were employed. In both cases, whenever needed, the intensity of the light intensity on the sample was reduced by neutral density filters to avoid its damage.

2.1.3. Raman mapping

A Raman map can be described as the "spectroscopic" image of a sample, be it a film, a crystal, or a crystalline agglomerate. The technique that allows for the construction of an 1D, 2D or 3D Raman image by acquiring spectra on spatial grid at high resolution. The recorded spectra are transformed into a map by using a colour code, which can be adjusted to describe the chemical composition of the material, the distribution of the phases or the modification of a material subjected to an external perturbation such as, for instance, stress. With this technique, it is therefore possible to analyse impurities of the materials and phase homogeneity.

The purpose of using this technique in the experiments of this thesis was to map the distribution of different polymorphs in physically non-homogeneous samples. In this kind of analysis, we must take into account that the penetration depth of the laser beam considerably depends on the numerical aperture (NA) of the objective used: the higher is the numerical aperture, the smaller, keeping all other conditions constant, is the depth of field. Moreover, the minimum size of the laser spot, i.e. $\frac{4}{3}\frac{\lambda}{NA}$, is inversely proportional to NA and directly proportional to the laser wavelength. These parameters must all be considered in the analysis on a micrometric scale. Table 2.1 shows the manufacturer's nominal values associated to the objectives used, experimentally determined analysing the Raman signal of a silicon oxide sample.

Table 2.1: Objective characteristics.

Magnification	Numerical aperture NA	Penetration depth	Spot size $\lambda = 647.1$ nm
6.3x	0.16	900 µm	5.39 µm
10x	0.25	450 µm	3.15 µm
20x	0.40	150 µm	2.16 µm
50x	0.75	25 µm	1.05 µm
100x	0.90	7.5 µm	0.88 µm

Employing different penetration depths can be useful in the analysis of samples which present structural and/or composition differences between surface and underlying layers.

2.1.4. Polarized measurements

Raman scattering in crystals is governed not only by the conservation of energy, but also by the conservation of momentum. Thus, as the lattice waves have directional properties, the nature of the Raman spectrum depends on the orientation of the crystallographic axes with respect to the direction and polarization of both the excitation and the scattered light. [35] The orientation of a single crystal in the Raman experiment is generally specified by the Porto's notation, [36] which results simplified in the backscattering experimental setup of this work, as the exciting and scattered beams propagate always in the Z direction of the laboratory frame. If the crystal is oriented so that at least one of its axes a, b, c (e.g. a) is collinear with one of the laboratory axes X, Y, the only possible configurations in back scattering geometry are represented in the Porto's notation by Z(aa)Z and Z($aa_\perp$)Z, where $a_\perp$ is the direction normal to a. The first letter identifies the propagation direction of the excitation, while the last one refers to the observation direction. They will be dropped as redundant in the notation here adopted. The letters in parentheses specify the polarization directions of the exciting and scattered light, respectively. Besides, and more importantly, they identify the particular element of the Raman tensor responsible for the observed scattering. A Table has been derived [37] which presents the form of this tensor for all the 32 crystal classes, classified by their symmetry point groups. This Table is particularly useful in the interpretation of the Raman spectra of crystalline samples. [35]

Usually polarization measurements cannot be performed on polycrystalline samples owing to reflections which tend to scramble the electric vectors of both the excitation and the scattered light. Nevertheless, with micro Raman spectroscopy, it is often possible to select optically a single microcrystal from a polycrystalline powder and record a polarization measurement.

In practise, firstly a suitable single crystal is selected and analysed on the polarized microscope, in order to identify the direction of their optical axis. A half-wave plate is used to rotate the polarization of the incident light, while a wire grid polarizer selected the polarization of the scattering. X-ray indexing of the crystal faces (when possible), morphology and extinction directions allow us to orient the crystals for measurements in polarized light. For measurements with no polarization analyser for the scattering, performed on randomly oriented crystals and powder, no polarization scrambler was applied to the incoming laser beam.

It should be pointed out here that when the investigated Raman-active fundamental is also infrared-active, further considerations apply. The dipole derivative is nonzero, and the electric field of the excitation interacts directly with the crystal vibrations. The transverse and longitudinal components of the vibrations have different frequencies, with a frequency separation proportional to the absorption intensity of the corresponding infrared band. In molecular crystals this effect is usually small while it might be more evident in ionic crystals. Otherwise, for the ten centrosymmetric crystal classes the rule of mutual exclusion applies, and no fundamental vibration can be both infrared- and Raman-active. [35]

2.2.   Single-crystal growth

Crystallization processes e methodologies play an important role in various fields and are the subject of numerous studies. In the present thesis, their application has been fundamental for the research of polymorphs. In fact, obtaining suitable single crystals is helpful for the determination of the intrinsic physical-chemical properties of the material, and is needed for recording polarized spectra.

The high vapor pressure, the low melting point and the good solubility of the organic materials in several organic solvents allow one to obtain high quality crystals of these compounds from solution, gas phase and melt-growth methods. The method of choice depends both on the nature of the individual molecule and on the specific interactions established in the condensed matter. In general, solution growth methods are preferable for materials with very low melting or decomposition temperatures in atmospheric conditions. If the compound has high vapor pressures but is unstable at high temperatures in oxygen, the gas phase technique at low pressures with inert gases is instead preferable. [38]

The solution, melt and gas-phase growth methods for organics, employed in this thesis, are described in the following.

2.2.1. Solvent evaporation method

Since most of the organic compounds are well soluble in organic solvents over a wide range of temperatures and pressures, the solvent evaporation method is often used to obtain suitable single crystals for XRD structure analysis. [38]

This method consists in the evaporation of a saturated solution to reach a super-saturation condition, where crystal nucleation starts spontaneously. If the process is slow, the initially formed seeds can then turn into larger crystals. Processes like the Ostwald ripening, which consists in the dissolution of small and defective crystals in order to grow new larger ones, contribute to the formation of a smaller number of large single crystals. [3]

The main variables in this method are the different solubility of the compound and the different volatility of the solvent. Commonly used solvents are methanol, ethanol, acetone, THF, acetonitrile, dichlorobenzene, dichloromethane, chloroform, etc. Since some of these have high volatility, their evaporation rate can be slowed by covering the sample with a perforated stopper (or with PARAFILM®) in order to obtain larger single crystals. Also temperature is another variable which can be employed to control the evaporation. Furthermore, the solubility can considerably increase as a function of temperature, requiring more material to reach the super saturation condition.

2.2.2. Melt growth method

Crystal growth techniques from the melt are used most frequently for inorganic compounds, characterized by high stability at high temperature and very low vapor pressures. However, they can be employed also to obtain crystals of organic compounds, which are sufficiently stable up to the melting point, without decomposition if not under long-term treatment. It is also possible to work in controlled atmosphere conditions to avoid oxidation processes or evaporation of materials with high vapor pressure. [38] Large and high-quality crystal may be grown with this technique for several materials.

2.2.3. Crystallization method from the gas phase: Sublimation

Sublimation processes employ the solid-gas equilibrium and, for this reason, they have to take place at low pressures and relatively high temperatures.

The scheme of the sublimator used is shown in Figure 2.3, but there are several variations of this tool (e.g. employing either static or dynamic vacuum environments). Depression was obtained with a rotary vacuum pump (p maximum 10^{-3} bar), with an atmosphere of N_2 or Ar as inert gases.

In the case of static conditions, a small amount of substance is placed under vacuum in a Pyrex tube, usually after conditioning the system with cycles of vacuum/inert gas. The material is thus heated from the bottom with a resistance or with a bath of

silicone oil to ensure a homogeneous heat distribution. The crystallization occurs when the gas of the substance encounters the water-cooled cold end at the top of the Pyrex tube. If the temperature gradient between the sublimation chamber and the cold end is excessive, the result is a too fast process, which yields twinned or statically disordered crystals. Instead, good quality crystals can be obtained by playing with the process conditions (e.g. by decreasing the temperature or the pressure of the system). Besides being a growth technique, sublimation is also used for the purification of commercial samples.

The method produces good quality crystals in hours or possibly weeks, depending on the volatility of the sample and the quality of the vacuum. Vacuum sublimation is also ideal for compounds with low vapor pressure or very air sensitive, and is also chosen when the low solubility of the material prevents the crystal growth by any solution method.
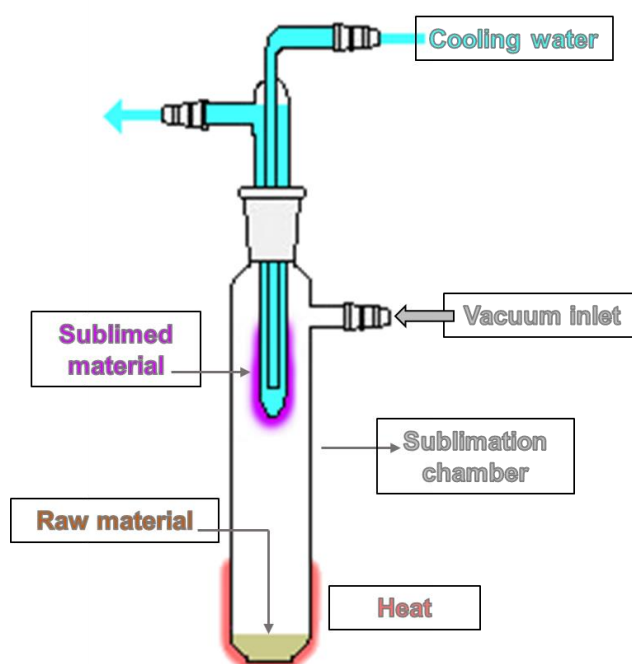
Figure 2.3: Sublimation experimental setup.

2.2.4. Crystallization method from the gas phase: Physical Vapor Transport

Physical Vapor Transport (PVT) [39] is a crystal growth technique which belongs to the gas-phase methods, like sublimation.

The PVT method uses an ampoule sealed under vacuum, at the two ends of which different temperatures are applied, so that the substance inside moves as a vapor under the resulting temperature gradient. [39] The ampoule is filled with the material, sealed after being evacuated in inert atmosphere, typically N_2 or Ar, and then horizontally placed in a furnace at two temperature zones, with the substance in the high T zone. The sublimation takes place at the hot end, and the vapor phase moves along the ampoule by buoyant convection motion, driven by the applied horizontal temperature gradient. [39], [40] Finally, the temperature gradient causes super-saturation, resulting in the deposition of the vaporized compound at the cold end. An illustration of the experimental setup is shown in Figure 2.4.

As for sublimation, the technique is suitable for the preparation of high purity single crystals, since a purification process takes place during the growth. Large high-quality crystals are obtained when the temperature gradient ΔT is not too high (max 25°C) and the hot end temperature is only slightly higher than the sublimation temperature of the material.
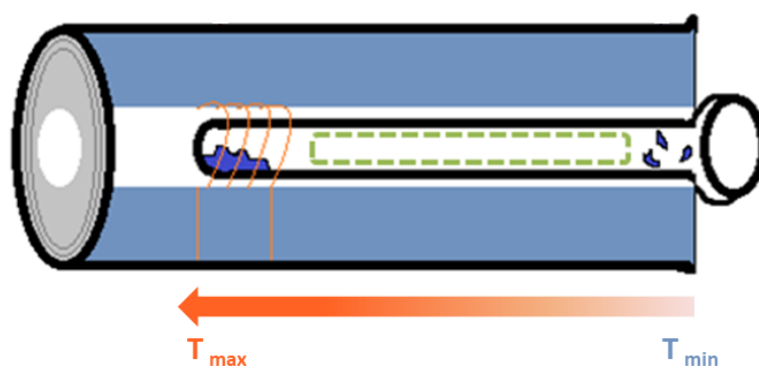
Figure 2.4: Physical Vapor Transport experimental setup.

2.3.   Films preparation

A relevant part of this thesis concerns the deposition of organic crystalline films, in order to study the material properties also on film and make a comparison with those on bulk. The deposition techniques employed are described in the following paragraphs: the first three methods are from solution, while the last one is from the gas-phase.

2.3.1. Drop casting method

The drop casting method (illustrated in Figure 2.5) can be used to obtain crystalline films of organic compounds with good solubility. The main advantage of the method consists in its simplicity, but the disadvantage is that it is difficult to control all the external parameters and obtain a homogeneous film.

A drop of solution is cast (e.g. with a Pasteur pipette or a micro-pipette) and let to dry on a solid substrate. When the drop is placed on the substrate, it can be either left untouched or carefully levelled on the surface with the pipette tip, to allow a more homogeneous distribution and drying process. As the solvent evaporates, a film of material forms on the substrate.

The evaporation speed of the solvent is a determining factor, which can influence the film properties. If the process is slow, the phenomenon of growth will prevail on the nucleation process, meaning that only a few nuclei, from which crystals will grow in conditions of thermodynamic equilibrium, will be present. Vice versa if the process is fast, the nucleation process will be favoured and therefore in kinetic conditions a high number of nuclei will form, resulting in many small crystalline domains, and metastable phases can grow. Other parameters, which can influence the properties of the film, are solution concentration and substrate temperature.

For solvents with high volatility, the formation of large single crystals can be favoured by slowing down the evaporation rate by covering the sample with a holed cap.
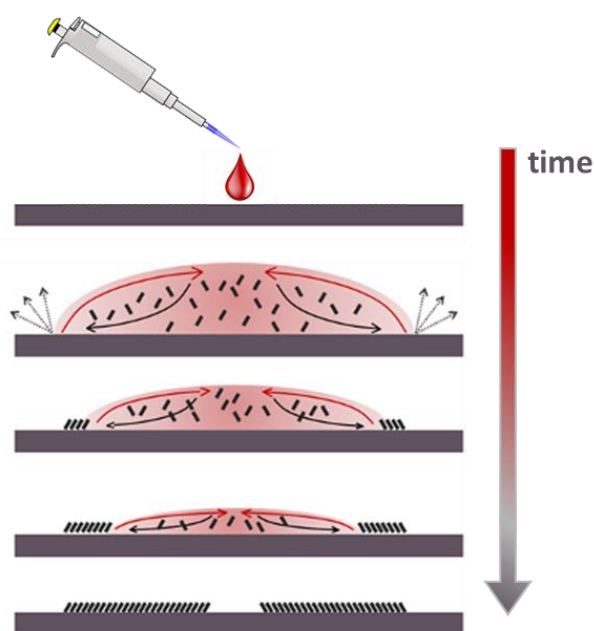
Figure 2.5: Scheme of a film deposition and growth by drop casting. [41]

2.3.2. Spin coating method

Spin-coating (illustrated in Figure 2.6) is one of the most common techniques for film deposition. It is used in a wide variety of industrial processes and technology sectors. The main advantage of the method consists in the simplicity of the experimental apparatus and in the velocity of the process, yielding uniform films with a thickness from nanometres to micrometres.

The method consists in the deposition of a desired amount of solution on a substrate and in the rotation of this while controlling speed, acceleration and time. The process exploits the centrifugal force acting on the solution that is pushed towards the edges of the substrate, covering it uniformly and yielding a homogeneous film. In fact, the high rotation speed of the substrate causes a centrifugal force, which, combined with the tension surface of the solution, forces the liquid to cover the entire area of the substrate. This technique can be used both to cover small (a few mm^2) and large substrates (meters or more in diameter) such as panels of TVs.

The main disadvantage is that it can use only one substrate at a time. [42] Furthermore, the high speed of evaporation of the solvent can cause a decrease in

performance for those nano-technologies in which a high degree of crystallinity of the deposit is required (OFETs of small molecules). Not to be neglected is the enormous quantity of wasted material, because the solution that actually remains on the substrate is not greater than 10% of that initially deposited. [41]
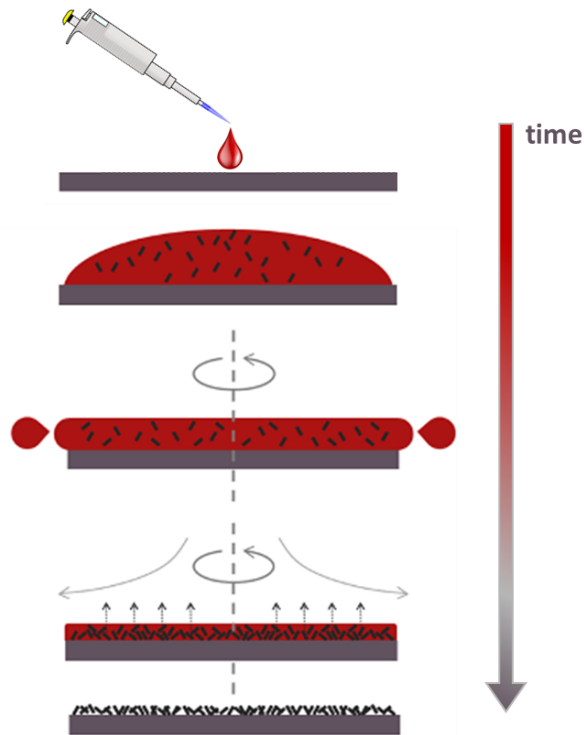
Figure 2.6: Scheme of a film deposition and growth by spin coating. [41]

2.3.3. Bar-Assisted Meniscus Shearing (BAMS) method

Bar-Assisted Meniscus Shearing – BAMS (illustrated in Figure 2.7) has proved to be an effective method to produce transistors in thin film, by depositing the organic material from solution directly on the dielectric layer. [43]

This technique uses a smooth cylindrical metal bar positioned at about 300 μm above a heated substrate. The bar moves at a controlled and variable rate depending on the compound and the required characteristic of the final film. The deposited solution forms a meniscus between the bar and the substrate, and is sheared by the moving bar in a uniform layer, producing a homogeneous film. The formation of the meniscus is due

to the capillary forces, which confine the liquid phase between the bar and the substrate, and is the crucial part of the process, involving various interface phenomena. Wettability, which is the ability of the solution to maintain contact with a solid surface, represents a particularly important parameter. Substrate heating favours the evaporation of the solvent, leading to supersaturation, and promotes the crystallization via heterogeneous nucleation, so that the film is produced in a single step. [44]
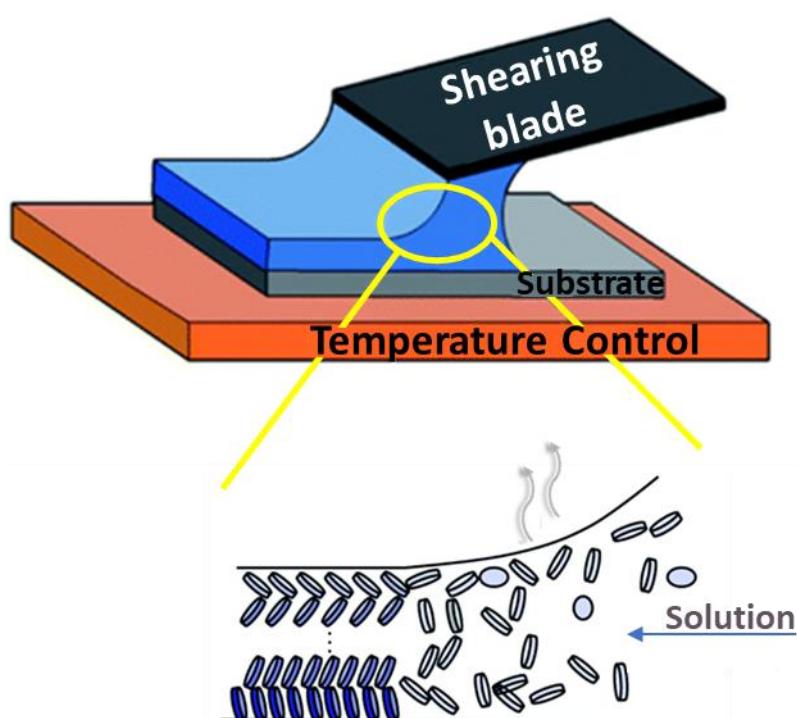
Figure 2.7: Scheme of a film deposition and growth with the BAMS technique.

2.3.4. Vapor deposition: Molecular Beam Epitaxy (MBE).

Physical Vapor Deposition (PVD) is a method for the deposition of thin films under vacuum conditions, which is very common for the manufacturing of electronic devices and also widely used in other areas. In this deposition process the material is evaporated, from a solid or liquid source, in the form of atoms or molecules and transported as a through a vacuum or plasma environment to the substrate, where condensation takes place. The technique can be used for coatings of $\approx 10 - 100$ nm, but also for deposits in

different layers (multilayer). The shapes of the substrate can vary from flat to very complex geometries (like utensils), and the deposit rate can vary from 0.1 to 10 nm/s, depending on the case. PVD is used to create both pure films or alloys with a variable percentage (graded composition deposit).

Molecular Beam Epitaxy (MBE) [45] is one of the most widely used PVD growth techniques in the field of thin film research. Molecules to deposit are sublimated in specific cells (called Knudsen cells) and are directed on the surface to be covered.

The key feature, which makes MBE more suitable than other deposition techniques, is the high degree of chemical purity and crystallinity of the obtained films with respect to the relative simplicity of operation. In addition, since it operates far from thermodynamic equilibrium conditions, structures difficult to achieve with other techniques can be obtained. From a technical point of view, the disadvantage is the need of working in the ultra-high vacuum conditions of $\approx 10^{-8}$ mbar. Nevertheless, MBE remains the preferred method for the fabrication of thin films of organic small molecules that exhibit low solubility. [46]

In the present thesis, the deposition of the Indigo molecules on silicon oxide and Tetoron® has been carried out with a ultra-high vacuum system (UHV) for MBE, by using a home-made chamber (illustrated in Figure 2.8) fitted with a sample heater, shutters and a quartz crystal micro (QCM) balance placed close to the sample holder. Powder evaporation was done by using a specially designed Knudsen cell with a quartz crucible containing the compound and a thermocouple for temperature control. The quartz crystal micro balance measures the instantaneous flow of particles coming from the Knudsen cell. The error associated with the measurement is ≈ 0.5 ng. With this apparatus it is also possible to control the distance between the substrate for the deposition and the Knudsen cell. A dedicated software displays the pressure of the chambers and the mass deposited on the scale in real time, allowing for the visualization of the time trend of the measured quantities.
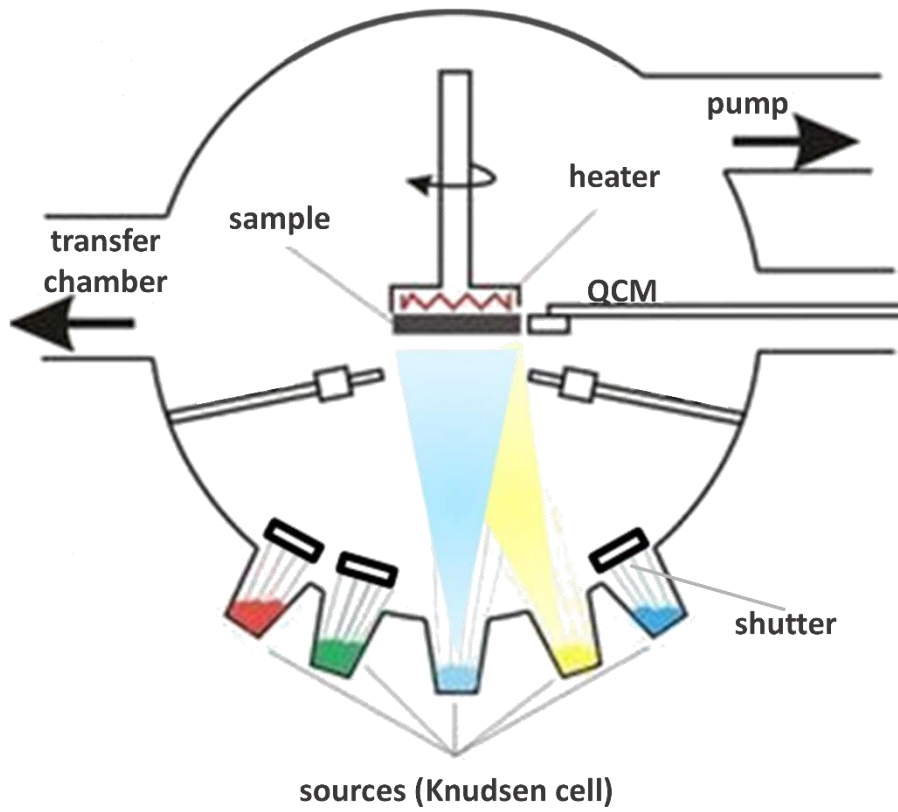
Figure 2.8: Scheme of the MBE apparatus employed for film deposition.

Chapter 3

3. Organic Semiconductors

Organic Semiconductors (OSCs) are a class of carbon-based materials, which combine the electronic advantages of semiconducting properties with the chemical advantages of organic compounds. [47]–[50]

At present, the research in the field of OSC-based devices has grown extensively and has led to mature Organic Light Emission Device (OLED) technology as well as to highly promising applications in Organic Photovoltaics (OPV) [51]–[53] and Organic Field Effect Transistors (OFETs). [54], [55]

Inorganic optoelectronic devices based on silicon are still the fundamental blocks of modern technology. However, attention to organics as a new class of functional materials [56]–[58] has arisen in response to the increasing interest of materials engineering for the development of low-cost, large-area, flexible, and lightweight optoelectronic devices. [56]

OSCs bear different properties from their inorganic counterparts, which comprise silicon, germanium, and metal oxide semiconductors. Inorganic semiconductors are either crystalline or amorphous covalent solids, where the bonds are formed between partially empty atomic orbitals, leading to the formation of almost filled valence or almost empty conduction bands. Because of the low band gaps (1.1 and 0.67 eV for Si and Ge, respectively), thermal excitation from a valence to a conduction band is sufficient to generate free charge carriers, behaving in accordance to the classical band theory. The relative dielectric constant in these systems is high (ε_r = 11 for Si), and, accordingly, the Coulomb interaction in hole and electron pairs is low.

The building blocks of OSCs are instead molecules, of either low (small molecules) or high (polymers) weight, generally characterized by extended π-conjugated systems, which determine their optical and electric properties. Importantly, the highly polarisable π electron densities also determine the nature and the strength of the Van der Waals intermolecular interactions, which are the forces mostly responsible for the cohesion in these materials. Since the intramolecular interactions are stronger, molecules as such remain intact in the materials, but the physical properties of interest arise both from the

chemical nature of the species and the extent of their interaction in the condensed phase. Typically, electronic absorption and emission occur in the near UV or in the visible energy ranges, close to the HOMO-LUMO electronic transitions observed for the corresponding isolated molecule. Thus, these materials have an extrinsic conductivity, induced by the injection of charges at electrodes, the dissociation of photogenerated electron–hole pairs or chemical doping. The observed onset of the optical transition identifies the so-called HOMO-LUMO optical energy gap E_{opt} of the material. Instead, measurements of transport properties yield the bandgap E_t, defined as the minimum energy needed to generate separated a free electron and hole pair. The two quantities differ by the electron-hole binding energy, which is defined as $E_{ex} = E_t - E_{opt}$. [47]
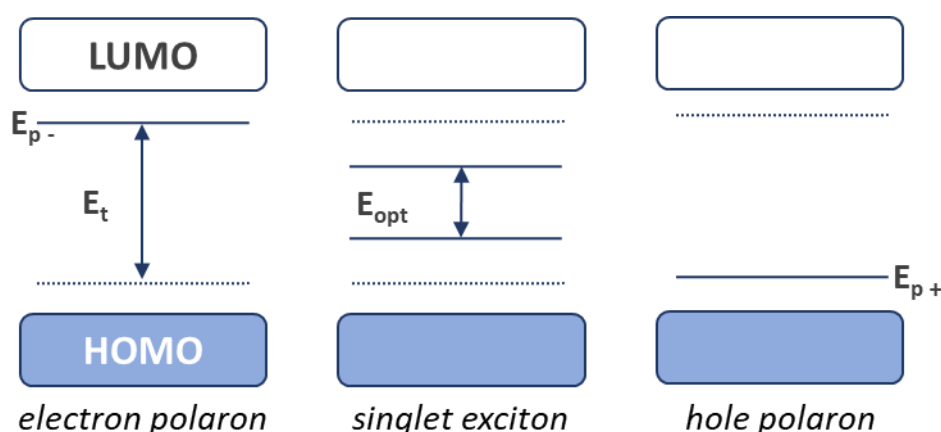
Figure 3.1: Energy band diagram illustrating the definitions used.

Unlike what happens in inorganic systems, relative dielectric constants are low (ε_r = 3-4) and therefore the binding energy of the electron-hole pair is high, implying that the HOMO-LUMO optical gap E_{opt} gives only an estimate of E_t, which is measured from transport methods. [59] In inorganic semiconductors charges are highly delocalized, and the binding energy is of the order of a few meV, so that $E_{opt} \approx E_{ex}$. In organic materials, charge localization leads to large E_{ex} values, and E_{opt} in fact corresponds to the formation of Frenkel (localized) excitons, with the electron and the hole on the same molecule. If the electron and hole pair is localized on close but different molecules, the corresponding bound state is called a localized charge transfer (CT) exciton. Charge transport involves

the generation of the so-called polarons, which are formed by the carrier and its distorted (polarized) surroundings. The combination of a hole polaron and an electron polaron, with binding energies E_{P+} and E_{P-}, respectively, results in the formation of a free exciton. Their energy difference corresponds to $E_t = E_{p-} - E_{p+}$. Figure 3.1 illustrates the definitions given above. [59]

An important difference between inorganic and organic semiconductors concerns the charge transport mechanism. Charge transport in organic semiconductors is controlled by the transfer of an electron in the LUMO of a site (donor) to the empty LUMO of another site (acceptor). Similarly, the hole transport involves the transfer between HOMO levels. In an ideal ordered organic system at 0 K, an electron (a hole) moves coherently within a band of states made of the LUMO (HOMO) orbitals of the constituent molecules, and the charge is delocalized in a propagating wave. However, because of the weak intermolecular interactions, exciton, valence and conduction bands are typically very narrow, ranging from 10 to 100 meV. In a real system at finite temperature, lattice and molecular vibrations are thermally excited and perturb the motion of the charge carriers: in these conditions band transport is possible only if the bandwidth exceeds the magnitude of the perturbation. At high temperatures, perturbations and disorder effects are such that the delocalization of the charge is fully destroyed, and the band model becomes unsuited to describe transport in the molecular system. In fact, charge carriers are localized at individual molecules and move via sequences of non-coherent events between them, in the so-called hopping transport mechanism.

A fundamental advantage of organic compounds over inorganic ones is that the former are almost endless in number and span in size from small molecules to macromolecules. This greatly increases the range of screening and design possibilities for OSCs. Their enormous variability implies that their physical properties can be modified through minor chemical changes, keeping the desired technical application in mind, to obtain synthetically tailor-made systems. [60] Thus, for instance, absorption and emission wavelengths, crystal packing characteristics and solubility can be fined-tuned.

Structurally, it is useful to classify OSC systems in i) molecular single crystals (of small molecules) and ii) films and thin films, either crystalline or amorphous, of small

molecules or polymers. Single crystals of OSC possess long-range periodic order and very few defects, and thus are ideal model systems to study intrinsic structure–property relationships. For applications, thin film technology has widely prevailed, despite the problems connected to the lack of long-range order, the grain boundaries and the defects of the crystalline systems. Compared to silicon-based electronics, organics offer the possibility of solution-processing for low-cost and large-area devices via numerous techniques such as spin coating, dip coating, spray coating, inkjet printing, Langmuir-Blodgett for film fabrication. [50], [54] The low processing temperature, combined with the mechanical flexibility of organic materials, has provided large opportunities to challenge silicon based devices. [11] Another advantage is that the extremely high chemical purity necessary for silicon is not such a stringent requirement for organics. What is instead crucial, in applications employing either single crystals or crystalline films, is the control of polymorphism, a most common phenomenon in organic materials where molecules are held together by the weak Van der Waals force field. Exerting such a control, as mentioned above, allows selecting the best suited polymorph for the sought application, but another issue is relevant in the engineering of the OSC system and needs consideration. This is the occurrence of phase mixing, i.e. the simultaneous presence of more solid phases, which typically constitutes an intrinsic source of disorder and has detrimental effects on charge transport properties. [14], [15] Despite being considered less important than chemical contamination, phase inhomogeneities are in fact widespread structural defects, because of the characteristics of the OSC molecules, which favour the occurrence of different polymorphs of close energy. The extended π-conjugation required to establish effective inter-molecular transfer integrals, which allow for electronic delocalization, is in fact often encountered in molecules having planar or quasi-planar cores, with flexible lateral substituents and functional groups, thus exhibiting many alternative packing arrangements (i.e. polymorphs) with energy differences as small as a few kJ. [61], [62] Notably, also the small differences among phases may affect the narrow bandwidth of the semiconductor or the coupling between the charge motion and the lattice vibrations. Thus, the point to stress is that, together with chemical purity,

physical purity is an important parameter to keep under control when seeking optimal and reproducible charge transport performance in crystalline systems.

Another very important aspect of polymorphism in OSC is that the thin films are obtained by growths at the solid interface of a variety of different substrates, spanning from silicon and aluminium oxides to polymers, composite materials and graphene and paper. [63]

As previously described, the material crystallizing in these conditions often displays polymorphs different from those observed in the bulk, which have been commonly called SIPs in the literature, [17], [18] but we prefer to group under the broad denomination of surface stabilized structures. Given the importance of the structural order in the OSC films in determining the charge carrier mobility and the performance of the device, the knowledge of the surface structures is of crucial importance and in fact the finding of new polymorph a resource to exploit. [64] A full structural characterization of such structure, however, is still a challenging task. To solve the structure of thin films from a few monolayers up to some hundreds of nm, grazing incidence X-ray diffraction (GIXD) is, together with electron diffraction, the method of choice. Unfortunately, measuring GIXD or even electron diffraction provides a limited number of Bragg reflections due to weak diffraction, small scattering volumes, high aspect ratio or defects. This restricts the usage of the conventional structure solving approaches suitable for single crystals and suggest to exploit the synergy of computational tools and complementary experimental techniques to gather information on the film characteristics.

Pigment based OSC

Very recently, the field of application of OSC has intercepted the requirements of the so-called "Green Electronics", which represents an emerging area of research finalized to the use of compounds of natural origin and to find green synthetic routes to obtain synthetic materials for environmentally safe i.e. biodegradable and/or biocompatible devices. [65] On one hand, the entire field of the electronic based on inorganics is energetically highly demanding, [66] more than that based on organics, and this makes the latter very appealing. On the other hand, the short lifetime of most plastic

electronics-based devices is certainly matter of concern, as their ever-increasing use will soon pose the problem of their disposal: hence, the importance of the search for bio-degradability and compatibility of non- toxic compounds. [65], [67], [68] Just to cite a few instances of a literature which is getting very extensive, nature and bio- inspired, environmentally friendly OSCs have already been tested in organic thin film transistors (OFETSs), [69]–[71] with very interesting results. Totally disintegrable and biocompatible semiconducting polymers for OFETS have also been synthesized, which hold the additional promise of being usable in implantable biomedical applications. [72], [73]

Among the compounds that have received much attention as being of natural or nature-inspired origin, there are the pigments belonging to the classes of Indigoids and Quinacridone. These are all hydrogen bonded dyes which include, together with the parent systems Indigo and Quinacridone, the Indigo isomer Epindolidione and various derivatives such as 6,6'-Dithienylindigo and 6,6-Dibromoindigo, the latter known as Tyrian purple. [74]–[78] OFET hole mobilities of the order of 0.1 to 2 cm^2/Vs have been measured for these systems, with Indigo and Tyrian purple displaying also p-type character. An interesting feature some of these compounds have in common is being somehow re-discovered systems, which have been known, synthesized and used on an industrial scale for a long time, and are therefore easily accessible at a low cost. Their excellent stability in air constitutes an appealing characteristic, compared to other OSC, [78] but the low solubility, typical of the vat dyes, limits their processability or requires chemical manipulations.

The origin of the low solubility lies mostly – but not completely – in the strong hydrogen bonds, which play an important role in determining the physical-chemical properties of these materials and govern the molecular organization of the crystal state. Strong π- π- stacking interactions are also present, characterizing the photo-physics in solution and the crystal packing, and, most importantly, regulating the charge transport properties in these small molecules in which the π-electron delocalization is limited, unlike the most common OSCs. That said, the reason why, Indigo, for instance, works as a semiconductor with performances comparable to carefully engineered material does not appear really clarified.

In the following of the chapter, the results for Indigo, Thioindigo and Quinacridone are presented, selected as representative for OSC pigments and shown in Figure 3.2.
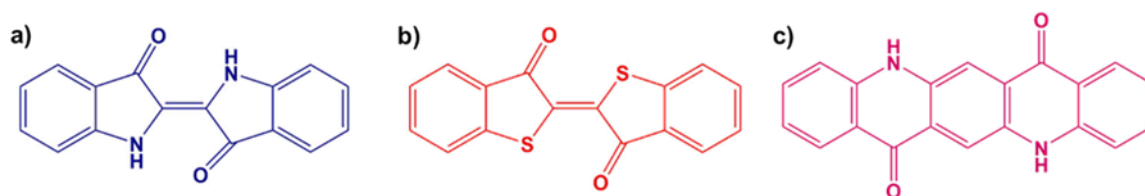
Figure 3.2: Molecular structure of a) Indigo, b) Thioindigo, c) Quinacridone.

Note that in Thioindigo, a synthetic Indigoid which has been since a long time commercially available, the intermolecular H-bonds characterizing the parent system are absent, but it nonetheless shares with Indigo structural and semiconducting characteristics.

As described in the introduction (see paragraph 1.1), similar approaches have basically guided the investigation. Starting from the bulk, various single crystals of the compounds were grown with different methods and then were structurally and spectroscopically characterized. Such a procedure makes possible to associate each crystal form to a measured Raman spectrum, which extends from the region of lattice phonons to the intra-molecular modes. The research group used DFT calculations to estimate the relative energies of the various polymorphic modifications, and to assist the spectral assignments.

Once the situation with the bulk state of a given system was clarified, investigation moved to films. Thin film samples were prepared by means of methods selected either following the literature or guided by the physical-chemical properties of the compound under examination.

3.1. Indigo

3.1.1. Introduction

Archaeological excavations have shown that Indigo [2,2'-Bis(2,3-dihydro-3-oxoindolyliden)] was used as a dye for textiles for millennia in the Indian subcontinent. Most likely, dye precursors were extracted from the plant Indigofera tinctoria, the cultivation of which spread from India to the rest of tropical Asia. In medieval Europe, the Indigo dye was produced from the woad plant (Isatis tinctoria). [76] However, in the 17th century imports of the better-quality Indigo from India destroyed the European woad industry. During this time, the Indian production was dominated by the British, but the death blow to the industry of the natural-origin material started with Adolf von Baeyer's discovery in 1883 of the Indigo chemical structure and the implementation of synthetic production routes, even though the early methods were not initially very competitive with natural Indigo. It was not until 1897, following major research investments, that K. Heumann developed at BASF a practical synthetic route, later improved by J. Pfleger. Synthetically produced Indigo was of superior quality to Indigo from plants and finally replaced it on the market. Nowadays, Indigo is the most widely produced low cost dye in the world, with a worldwide production of thousands of tons, most of which used for dyeing denim fabric. [79]–[82]

In addition to its largely exploited properties as a dye, Indigo has attracted a novel interest in material science. It has been shown to be a most promising biocompatible semiconductor, exhibiting ambipolar transport in OTFTs, [74], [77], [83], [84] with a bandgap of 1.7 eV, well-balanced electron and hole mobilities of 1×10^{-2} cm^2 V^{-1} s^{-1} and good stability against degradation in air. [83] In the field of organic electronic, ambipolar charge

transport is an important requirement for the development of integrated microelectronic circuits and optoelectronic devices, but the narrow choice of organic materials available currently impede widespread applications. [83]

As a pigment, Indigo is highly insoluble in most solvents, a feature which makes difficult the fabrication of the thin films for device employment by wet deposition methods, and dry physical deposition processes are usually preferred. [85], [86] Its properties in films were found to be strongly dependent on the growth surface, [85], [86] with hydrocarbon-based materials such as polyethylene and tetratetracontane outperforming other dielectrics. This has been attributed to a polymorphic modification, induced by the dielectric acting as a template. [86] This suggestion needed further scrutiny for a number of reasons. First, a surface induced polymorph was detected and characterized in Tyrian purple films, [75] and the occurrence of the same in Indigo could constitute an interesting parallel. Secondly, the study of the Indigo films presented some complexities, [85] and characteristics such as degree of crystallinity, polymorphism, morphology and molecular orientation at the solid interface, all contributing to regulate the transport properties the material, were far from being clarified.

A first issue concerns the solid phase present in the films. In its bulk crystal state, Indigo is known to display two polymorphs, named A and B, having very similar structures. [87]–[92] As illustrated more in detail in the next paragraph, both forms are monoclinic with very close unit cell parameters and were found in this work to grow as concomitant in most conditions.

In a X-ray characterization of vapor deposited 40 nm thick Indigo films on Si/SiO_x, [85] the specular scan showed only two reflections, which could be assigned to weak crystallographic orientations along the $(1\ 0\ 0)$ and $(2\ 1\ 0)$ planes of either polymorph A or B. This left the film phase undetermined and prevented the detection of the possible concomitant growth observed in the bulk. In another study, [83] vapor grown films of different thicknesses and on various substrates were shown to display a sharp single diffraction peak, which was taken as an indication of a crystalline texture with a single preferential orientation, with no reference to a specific polymorph. Together with the usually observed $(1\ 0\ 0)$ reflection, a new peak was detected in the GIWAXS pattern of a

film grown on paraffin. [86] This was in fact the feature identified as due to a new crystal modification, described as a distorted monoclinic structure of polymorph A.

Concerning the morphology, Indigo films were either found uniform and highly crystalline on most substrates, [83] or, on the contrary, rough and poorly homogeneous, [86] thus denoting a strong dependence on the growth conditions. Lastly, when analysing the forces driving the formation and shaping the characteristics of the film crystal state, the role of strong intermolecular H-bonds has been either stressed [83], [85] or considered overestimated. [86]

Aiming to clarify the still open issues mentioned above, related to the polymorph landscape of the Indigo system, a first part of the work dealt with the structural and Raman properties of crystalline Indigo in the bulk state and drop cast films. This allowed us to understand which polymorphs grow under specific conditions and under what circumstances the coexistence of polymorphic structures has to be expected.

A combination of single-crystal and powder X-ray diffraction (XRD) techniques provided a clear "picture" of the polymorphic composition in the bulk samples, showing that A and B modifications often coexist and that, unlike what previously assumed, [87] phase B seems to be the predominant one.

In the films obtained by drop casting, the XRD could not identify unambiguously the polymorph present, in agreement with what reported in the literature for the vapor grown samples, as detailed above. However, the Raman investigations on the bulk samples were able to identify the vibrational fingerprint of each polymorph and such a knowledge could be successfully transferred to characterize the drop-cast samples and to reveal that the polymorphs coexist at the micron scale in crystallites. The spectral investigation focused both on the low-energy region (10–150 cm^{-1}), where the lattice phonons are recorded, and on selected intramolecular modes in the ranges 100–200 and 1550–1600 cm^{-1}. The frequencies of the latter were found to be sensitive to the slight modification of the H bond patterns deriving from the different molecular packing of the two structures. Indeed, these two energy regimes supply reliable spectroscopic markers for Indigo polymorph discrimination and an estimate of the degree of crystallinity.

The investigation of structure and morphology of Indigo thin films was conducted on samples obtained by ultra-high vacuum deposition at the CNR-ISM institute of Bologna, carefully determining the required conditions of chemical purity and the growth parameters, which allowed us to obtain reproducible film morphologic characteristics, as checked by the AFM characterization performed at the same institution. In addition to Si/SiOx substrate, we tested film growth on the Tetoron® polymeric substrate (polyethylene terephthalate or PET film), which owing to its properties of flexibility, optical transparency and chemical resistance could be used for flexible devices.

Relying on the results given by the spectroscopy analysis of the Indigo bulk crystals, the Raman spectra showed that B is the only polymorph which grows in the films. Such an information was not accessible to the XRD measurements, which met the already mentioned difficulties in the phase identification. Finally, Transmission Electron Microscopy (TEM) measurements performed at the CNRS Charles Sadron Institute in Strasbourg were used to shed light on the molecular organization of the Indigo molecules at the solid interface.

The picture that emerges from this investigation is that of a molecular arrangement in the film in fact driven by the formation of strong hydrogen bridging bonds, which determine the development of the structure in a preferential lattice direction, along which such interactions are exerted. Consequently, the crystallinity of the film is generally poor even though it can be improved with a solvent vapor annealing (SVA) treatment.

3.1.2. Sample preparation

Single Crystal growth: Indigo (TCI Chemicals, 97%) was purified by double sublimation at 200 °C at low pressure of nitrogen to avoid thermal oxidation, obtaining microcrystals of irregular shape. By using cooling water at ≈ 20 °C at the apparatus cold finger, we found that both the polymorphic composition and the dimensions of the microcrystals forming the sublimed material were strongly dependent on the deposition temperature. In fact, the largest crystals were obtained without the cooling fluid, with a

temperature of ≈ 130-140 °C on the cold finger condenser (see paragraph 3.1.8 – Appendix II). Small, elongated, single crystals (about 200 μm long) were grown by Physical Vapor Transport (PVT). For PVT growth, the material was placed at one end of an evacuated glass ampule, which was sealed after three cycles of evacuation and nitrogen purging. The end of the ampule containing the material was then placed horizontally in a furnace kept at 250 °C. At equilibrium a temperature gradient of ≈ 13 °C/cm was measured.

Despite the low solubility of Indigo in most organic solvents, crystals were also obtained by dissolving the compound in boiling DMSO and leaving the resulting filtered solution to slowly evaporate.

Drop cast films preparation: Crystalline films were obtained by drop casting filtered (0.2 μm filter) saturated solutions in 1,2-dichlorobenzene and acetonitrile onto a Si/SiO_x wafer previously cleaned by an ultrasonic bath in acetone, isopropyl alcohol, and deionized water, and finally dried under nitrogen. After drop casting, the films were dried on a hot plate at 50°C.

Vapor grown thin films preparation: Commercial Indigo powder (TCI Chemicals, 97%), entirely composed of polymorph B, was first purified by double sublimation at 200 °C in low pressure of nitrogen to avoid thermal oxidation, as described above for single crystal preparation. The purification stage of the raw material is an essential step to obtain homogeneous and reproducible films, due to the high content of impurities of the commercial product. The large crystals at the highest deposition temperature of ≈ 130-140 °C were used as the starting material for the film growth in the UHV chamber, as it was verified that they yielded optimal characteristics of reproducibility, probably due to increased purity or to segregation of contaminants. Indigo films were deposited on silicon wafer with 100 nm thick layer of thermally grown silicon oxide. Substrates were cleaned with acetone vapors to get rid of organic contaminants prior to Indigo deposition. Thin films growth was performed by thermal sublimation under ultrahigh vacuum, with a base pressure of ≈ 10^{-7} mBar. By keeping constant the total amount of material on the sample

(1000 ng), different rates were tested for the deposition (10, 20, 42, 70, 101, 170 and 200 ng/min) and Si/SiO$_x$ substrate was held at room temperature.

Three representative deposition rates (namely, 10, 70 and 200 ng/min) were used in the fabrication of thin films on Tetoron® (DuPont Teijin Films^{TM}), a polymeric substrate based on polyethylene terephthalate (PET). Tetoron® is a thermoplastic semi-crystalline and biaxially oriented PET film, industrially prepared by roll to roll processing. [93] In this process, the stretching of the melt in two perpendicular directions induces the biaxial orientation, while post-processing thermal treatment induces the partial crystallinity. The material displays high mechanical strength, good resistance to a wide range of chemicals and solvents (including acetone, used for cleaning procedures), low water absorption, high optical transparency, excellent dielectric properties, good dimensional stability and good thermal resistance in terms of shrinkage and degradation of the polymer chains. [93]

The substrate (1x1 cm^2 size) was cleaned by an ultrasonic bath in Milli-Q water, then rinsed in acetone and finally dried under nitrogen. To achieve a surface roughness comparable to the silicon oxide substrates, Tetoron® substrates, sandwiched between two wafers of Si/SiO$_x$ and weighted with a total of 1800 g, were subjected to thermal annealing at 110 °C on a hot plate and cooled under nitrogen. The achieved roughness was of (0.7 ± 0.1) nm, as determined by AFM. The total amount of material deposited, and the other growth parameters, were kept constant in all samples and identical to those used for the Si/SiO$_x$ substrates.

3.1.3. Experimental methods

Raman Spectroscopy: Raman spectra in the energy interval of the lattice phonons with excitation wavelengths at 647.1 and 752.5 nm. Instead in the energy interval of the intramolecular vibrations was used the excitation wavelength at 785 nm. For the Indigo case, power was reduced by neutral density filters to avoid sample damage.

X-ray diffraction: Single-crystal data for Indigo grown by PVT were collected both at RT and at LT (210 K) on an Oxford X'Calibur S CCD diffractometer equipped with a

graphite monochromator (Mo-Kα radiation, λ = 0.71073 Å) and with an Oxford CryoStream800 cryostat. All non-hydrogen atoms were refined anisotropically. HCH atoms were added in calculated positions, HNH atoms were directly located on the N atoms and refined riding on their respective atoms. SHELX97 [94] was used for structure solution and refinement on F^2. The program Mercury [95] was used to calculate intermolecular interactions and to simulate the BHDF crystal morphology, which was compared with the experimental one determined with the software Oxford CrysAlisPro171.34.36. [96] VESTA3 [97] and Mercury [95] were used for molecular graphics.

For single crystal face indexing, phase identification of polycrystalline samples and films samples, X-ray powder diffraction patterns (XRPD) were collected in the 2θ range between 5°–40°. This was done on a PANalytical X'Pert PRO automated diffractometer with Bragg-Brentano geometry equipped with an X'Celerator detector, in the 2θ range 5–40°, using Cu Kα radiation without a monochromator (step size, 0.02°; time/step, 20 s; 0.04 rad soller; 40mA x 40kV). The program Mercury [95] was used for the simulation of X-ray powder patterns on the basis of single crystal data retrieved from the Cambridge structural database - CSD (CSD refcodes MIXCEE and INDIGO02 for polymorphs A and B, respectively). [98] Chemical and structural identity between bulk materials and single crystal structures was always verified by comparing experimental and simulated powder diffraction patterns. For Rietveld refinement purposes, X-ray powder diffraction patterns (XRPD) in the 2θ range between 3–70° were collected on a PANalytical X'Pert PRO automated diffractometer equipped with Focusing Mirror and Pixcel detector in transmission geometry (step size 0.0260°, time/step 200 s, 0.02 rad soller; VxA 40kV x 40mA). Powder diffraction data were analyzed with the software TOPAS4.1. [99] A shifted Chebyshev function with 7 parameters and a Pseudo–Voigt function (TCHZ type) were used to fit background and peak shapes, respectively. A spherical harmonics model was used to describe the preferred orientation. An overall thermal parameter for the C, N, O atoms was adopted. Refinements converged to Rwp = 7.2%, Rp = 5.3%; Rwp = 10.3%, Rp = 8.0 % for sublimed and commercial powders, respectively.

Profilometer and AFM: As reported above, Indigo films were grown by depositing the same amount of molecules, i.e. 1000 ng. Films thicknesses were measured by averaging the thickness of each film in three different step edge positions by means of a stylus profiler (P-7 KLA Tencor, Milpitas, California, USA). Topographic images, collected by AFM operating in intermittent contact (SOLVER HV-MFM, NT-MDT Zelenograd, Moscow, RU), were morphologically analysed in order to investigate the evolution of Indigo films vs the deposition rate v.

Transmission Electron microscope: TEM was performed, both in bright field electron microscopy and electron diffraction modes, by using a Philips CM12 TEM fitted with a LaB6 filament and equipped of an SIS Megaview III CCD camera. The following flotation technique was adopted to transfer the film on the copper electron microscopy grids (200 mesh) and prepare the Indigo thin films for TEM analysis. First, the samples (Indigo on silicon wafer) were coated with a thin carbon film in an Edwards E306A coating system. Second, the carbon-coated Indigo films were removed from the Si/SiO_x substrate by gently submerging the samples in a 5%HF acid solution in water. The carbon and Indigo films were retrieved with TEM grids directly from the HF solution. They were subsequently washed with a large amount of Milli-Q water.

Diffraction measurements were taken in the selected area electron diffraction (SAED) mode. The accelerating voltage was 120 kV and, in order to minimize the beam damage, we constantly used the low dose mode of the microscope together with small C2 aperture and low current (spot 5–7 setting and 24000x). The selected area electron diffraction patterns patterns were recorded at a 2.05 m chamber length using a 5µm condenser (C2) aperture in order to have a near-parallel illumination, about 50 µm wide on the specimen. In Selected Area Electron Diffraction (SAED) mode an aperture of 100 µm is inserted in the image plane in order to pick a specimen area of about 500 nm. For the analysis of the diffraction, we employed the Cerius2 simulation package (Accelrys, Waltham, USA and Cambridge, UK).

3.1.4. Indigo crystal structures

This paragraph summarises the literature structural information on Indigo polymorphs, updated with our recent experimental and computational results. Table 3.1 reports all the available experimental published data and compares them to the computations reported in the work by Salzillo *et al.*, [89] which will be detailed in the following.

Indigo is known to crystallise in two very similar structures, named A and B. [87]–[92] In Ref. [92] the occurrence of a second structure, corresponding to polymorph B is reported for the first time. In that work it was noted that the cell parameters of form B were such that only the cell length *a* and the monoclinic angle β differed from those of polymorph A. Besides, B was found to be strongly metastable, so that the structural transformation into A could be driven by mechanical action, simply sectioning a sample perpendicularly to the growth direction. The spontaneous transition was described as due to a slip by *c*/4 of the molecular layers with respect to each other, bringing the lattice into the denser packing of A. In the two later reports of B, [87], [88] the lack of stability was not detected, even though in the former paper it was always obtained as a by-product together with form A, and its selective growth as single crystal was only possible close to the decomposition temperature of the compound. [88] Structurally very similar to form A, form B is reported as monoclinic P2$_1$/c [87] or P2$_1$/n. [88] Its larger cell volume (about 3% at RT) suggested that B is metastable at low T, but no phase transition was detected by cooling down to 213 K. [88]

Polymorphs A and B contain two molecules per unit cell (Z=2), having C$_i$ molecular symmetry and related to each other by a 2$_1$ screw axis**.** The planar molecular geometry in the crystal differs very little from C$_{2h}$ symmetry corresponding to the minimum energy configuration determined by the DFT calculation for the isolated molecule, showing that the influence of crystal packing on it is negligible. Both A and B polymorphs display analogous intermolecular interaction patterns: translationally equivalent molecules form stacks with face-to-face π-π interactions, and are connected by a network of hydrogen bondings which weaken the intramolecular ones. Even the packings are nearly identical

and the main difference between the polymorphs is in a subtle reciprocal orientation of the molecules, which leads to slightly different stackings (see Figure 3.3). Although small, this difference could affect electrical properties of Indigo based thin film devices, hence the need to know exactly what polymorph we are dealing with.

Figure 3.3: Comparison between the two structures of the Indigo polymorphs.

The mass densities are slightly different with 1.50 g/cm^3 for polymorph A and 1.46 g/cm^3 for polymorph B. [85] Although small, this difference could affect electrical properties of Indigo based thin film devices, hence the need to know exactly what polymorph we are dealing with.
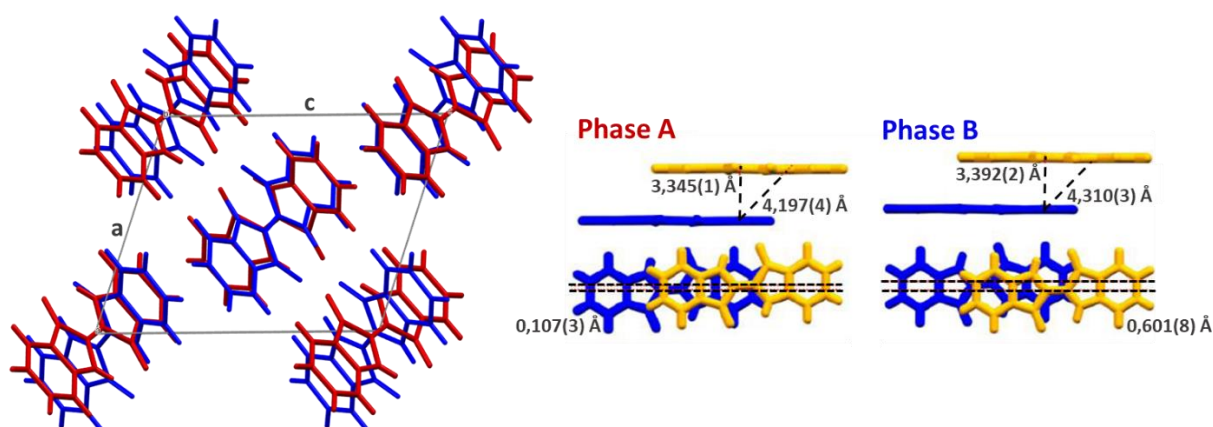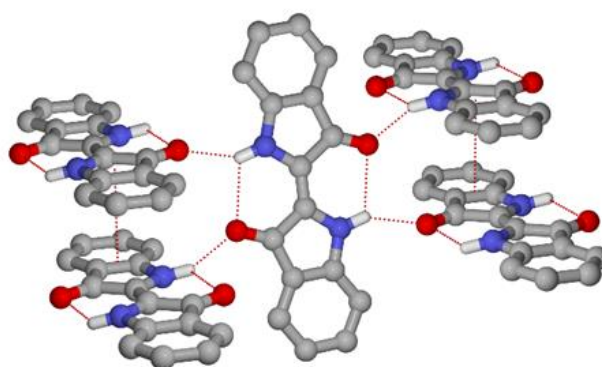

Figure 3.4: Network of intra- and inter-molecular hydrogen bonds detected within crystalline indigo grown by PVT and corresponding to form A.

A clear representation of the network of intra- and inter-molecular hydrogen bonds is given in Figure 3.4.

Table 3.1: Lattice parameters and sublimation energies ΔsubH (T) of crystalline Indigo. Experiments are compared to calculations, either with the Tkatchenko-Scheffler (TS) [100] or many-body dispersion (MBD) DFT [101] method. All the structures are monoclinic with Z=2.

REFCODE	Form	a (Å)	b (Å)	c (Å)	β (deg)	Volume (Å³)	T (K)	Space Group	ΔsubH (T) (kcal/mol)
Our work [89]	A	9.2850(9)	5.7941(4)	11.5722(9)	108.710(10)	589.66(8)	RT	P2$_1$/n	
	A	9.1942(8)	5.7876(6)	11.4878(8)	108.268(9)	580.48(9)	211	P2$_1$/n	
INDIGO [92]	A	9.24(3)	5.77(2)	12.22(3)	117	580.497	RT	P2$_1$/c	
INDIGO01 [91]	A	9.23	5.74	12.25	116.5	580.819	RT	P2$_1$/c	32
INDIGO03 [90]	A	9.24	5.77	12.22	117	580.497	RT	P2$_1$/c	
INDIGO02 [87]	B	10.84(1)	5.887(6)	12.28(1)	130.02(5)	600.134	RT	P2$_1$/c	
INDIGO04 [88]	B	9.799(2)	5.9064(10)	10.755(3)	106.781(18)	595.958	213	P2$_1$/n	
DFT (TS) [89]	A	9.107	5.741	11.489	108.53	569.6			45.5
DFT (MBD) [89]	A	9.148	5.779	11.465	108.81	573.71		P2$_1$/n	37.4
DFT (TS) [89]	B	9.633	5.922	10.468	105.94	574.16			45.2
DFT (MBD) [89]	B	9.732	5.885	11.559	106.9	578.68			37.4

The samples grown by PVT for the work of this thesis were analyzed with single crystal XRD at both room and low temperature, as reported in the Experimental Methods paragraph. They have been unambiguously identified as A and the structure was solved and refined in the monoclinic P2$_1$/n space group. We determined accurate distances for the intra- and inter- molecular hydrogen bondings between N-H and C=O groups, which were found to be of 2.915(2) Å and 2.875(2) Å, respectively] leading to the assembly shown in Figure 3.5.
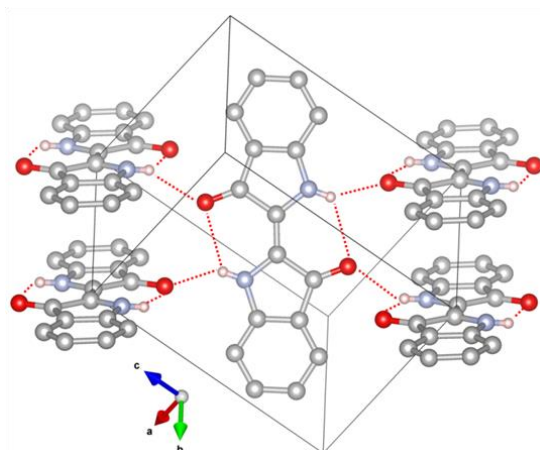
Figure 3.5: Network of intra- and inter-molecular hydrogen bonds detected within crystalline Indigo grown by PVT and corresponding to form A.

To confirm the absence of any phase transition upon cooling, additional data sets were acquired at 210 K and the unit cell was determined also at 150 K. Data collection and refinement details are listed in the Table A1 in the Appendix I (paragraph 3.1.8).

With the aim of recording polarized Raman (explained in paragraph 2.1.4) of the newly obtained Indigo samples, PVT grown single crystals of form A were also analysed for face indexing. In particular, we analysed their crystal morphology by comparing the simulated BFDH morphology with that experimentally determined after face indexing. As can be seen in Figure 3.6 the agreement is good, as the smaller facets are not actually observed.
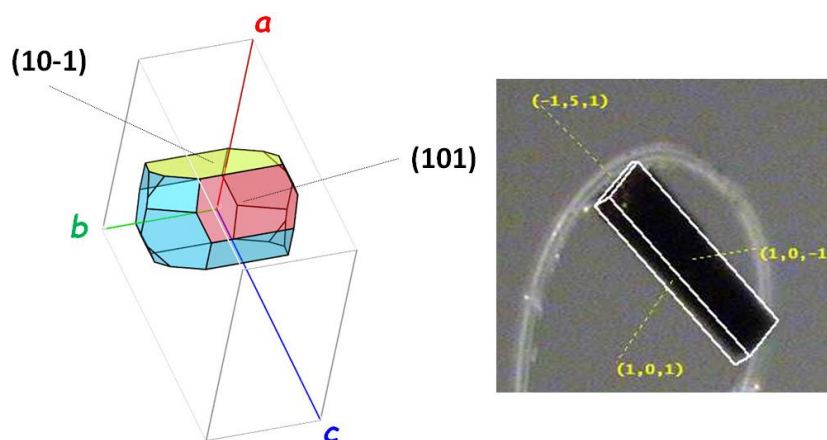
Figure 3.6: External morphology for single crystals of Indigo grown by PVT (form A): simulated BDFH on the basis of single crystal structure (left), and experimentally determined after face indexing (right).

To confirm this result, XRD patterns on the flat crystal surface were also recorded, as this would provide information about the face oriented parallel to the surface on which the crystal lies. Thus, the very crystal used for data collection was placed onto the sample holder for ten different times, each time recording its pattern. Seven out of ten times only the diffraction peaks corresponding to the (n0-n) Miller planes were observed, whereas the remaining times the (n0n) ones were detected, (see Figure 3.6) This fully agrees with the face indexed from single crystal XRD data, yielding namely, a parallelepiped-shaped sample with the former facet (n0-n) larger than the latter (see Figure 3.7).
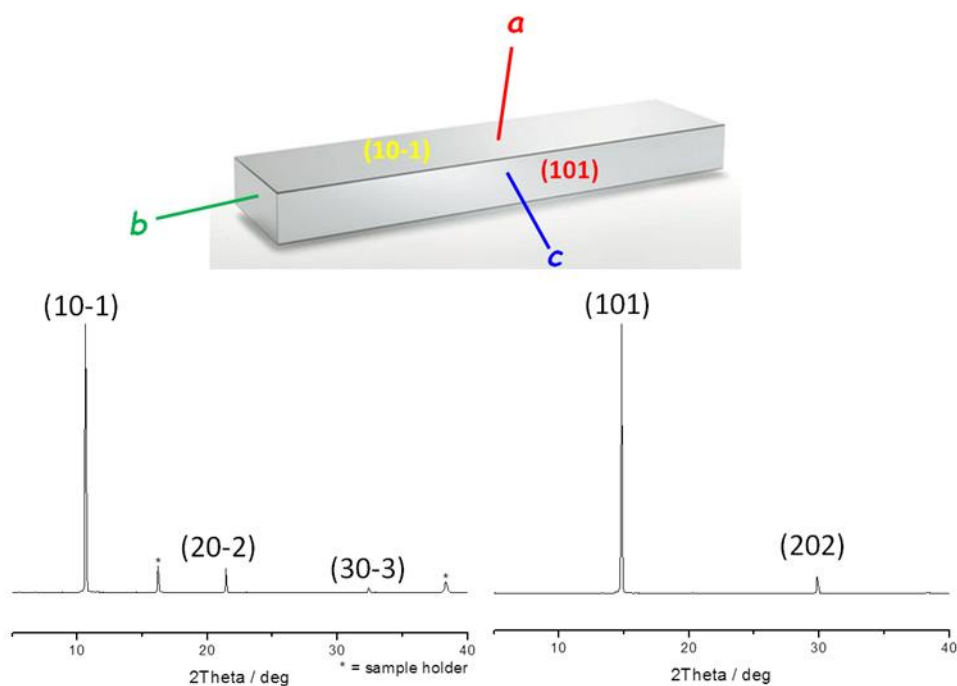
Figure 3.7: Crystal morphology (modeled, top) and XRD pattern of a single crystal lying flat on the sample holder (bottom). Peaks with an asterisk belong to the sample holder.

Commercial and sublimed Indigo were not available in sufficiently large single crystals and were only analyzed only by powder XRD. The corresponding diffractograms are reported in Figure 3.8.
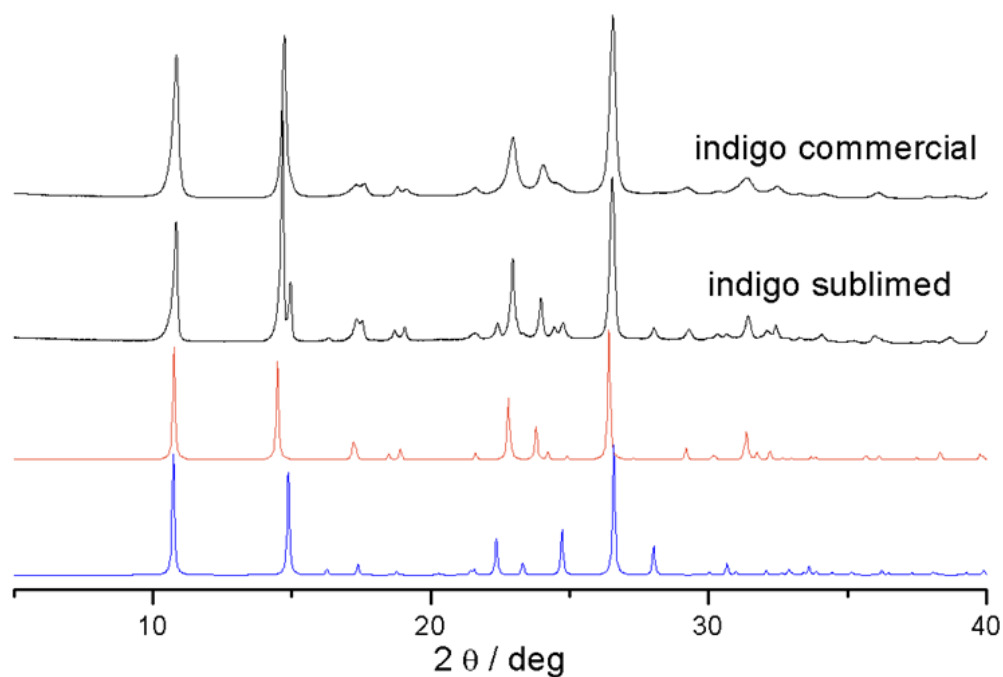
Figure 3.8: Comparison between calculated (blue- and orange-lines for A and B, respectively) and experimental (black lines) XRPD patterns for commercial and sublimed Indigo samples.

In commercial Indigo, the peaks appear slightly broadened, but the pattern corresponds to that of polymorph B, with possible presence also of A. The sublimation process produces an enrichment in A, in agreement with the literature findings [88] Specifically, polymorph A content depends on the sublimation deposition temperature: the higher the temperature, the higher the content. To evaluate the relative amounts of polymorphs after sublimation, *Rietveld* refinement was used, as shown in Figure 3.9. Whereas, as mentioned above, B is largely prevailing (*ca.* 93%) in the commercial specimen, by sublimation the A amount rises to nearly 30% and ≈50% when the cold finger temperature in brought up to 30 °C and 130 °C, respectively.
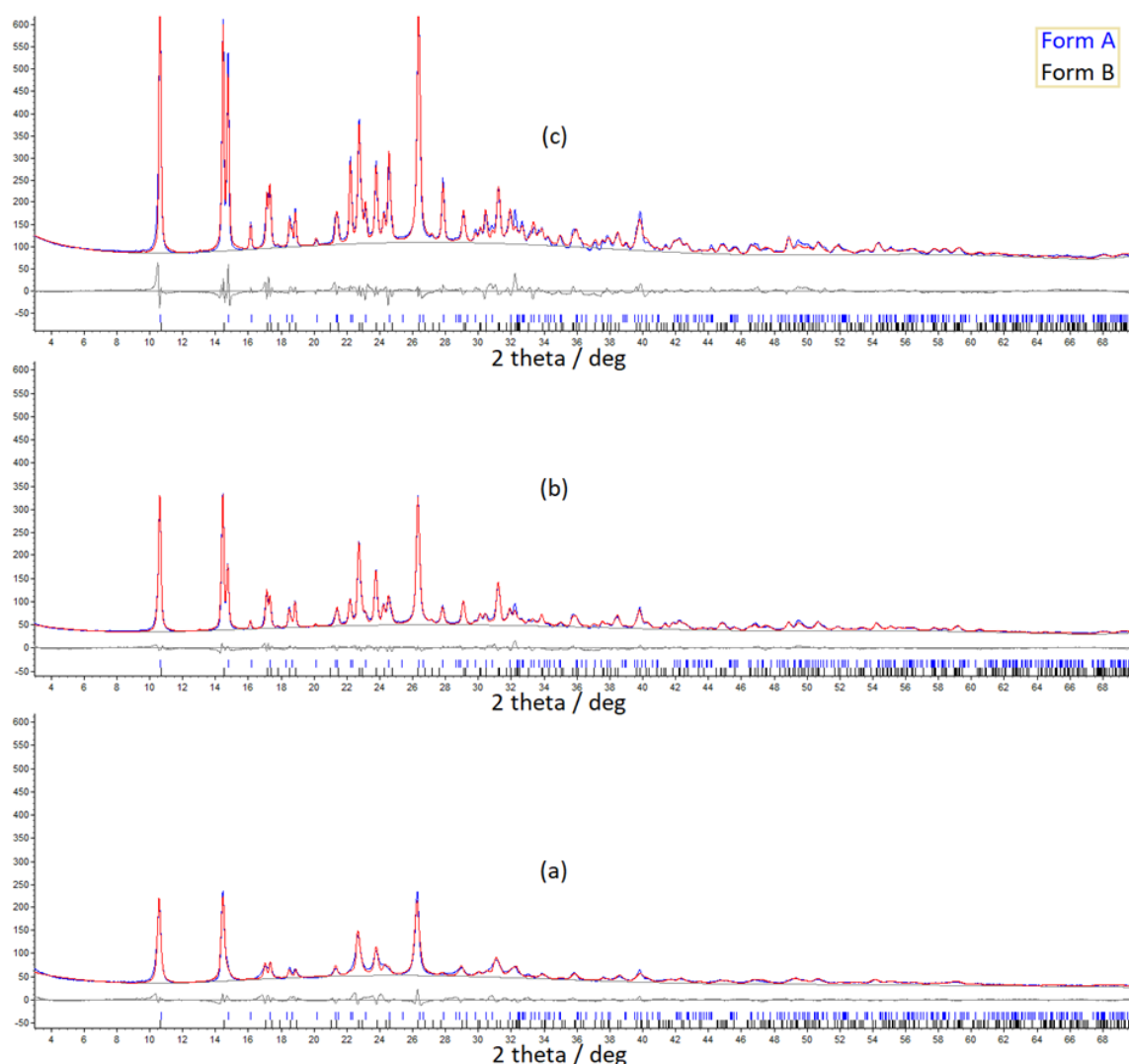
Figure 3.9: Experimental (blue), calculated (red), difference (grey), and background (light-gray) patterns for), sublimed (a) commercial (b), and sublimed without cooling the sublimator cold finger (c) samples of Indigo; x axis is in degrees of 2ϑ.

Altogether, the new collected data agree with previous literature findings about the number and the nature of Indigo polymorphs in the bulk. However, with the presence of a collection of structures determined over a time span of several years and in experimental conditions either variable or unspecified, it is legitimate to wonder whether the polymorph assignment is actually correct in all cases. To probe this, our group has applied the "Crystal Inherent Structure" method,[102], [103] which is an efficient way of discerning experimental structures which, appear to be very similar albeit not identical. The method relies on the calculation of the crystal structure of minimum energy, identified as the local minimum corresponding to the configuration of mechanical

equilibrium for a given lattice. Details of the approach, which employed an atom-atom potential model combined with point charges interactions to account for electrostatic contributions for energy calculation, can be found in Ref. [89] Such an analysis enabled us to confirm that for all the experiments only two distinct minima can be identified, corresponding to form A (this work and CSD refcodes INDIGO, [92] INDIGO01, [91] INDIGO3 [90]) and form B (INDIGO02, [87] INDIGO04 [88]).

Once the existence of only two Indigo crystal structures was assessed, the more computer time consuming DFT-vdw calculations were run for these, to obtain information about their relative energy stability and to understand whether form B could really be identified as the form metastable at ambient conditions. We first notice the satisfactory agreement between experimental and computed call parameters. This makes us confident of the reliability of the method also in the simulation of the crystal vibrational properties, as described in the next paragraphs. The computed volume for polymorph A is smaller than for polymorph B in agreement, and regardless of the details of the correction adopted to account for dispersion interactions, the A phase turns out to be (slightly) more stable than the B phase at 0 K. When temperature effects are accounted for, the energy difference between the phase gets narrower, and even though the incertitude affecting the calculation does not afford intercepting a transition temperature, the general trend suggests that B should be located in the higher temperature region of Indigo phase diagram.

3.1.5. Micro Raman characterization of Indigo in the bulk state

The first crucial step in employing Raman spectroscopy to identify polymorphs is to measure and/or calculate the reference spectra for samples in which the actual structure has been determined by XRD.

In packing polymorphs like Indigo, in which the molecular configuration remains the same due to the system rigidity, the low energy range of the vibrational spectrum usually carries all the spectral differences among distinct lattices. As explained in the introduction (see paragraph 3.1.1), this is because modes observed here hold the

character of lattice phonons, or vibrations in which molecules oscillate as a whole around the lattice equilibrium positions, subjected to the force field of the dispersion intermolecular interactions. The weak restoring forces, combined with the high inertia moments of the molecular body, determine the low energy of the modes, while the spectral features depend on the details of interaction pattern in the crystal packing. This makes Raman spectra in this range an optimal probe of structural properties, as here each polymorph displays its own unique spectrum.

The process of associating a spectrum to a structure may appear a straightforward one when described in published papers, but it is most often a trial and error procedure. In our case, for instance, we selected the samples to probe by XRD by recording a-priori Raman spectra on many of them and choosing those displaying a range of different spectral features. In response to the XRD results, growth methods were modified, growth conditions adjusted and speculations on the obtained results made. This confirms that crystal growth, and polymorph selection, are subjected to a sort of gray magic, the outcome of which is in the hand of the PhD student playing the sorcerer's apprentice role.

The lattice phonon Raman spectrum of polymorph A was provided by the Indigo samples grown by PVT, studied by single crystal XRD. Some of the crystallites grown by sublimation, which could only be analyzed by powder XRD, had dimensions and morphological characteristics suited to single crystal micro-Raman analysis. The lattice phonon Raman spectra of all these samples, together with that of the commercial powder, are shown in Figure 3.10. Extensive samplings of various specimens confirmed that only two different spectral patterns could be detected on individual crystallites: the one safely assigned to form A, because of the analyses on the PVT grown crystals, and another one, characterizing the larger fraction of the crystallites and assigned to form B. As expected, the spectrum of the commercial product displayed broader bands compared to the single crystals, but could be associated to form B, in agreement with the powder XRD results.

The images of A and B crystals in Figure 3.10 clearly indicate how consideration on morphology differences cannot assist in discriminating the two polymorphs. However,

even though the strong similarity between the two lattices reflects on a similarity of spectral patterns, the distinction can be safely made by Raman.
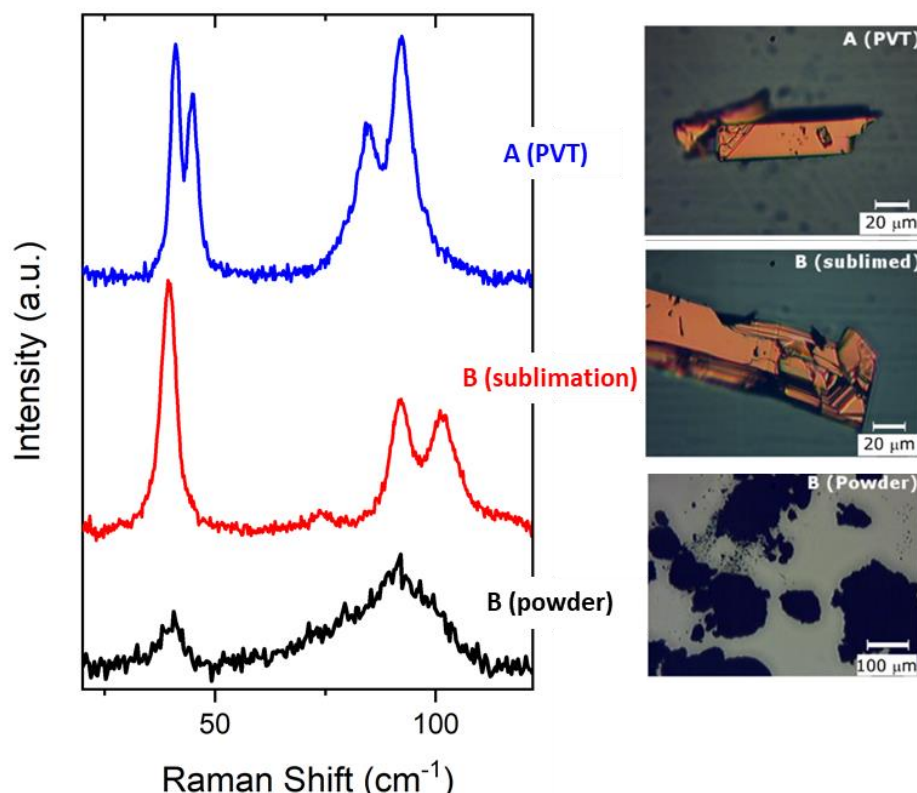
Figure 3.10: Left: Lattice phonon Raman spectra of the various samples of crystalline Indigo, with the two unique patterns that can be identified from the analysis; Right: images of the samples.

The satisfactory reproduction of the experimental spectral features by the DFT simulations, extensively discussed in Ref., [89] contributes to the validation of the assignment the Raman spectra to a specific polymorph made with the aid of XRD measurements.

In Figure 3.11 Indigo lattice phonon Raman spectra are deconvoluted as sums of Lorentzian bands to identify the peaks and proceed to the vibrational analysis. Based on the $P2_1/n$ crystal symmetry, which is the same for both polymorphs A and B of Indigo, six lattice modes of gerade symmetry $3A_g + 3B_g$ are predicted to be Raman active. Such a prediction relies on the assumption that Indigo behaves as a rigid molecule, in which the lattice phonons lie at energies lower than those of molecular vibrations and can be considered separately. The six lattice modes correspond to either in-phase (B_g) or out-of-

phase (A_g), rotations (librations) of the molecules in the unit cell around their axes of inertia and give rise to three doublets in the Raman spectrum.
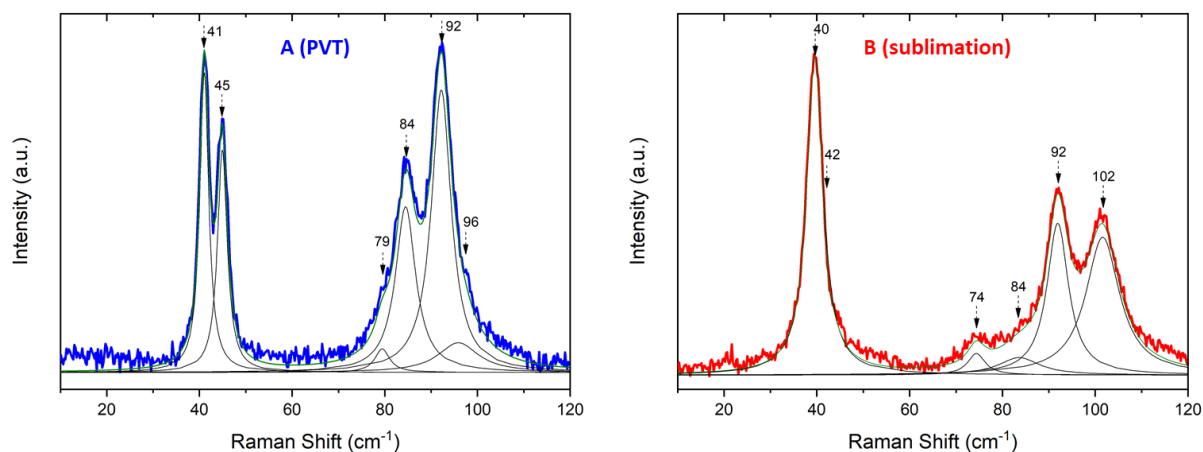
Figure 3.11: Raman spectra for A and B Indigo polymorphs in the lattice phonon region, deconvoluted as sums of Lorentzian bands. The weaker peaks of the B polymorph (as the one at 42 cm $^{-1}$) can be resolved only in the Raman polarized spectra as shown in the next Figure.

This preliminary analysis is the key to the interpretation of Indigo spectral features, supported by polarized Raman spectroscopy, as illustrated in the Figure 3.12 and with the assistance of the calculations. The latter [89] show that for both A and B crystal structures the eigenvectors of the six lowest energy Raman active normal modes do correspond to pure librations, with no intramolecular contributions. This given, the assumption of pure lattice phonons in rigid bodies is for Indigo correct. Accordingly, the six bands obtained by deconvolution is A form spectra do correspond to lattice phonons the symmetry of which is readily determined by Raman polarized experiments and comparison with the simulations. In the case of polymorph B, the polarized Raman spectra analysis, which completes the mode assignment, are needed to identify all the expected bands. Such an analysis requires the knowledge of the facets exposed and of the crystal orientation under the conditions of normal incidence and backscattering geometry for the exciting beam of our Raman experiment. Polymorph B needles displayed extinction in cross-polarized illumination when the crystal long axis was aligned to the exciting light polarization. Face indexing by XRD was not possible, because of the lack of suitable single crystals. However, in analogy with the face indexing found for

polymorph A, we assumed that on the exposed crystal faces the direction of fastest growth was coincident with the *b* axis, which corresponds to an extinction direction of the monoclinic system. This makes the interpretation of the Raman experiment in polarized light straightforward. Raman spectra collected in backscattering geometry with the polarization of the incoming and scattered light parallel to each other (labelled as parallel polarizers in the orange trace of Figure 3.12) and to the sample extinction direction reveal modes of A_g symmetry. Modes of B_g symmetry can instead be detected by rotating by 90° the polarization direction of the incoming light (spectra labelled as crossed polarizers in the red trace of Figure 3.12). By comparing these polarized Raman spectra of Indigo B with the unpolarized spectrum, the broad band at ≈ 40 cm^{-1} can be solved in two peaks at 39.8 and 41.6 cm^{-1}, belonging to modes of B_g and A_g symmetry, respectively.
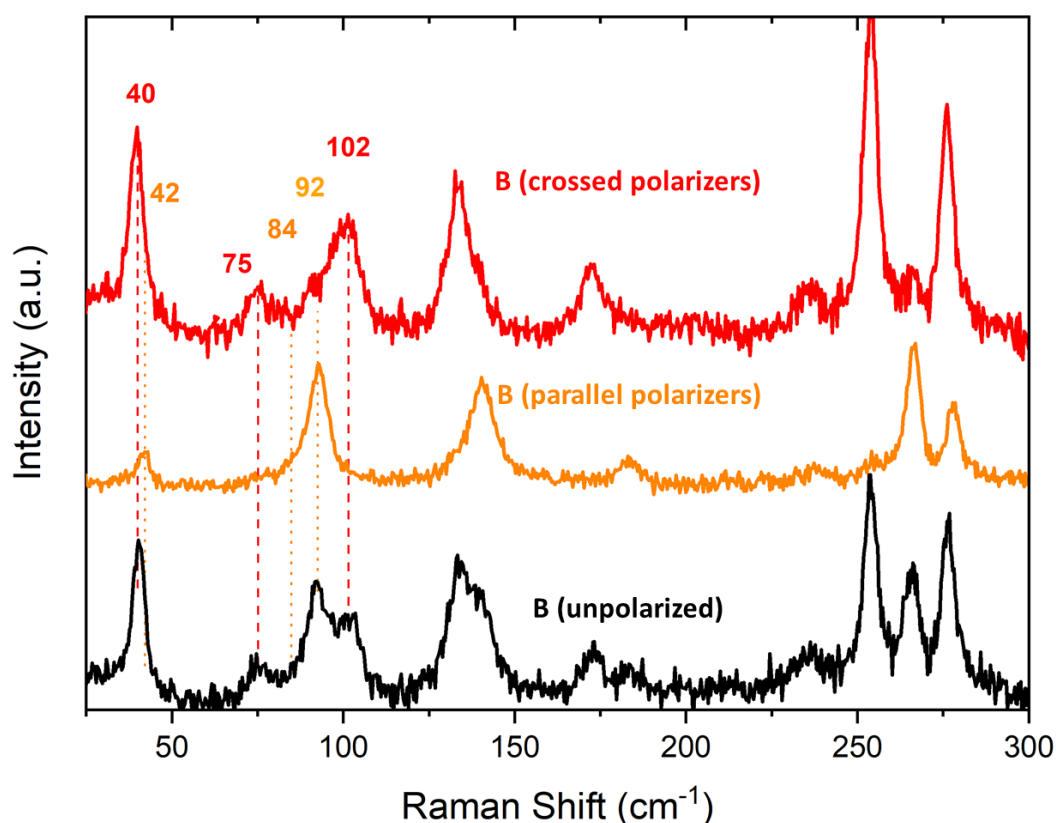
Figure 3.12: Polarized Raman spectrum of the Indigo B polymorph and the vibrations in the lattice phonon region are highlighted (orange dots shown the A_g bands while the red dash shown the B_g one). The analysis clearly shows that the ≈ 40 cm^{-1} band can be resolved in two distinct peaks.

Notwithstanding the irreplaceable role of the lattice phonons, intra-molecular vibrational spectra (either IR or Raman) often provide a valid diagnostic tool for the identification of conformational polymorphs. This is because conformation modifications induce detectable changes in the positions and the intensities of the chemical group involved. These spectra are, however, ineffective for packing polymorphs, which share the molecular geometry and, thus, the vibrational spectral features. In this respect, Indigo polymorphs A and B are an interesting exception, as they can be discerned by some of the strongest bands of their intra-molecular Raman spectra. This can be observed in Figure 3.13, where the central panel shows these spectra for samples of the two polymorphs in the wavenumber region from 100 cm^{-1} to 2000 cm^{-1}, while in the insets two ranges of interest have been zoomed in: i) 100-200 cm^{-1} and ii) 1450-1650 cm^{-1}.
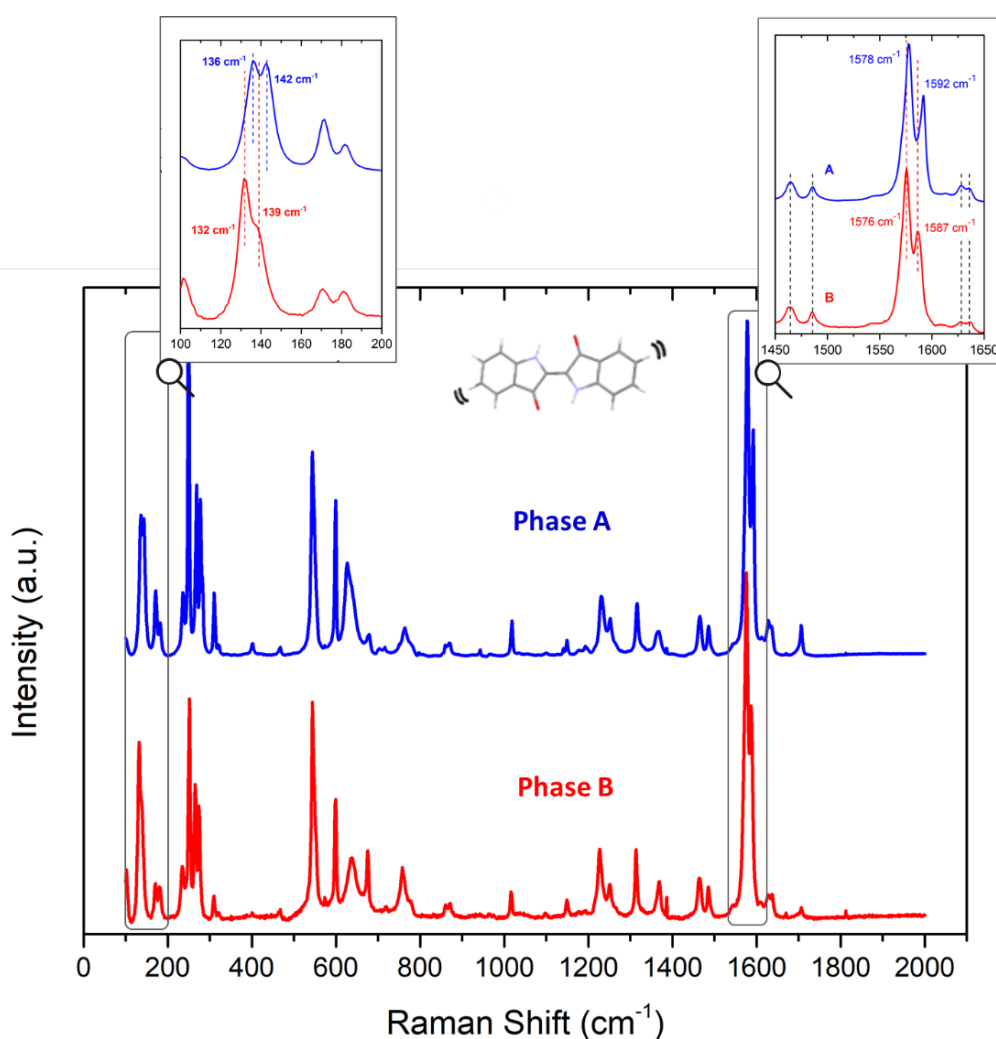
Figure 3.13: Raman spectra of Indigo polymorphs A (blue) and B (red) in the 100-2000 cm^{-1} range. In the picture are shown two zooms into specific wavenumber intervals in which polymorph discrimination can be made on the basis of intra-molecular vibrations.

As expected for packing polymorphs, most bands of forms A and B coincide. The zoomed region from 100 to 200 cm^{-1} of the Figure puts in evidence the bands of the lowest energy intra-molecular mode, which in the crystal, with two molecules per cell, gives rise to an $A_g + B_g$ doublet as a result of the Davydov's splitting [104] between interacting molecules. The two peaks are found at 132 and 139 cm^{-1} in polymorph A and at 136 and 142 cm^{-1} in polymorph B. The analysis based on the calculated eigenvectors [89] has allowed to visualize this vibration as a large amplitude mode comprising intramolecular rotations, which involves the entire molecular scaffold (top images of Figure 3.14). The nature of this motion suggests it to be a sensitive probe of the strength of the intermolecular hydrogen bonds, as the presence of these, or a change in their

pattern, could affect the intramolecular rotations. Hence, the frequency difference observed between the two forms. Note that similar frequency shifts are not observed for the weaker peaks of the adjacent doublet, around 172 and 182 cm $^{-1}$, also reported in Figure 3.13.
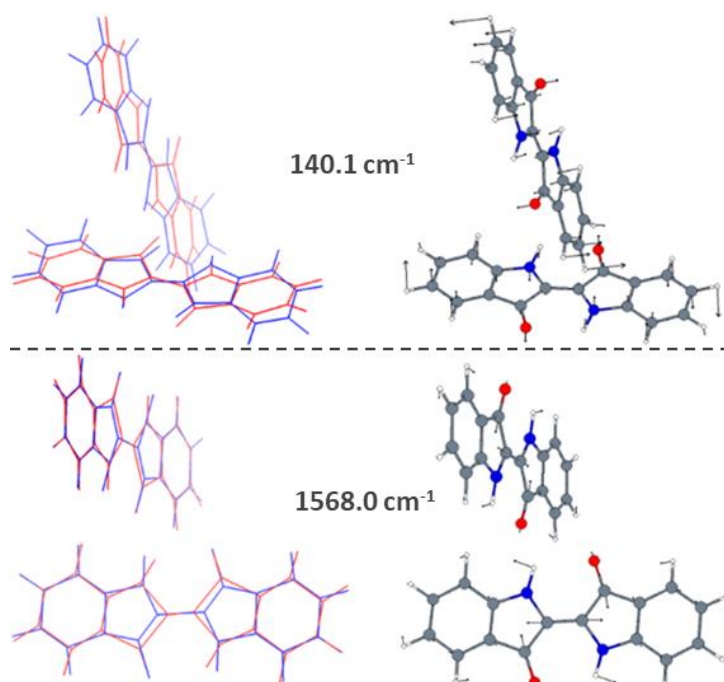
Figure 3.14: Top: Representation of the lowest energy Ag intramolecular of Indigo (the calculated wavenumber for the A polymorph is given); Bottom: Representation of the Ag intramolecular mode corresponding to the most intense and typical band of Indigo (calculated at 1568.0 cm^{-1} for the A polymorph). The arrows display the direction of the atomic displacements; while blue and red molecular geometries are used to represent the movement of the system. [105]

The most easily detectable difference between the Raman spectra of the two polymorphs, however, involves the doublet of the most intense and typical band of Indigo, [106]–[108] which is shown in the second zoom of Figure 3.13. The doublet occurs at 1578 and 1592 cm^{-1} in polymorph A and at 1576 and 1587 cm^{-1} in polymorph B. The corresponding mode (Figure 3.14) has been described in detail in the literature [106], [107] and corresponds to a combination of the central C=C and the C=O stretchings. It actually entails the motion of the entire functional group – called the cross-conjugation chromophore - formed by the central bond together with C=O bonds and N-H bonds, which act as acceptor and donor systems, respectively. Since the early measurements on solid Indigo, it was noted that, in the condensed phase, this mode is strongly red shifted

compared to the isolated molecule DFT calculations, which gives a wavenumber of 1596 cm^{-1}. [107], [108] Based on the calculations on a model Indigo dimer, [108] such a shift has been interpreted as due to the presence of the strong intermolecular hydrogen-bonds, which affect the bond strength and the vibrational dynamics of the functional groups involved in the interaction. The different shifts observed in forms A and B, and the different Davydov's splittings, hint to differences in the interaction motifs involving pairs of non-translationally equivalent molecules, in a way similar to what described above for the large amplitude motion.

From a practical perspective, these findings show that polymorphs A and B can be efficiently discriminated through intense Raman bands in energy ranges more easily accessible than the lattice phonon region. As a matter of fact, we have resorted to their inspection every time the nature of the sample or the amount of material made difficult a measurement of the lattice phonons. More interesting though, is the spectroscopic evidence of a subtle but specific difference between the two forms, which originates from the strongest intermolecular interaction that characterizes them both.

The difficulties encountered for obtaining separately Indigo polymorphs A and B identify them as concomitant, following the description given in the review article by Bernstein. [4] Thus, it was interesting to apply the micro Raman investigation to check whether this system displayed polymorph co-existence at the micrometric scale, [11] with possible implications on domain and grain boundary characteristics. Indeed, an instance of co-existence of the two Indigo morphic modification was detected by Raman spectroscopy on a sample having the appearance of a single crystallite and is reported in Figure 3.15. Spectra of the A and B forms are given as references. The spectrum labelled in the Figure as A+B (green trace) was recorded on an Indigo microcrystal obtained by sublimation, with the highest lateral resolution available (≈ 1 μm) for the used Raman setup. As evidenced by the lines marking the bands, such a spectrum corresponds to the overlap of those of the pure forms. Here the micro-Raman measurement clearly pinpoints a situation in which the two polymorphs co-exist as different micrometric domains in the same specimen, despite the macroscopic appearance of this as a single crystal.
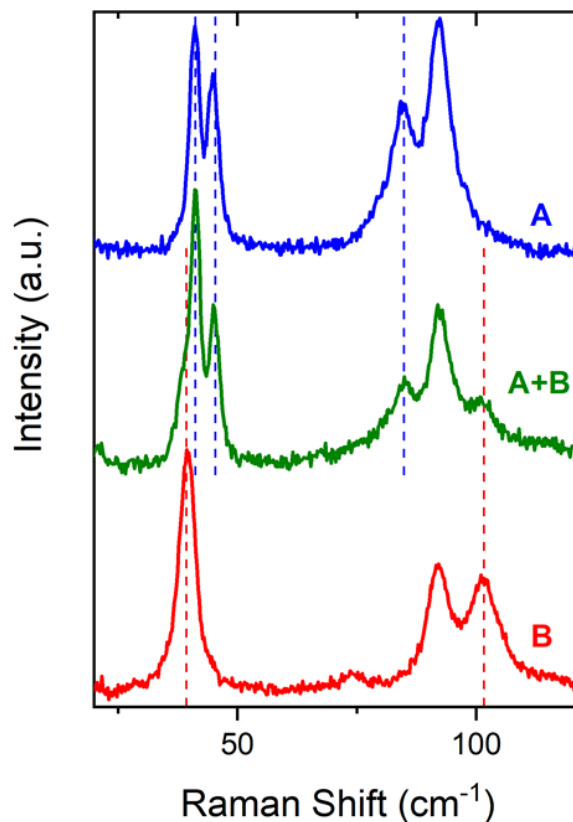
Figure 3.15: Green trace: Lattice phonon Raman spectra recorded on an Indigo microcrystal obtained by sublimation with the highest lateral resolution available (≈1 µm). This one, labelled as A+B, shows the co-existence of the two forms at a micrometric scale. Blue and red traces: reference spectra of the pure A and B forms, respectively.

3.1.6. Fabrication and characterization of Indigo films

X-ray and Raman measurements on films prepared by drop casting

As reported in "Experimental Methods" (paragraph 3.1.3) a first attempt at film fabrication was done by using the drop cast method on glass surfaces. Other solution deposition techniques were not in fact pursued because, as the results presented below will show, the low solubility of Indigo really represents a limiting factor in obtaining homogeneous and continuous film suitable for applications (and this was well known from the literature). Nonetheless, the samples provided precious information, such as the phase selectivity of the surface, which applies also to the films grown by the vapor

deposition method. Besides, they were the benchmark systems on which to test the effectiveness of Raman spectroscopy in situations where XRD fail.

The XRD diffractograms of films obtained by the drop casting of Indigo solutions in 1,2-dichlorobenzene or acetonitrile are reported in Figure 3.16.
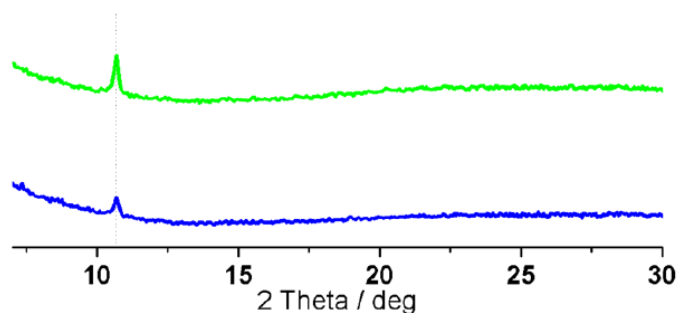
Figure 3.16: XRD pattern of Indigo thin films deposited on Si/SiO$_x$ wafer by drop casting of 1,2 dichlorobenzene (green line), and acetonitrile (blue line).

They show very similar diffraction patterns with one peak at 10.7°, corresponding to a d-spacing distance of 8.3 Å. The degree of uncertainty is, however, too high to allow for a safe and unambiguous determination of the type of polymorph from these measurements. We are facing the already mentioned problem previously encountered by Scherwitzl et al. [85] and by Anokhin et al., [86] who reported similar results for films grown from vapor on various substrates.

Figure 3.17 shows Raman spectra recorded on the same films, along with their images at the optical microscope. The lattice phonon region (here not shown) displayed weak broad bands, with a pattern corresponding to that of the commercial powder. Using as polymorph markers the intramolecular modes, i.e. the doublets at 132-1369 and 1576-1587 cm^{-1}, we checked phase identity and purity by performing extensive random sampling on the film surfaces. All measurements clearly indicated that B is the only form present.
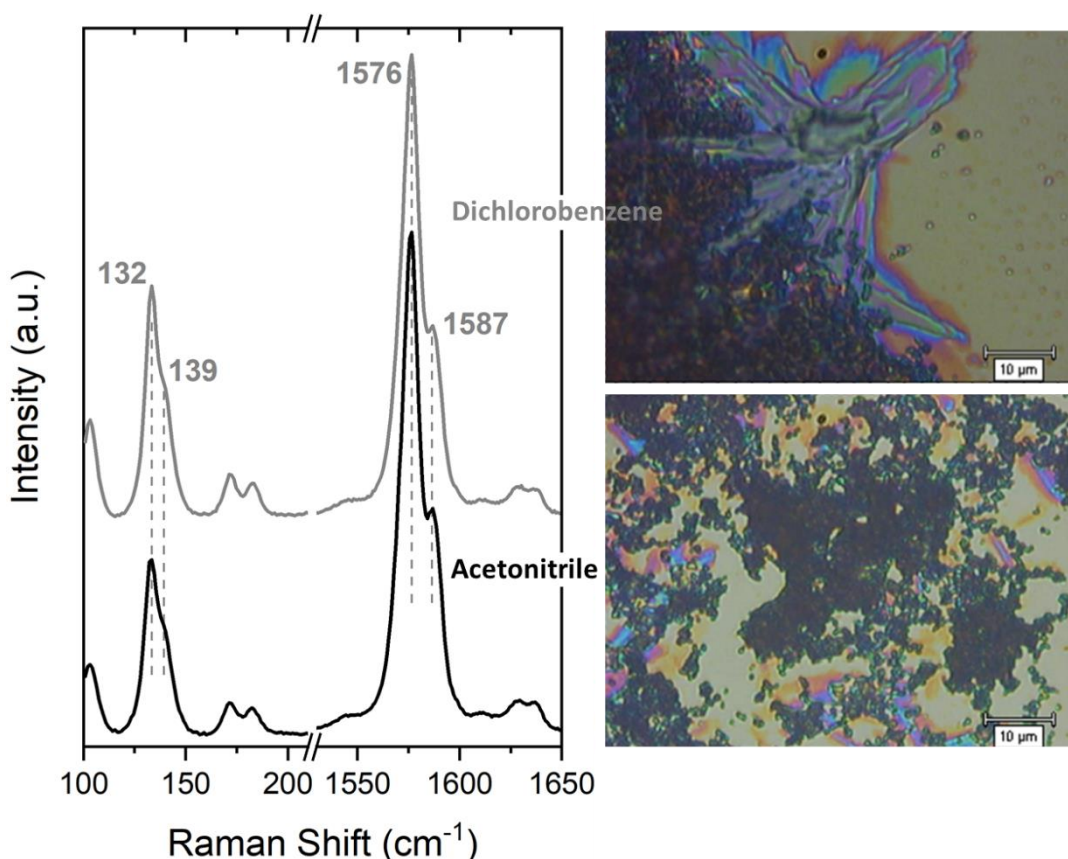
Figure 3.17: Raman spectra of films of Indigo drop cast from solutions in 1,2-dichlorobenzene (grey trace) and acetonitrile (black trace). The wavenumber ranges suitable for polymorph identification are shown. On the right side: Image of the sample where the Raman scattering has been collected.

The films prepared for these measurements are quite thick; the Raman technique, however, is very sensitive, as can be judged by the high signal/noise ratio of the spectra presented and befitting to be transferred to polymorph identification in thin films.

Fabrication of films prepared by MBE

The fabrication of Indigo thin films by the vapor method met some difficulties, which we believe connected to the chemical purity of the starting material (see more details in the Appendix II - paragraph 3.1.8).

Depositions were performed on Si/SiO$_x$ at room T, following the thermal sublimation at 200 °C under ultrahigh vacuum ($\approx 10^{-7}$ mBar) conditions. The total amount of material on the sample (1000 ng) was kept constant, while different deposition rates v were tested. The choice of varying the deposition rate while keeping the amount of

deposited material constant had the purpose of monitoring the morphological transformation of the film as the rate changed, so to estimate thickness, structure and size of the grains.

In a first check to optimize conditions, the commercial powder was used without further purification, but it turned out that it was not possible to keep under control the sublimation rate in the vacuum chamber, *i.e.* to achieve a constant material flux.

Films were fabricated at the deposition rates of 10, 20, 50 and 100 ng/min rates with the sublimed product deposited at 30 °C as the starting material. The acquisition of good quality AFM images was hampered by the lack of a stable interaction between the tip and the sample surface, likely due to residual electrostatic charges present on the surface and ascribed to impurities. Soaking the films in Milli-Q for 1 h made the AFM measurements possible. An instance of the collected AFM images is shown in Figure 3.18, along with some representative lattice phonon Raman spectra of the same films. The image reveals that they are very disordered, porous and discontinuous. The thickness, measured by the profilometer, was 50 nm for the sample grown at the lowest rate (10 ng/min) and ca while 100 nm for that at 20 ng/min. Crystallinity was probed by the lattice phonon Raman spectra, but with unclear outcome. The bands were very broad, an indication of a powder-like system. The peak positions suggested the presence of the B form, which was confirmed by the detection of the corresponding intramolecular vibrations. However, the band relative intensities (see for instance the grey spectral trace of the film in the Figure 3.18) were unusual with respect to all the samples measured so far. Analysed after some months, the films displayed only spectral features similar to the black trace of the Figure, hinting to some intervened structural reconstruction.
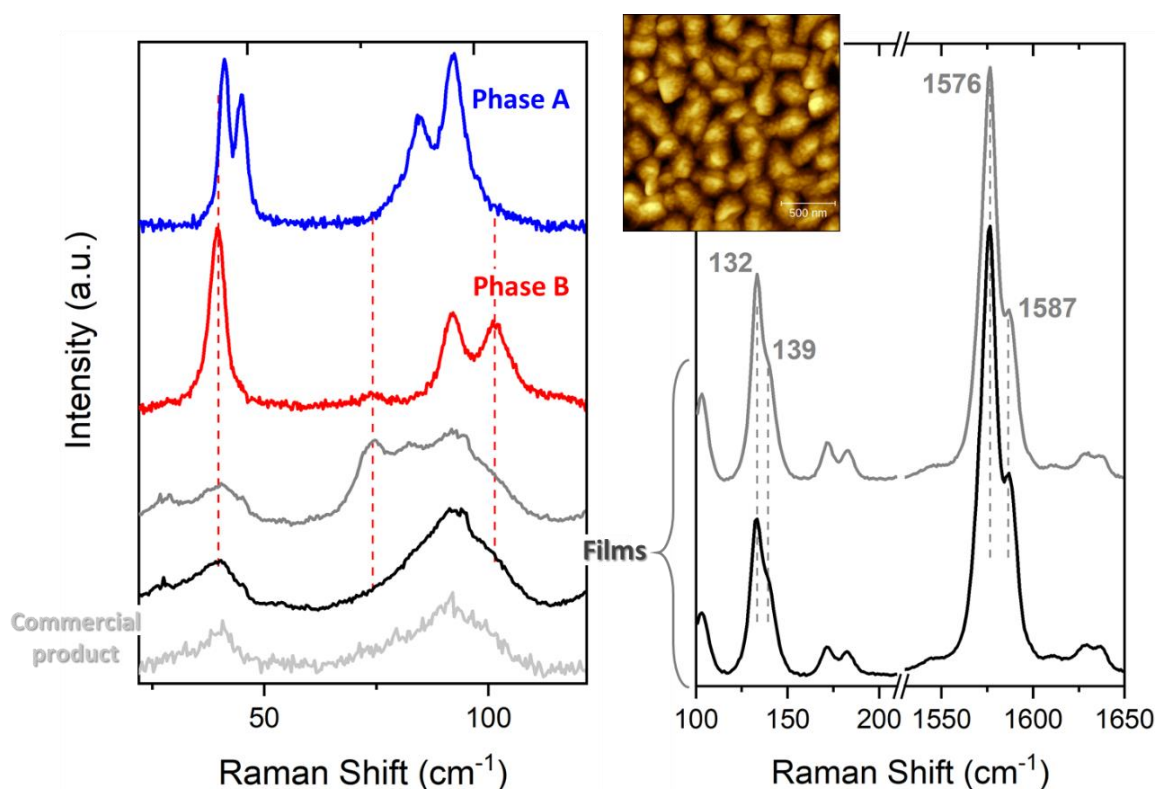
Figure 3.18: Left: Raman measurement performed in the lattice phonon region on thin films obtained with the sublimed powder recrystallized at 30°C. Black and grey traces show the Raman pattern typically observed on these samples. Blue and red traces are reported as references for the known polymorphs, together with the spectrum of the commercial powder (light-grey trace). Red dash lines highlight the relevant similarities between the known spectra and the new ones. Right side: Raman spectra of the film samples collected in the energy interval of the intramolecular vibrations (here the wavenumber ranges displayed is suitable for polymorph identification). In the inset: the AFM image of a representative sample shows the average morphology observed.

In the attempt to improve film morphology and stability, films were finally fabricated using as starting material the microcrystalline powder obtained at 130°C, with film deposition rates of 10, 20, 42, 70, 101, 170 and 200 ng/min. After soaking in Milli-Q water for 1 h, these samples yielded AFM images finally stable and reproducible, showing the morphologic characteristics of compactness and homogeneity described below. At the same time, also the film Raman spectra highlighted a constancy of spectroscopic characteristics. Contact profilometer measurements confirmed the film thicknesses to be independent of the deposition rate, i.e. 1000 ng of deposited molecules corresponds always to films (36 ± 9) nm thick.

Films on the thermally planarized Tetoron® were subsequently prepared following the same procedure as those on Si/SiO$_x$. The deposition rates of 10, 70 e 200 ng/min were

chosen, which corresponded to the two boundary values and the intermediate one of the deposition on Si/SiOₓ, while all the other conditions were kept constant, so to be able to compare morphologies in the two substrates. Details on the preparation and planarization of the substrate are given in paragraph 3.1.3 - Experimental methods.

The conditions tested for Indigo film fabrication by the physical deposition method MBE are summarized in Table 3.2, along with the thickness of obtained films. More details about the sublimed powder are reported in paragraph 3.1.8 – Appendix II.

Table 3.2: Summary of the deposition conditions tested for the fabrication of Indigo films by MBE

Crystalline Powder used for fabrication	Substrate	Deposition rate (ng/min)	Thickness (nm)
Commercial Powder	Silicon oxide	no film	no film
Sublimed 200 °C - recrystallized ≈ 30°C	Silicon oxide	10, 20, 50, 100	from 50 to 100
Sublimed 200 °C - recrystallized ≈ 130°C	Silicon oxide	10, 20, 42, 70, 101, 170, 200	36 ± 9
Sublimed 200 °C - recrystallized ≈ 130°C	Tetoron®	10, 70, 200	≈ 30

The last test made for studying the Indigo behaviour on film was to grow some films by using the sublimed powder at 200 °C and recrystallized at 130 °C for three times. Only one sample was deposited at 10ng/min on silicon wafer and its Raman spectrum displays the same pattern of the other samples (such as Figure 3.21) while its AFM analysis was possible even without the treatment of 30' in Milli-Q water.

Morphological Characterization

As shown in the AFM images of Figure 3.19, Indigo films are composed of grains, that evolve from large faced structures to spherical ones, for the lowest (10 ng/min) and the highest (200 ng/min) deposition rate v, respectively (Figure 3.19a, g). The films are just above the percolation limit for v = 10 ng/min (surface coverage $\theta \approx 80 \%$ [109] and reach full coverage for higher v. The grains surface density N (i.e. number of grains per unit surface) increases as $\sqrt{v}$, while the average radius of the grains and their volumes

decay exponentially *vs* v (Figure 3.19h), similarly to what reported in the literature for perylene films. [110] Thermodynamically, the deposition rate drives the films equilibrium from a 3D (rough) toward a 2D (flat) growth regime, by increasing the super-saturation of the sublimated molecules [111] or, equivalently, to increasing v corresponds a decreasing of the molecular diffusion length.
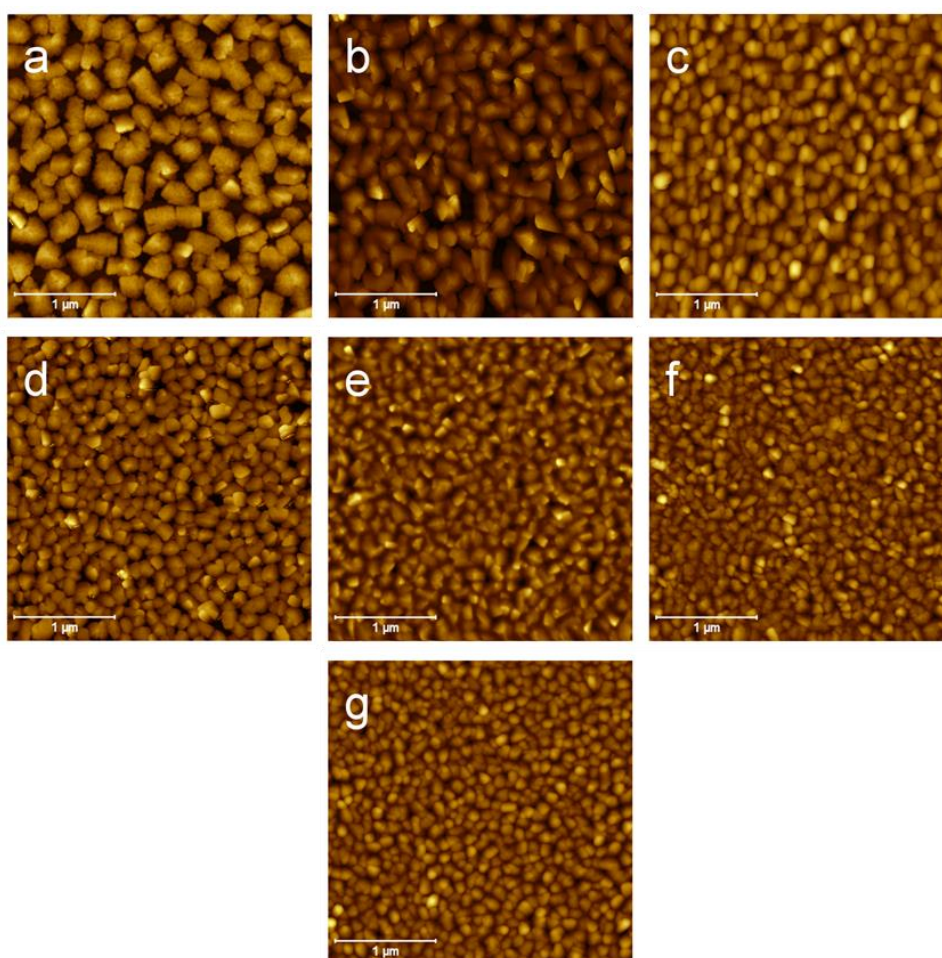
Figure 3.19: Topographic images of Indigo films deposited on thermal Si/SiO$_x$ at room temperature for increasing deposition rates: 10 (a), 20 (b), 42 (c), 70 (d), 101 (e), 170 (f) and 200 ng/min (g). In order to highlight the morphological evolution of grains, 3 x 3 µm^2 topographic images were presented.

Independently of the deposition rate, the roughness analysis of images with different lateral sizes (from 40 to 1 µm) highlights a roughness saturation above 5 µm. [112] Accordingly, the evolution of the surface roughness σ with respect to the rate v was investigated by analysing 7 x 7 µm^2 topographic images. The plot of Figure 3.20 shows an

initial plateau for v < 20 ng/min and then decays as a power law with exponent δ = 0.39 ± 0.03. This value is close to what found for all films made by ultra-fast thermal deposition ≈ 0.49 [113] but, notably, it is higher than that of (0.28 ± 0.01) obtained for simulated non-equilibrium growth with anomalous scaling, [114] like the case of Pentacene films deposited on SiO_2. [115]
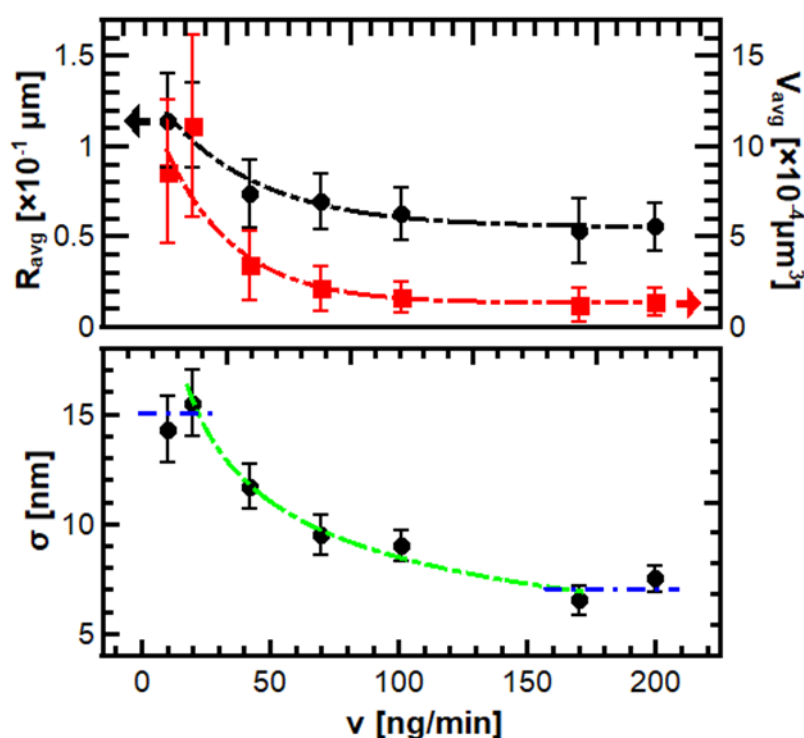
Figure 3.20: Top plot: Exponential evolutions of the average grains sizes (radius R_{avg} and volume V_{avg}) vs the deposition rate. Bottom plot: Surface roughness σ vs the deposition rate. In the range v > 20 ng/min, σ scales as a power law $a·x^b$ (dot-dashed line).

The films deposited on the polymer substrate displayed trends of the morphological parameters very similar to those recorded in silicon oxide, with the roughness σ decreasing with increasing deposition rate, showing the formation of increasingly compact, homogeneous and flat films. The same applies to volume, area and size of the grains, with the presence of smaller, spherical structures characterizing the highest rate. Together with these strong similarities, there are relevant differences. At the same deposition rate, on the polymer the roughness is higher, (20 ± 1) nm and (13 ± 1) nm at the highest and lower deposition rates, respectively; correspondingly, grain

dimensions are larger. These experimental evidences point to a lower interaction of the Indigo molecules with the polymeric substrate, which results in less smooth and worse organized films compared to silicon oxide.

Raman and XRD characterization

The AFM morphologic characterization, and in particular the behaviour of the roughness σ vs the deposition rate ν, suggested narrowing the field of investigation to the samples prepared at the deposition rates of 10, 70 and 200 ng/min, *i.e.* the lowest, intermediate and fastest rates, as representative of Indigo behaviour in films.

Raman spectra reported in Figure 3.21 were acquired on the three representative samples on Si/SiOx and provide information on the solid phase in the films. The analysis relies on the previous Raman characterization of Indigo in bulk crystals. This showed how polymorphs A and B can be discriminated by their different spectra in the lattice phonon region. Unexpectedly for packing polymorphs, these can be distinguished also by marker bands in the energy region of the molecular vibrations, due to their different patterns of intermolecular H-bonds.

Figure 3.21: Micro Raman analysis of Indigo film obtained at rate 10, 70 and 200ng/min on silicon wafer. On the left side: Raman spectra in the energy interval of the lattice phonons. Right side: Raman spectra collected in the energy interval of the intramolecular vibrations (here the wavenumber ranges displayed is suitable for polymorph identification).

The lattice phonon region collected for all the Si/SiO$_x$ films displays a broad band centred around 42 cm^{-1} and two more broad peaks at 92 and 102 cm^{-1}, which allow us to identify B as the polymorph present in the samples, based on the results both of its single crystal spectrum and of power samples previously reported. The assignment is confirmed by the Davydov splittings at 132/139 cm^{-1} and at 1576/ 1587 cm^{-1} (see Figure 3.13), which have been identified as the molecular modes lying at different wavenumbers in the two polymorphs. Spectra were collected at several spots of the films, detecting always the same peaks, patterns and background, with no relevant changes in band relative intensities, which would denote different crystalline orientations in the microdomains. Thus, the picture given by Raman is that of films appearing homogenous on a microscale and containing only one polymorph. The analysis cannot provide much information about the film molecular organization: the broadening of the lattice phonon peaks compared to the single crystal's as well as the general appearance of the spectra, similar to those of

the crystalline powder, suggest a lack of order, which will be more accurately investigated by other techniques, as explained in this chapter.

Raman spectroscopy was applied also to the identification of the phase in the films deposited on Tetoron® (reported in Figure 3.22). The lattice phonon spectra are alike those recorded on silicon wafer of Figure 3.21 and confirm the presence of the sole B phase in a powder-like state. However, compared to silicon wafer, the spectra have a worse signal-to-noise ratio, a feature probably due to a lower degree of crystallinity of the film, as suggested by AFM. Given the only semi-crystalline nature of the polymer, no bands ascribable to lattice phonons were observed in the low energy range, interfering with Raman measurements. The overlap between substrate and Indigo's vibrational bands is instead large in the intramolecular energy range. This makes complicated over this interval the polymorphic identification, which can only be based on the band of the B form at 1576 cm^{-1}.
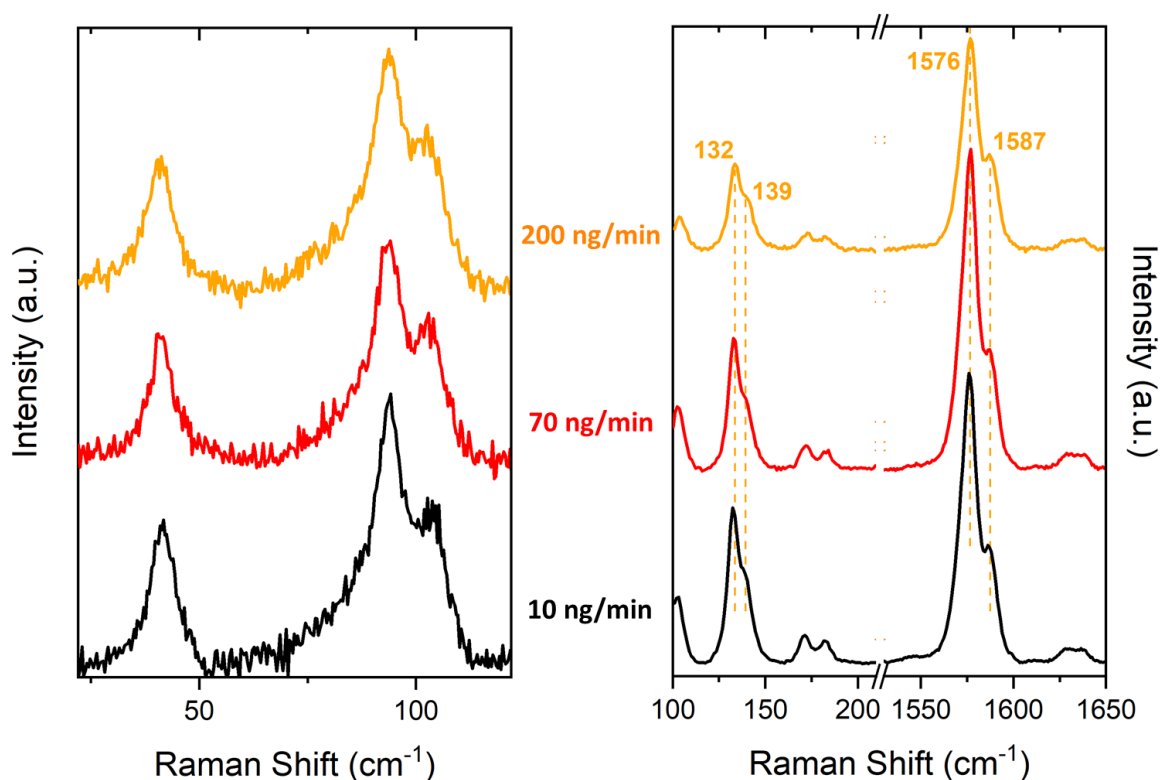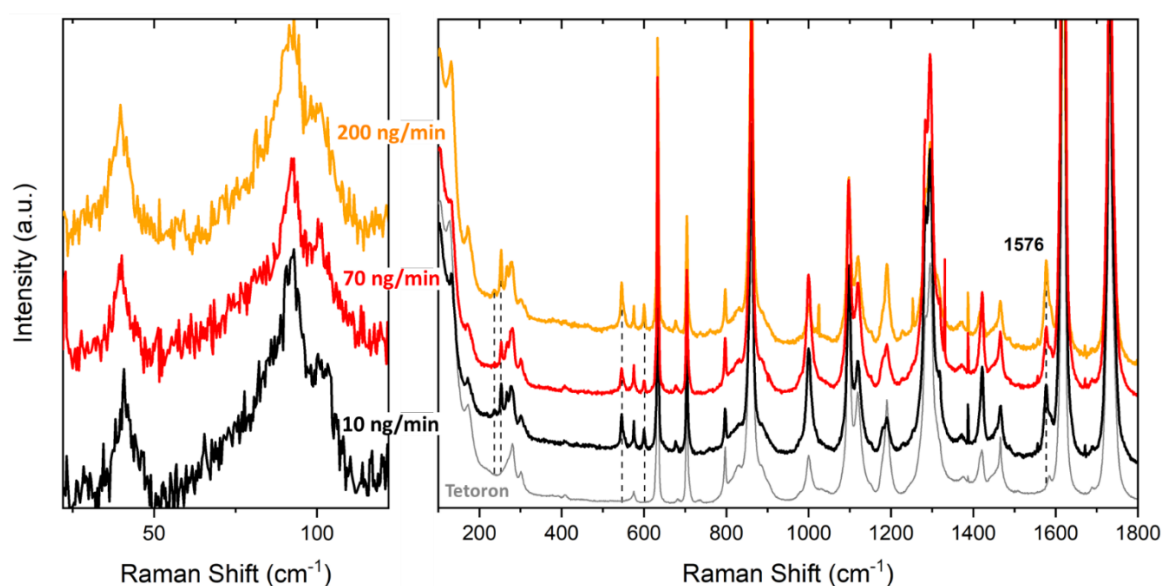

Figure 3.22: Micro Raman analysis of Indigo film obtained at deposition rates 10, 70 and 200ng/min on Tetoron®. Left side: Raman spectra in the energy interval of the lattice phonons. Right side: Raman spectra collected in the energy interval of the intramolecular vibrations; the grey trace is for the pure substrate. Black dash lines highlight the few Indigo peaks not covered by the substrate bands.

Even though the failure of the X-ray investigation to recognize the Indigo crystal modifications was known, we to apply the technique for a screening of the films grown

on silicon wafer substrate. The reason was this was twofold: check for crystallinity and comparison with the previous literature results for reproducibility. [85], [86]

Figure 3.23 shows the patterns for the samples with the three selected deposition rates. The film deposited at the rate of 200 ng/mg does not show any peak attributable to Indigo. Instead, those obtained at lower deposition rates, namely 70 and 10 ng/min, display virtually identical diffraction patterns with two peaks: the first at 10.7°, already observed in the drop casted films, corresponding to a d-spacing of 8.3 Å, and the second at 33°, due to the substrate. The peak position and the inter-plane distance agree with the previous determinations. [85], [86] By combining this information with the knowledge that the structure is that of the form B, obtained from the Raman, we can infer that the films are weakly oriented alongside the (1 0 0) Miller plane. The Scherrer equation [116] was used to evaluate the average crystallite size, which turn out to be 19.85 nm and 16.03 nm for the film obtained at 10 ng/min and 70 ng/min, respectively
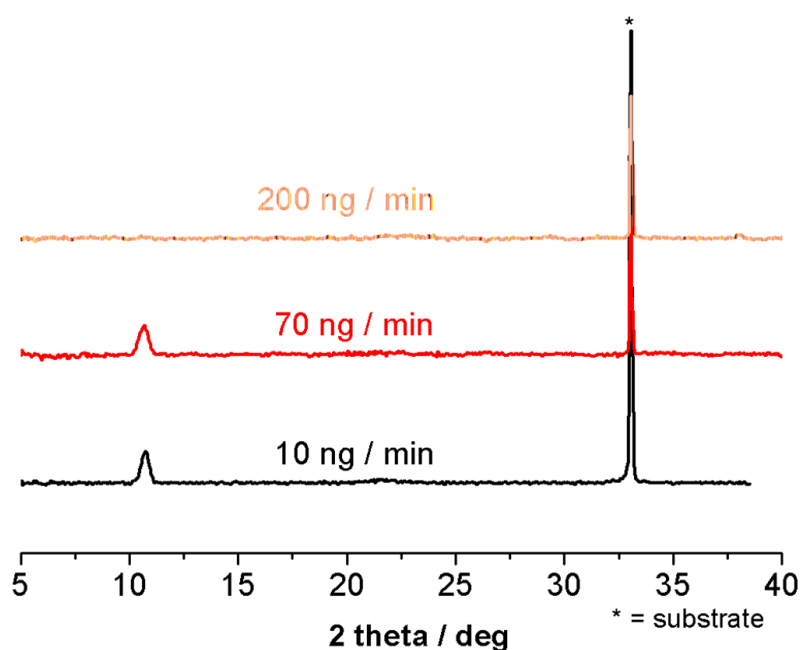
Figure 3.23: XRD pattern of Indigo thin films grown on Si/SiOx wafer by sublimation at different deposition speeds: 10 ng/min (black-line), 70 ng/min (red-line), and 200 ng/min (orange-line).

TEM measurements

TEM analysis was carried out on the films on Si/SiO$_x$, both in bright field (BF) electron microscopy and electron diffraction (ED) modes.

To compare the information provided on the nanomorphology of the samples by the AFM and BF images, these are shown in Figure 3.24. The BF image of the 10 ng/min sample clearly reveals that the grains detected by AFM are not single crystals, even when they appear to have neat edges. They are instead made of randomly oriented, smaller crystalline domains of irregular shape, embedded in each grain and identified by a sharper contrast in Figure 3.24. Their average dimensions can be roughly estimated by increasing the resolution. The much smaller grains of the films deposited at rates 70 and 200 ng/min are defined by the brighter boundaries in the BF image of Figure 3.24 and also here at higher resolution the presence of nanosized subdomains is evident.
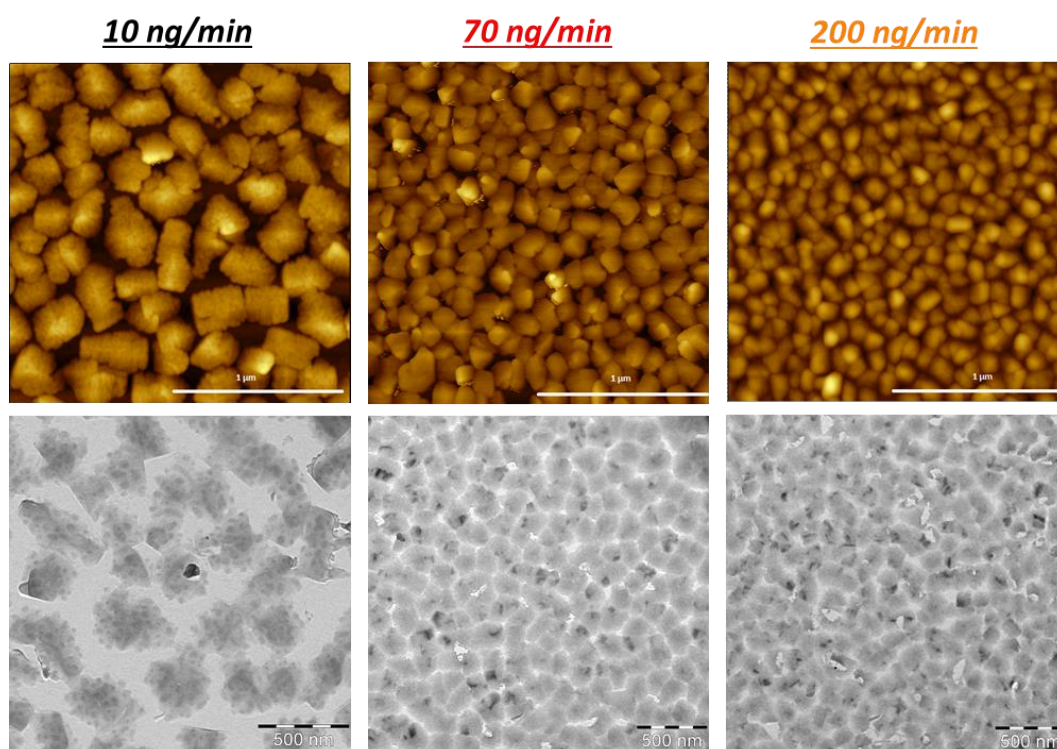
Figure 3.24: Comparison between AFM analysis (on the top) and TEM measurements in bright field (on the bottom) performed on the Indigo film on silicon wafer.

The evolution of the ED pattern as a function of the deposition rate is displayed for the three representative samples in Figure 3.25, where both the SAEDs, large area ED and the corresponding averaged radial profiles of large scale ED are reported. At the lowest deposition rate, we observe a set of few, sharp reflections in the SAED, which increase on increasing rate, finally evolving into the almost continuous ring of a highly polycrystalline sample. In particular in the SAED (Figure 3.25 at 10ng/min) only one fragment of Indigo is selected. The crystals exhibit a twinning structure and the SAED pattern can be thoroughly indexing as three twin domains oriented along the [2,1,1] axis.

This result is in agreement with the observation of larger crystal domains in the low rate grown sample. One reflection is clearly dominant in all cases and corresponds to an inter-planar distance of 6.11 Å, that can be indexed as $(1\ 0\ \bar{2})$ on the bases of Indigo polymorph B structure. The large area ED patterns reveal the presence and the evolution with deposition rate of the rings with indexes $(1\ 0\ \bar{2})$ and $(1\ \bar{1}\ \bar{1})$ in all the films. Overall, the ED patterns show that even when larger crystallites are present, the film still is characterized by a poor order, even though there appears to be a preferred direction of growth as suggested by the prevailing $(1\ 0\ \bar{2})$ reflection.

The picture emerging is that in the samples deposited at lower rate, the first layers produce a quasi-uniform film on which fragments poorly aligned and much smaller crystallites with random orientation grow. This results in the polycrystalline pattern observed in the large area ED, while the SAED measurements, selecting single fragments, identify well defined orientations.
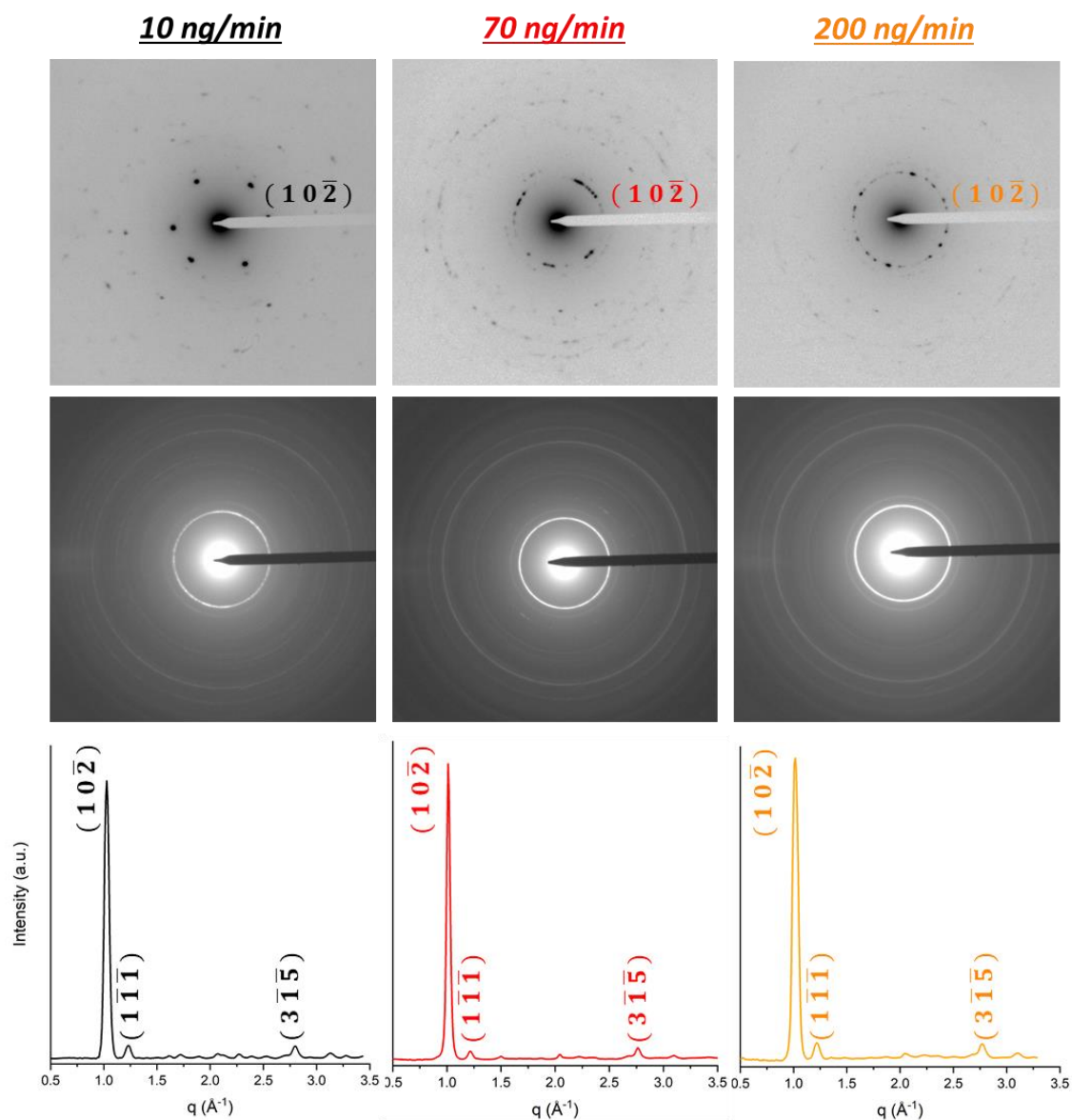
Figure 3.25: The figure shows a comparison between the three samples in SAED (on the top) and large area (about 50 µm) ED in the centre and the corresponding radial averaged profile evidencing the major reflections.

To induce a better crystallinity and improve the organization of the film micro-domains, the grids were subjected to SVA with methanol for 24 h, as this method has proven to be very effective in improving crystallization while avoiding the destruction of the material. [117] In such a process the film is partially dissolved by solvent molecules diffusing at the interface and can re-organize by self-assembly.

Following the treatment, all the films displayed modification of the ED patterns which indicated some sort of re-organization. For instance, a SAED (Figure 3.26) recorded

on the 10 ng/min film after SVA could be indexed and simulated assuming a [4 1 2] zone axis (perpendicular to the contact plane) of Indigo polymorph B, thus confirming the phase assignment.
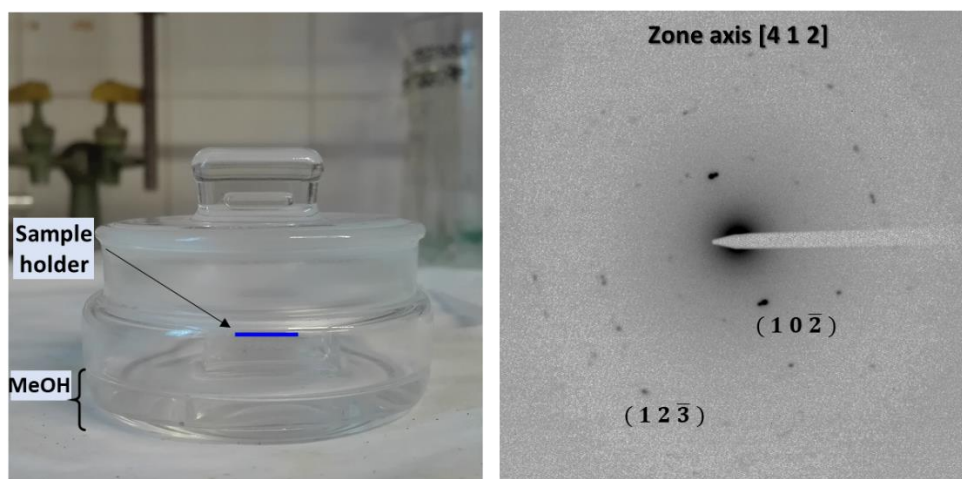
Figure 3.26 Left: chamber used for the SVA processing of the Indigo films; right: The SAED pattern obtained on the 10ng/min film after SVA, corresponding to the [4 1 2] zone axis.

To describe in detail the effect of the annealing, we focus on the outcome for the 200 ng/min sample, where changes were more pronounced, probably due to the smaller size and higher proximity of the grains, which allowed for a larger molecular mobility compared to the other films. In the SVA treated sample we can observe better defined edges of the grains, while on the surface crystals display some terraces. Very likely, the SVA treatment removes the smallest crystallites, sort of cleaning of the film surface, which can thus display the underlying texture. In addition, the polycrystalline domains might have undergone a re-organization through intramolecular rearrangements. Noteworthy, the untreated film did not display any peak in the X-ray analysis of Figure 3.23, whereas now the (1 0 0) reflection is clearly detectable.
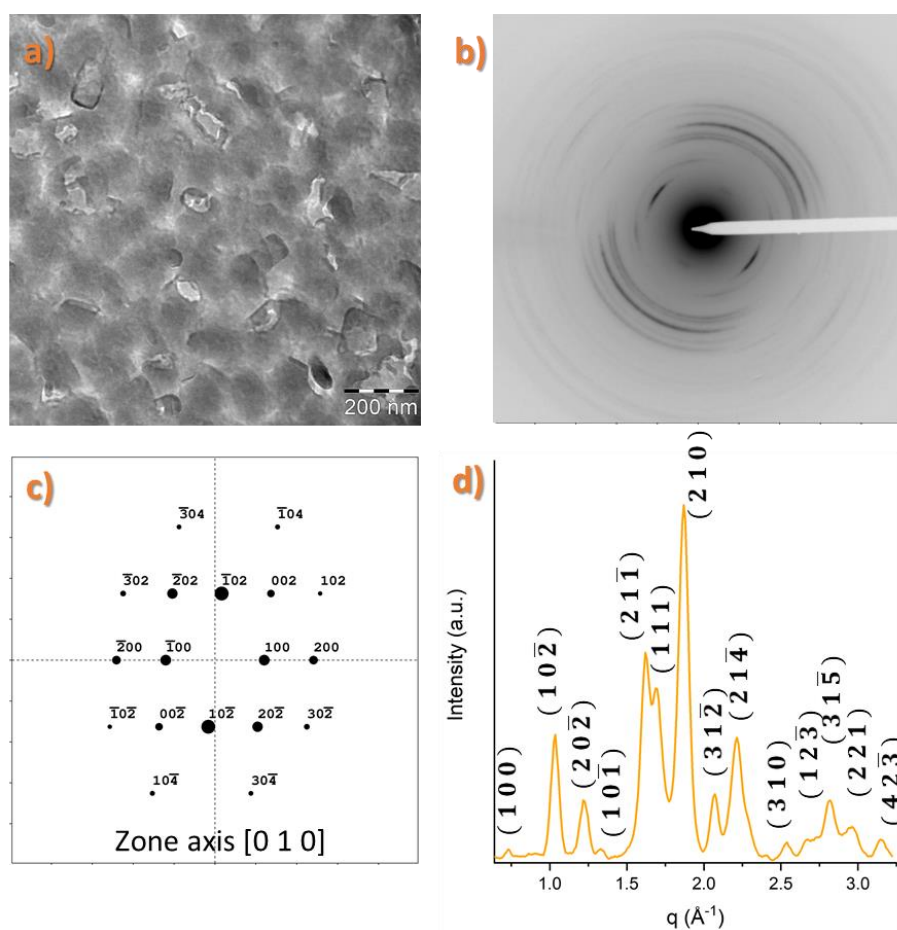
Figure 3.27: a) BF image performed on 200 ng/min Indigo film after SVA treatment; b) ED pattern of the SVA treated sample, c) Simulated pattern that reproduces crystals with the [0 1 0] *zone axis, d) Averaged section profiles of large-scale made on the ED shown.*

In Figure 3.27 the angular averaged ED pattern of the SVA-treated film is shown. Reflections have greatly increased in number and intensity, to indicate the reorganization that has taken place in the sample. However, the SAED pattern does not display a corresponding quality improvement, with the previously observed $(1\,0\,\overline{2})$ still clearly predominant. Figure 3.27 shows a SAED along with the calculated ED pattern corresponding a to [0 1 0] zone axis, which accounts for some of the observed features.

The electron diffraction pattern Figure 3.27 collected on the film might be described as a superposition of two sets of features. The former represents the minority of the crystals and consists of the sharper reflections ascribed to crystals having the crystallographic $(0\,1\,0)$ contact plane, corresponding to the [0 1 0] zone axis, whose simulated ED pattern is shown in Figure 3.27, together with the resulting arrangement of

the molecules at the solid interface. The latter is a fibre (arc) pattern around the $(1\,0\,\bar{2})$ direction and represents the majority of the crystals. This pattern pictures a situation in which most of the crystals share the in-plane orientation of the *c* axis, which thus lies always on the contact plane. Only the *c* axis seems to be well in-plane oriented, while the crystals have all the possible orientations around it, with (h k 0) contacts planes. However, a certain degree of mosaicity is still present in the sample, that is the *c* crystal axis in some domains might not be strictly lying on the contact plane, thus making accessible to the other techniques a variety of crystallographic faces. This might explain the X-ray observations and especially the Raman spectra, which in fact probe on a micrometric scale a condition similar to that of a powder sample.
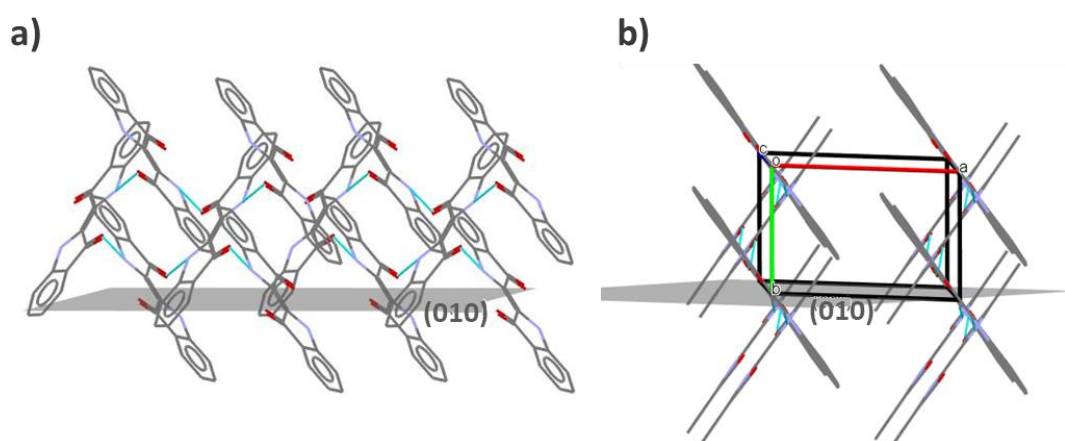
Figure 3.28: The two pictures shown the organization of the molecule compared to substrate by two different prospective, as described in the main text.

The predominant $(1\,0\,\bar{2})$ reflection, as mentioned above, corresponds to an inter-planar distance of 6.11 Å in Indigo polymorph B. This is the direction in which, as can be seen from Figure 3.28a, the strong intermolecular H-bond interactions characterizing the Indigo solid-state are exerted. Such interactions appear to govern the crystal growth, in fact hampering the development along other lattice directions. Accordingly, other reflections are of low intensity or undetectable. The SVA treatment helps re-organizing the film, but the dominating H-bond interactions impede its transformation in a more crystalline form. This appears to be a case of H-bond induced frustration of 3D crystallization caused by a prevailing one-dimensional H bond pattern

in the lattice and could explain the difficulties normally encountered in obtaining films of this material, as well as the likely occurrence of a quasi-amorphous state. However, the time this thesis must be finalized, further analyses are in progress to increase the information provided by the TEM measurements.

3.1.7. Conclusions

The characteristics of the concomitant Indigo A and B polymorphs have been revisited by our work. Phases A and B are very similar, with close lattice parameters, almost identical packings and closely corresponding interatomic distances. With a threshold of 1 Å, typically used in crystal predictions to identify different structures by comparing their lists of interatomic distances, the two forms would be considered identical. Nevertheless, we have shown that they are indeed different: experimentally because they exhibit clearly different XRD and Raman spectra; computationally because they converge to distinct minima.

With a combination of single-crystal and powder X-ray diffraction (XRD) techniques, we were able to characterize the bulk phases and provide a clear "picture" of the polymorphic composition of the samples. A and B modifications often coexist in bulk, even if phase B seems to be the predominant one. It must be noticed that, in contrast to what has been described literature, the commercial powder available to us is almost entirely composed of the B form, which since its first identification has been assumed to be not trivial to isolate and possibly metastable. The same applies to the product of sublimation, where the B form dominates, but which can be enriched in A by changing the deposition conditions.

In the films, XRD cannot generally identify unambiguously which polymorph is present, a complication that has already been reported in the literature. [85] We successfully tackled this problem carrying out a Raman investigation on the bulk phase, both on the lattice phonons region and on selected intramolecular modes, where spectral features for Indigo polymorph discrimination can be found. With the situation of the polymorphs clarified by the experiments in the bulk, the characterization of the films has

become possible. We have shown that in all the cases in which the close similarities of the two structures impairs their identification by XRD investigations, the micro Raman technique is sensitive enough for polymorph discrimination, identifying the B form as the only one present in films obtained by drop casting and by ultrahigh vacuum (UHV) deposition. In fact, it was the knowledge of the phase yielded by Raman which was used to index the TEM reflections, even though the spectroscopic approach did not enable us to gather understanding on the molecular orientation on the films.

Concerning the characteristics of the films, we have demonstrated that homogenous, stable and reproducible samples can be obtained both on silicon wafer and Tetoron® substrates, but high chemical purity is a necessary prerequisite for this. By AFM we have studied their morphology as a function of the deposition rate, while the TEM analyses have been carried out to determine the molecular organization of the samples at the interface. The poor crystallinity displayed in all our specimens has been improved by the SVA treatment and the obvious next step will be the measurements of their charge transport characteristics.

3.1.8. Appendices

Appendix I: Crystal data and details of measurements for Indigo A

Table A1: Crystal data and details of measurements for crystalline Indigo grown from PVT collected at RT and at 210K and corresponding in both cases to Indigo form A.

	A (RT)	**A (210 K)**
Formula	$C_{16}H_{10}N_2O_2$	$C_{16}H_{10}N_2O_2$
Fw	262.26	262.26
Cryst. System	Monoclinic	Monoclinic
Space group	P21/n	P21/n
Z	2	2
a (Å)	9.2850(9)	9.1942(8)

b (Å)	5.7941(4)	5.7876(6)
c (Å)	11.5722(9)	11.4878(8)
α (deg)	90	90
β (deg)	108.710(10)	108.268(9)
γ (deg)	90	90
V (Å^3)	589.66(8)	580.48(9)
D_{calc} (g/cm^3)	1.477	1.500
μ (mm^{-1})	0.100	0.101
Measd reflns	3667	2516
Indep reflns	1030	1325
R_1[on $F_0{}^2$, I>2σ(I)]	0.0441	0.0662
wR_2 (all data)	0.1475	0.1709
highest diff. peak (e/Å^3)	0.198	0.320
Deepest hole (e/Å^3)	-0.341	-0.307

Appendix II: Comments on the purification of Indigo in view of film fabrication

This paragraph is dedicated to the processes of fabrication of Indigo films and thin films and to their structural characterization.

Preliminarily, it is necessary to spend some words on the important issue of the chemical purity of the material, which in this case has turned out to greatly affect both morphology and phase composition of the solid compound. The implication of this is that quality of the starting material has significant consequences for the quality and reproducibility of thin films prepared by UHV deposition. Note the raw product employed (TCI Indigo) was one of the purest on the market, but still declared to contain 3% of impurities. Possible problems of chemical contamination are not mentioned in the literature and the sublimation conditions adopted for the material purification are not

given. The procedure followed to achieve by sublimation the crystalline powder suited for Indigo film fabrication, starting from the commercial raw material, is in the paragraph 3.1.3 - Experimental Method. Phase composition and crystal morphology of the sublimed material are reported in the paragraph 3.1.4 - The Indigo crystal structures. Here we widen the information by describing in more detail the purification attempts finally leading to the crystalline powder used for the film deposition.

Table A2 contains the list of the tested sublimation conditions, chosen after realizing that the phase composition could be shifted and adjusted in favour of one or the other polymorph, by acting both on the sublimator hot stage and on the deposition temperatures. Each item of the list corresponds to a crystalline batch that has been analysed by Raman and powder XRD.

Table A2: The parameter used for the sublimations are described in this table. All these processes took about 1 or more days, depending on the number of cycles performed.

T hot stage (°C)	T cold finger (°C)	Cooling water	Cycles (n)
120 - 170	≈ 30	√	1
185	≈ 30	√	1
	≈ 30	√	1
	≈ 30	√	2
	70	√	1
200	60	√	1
	50	√	1
	≈ 130	X	1
	≈ 130	X	3

The optimal hot stage temperature was found to be of 200°C; at lower temperatures Indigo vapor pressure is insufficient, but discoloration was observed at higher temperatures, even in inert atmosphere. In no condition was the sublimated material composed of a single crystalline phase, and the situations closer to such a case were the commercial powder (97% of B) and the product of a triple sublimation at a high deposition temperature (10% of A). The relative amounts of the two polymorphs,

determined through a Rietveld refinement, are reported in Figure A1 as a function of the deposition temperature (at the left-hand side of the temperature coordinate the datum for the commercial powder is given). There appears to be a trend in the range 30 to 80 °C, where the A content increases on increasing the temperature. It should be noted, however, that this is counterintuitive with the notion of B being the less dense form, probably with a range of thermodynamic stability at temperatures higher than A. Besides, such a trend does not seem to occur for the highest deposition temperature, where comparable amounts of the two forms are observed.
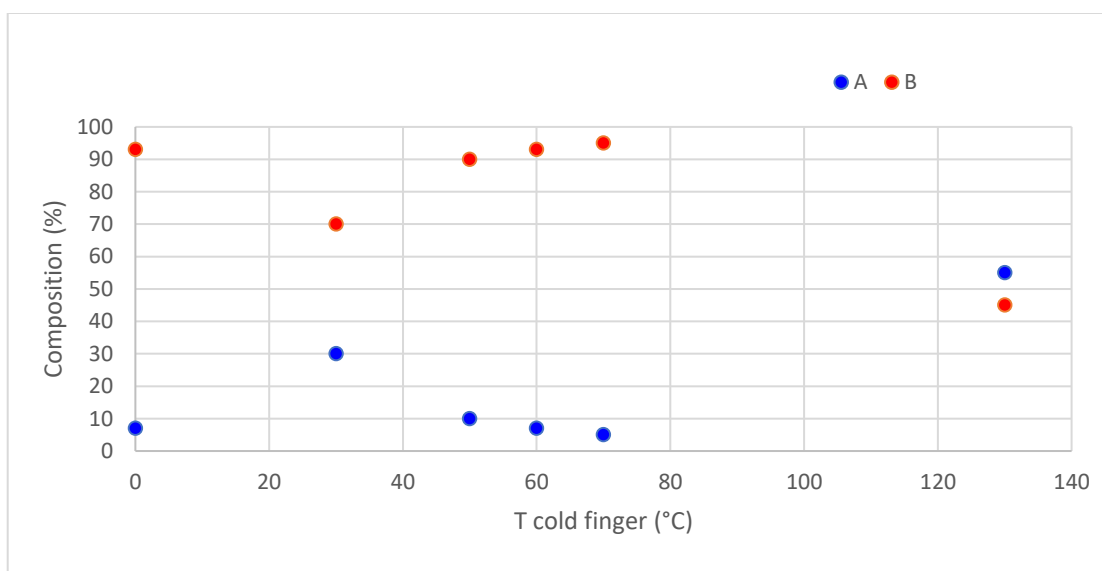
Figure A1: Compositions (%) of crystalline powder vs deposition temperature.

A high deposition temperature certainly contributes to the formation of larger crystals of regular shape, favoured by the slower growth process, as verified by both the XRD diffractograms and the Raman spectra. For instance, in Figure A2 we compare the typical lattice phonon Raman spectra of crystallites obtained at the lowest and the highest deposition temperatures. The former is virtually identical to that of the commercial powder; the latter displays narrower, and therefore better resolved bands, an indication of an improved order and crystallinity. Furthermore, in the specimens collected at high T we observed a drastic reduction of the spectral background, which can be taken as a diagnostic of an improved chemical purity of the material. As shown in the

following, these pieces of information, that is the need of keeping the deposition temperature high to achieve a better crystallinity and a higher degree of purification, were the guidelines for the fabrication of film in UHV conditions.
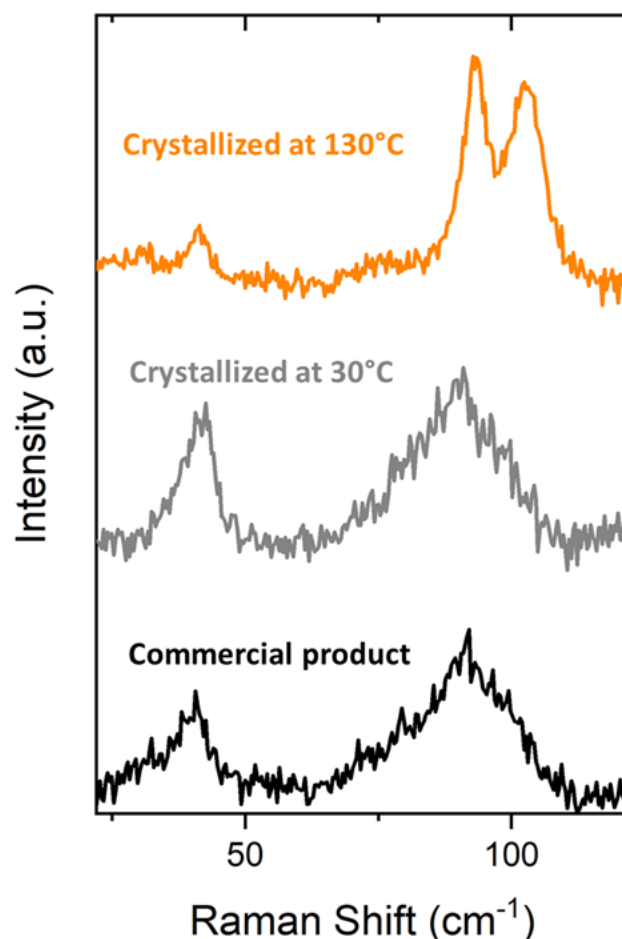
Figure A2: The Figure shows the trend of the lattice phonon Raman spectra with the crystallization temperature.

ESI Mass spectroscopy (ESI-MS) and NMR analyses were performed on the powders obtained in different conditions, trying to clarify their different behaviour when employed in film fabrication, even though the application of these techniques was not trivial due to the low Indigo solubility. In fact, the results obtained by ESI-MS could not be used, due to reproducibility problems. The NMR spectra instead, did not evidence any difference between the samples. To prove this, we report in Figure A3 the spectrum of the commercial powder along with those of the powders obtained at the lowest (30°C)

and highest (130°C) temperatures of our range. They all look identical. Whatever the impurities, their concentrations remain below the detection limit of the technique and no clue is given of the chemical origin of a distinct behaviour.
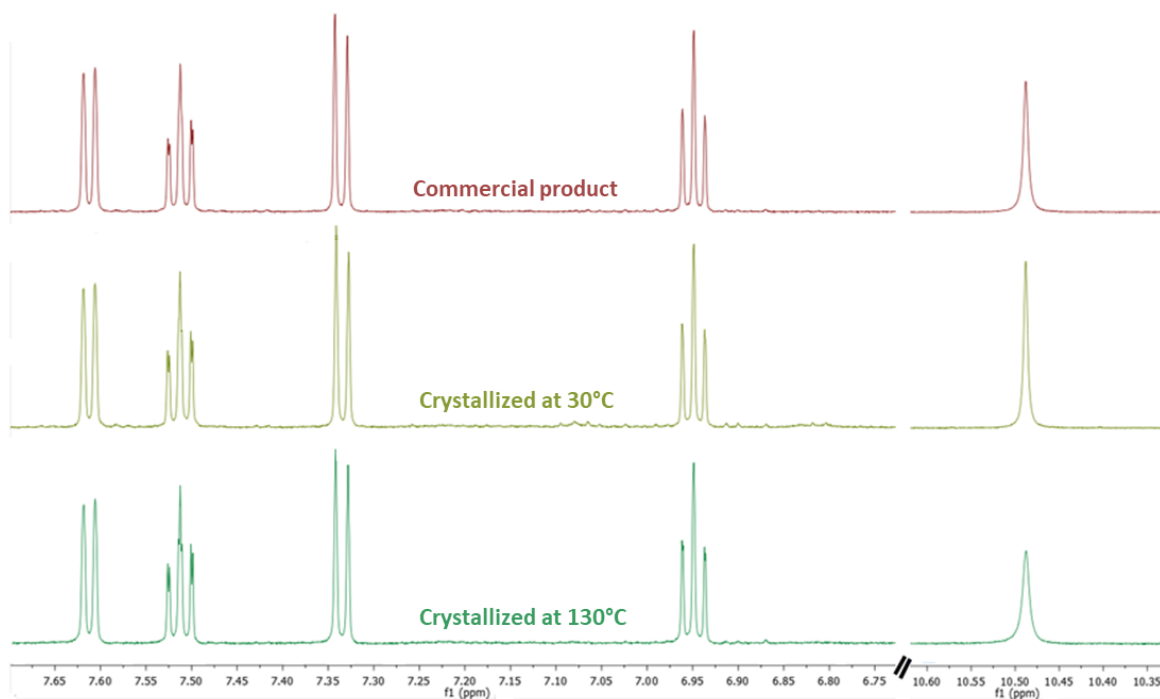
Figure A3: HNMR spectra of the Indigo powders. The regions shown are corresponding to the aromatic (left side) and amine (right side) hydrogen.

3.2.   Thioindigo

3.2.1. Introduction

Thioindigo   (2-(3-oxo-1-benzothiophen-2(3H)-ylidene)-1-benzothiophen-3(2H)-one) is a synthetic Indigoid which is known as a vat dye [118] and, as the other compounds of this family, is characterized by a very low solubility in virtually all solvents. At the beginning of the 19th century, its proprieties as a pigment appeared interesting for companies' applications and a synthetic route suitable for industrial scale production was implemented. The way to produce it is by the alkylation of the sulfur in thiosalicylic acid with chloroacetic acid. The resulting thio-ether cyclizes to 2-hydroxythianaphthene and can be easily converted to Thioindigo. [119]

In addition to its very good properties as the vat dye, recently Thioindigo has aroused the interest for its employment as a functional material in a number of applications. In fact, albeit smaller than Indigo, also this compound exhibits hole field-effect mobility. [83] In addition, the electrical properties of the silicon/Thioindigo heterojunction were studied in view of applications in organic photodiodes and organic photovoltaic devices. [120] However, a satisfactory characterization of its solid-state is still lacking. Given the effect that the fabrication process can have in determining the phase in which the final product is obtained, [121] this knowledge is important. For crystalline products, the link between chemical-physical and structural properties implies that a sound knowledge of polymorphism and degree of order is a necessary requirement. This is why we included this synthetic Indigo derivative, which is known to display polymorphism, [92], [122] in our studies on the relationship between crystal structures and physical properties of organic dyes, aimed to explore their applications as functional materials in the field of organic electronics.

In all the applications so far demonstrated, thin films of this material were fabricated by evaporation techniques, without reporting the polymorph obtained and thus without identifying the phase responsible for the final electronic properties. [123]

Currently, Thioindigo is known to display two crystal phases, named here α and β. Their full characterization was performed as part of the PhD research activity in collaboration with various groups. Simulations and X-ray experiments were performed, concurrently to the Raman work, by co-workers at Bologna University. A "Marco Polo" grant, with a three months secondment, was spent at the University of Graz in Austria, where specular X-ray diffraction, GIXD and AFM were employed on films obtained by drop-cast, with the opportunity of joining the Graz research group for synchrotron measurements in Trieste. Finally, homogeneous films were made using the BAMS deposition method in collaboration with the ICMAB Institute of Barcelona.

3.2.2. Thioindigo crystal structures

Table 3.3 reports the cell parameters collected in our work, compared to the literature data. The Table also contains the structural parameters predicted by the DFT-D3–vdw calculations.

Table 3.3: Crystallographic data for Thioindigo polymorphs, as determined in this work and from the literature. Experiments are compared to the results of the DFT-D3–vdw calculations also by means of the RMSD≥15 between the interatomic distances.

Form	REFCODE	a (Å)	b (Å)	c (Å)	β (deg)	Volume (Å³)	T (K)	Space group	RMSD≥15 (Å)
α	SINDIG [92]	7.91(3)	3.97(2)	20.41(3)	93	640.051	RT	P2₁/c	/
	Our work [124]	7.8130(16)	3.8820(8)	20.503(4)	93.10(3)	620.947	100	P2₁/c	0.05
		7.8770(16)	3.9390(8)	20.542(4)	92.67(3)	636.675	RT	P2₁/c	0.05
β	SINDG02 [122]	3.981(3)	20.65(2)	7.930(7)	98.84(5)	644.163	RT	P2₁/n	/
	Our work [124]	3.8644(3)	20.3897(14)	7.8016(5)	98.610(6)	607.791	100	P2₁/n	0.043
		3.9342(3)	20.4464(11)	7.8580(6)	98.074(7)	625.834	RT	P2₁/n	0.045
α	DFT calc [124]	7.8408	3.8347	20.1538	93.147	605.053	0	P2₁/c	/
β	DFT calc [124]	3.8481	20.1325	7.8525	97.539	603.089	0	P2₁/n	/

The unit cell of polymorph α is monoclinic (P2₁/c) with two molecules (Z=2) residing on crystal inversion centres. The molecular geometry is C_i, with very little deviation from a planar C_{2h} and, for this phase, molecules are stacked along the very short monoclinic axis *b*. Accordingly, in the projection along *b*, molecules appear lying in parallel rows on the plane *ac* (see Figure 3.29). The polymorph β single-crystal structure yields a monoclinic (space group P2₁/n) and also in this case the unit cell contains two molecules on inversion centres. The molecular geometry is virtually identical in the two polymorphs, but the packing of β is quite different from that of form α, with the molecules stacked along the shortest axis *a*, and appearing in a projection along this axis as shown in Figure 3.29. In both polymorphs, π-π stacking interactions are exerted between the molecules aligned along the short axes of the structure, but while in the α polymorph all the stacks are arranged parallel to each other, the β neighbour stacks are rotated with respect to each other. Intra-stack distances and relative molecular orientations within the stacks are very close in the two structures.
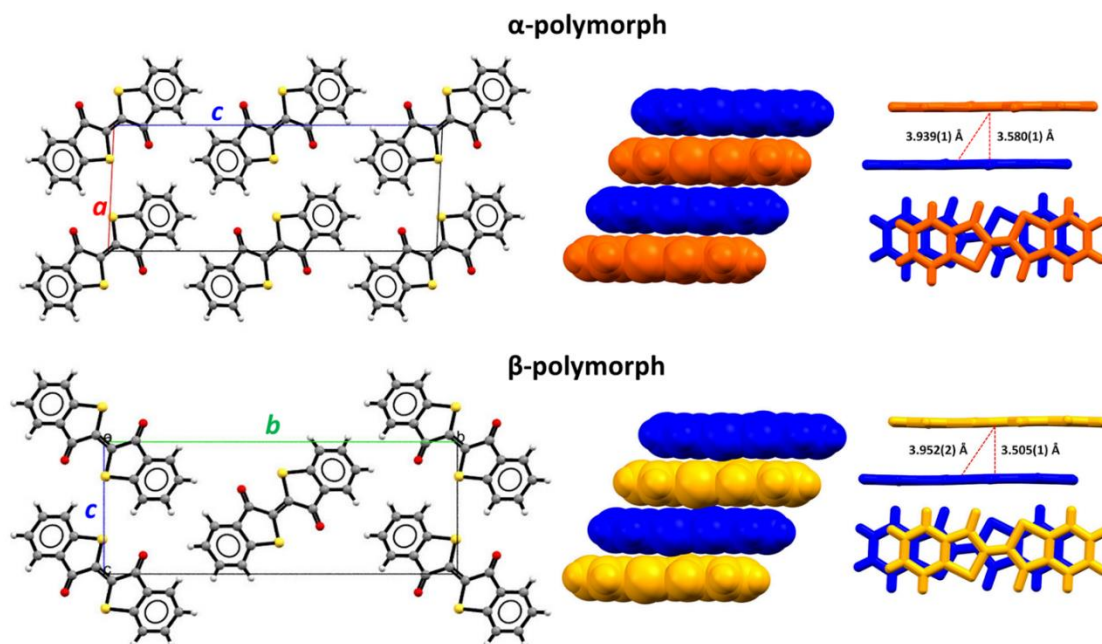
Figure 3.29: Packing of the α- and β-Thioindigo polymorphs; left: projection along the crystallographic axes b and a for polymorphs α and β, respectively; right: representation of the packing along the stacking direction. [124]

In our re-determination of the Thioindigo structures, data were collected at 100 K and room temperature (RT) for both forms, always finding form β slightly denser (by about 2% at RT), with a trend indicating a decrease of density difference on increasing temperature.

In agreement with the experimental findings at finite temperature, polymorph β is calculated to be slightly denser than polymorph α at 0 K. The energy difference between the two phases (≈ 0.02 kcal/mol), however, is smaller than the computational accuracy reported for these calculations [125] and, in fact, it is impossible to reliably predict which modification is the more stable. Even though the calculated volumes at the minimum energy, which do not include the thermal expansion, are smaller than the experimental ones, the agreement is very good, and has been quantitatively determined by computing the $RMSD_{\geq 15}$ between the interatomic distances. [126] The latter is an effective way of comparing crystallographic structures, in which all the interatomic distances between a reference molecule and at least 15 neighboring molecules in a spherical environment are

listed, and pairs of structures are then compared by means of the root-mean-square-deviation (RMSD$_{15}$) between the distance lists.

The precious information on how the single crystal of polymorph α were originally obtained is not reported in the article where this form was the first described. [92] At present, commercially available Thioindigo is found to be entirely composed of polymorph β, and, as reported in the following, most of the methods used to grow bulk crystals in our work have yielded this modification. This case appears similar to Indigo's, where the phase described in literature as metastable turns out to be, in fact, ubiquitous.

3.2.3. Samples preparation

Crystal growth: Thioindigo (TCI Chemicals, 95%) was purified by sublimation in low pressure at 250 °C in an inert atmosphere and by using cooling water at ≈30°C, obtaining microcrystals of irregular shape. Both the commercial and the sublimed crystalline powders are made of polymorph β. Different standard solvents were used to obtain crystals by slow evaporation, but, only from solutions of dichloro- and trichloro-methane, small needle-shaped crystals (about 1 mm long) of the β polymorph were grown. Single crystals of the same phase were also obtained by PVT. In this case, two hot end temperatures were selected in distinct experiments: 250 and 285°C, and temperature gradients of approx. 13 °C/cm and 15 °C/cm, respectively, were measured at equilibrium.

Films obtained by drop casting deposition: Crystalline non-homogeneous films were obtained by drop casting filtered (0.02 μm filter) saturated solutions of various solvents onto 1.5 x 1.5 cm^2 Si/SiO$_x$ wafers or glass slides. Substrates were previously cleaned by an ultrasonic bath in acetone, then deionized water, NaOH, and finally dried under nitrogen. Most solvents (among which dichloromethane, nitrobenzene, acetonitrile) yielded both α and β polymorph crystals of a few microns, indistinguishable for morphology, but that could be identified by micro Raman measurement of their lattice phonon modes. Deposition from xylene solution of sublimed Thioindigo powder

yielded only the α form: in this case, 25 μL of filtered 10^{-3} M solution was deposited on a glass substrate kept at 60 °C, removing the excess solution by a fine tip of paper while spreading. The same procedure was applied while seeking for a third polymorph (see paragraph 3.2.8 - Appendix III), depositing 8 μL of solution directly on the grid used for TEM detection.

Films obtained by BAMS deposition: These samples were fabricated on highly n-doped Si wafers with 200 nm of thermally grown SiO_2 (from SiMat), cleaned in ultrasonic bath with acetone and isopropanol and dried with nitrogen. This type of deposition is a shearing method where a Teflon bar is positioned above the substrate heated, in this case, at 150 °C and 40 μL of solution 0.5 mg/ml (ca 1.5×10^{-3} M) were placed at the interface and sheared at the speed of 1 mm/s. The quality of the films was found to be strongly solvent-dependent: a Thioindigo saturated solution in 50/50 Benzonitrile/dimethyl formamide (v/v) yielded non-homogeneous films of the pure α form, whereas highly textured films of the same polymorph were obtained from pure anisole. The influence of the ink formulation and coating conditions during the deposition of organic semiconductors by BAMS has already been demonstrated to have an impact on the formed polymorph. [127], [128] All the solvents used (Sigma Aldrich) were of spectroscopic grade.

3.2.4. Experimental methods

Raman spectroscopy: Raman spectra in the energy interval of the lattice phonons with excitation wavelength at 647.1 nm. For Thioindigo, power was reduced by neutral density filters to avoid sample damage.

X-ray Diffraction: For α-Thioindigo, single-crystal data collections were performed at the X-ray diffraction beamline (XRD1) of the Elettra Synchrotron, Trieste (Italy). [129] Individual crystals were obtained by removing them from the substrate surface of a microcrystalline film obtained by solution deposition in acetonitrile. To do this, the

crystals were dipped in NHV oil (Jena Bioscience, Jena, Germany) and mounted on the goniometer head with a nylon loop. The full datasets were collected at 300 K and 100 K (nitrogen stream supplied through an Oxford Cryostream 700 - Oxford Cryosystems Ltd, Oxford, UK) through the rotating crystal method on two distinct samples while data were acquired using a monochromatic wavelength of 0.700 Å, on a Pilatus 2M hybrid-pixel area detector (DECTRIS Ltd, Baden-Daettwil, Switzerland). Then the diffraction data were indexed and integrated using XDS. [130] The structures were solved by the dual space algorithm implemented in the SHELXT code. [131] Fourier analysis and refinement were performed by the full-matrix least-squares methods based on F2 implemented in SHELXL (Version 2018/3) [132] while the Coot program was used for modelling. [133] Anisotropic thermal motion refinement has been used for all atoms. Hydrogen atoms were included at calculated positions with isotropic Ufactors = 1.2 Ueq (Ueq being the equivalent isotropic thermal factor of the bonded non-hydrogen atom). Crystals show non-merohedral twinning (reciprocal lattice two-fold twinning axis (0 0 1)), with a twin fraction of ≈45%, identified using PLATON TWINROTMAT algorithm. [134] Twinning is responsible for distortions on heteroatoms connectivities, therefore, carbonyl group geometric parameters have been restrained (using SHELXL DFIX and DANG cards).

Single-crystal data obtained by slow evaporation of a dichloromethane solution were collected as described in the paragraph 3.1.3, and identified as Thioindigo form β (see cell parameters shown in Table 3.3). Its structure was redetermined to get data with more accuracy. All non-hydrogen atoms were refined anisotropically. HCH atoms were added in calculated positions. SHELX97 [94] was used for structure solution and refinement on F2. The program Mercury [95] was used to calculate intermolecular interactions and for molecular graphics.

Grazing Incidence X-Ray Diffraction: GIXD measurements were performed in order to confirm the crystallographic phase on the film samples and to determine the direction of the unit cell axes with respect to the shearing direction in the BAMS deposition. The beamline XRD1 at the Elettra Synchrotron Trieste (Italy) was used with a set wavelength of 1.4 Å. Diffracted intensities were recorded using a Pilatus 2M detector

approximately 200 mm after the sample. For reducing the size of the incident X-ray beam on the sample and thus the peak widths, a relatively high incident angle of 1° was chosen. Due to the expected in-plane alignment introduced by the preparation technique, the sample had to be rotated around its surface normal during the GIXD measurement to ensure that all diffraction information was collected. A total of 150 separate diffraction images, each integrating over 2° of azimuthal sample rotation, were taken, that is a 300° azimuthal sample rotation was performed, which is enough to gain all the relevant information. In the first step, these data allow for the determination of the crystallographic phase after the summation of all the images. In the second step, that is evaluation of the in-plane alignment of the crystallites, the data from the 150 images of distinct azimuths can be used to calculate the pole figures for different peaks. Conversion of the measured data to reciprocal space, crystal phase analysis and pole figure calculations were performed using GIDVis. [135] The orientational analysis of the pole figure evaluation was performed using the software Stereopole. [136]

3.2.5. Characterization of α and β Thioindigo phases

By applying Raman spectroscopy in the lattice phonon energy region, we were able to discriminate between α and β Thioindigo phases and establish the reference spectra characteristic of each phase. The results obtained, complemented with the Raman measurements in polarized light, can be explained in terms of the structural organization of the two solid phase, also relying on the DFT-D3–vdw simulated spectra at the room temperature structures.

On the left of Figure 3.30, we show simulated and experimental Raman spectra of α-Thioindigo crystal at wavenumbers lower than 200 cm^{-1}. The spectra were measured on single microcrystals grown from Thioindigo drop cast samples in acetonitrile (crystal image in the Figure inlet) and xylene. On the right of Figure 3.30, we report the β-Thioindigo spectra of the commercial powder, the crystals obtained by the PVT method and those from dichloromethane (image in the Figure inlet) solution, together with the simulations. The two polymorphs correspond to two significantly distinct profiles, and

this allows us to predict that their presence can be easily recognized when a still unknown sample is analysed.

It is worth noticing that, like in Indigo, the commercial powder contains only the phase assumed so far to be the less stable one, i.e. β, which was obtained also in most of the common growth methods like sublimation, recrystallization in solution or PVT.

Following the calculations, the α polymorph displays six vibrational modes at wavenumbers lower than 80 cm^{-1}. Over this range, experiments yield two broad bands that can be deconvoluted into the predicted number of closely located peaks, rendered in the computed trace by the convolution of Lorentzian bands with a HWHM (half width at half maximum) of 4 cm^{-1}, adjusted to the experimental widths. The β polymorph shows a better-resolved profile that, again, can reproduced by the appropriate convolution of the first six modes calculated for this phase.

Table 3.4 reports the low energy calculated and experimental Raman shifts along with the symmetry assignments of the monoclinic P2$_1$/c space group and the component analysis of the calculated eigenvectors. Both structures correspond to centrosymmetric monoclinic lattices with two molecules/cell, thus with six Raman-active lattice phonons of symmetry 3A$_g$ + 3B$_g$, having the character of pure rotations if the unit cell molecules are treated as rigid bodies. Such an approximation is certainly valid for a molecule such as Thioindigo, with a rigid skeleton and no flexible substituents, and is supported by the eigenvector analysis of the Table. At higher wavenumbers, other weaker bands can be observed, as shown in Figure 3.30, and they are correctly reproduced in both energy and intensity by the DFT simulations. These bands identify intra-molecular modes, common to both polymorphs, as evinced by comparing the two patterns. Note that, unlike what was reported for Indigo, over this region we have not observed bands that can be used as polymorph markers. This appears to confirm the hypothesis that only the H-bonds, which are absent in Thioindigo, are responsible for frequency differences between Indigo polymorphs in this interval.
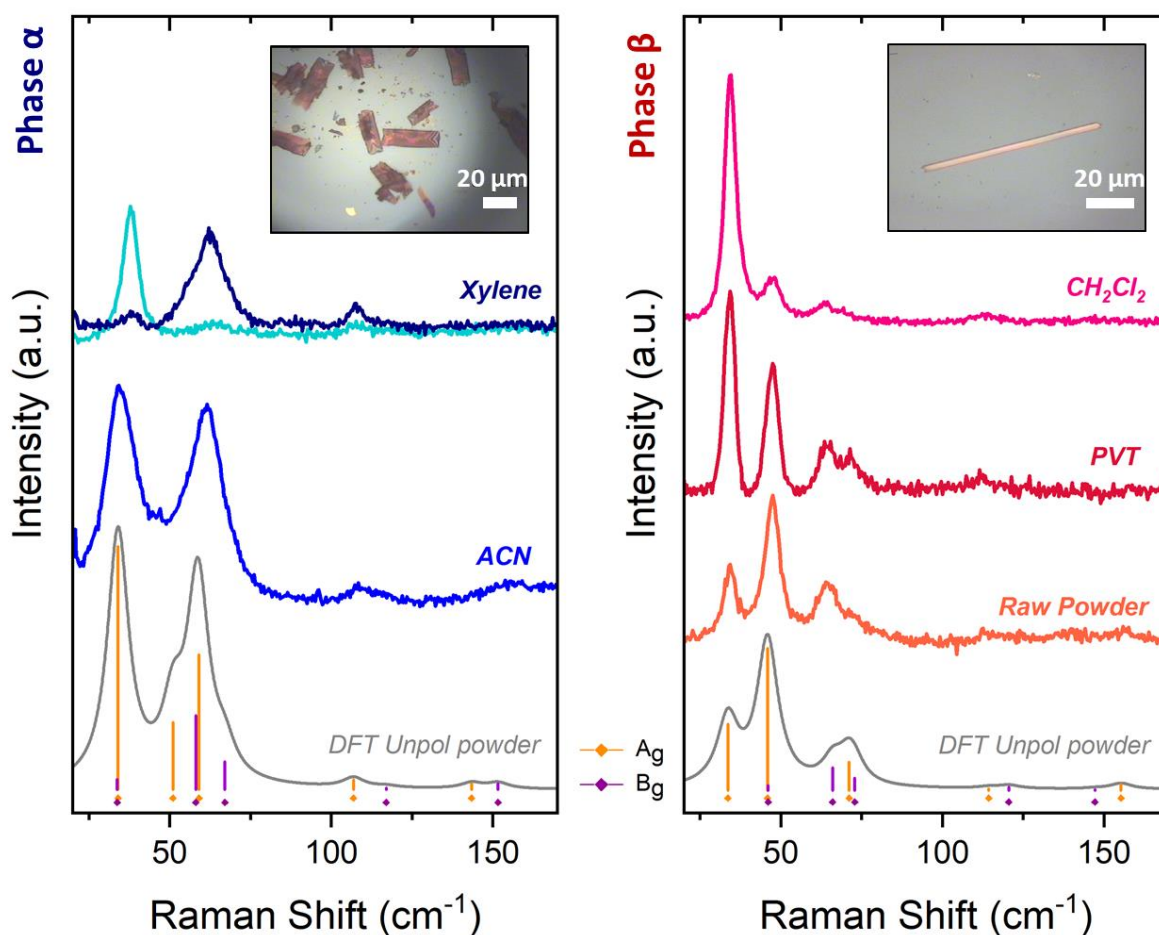
Figure 3.30: Experimental (crystal samples) and unpolarized (powder) simulated DFT-D3-vdw Raman spectra, in the lattice phonons range. The spectra of α-Thioindigo (left side) from xylene in are given for two different orientations of the crystal as an instance of crystal anisotropy. Vertical bars of height proportional to the intensity of the mode identify the calculated values, with colour codes yellow and violet for modes of symmetry A_g and B_g, as indicated. The spectral profiles are built by convolution of Lorentzian bands (see text for details). The spectra of β- Thioindigo is reported on the right side (see images in the inlets).

The anisotropic behaviour of the α phase in single crystal is shown in the top left spectra of Figure 3.30, where the two traces for the crystal grown from xylene have been recorded for two distinct orientations of the same crystal. We can investigate the anisotropy by measuring spectra in polarized light, obtaining information which, as we will see below, can be usefully transferred to the interpretation of the film spectra. In the polarized Raman experiment (explained in paragraph 2.1.4) we must select the polarizations of both the incoming laser and the scattered radiation, finding the correspondence between each phonon band and its symmetry. [30] By decreasing the number of bands detected in each experiment, polarized measurements help in the

deconvolutions by resolving spectra with broad bands which originate from overlaps. From these deconvolutions we have determined the experimental wavenumber of Table 3.4.

Table 3.4: Wavenumbers of the six lowest energy modes of the α and β forms calculated the at RT structure and their symmetry assignments. The lattice phonon character of each calculated mode is reported as the sum of the squared components for the rigid body rotations of the corresponding eigenvector. In the column called "Exp" we have tried to associate the calculated vibration with the experiments.

Polymorph α				Polymorph β			
Sym	Exp (cm^{-1})	Calc (cm^{-1})	Lattice Phonon (%)	Sym	Exp (cm^{-1})	Calc (cm^{-1})	Lattice Phonon (%)
A_g	37	34.1	100	A_g	34	33.6	98
B_g	36	33.7	100	A_g	47	45.9	100
A_g	54	51	98	B_g	48	46.1	100
B_g	62	58	98	B_g	65	66	96
A_g	61	59	98	A_g	71	71.1	98
B_g	65	67	88	B_g	74	72.8	98

The results of the polarized Raman experiment, obtained from oriented single crystals of both phases, are shown in Figure 3.31. The left side is representative of the α polymorph. The scattering plane of the crystals in the image of Figure 3.31 was determined by X-ray measurements and corresponds to the crystallographic face *ab* or (0 0 1), with *b* being the axis of fastest crystal growth. We can thus decode the spectra measured with polarized light in backscattering geometry. The labels (*aa*), (*bb*), and (*ab*) in the Figure are used to indicate the polarization vectors of incident (first letter) and scattered (second letter) light in relation to the crystallographic axis of a sample oriented along its extinction directions. [35] The unpolarized spectrum is given as a reference at the bottom of the Figure and corresponds to a situation where the exciting light is normal to the randomly oriented face (0 0 1) and there is polarization discrimination for the scattered light. DFT-D3–vdw polarized spectra calculated for the given face (0 0 1) are

also shown. Due to the symmetry properties of the polarization matrix, the spectra indicated with labels (*ab*) and (*ba*), recorded in cross-polarization, display only modes of B_g symmetry with identical intensities. Instead, spectra indicated with (*aa*) or (*bb*) display A_g modes only, but the intensities in the two spectral profiles depend on the two distinct matrix elements, (*aa*) and (*bb*), respectively. For instance, these considerations enable us to solve into an A_g/B_g doublet the broad feature centred at 36 cm^{-1}, recording a frequency shift compared to the spectra in Figure 3.30. Also, we can interpret the shift of the maximum of the other broad feature, centred around 61 cm^{-1}, as depending on the presence of two unsolvable A_g modes in the spectra labelled as (aa) and (bb) and two B_g modes in the (ab) spectra. This kind of experiment is strongly assisted by the computed frequencies and its results are supported by the good agreement of the theoretical model with the experiment. Note that in this measurement, more than in the symmetry assignment of each detected mode, we were interested to linking the spectral features and their intensity in polarized light to the crystal orientation, as this turned out to be the crucial information for the study of the films.

The polarized Raman spectra of β-Thioindigo are shown on the right of Figure 3.31 with the single needle-like crystal pictured in the inset. As probed by X-ray diffraction, the excitation beam of the Raman experiment impinges on the face $(0\ 1\ 1)$. Here the needle axis corresponds to the crystallographic axis *a*, so that in the (*aa*) configuration, only Raman-active modes of A_g symmetry are allowed. In cross-polarization, the scattering perpendicular to *a* does not probe a principal component of the polarizability tensor and a mixture of A_g and B_g modes is observed.
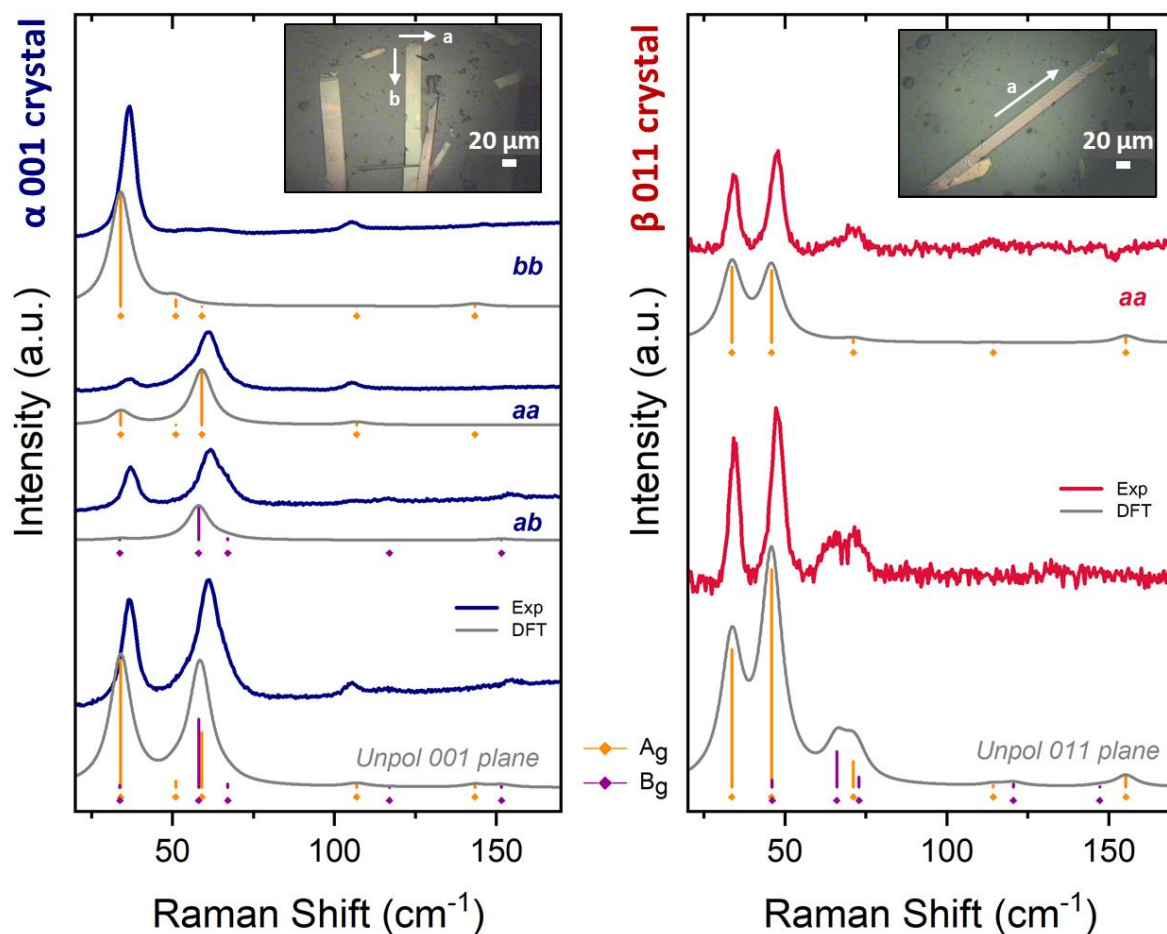
Figure 3.31: Polarized experimental and calculated Raman spectra for both Thioindigo crystal forms. In the crystal images the crystallographic directions are given. Vertical bars of height proportional to the intensity of the mode mark the calculated wavenumbers, with colour codes yellow and violet for modes of symmetry A_g and B_g, as indicated in the Figure.

3.2.6. Characterization of Thioindigo films obtained by BAMS method

Films prepared with by drop casting methods are often scarcely homogeneous, characterized by the presence of nano- and microcrystals. Moreover, as explained above, small variations in the evaporation rate of the solvent might change the polymorphic composition of the sample. Remaining in the field of solvent deposition methods, we applied the BAMS growth method for the film fabrication, as this has turned out to be an effective technique for controlling film morphology and polymorphism by allowing finer control of the crystallization kinetics and thermodynamics. [127], [128], [137] We noticed that on surfaces polymorph β could never be obtained as a pure phase, whereas this was the

only route to acquire measurable samples of the α polymorph and even to induce only its growth, as in the case of xylene. In fact, we were able to single out some single crystals of this form for the structural characterization by removing them from the substrate. Thus, different temperature and solvent conditions were tested, trying to achieve both a selective phase growth and an improved film quality in terms of homogeneity. The best-looking films at the optical microscope were analysed by X-ray diffraction to probe phase and alignment, while by polarized Raman spectroscopy we systematically investigated, by micrometric mapping, the deposition conditions yielding a pure phase. In all of them, only the phase α was present, and an instance of one of the best oriented film, obtained from anisole solution, as described in the sample preparation section is given in Figure 3.32.
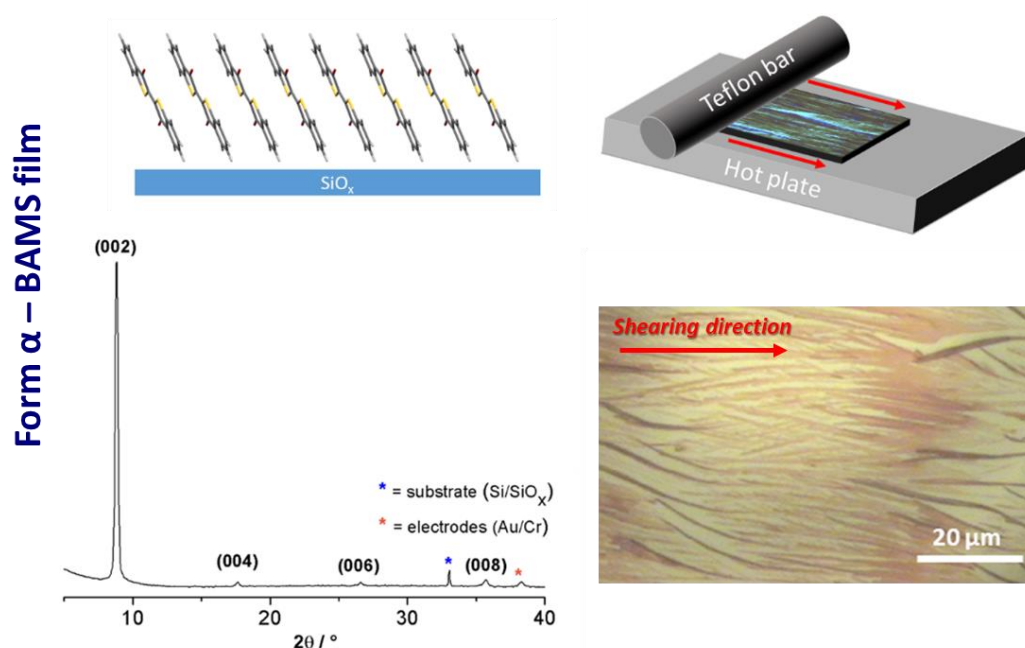
Figure 3.32: In the left side: XRD spectrum (bottom) of the anisole solution sheared film with the representation of the molecule arrangements (top). In the right side: optical image in bright field of the sample (bottom), scheme of the BAMS with the optical image in cross-polarization (top).

In the Figure also an image exemplifying the functioning of the BAMS shearing method appears: while the solution is dragged along the surface by the moving bar, the evaporation takes place at the meniscus between the two solid interfaces.

As inferred by the XRD measurements of the film of the Figure, the contact plane corresponds to the crystal face *ab*, meaning that the Thioindigo molecules are nearly standing at the interface, with the long molecular axis forming an angle of 22° with the normal to the substrate. Moreover, the optical images (in bright field and in cross-polarization) suggest the presence of a macroscopic alignment of the domains along the shearing direction.

To gain access to the other crystallographic directions of the BAMS film, rotating grazing incidence X-ray diffraction measurements were used. Such a method allows to construct pole figures from which the orientation of the crystal planes with respect to the shearing direction can be deduced. Details of the GIXD measurements, confirming the presence of the α phase, with the crystallographic (0 0 1) plane parallel to the substrate surface can be found in the paragraph 3.2.8 - Appendix II. The results show that the film clearly displays a preferential in-plane alignment. In particular, the *a* axis is found to be parallel to the shearing direction. Optical microscopy reveals that adjacent crystals are slightly inclined in their growth direction, which is often observed when using shearing methods on isotropic surface. Using the rotating GIXD this variation is determined to be about 20°

In order to probe the degree of order at a microscopic level by the spectroscopic technique, we made use of polarized experiments, acting on both the direction of polarization on the sample and that of the scattered radiation from the film. In the Raman polarized measurements, shown in Figure 3.33, the film was thus oriented either parallel or perpendicular to the shearing direction, while the polarizations of the exciting and scattered field were set as shown in the Figure.

The result shown in Figure 3.33 is very interesting, as all polarized Raman profiles of the film appear very similar to that of the (0 0 1) face of the single crystal of the α polymorph of Figure 3.31, in agreement with an extended iso-orientation of the crystal domains where the *a* axis is aligned with the shearing direction. This is supported by the comparison of the experimental profiles to the corresponding DFT simulated polarized spectra. Thus, the diffraction methods identify the molecular organization at the solid

interface, and the polarized Raman spectra show that the deposited films behaves like a single crystal, even though the responses of a single crystal perfect lattice and of a film are physically different. As one can gather from Figure 3.33, the DFT simulated Raman spectra of oriented crystals can be employed to fit the experimental data and determine the spread of the *ab* plane alignment on the shearing direction detected by the rotating GIXD measurements. This is obtained by fitting the experiments to the sum of single crystals spectra simulated assuming a Gaussian distribution of angles about the shearing direction. Such a distribution is found to have a standard deviation σ = 21°, in excellent agreement with the GIXD result. Possible mismatches between experiments and calculations can be explained on the bases of a limited mosaicity of the sample, exposing faces different from the (0 0 1).
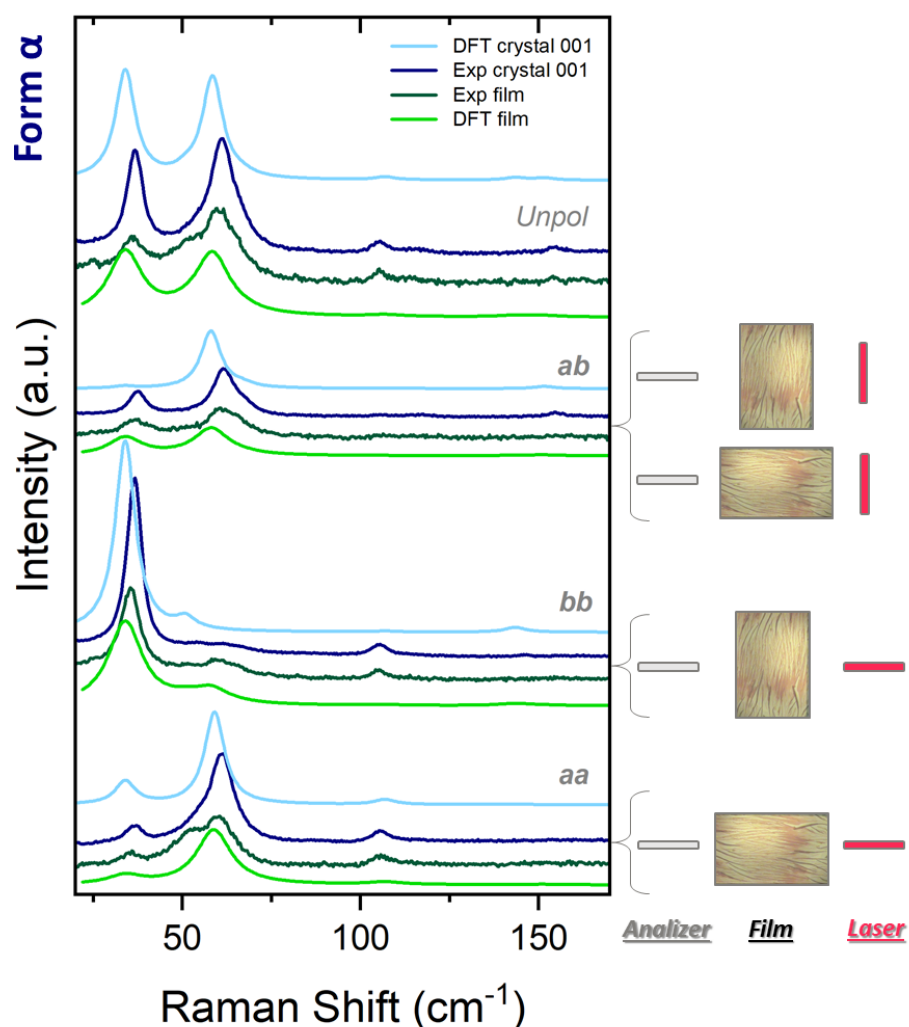
Figure 3.33: Polarized Raman Spectra in the lattice phonon energy range of the Thioindigo film obtained by BAMS from anisole solution. The sample has been aligned with respect to the shearing direction as shown on the right. Red bars give the direction of polarization for the exciting and scattered light as selected by the analyser (grey bars). The film spectra are compared to those measured on the $(1\,0\,0)$ face of a single crystal, to the DFT simulations for the same face and to the spectra resulting from the fit of a Gaussian distribution of crystal orientations about the shearing direction (see text).

All the collected information allows us to conclude that the BAMS methods produces nicely oriented film containing the α phase only. Despite the fact that the literature reports many instances of selective polymorph stabilization by surfaces, [21], [138] the combination of selectivity and high degree of iso-orientation is not, to our knowledge, very common.

3.2.7. Conclusions

In studying Thioindigo, we have followed the usual approach adopted for H-bonded pigments, i.e. we have dealt with its polymorphism, with the specific purpose of defining the phases present in growths at solid interfaces through their structural and spectroscopic characterization. This has been done by the synergic application of many experimental techniques, on which this thesis focuses, and has been supported by the computational results produced within the research group. Each method added a "mosaic tile" to the overall picture of the system

While revisiting the bulk behaviour, similarly to Indigo, we have found that β-Thioindigo, the polymorph thought to be the less stable on the assumption that was the second one to be characterized, is instead present in the commercial product and is obtained in most of the common growth methods we tried. The α form (supposed to be the most common) can be instead easily detected on surfaces and, in some cases, together with β but without forming mixed phases. Actually, we reckon that we are dealing with another case of concomitant polymorphs, where it is very difficult to bracket the thermodynamic conditions in which either is more stable, even though experimental clues in this research and from previous works suggest that the α phase might be metastable at room T.

The important finding is that the α polymorph gets stabilized in growths on substrates, so much as to become the only one present. This result has been achieved by exploiting the potentialities of the BAMS deposition method, which intrinsically supplies a control on the molecular alignment of Thioindigo dissolved in anisole. The pure α phase films so obtained are macroscopically oriented along the *a* crystal axis, which represents the shearing direction of the solution deposited on the hot plate. Polarized Raman and GIXD results confirm the high iso-orientation of the film structures, which in Raman turns out to be reminiscent of that of a (0 0 1) plane of the single crystal. Given the surface selectivity for this phase, it is likely that the charge transport performances reported for devices fabricated with Thioindigo must be ascribed to this polymorph.

The search for substrate-mediated crystal structures has paved the way to a fresh approach to the phenomenon of polymorphism, with the focus on the capability of interfaces to tune a specific nucleation event, although the underlying mechanisms are not really understood. The substrate can act as a template for molecular deposition [42] or the interplay of weak interactions at all the interfaces present eventually produces fully new molecular arrangements that can be named SIP, not reproducible in the bulk. Finally, the surface stabilizes a form metastable in the conditions of growth, and this appears to be the case with Thioindigo, in a way similar to many of the cases described in this thesis.

This chapter ends with Appendices in which further experimental details, not essential to the discussion on the Thioindigo results, are given. Appendix III, however is dedicated to the report of the search for the third Thioindigo polymorphs, the existence of which was suggested by misleading experimental evidences that later on turned out to be due to chemical impurities of the samples. Useless as this report may appear, it is nonetheless the result of a great deal of work, which taught the PhD student two lessons: the use of many of the techniques needed in her research and their data treatment; the necessity of pursuing the important issue of chemical purity.

3.2.8. Appendices

Appendix I: Crystal data and details of measurements for α- and β-Thioindigo

*Table A1: Crystallographic data and refinement details for **α-Thioindigo** at 300K and 100K.*

	300 K	100 K
CCDC Number	1920129	1920128
Chemical Formula	$C_{16}H_8S_2O_2$	$C_{16}H_8S_2O_2$
Formula weight (g/mol)	296.34	296.34
Temperature (K)	300(2)	100(2)
Wavelength (Å)	0.700	0.700
Crystal system	Monoclinic	Monoclinic
Space Group	$P\,2_1/c$	$P\,2_1/c$
Unit cell dimensions	a = 7.877(2) Å	a = 7.817(2) Å
	b = 3.939(1) Å	b = 3.886(1) Å
	c = 20.542(4) Å	c = 20.506(4) Å
	α = 90°	α = 90°
	β = 92.67(3)°	β = 93.07(3)°
	γ = 90°	γ = 90°
Volume (Å^3)	636.7(2)	622.0(2)
Z	2	2
Density (calculated) (g/cm^{-3})	1.546	1.582
Absorption coefficient (mm^{-1})	0.391	0.401
F(000)	304	304
Crystal size (mm^3)	0.12 x 0.04 x 0.04	0.08 x 0.02 x 0.02
Crystal habit	Orange thin rods	Orange thin rods
Theta range for data collection	1.96° to 23.87°	1.96° to 25.91°
Index ranges	$-9 \leq h \leq 9$ $-4 \leq k \leq 4$ $-24 \leq l \leq 24$	$-9 \leq h \leq 9$ $-4 \leq k \leq 3$ $-24 \leq l \leq 25$
Resolution (Å)	0.86	0.80

Reflections collected	3175	3113
Independent reflections (data with I>2σ(I))	994 (577)	1224 (533)
Data multiplicity (max resltn)	2.82 (2.60)	2.34 (2.13)
$I/\sigma(I)$ (max resltn)	6.80 (1.66)	2.59 (0.70)
R_{merge} (max resltn)	0.0733 (0.4044)	0.1602 (0.6411)
Data completeness (max resltn)	97.1% (93.5%)	96.9% (97.2%)
Refinement method	Full-matrix least-squares on F^2	Full-matrix least-squares on F^2
Data / restraints / parameters	994 / 3 / 80	1224 / 3 / 80
Goodness-of-fit on F^2	1.018	1.081
Δ/σ_{max}	0.000	0.001
Final R indices [I>2σ(I)]	$R_1 = 0.1122$, $wR_2 = 0.2392$	$R_1 = 0.1365$, $wR_2 = 0.2859$
R indices (all data)	$R_1 = 0.1636$, $wR_2 = 0.2697$	$R_1 = 0.2393$, $wR_2 = 0.3436$
Largest diff. peak and hole (e·Å^{-3})	0.703 and -0.682	0.959 and -0.804
R.M.S. deviation from mean (e·Å^{-3})	0.111	0.159

CCDC 1920129 and 1920128 contain the supplementary crystallographic data for **α-Thioindigo** at 300K and 100K. These data can be obtained free of charge from The Cambridge Crystallographic Data Centre via https://www.ccdc.cam.ac.uk/structures.

*Table A2: Crystallographic data and refinement details for **β -Thioindigo** at 300 K and 100 K.*

	300 K	100K
CCDC Number	1919969	1919968
Formula	$C_{16}H_8O_2S_2$	$C_{16}H_8O_2S_2$
FW (g/mol)	296.34	296.34
Cryst. System	Monoclinic	Monoclinic

Space group	P2$_1$/n	P2$_1$/n
Z	2	2
a (Å)	3.9342(3)	3.8644(3)
b (Å)	20.4464(11)	20.3897(14)
c (Å)	7.8580(6)	7.8016(5)
α (°)	90	90
β (°)	98.074(7)	98.610(6)
γ (°)	90	90
V (Å^3)	625.83(8)	607.79(7)
D$_{calc}$ (g/cm^3)	1.573	1.619
μ (mm^{-1})	0.421	0.434
Measd reflns	3962	2065
Indep reflns	1100	1070
R$_1$[on F02, I>2σ(I)]	0.0501	0.0499
wR$_2$ (all data)	0.1341	0.1460

CCDC 1919969 and 1919969 contain the supplementary crystallographic data for **α-Thioindigo** at 300K and 100K. These data can be obtained free of charge from The Cambridge Crystallographic Data Centre via https://www.ccdc.cam.ac.uk/structures

Appendix II: Grazing Incidence X-Ray Diffraction

Figure A1 shows the reciprocal space map which results from the summation of all the 150 images collected from the azimuthal sample rotation of a film of Thioindigo fabricated by the BAMS deposition method, as explained in the paragraph 3.2.4 - Experimental Methods.

The intensity is color-coded and Lorentz, polarization, solid angle, pixel distance and detector efficiency corrected. Besides a strong peak from the silicon substrate (red marker) and the diffraction signal of gold (top right), several peaks of Thioindigo can be observed. These non-substrate peaks can be assigned to polymorph α. The

crystallographic (0 0 1) plane is determined to be parallel to the substrate surface and the unit cell *a* and *b* axes thus lie in the plane of the substrate surface. To compare the structure factors of the experiment with those of the known crystal structure, circles around each expected peak are drawn whereby the size/area is proportional to the expected intensity. Overall, a very good agreement is present, showing that the GIXD pattern belongs to the α polymorph. Slight deviations between expected and measured cell parameters might be related to the incomplete sample rotation or the larger extension along some direction compared to another.
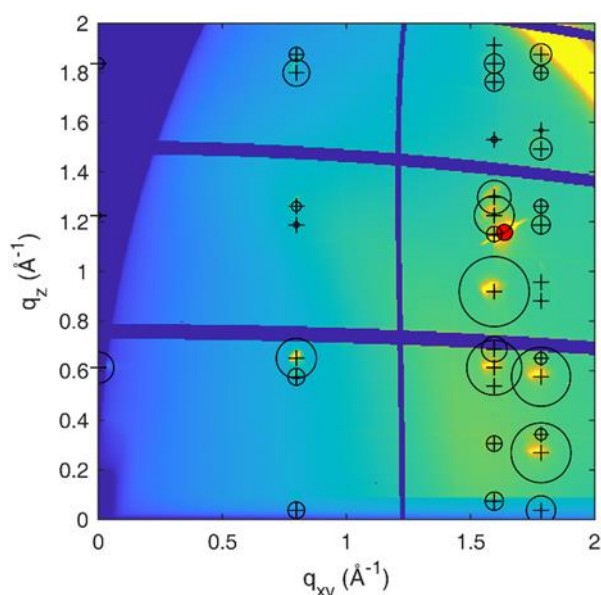

Figure A1: Reciprocal space map obtained from summing the 300° sample rotation, overlaid with the Thioindigo α phase reported in the main text (+ symbols). Expected intensities are proportional to the area of the rings. The silicon (1 1 1) peak is denoted by a red marker.

A pole Figure is the measurement of one netplane distance as function of the sample rotation or azimuth (φ – rotation) and inclination (Ψ) with respect to the sample surface normal (Ψ = 0°). From this, the directional information can be derived. Figure A2a shows the pole figures of the (1 0 2) net planes extracted from the GIXD data. At an inclination of about 50°, segments of high intensity were observed. These poles can be explained by the (1 0 2) planes of the α phase in (0 0 1) texture (red) and by another texture of the same phase with (0 0 $\bar{1}$) orientation (blue), equivalent to the former but with the structure inverted of 180°.

Figure A2d shows the azimuthal intensity distribution of the pole figure A2a, for Ψ = 50.80°. The two maxima at 90° and 270° indicate the main $(1\,0\,2)$ and $(\bar{1}\,0\,\bar{2})$ directions, respectively. The width of the peaks is an indication a certain amount of material grows also along other directions. Analogous conclusions can be drawn from the data in Figure A2b.

The pole figures can now be used to identify the crystal orientation with respect to the shearing direction. Given the geometry of the experimental setup and the sample mounting, planes perpendicular to the shearing direction are probed at Ψ=90°, ɸ=0° or ɸ=180°, while planes parallel to the shearing direction are probed at Ψ=90°, ɸ=90° or ɸ=270°. As shown in Figure A2c, the $(1\,0\,0)$ direction of both possible orientations can be found at Ψ=90°, ɸ=90°. This means that the *a* axis of the unit cell is parallel to the shearing direction, with a maximum spread of misalignment of about 20°. Optical microscopy also reveals that adjacent crystals are slightly inclined in their growth direction, which is often observed when using shearing methods on isotropic surface. Improvement of the overall growth direction might be obtained by using structured surfaces as demonstrated for similar sample preparations. [42]
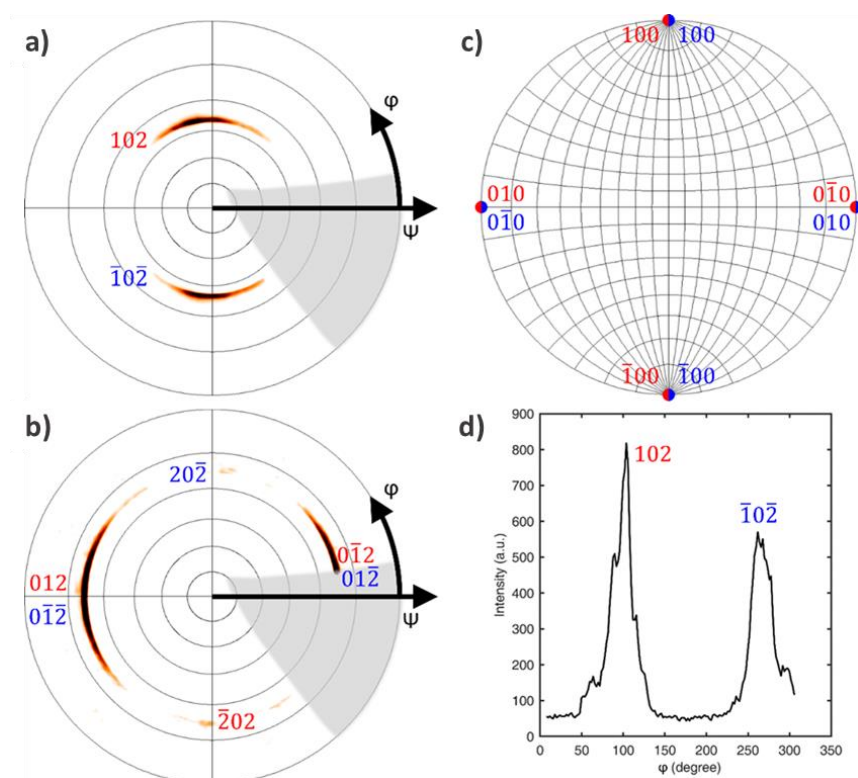
Figure A2: Pole figures of two peaks of Thioindigo overlaid with expected peak positions in $(0\ 0\ 1)$ (red) and $(0\ 0\ \bar{1})$ (blue) orientation (a,b), epitaxial relationships (c) and azimuthal intensity distribution of the $(1\ 0\ 2)$ and $(\bar{1}\ 0\ \bar{2})$ peak.

Appendix III: Notes on the search for the third Thioindigo polymorph

As explained in the previous paragraphs, before resorting to the use of the BAMS method to obtain Thioindigo films, drop casting deposition was attempted, finding that acetonitrile yielded the best results in terms of surface coverage and film morphology. Preliminary GIXD measurements performed on these samples showed the presence of the α form, but in addition to this we recorded a new peak that could not be attributed to either of the known polymorphs and suggested the occurrence of a different or distorted structure of the same system. Micro Raman measurements did not agree with this finding, showing always the lattice phonon patterns of either α or β form. We thought, however, that the matter was worth investigating by means of GIXD and AFM

experiments at the Department of Pharmaceutical Technology, Karl-Franzens-Universität of Graz (Austria), after preparing samples in different conditions.

The rationale consisted in changing systematically three parameters, i) solvents (*e.g.* in methanol, tetrahydrofuran, acetone, acetonitrile, isopropyl alcohol, toluene, xylene, chlorobenzene, nitrobenzene, dichloromethane and trichloromethane), ii) substrates (glass, silicon and mica), iii) fabrication methods (dip coating, drop casting and spin coating). In some cases, the obtained films were also post-treated by SVA technique.

Dip coating did not give any interesting results. The poor solubility limited the amount of material deposited onto the substrates of interest. Neither a treatment of silicon and glass substrates with 3-aminopropyl-triethoxysilane (APTES) to induce silanization and make them more reactive nor the use of polymeric dispersion of the powders produced any real improvement of the film quality. Above all, the unknown peak could not be reproduced.

Intriguing results were obtained by placing two paired microscope glass slides in a small becker with a THF solution. For capillary effect, the liquid flows between the slides and crystallization can take place in the interstice. After one month, at the microscope some spherulites (see Figure A3Figure A3) were clearly visible, with an unusual morphology for Thioindigo. X-ray specular spectra revealed a pattern different from those of the known phases, thus hinting to the presence of a different polymorph. Unfortunately, the sample was too thin, and spectra too noisy to provide enough information on the structure.
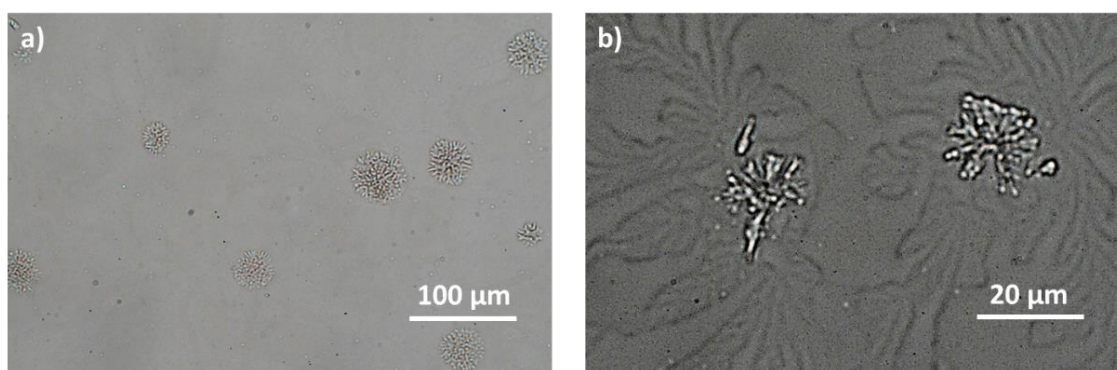

Figure A3: Microscope images of a film deposited for capillary effect of a THF solution between two glass slides.

Besides this, most interesting results were obtained in the AFM measurements performed on some spin-coated and, in particular, drop casted samples. For instance, after several tests in which amount of material, concentration and rate of evaporation were changed, we were able to finally fabricate films showing the new peak in the specular X-ray measurements. The recipe for those samples, that proved to give highly reproducible results, involved to prepare a saturated solution in acetonitrile, remove the supernatant, filter it with a filter of 0.02 μm size and deposit 150 μL of it by drop casting. AFM analyses revealed in this case an unexpected morphology, with a layer by layer organization within an inter-layer distance of 3 nm, as shown in Figure A4, which did not agree with either α or β form's lattices.
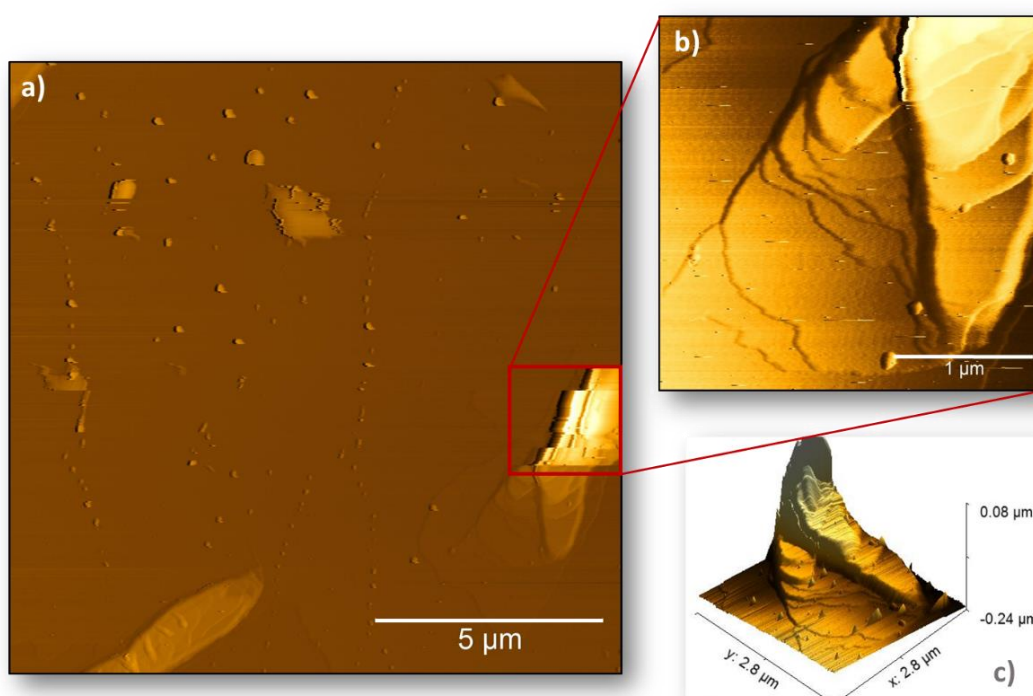
Figure A4: AFM image of Thioindigo in acetonitrile deposited by drop casting on silicon substrate (see text for details).

Also Specular X-ray and GIXD synchrotron measurements, displayed a pattern of new peaks. Figure A5 shows some representative spectra collected on one of the samples and the synchrotron measurements performed on it, with the peaks attributed to the new phase drawn in yellow.

Despite all our attempts to improve the results and isolate the new phase, this was found always to occur mixed with other ones, especially. From the peaks in Figure A5, the determination of a set of lattice parameters was attempted but, because of the insufficient number of peaks, the fit yielded an unacceptable triclinic unit cell with a density that predicted a non-integer number of molecules/cell (between 3 and 4).

Figure A5: Specular X-ray spectra (on top) and synchrotron measurement (on the bottom) performed on the ACN drop cast samples. Yellow spots (and lines on top) corresponding to the new structure while the green one to the known phase.

As the situation was not understood yet, some the TEM beamtime in Strasbourg was devoted to check whether more information could be obtained. The same recipe was adopted for sample preparation, depositing 8 µL of the solution directly on the TEM grid, and we observed an ED pattern in agreement with the unknown structure as detected by GIXD, but still of insufficient quality to give trustable lattice parameters. At this stage, however, after learning from the Indigo case, in which the chemical purity had contributed so much to the quality of the films, samples were prepared with doubly sublimed Thioindigo powder. After that, any indication of the new phase disappeared in all kinds of preparation, meaning that it was the effect of some Thioindigo by-product particularly soluble in ACN.

Therefore, the great deal of work dedicated in Graz to the search of the third, possibly surface induced, polymorph, ended with a defeat. However, all the work done on it was all but wasted, as it involved preparing and analysing many different samples with the various available techniques. It was during this search, for instance, that we finally observed that the substrate was selective towards the α form, as this was the one always present. Here we also realized that fast evaporation processes, involving the heating of the sample and rapidly reaching solution supersaturation conditions, favoured the α form. The TEM and GIXD results are reported in Figure A6.
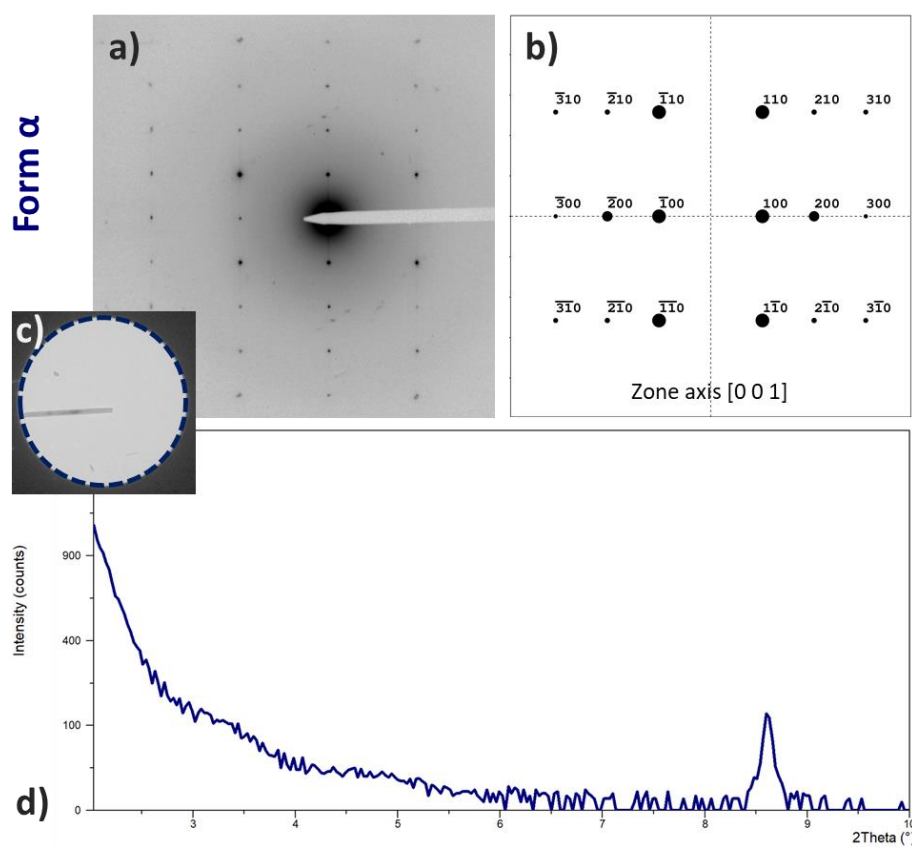
Figure A6: a) Measured TEM diffraction patterns for drop cast film of xylene (solution 10^{-3} M) and containing thioindigo α polymorph; b) Simulated pattern corresponding to the [0 0 1] zone axis; c) The inset shows the corresponding defocused image of the diffracting area; d) Specular X-ray spectrum corresponding to a drop cast sample of xylene.

3.3.   Quinacridone

3.3.1. Introduction

Quinacridone (5,12-dihydroquinolinoij2,3-b-acridine-7,14-dione, abbreviated as QA) is one of the most important pigments with widespread industrial applications for red-violet shades, internationally known with the Colour Index of ''C.I. Pigment Violet 19''. Chemically, it belongs to the hydrogen- bonded class of acridone pigments, which include also derivatives such as Dimethylated Quinacridone and Dichlorinated Quinacridone) The annual production of QA totals several thousands of tons with a sales volume of more than 100 million euros per year. [139] The compound has been known since 1935, [140] has been industrially produced since 1958 [141] and there are currently known several possible synthetic routes. It is used for the coloration of lacquers and paints, plastics, printing inks, and many other applications, sought for its stability and low production costs. [142]

In addition to its properties as a pigment, it has been recently proposed as a field-effect transistor [77] and photovoltaic material. [143] Its structure is assumed to be chemically similar to Pentacene, which is a well-known organic semiconductor with very good performances, and it has shown good stability to high temperature, light, and solvents, also for many years. Despite the weak π-conjugation which characterizes the QA molecule, similarly to the other pigments studied in this thesis, the cooperative effect of very strong H-bonds and π-π stacking interactions in the aggregation process, produces crystalline organizations displaying good ambipolar charge-transport properties. This was the case with Indigo and its derivatives, and the same occurs for QA and related molecules. [83]

In this chapter, we address the question of polymorphism in QA, in view of its employment in the field of OSC. QA polymorphism it has been subjected to many investigations, but still a remarkable confusion about it is present especially in the literature concerning pigments and their applications. Many polymorphs of this compound are described in patents and papers, all declared to be characterised or identified by X-ray powder diffraction. In fact, confusion and mis-assignments are partly generated by patent issues and nomenclature rules, which in the case of pigments refer directly to colour (for instance Pigment Violet 19), without any reference to the solid phases with that specific shade. At the same time, the generic name "Quinacridone" has been used for both the actual QA and some derivatives (like the 2,9-dimethyl-QA). [144]

A series of accurate structural studies and a closer look at the powder diagrams of the individual phases, have shed some light and it is now accepted that pure QA can be obtained in four different forms, named α', α'', β and γ. [139], [145] The β and γ phases have high photo stabilities and high fastness to weathering so that they can be used for applications. The α-forms instead are not commercially available as they easily convert to the β or γ polymorphs, especially at elevated temperatures (as in coating).

Table 3.5 summarizes the crystallographic data of the α', α'', β and γ polymorph available in the literature. The existence of the α'' structure has been assessed by its X-ray powder diffractogram, but in fact its lattice parameters are not yet well defined and are not given in the Table.

Table 3.5: Crystallographic data of the polymorphs α', β and γ. [139]

Form	α'	β	γ
Space group	P1	P2$_1$/c	P2$_1$/c
Z	1	2	2
a (Å)	3.802(2)	5.692(1)	13.697(9)
b (Å)	6.612(3)	3.975(1)	3.881(3)
c (Å)	14.485(6)	30.02(4)	13.4020(10)
α (deg)	100.68(8)	90	90
β (deg)	94.40(6)	96.76(6)	100.44(1)
γ (deg)	102.11(5)	90	90
Volume (Å^3)	346.7(1)	674.5(9)	700.6(7)
T (K)	293(2)	293(2)	293(2)

Differently from what happens for the other pigments we have treated in this thesis, polymorphism in QA affects an important characteristic of the pigment, namely its colour, demonstrating how important it is to know the structure-property relationship. In particular, despite the fact that QA solutions are yellow, the β-phase is known to be a reddish violet, while the γ-phase is red. Also the colours of α' and α'' are considerably different: whereas α' has a dull reddish-violet shade, α'' is red, but with a blue shade compared to γ. [139]

In view of its application as an organic semiconductor, recent works by different groups have published a wide range of mobility values for QA films. For example, Berg and co-workers [146] measured an average charge mobility of 1.5×10^{-3} cm^2/Vs in films evaporated on silicon wafers. Their X-ray diffraction data showed that the film crystal structure was not homogeneous but consisted of a mixture of morphologies and polymorphs (namely, α and β), with a composition dependent on the temperature of sublimation of the material. In a similar work by Głowacki *et al.*, [147] the Authors found a mobility of 0.11 cm^2/Vs for films evaporated on ITO (indium tin oxide), while for the structure the measurements suggested the presence of phase γ. Thus, after reading the literature, one reaches the conclusion that QA might as well be considered an excellent

candidate as a semiconductor, but the relationship between crystalline structure and electrical properties is not clarified yet.

With our work presented, we cannot say whether one of the many QA polymorphs would perform the best in OFETS. However, we can demonstrate how the combination of different non-destructive spectroscopic techniques such as Raman, infrared, and luminescence, quickly applicable to a working device, can be used to identify the polymorphs, also in films. This is always the necessary starting point to tune the growth conditions towards the formation of the polymorph with the best performance for the sought application.

The work on QA has been the fruitful outcome of the close collaboration among research groups, which involved research groups in Bologna and Parma Universities for sample preparation, structural determination and Infrared and emission spectroscopy characterization. Our group contributed with the micro Raman measurements.

3.3.2. Samples preparation

Crystal growth: QA α' phase was obtained as powder following the literature procedure. [148] In detail: powders (100 mg) of commercial QA (Sigma-Aldrich) were dissolved in 96% sulfuric acid (10 mL), sonicated for 1 h, filtered, and kept under stirring overnight at room temperature; α'-QA was finally precipitated by adding dropwise the resulting solution to a beaker filled up with ice. The filtered precipitate was thus rinsed with abundant water (50 × 10 mL). Powders of the β and γ phases,[139] were kindly provided by M. Schmidt. Single crystals were grown by the PVT method, starting from the commercial powder (TCI, purity > 93.0 %). Crystals subsequently characterized as β-QA were obtained by inserting the powders in a glass tube about 10 cm long. This was sealed under low vacuum pressure ($\approx 10^{-3}$ mbar) inserted in a furnace with a linear temperature profile, setting the hot end at 340 °C (sublimation zone) and the cold end at 300 °C (crystallization zone). The growth was stopped after 6 days. Single crystals of the γ-phase were instead obtained in an open-tube PVT apparatus, [39] in which a controlled constant

flux of nitrogen was applied during growth (80 h). The sublimation temperature was 300 °C, and the estimated temperature in the crystallization area was ≈250–200 °C.

Films preparation: QA films were fabricated on glass and KBr plates, by using an in-house modified vacuum metal coater, which could attain ≈10^{-6} mbar of dynamic vacuum through an oil diffusion pump. For the film samples we have denoted #1, #2, and #3, the vacuum chamber was isolated from the pump during deposition, which thus occurred at pressures in the range 10^{-3} -10^{-2} mbar, whereas for film #4 a condition of higher vacuum (≈10^{-6} mbar) was maintained. The temperature of the furnace, which consisted in a glass basket loaded with QA, was slightly lower than 200 °C for film #2 on glass and film #3 on KBr, and slightly higher than 200 °C for film #1 on glass and film #4 on KBr. The substrate was kept 3 cm above the furnace. No cooling nor temperature control of the substrate was applied, and the growth was stopped when the presence of the film could be detected visually by its colour. The exposure time varied from 3 hours (film #1) to one full day (film #2). Samples #3 and #4 will be here labelled as thin and thick film, respectively, depending on their exposure time and measured optical density.

3.3.3. Experimental setup

X-ray Diffraction: X-ray diffraction methods and optical and spectroscopic analyses were used to determine crystal faces and axes of the crystalline. X-ray powder diffractograms, both for the face indexing of single crystals and the phase identification of polycrystalline samples, were collected as described in the paragraph 3.1.3. Identity between bulk materials and crystal structures was verified by comparing experimental and calculated powder diffraction patterns.

Raman Spectroscopy: Raman spectra in the energy interval of the lattice phonons with excitation wavelengths at 647.1, 752.5 nm. For Quinacridone, power was reduced by neutral density filters to avoid sample damage and reduce its fluorescence.

Infrared spectroscopy: IR spectra were recorded with a Bruker IFS66 FTIR spectrometer, coupled to a Hyperion 1000 IR microscope equipped with liquid nitrogen-cooled mercury cadmium telluride (MCT) detector. Polarized light was obtained using a rotating wire grid polarizer.

Luminescence: Spectra of the QA powder and films were recorded with an Edinburgh Instruments FLS 1000 spectrometer.

3.3.4. Results and discussion on bulk samples

Single crystal analyses by Raman and IR polarized spectra

The Raman investigation of the lattice phonon spectra of QA polymorphs presented some difficulties because of the interfering effect of luminescence, which is different for the various structures. The problem was not relevant for excitation in the red (namely: 647.1 and 752 nm) and detection below 200 cm^{-1}, even though some baseline correction was still needed. The region between 400 and 3500 cm^{-1} was instead heavily affected and needed large and not linear baseline correction both under the excitation wavelengths of 647.1 (red) and 476.2 nm(blue). This actually prevented us from analysing these spectra and detecting differences depending on the polymorph.

Figure 3.34 shows the polarized low-frequency Raman spectra of β- and γ-QA single crystals (explained in paragraph 2.1.4). Both polymorphs are monoclinic, P2$_1$/c (C$^5_{2h}$) with two molecules per unit cell. [139] On the assumption that the QA molecule behaves as a rigid body, the theory predicts six Raman active lattice vibrations, with symmetry 3 A$_g$ + 3 B$_g$, [149] as evidenced in the Figure. In a crystal aligned along its extinction direction, the A$_g$ modes are visible in the (*aa*), (*bb*), (*cc*) and (ac) polarization, the B$_g$ ones in the remaining (*ab*) and (*bc*) polarization. Since the β crystals are often irregular in shape and germinated, good polarized spectra are difficult to record and this makes more complicate to assign all the peaks by their correct symmetry. Despite these difficulties, the face *ab*, or (0 0 1), was identified as the predominant. γ-QA usually presents elongated crystal faces identified as *bc* or (1 0 0). The regular shape of the γ

crystals have allowed us to record nice spectra and easily assig the peaks corresponding to the A_g and B_g symmetries. All the bands are highlighted in Figure 3.34. In any case, in the lattice phonon region the two polymorphs clearly display different spectral features and can be promptly distinguished.
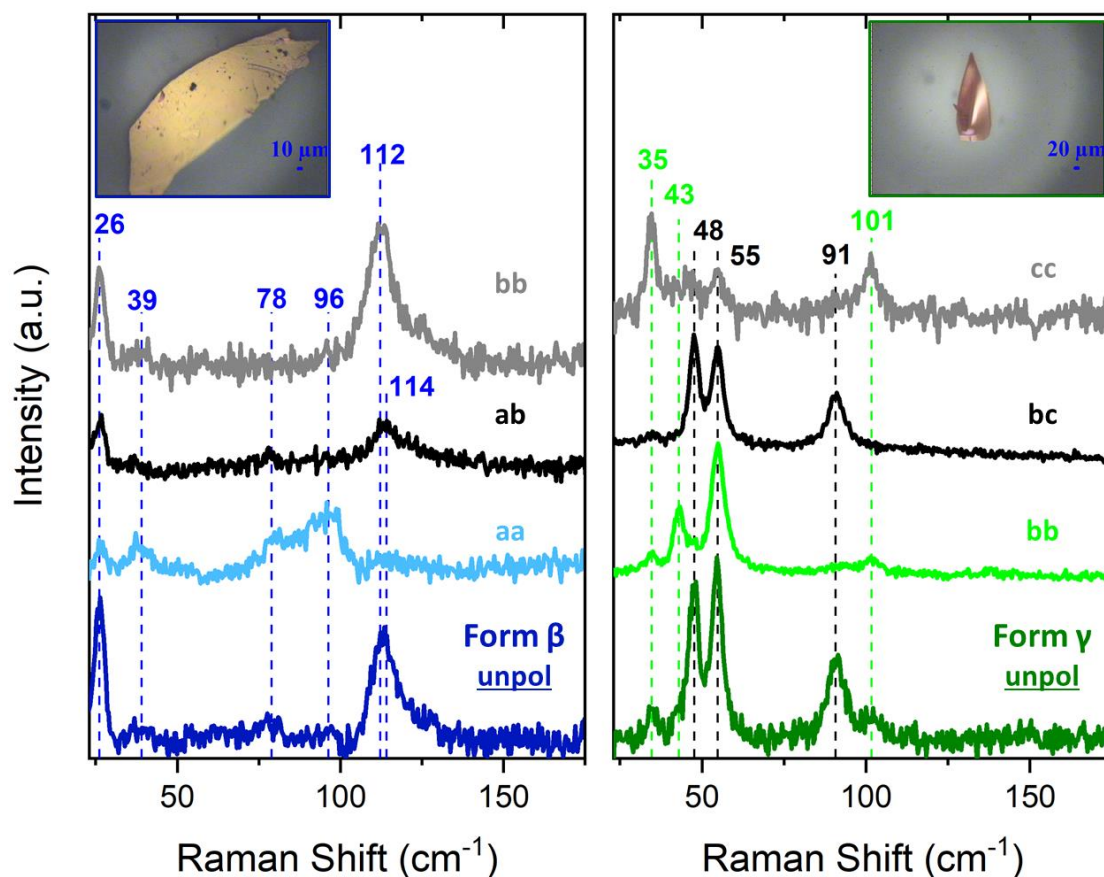

Figure 3.34: Polarized low-frequency Raman spectra of β (left panel) and γ (right panel) single crystals with the microscope image in the inset. Except for the unpol spectra, the black trace was recorded with crossed polarization (B_g modes) while the others (grey, light blue and light green curves) with parallel polarization (A_g modes).

The β- and γ- polymorphs can be distinguished also by Mid-IR spectroscopy and in particular by looking at the CH stretching region. [150], [151] Polarized single-crystal IR absorption spectra are presented in Figure 3.35, where the orientations of the radiation electric field with respect to the crystal axes of the two polymorphs are also given.
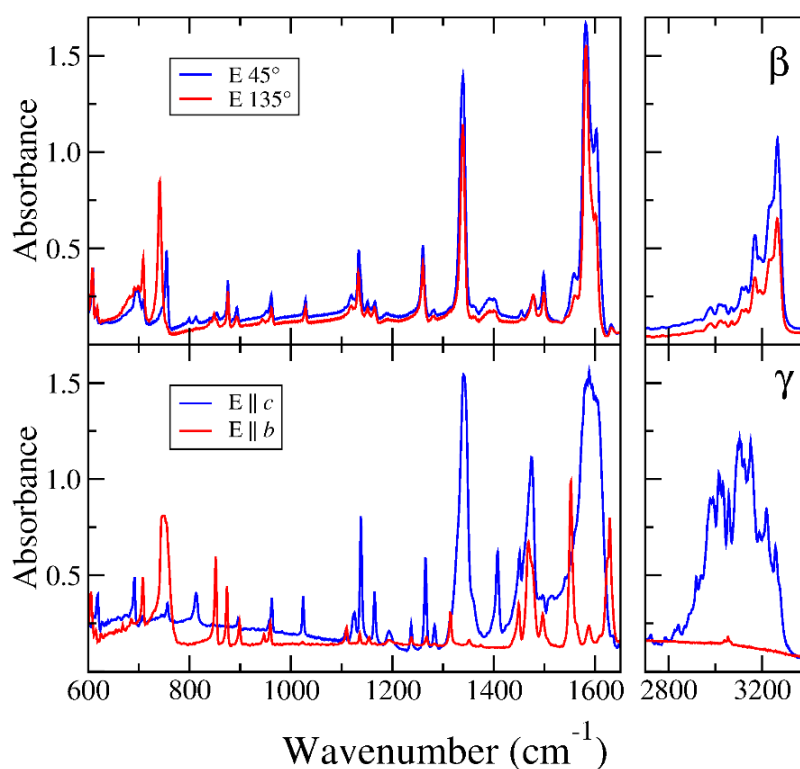
Figure 3.35: Polarized IR spectra of β- and γ-QA single crystals. The insets indicate the orientation of the radiation electric field with respect to the crystal axes

The spectra of γ-QA appear very strongly polarized compared with the two polarizations in β-QA. Besides variations in the band shape, the difference in the spectra can be easily understood by observing the crystalline structures of β-QA and γ-QA11 (refcode in the CCDC: QNACRD07, QNACRD08) shown in Figure 3.36.
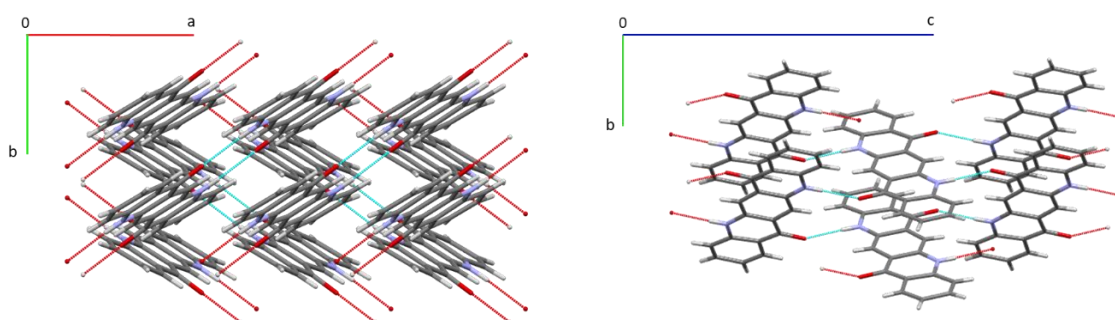

Figure 3.36: X-ray crystal structure of β-QA (left) and of γ-QA (right) viewed normal to the ab and bc planes, respectively.

The Figure shows the structures viewed normal to the most developed crystal planes, that is the *ab* for the β-QA and *bc* for the γ-QA, used for polarized analysis. In both cases, the planes are dominated by the H-bond motifs, which have different patterns in the two forms. [139] In β-QA each molecule is bonded by means of two H-bonds to the nearest two neighbouring molecules, forming two non-parallel chains. One half runs in the [1 1 0] direction, and the other half in the [1 $\bar{1}$ 0] direction, creating a zig-zag arrangement, roughly along the diagonals of the crystal face. Consequently, we do not expect relevant spectral changes on switching polarization. Instead, each γ-QA molecule is connected by single hydrogen bonds to four neighbouring molecules, giving rise to a criss-cross pattern rather than a chain as in the β structure. Here, the H-bond network develops roughly along a single direction parallel to [0 0 1] (i.e. the *c* axis); accordingly the polarization is dominant in the same direction. The same kind of considerations should apply to the vibrations with the dipole moment oscillating along the in-plane short axis of the QA molecule, such as the C=O stretching mode located around 1600 cm^{-1}, or, with opposite polarization, the CH out-of-plane bending mode around 780 cm^{-1}.

Spectroscopic characterization of QA powders

So far, we have shown that Raman and IR polarized spectra are good analytical tools in single crystal investigations. However, the films used for devices are polycrystalline, with possibly a mixture of different phases, or even amorphous. In addition, they may contain the α' form, which we were not able to obtain as a single crystal. [139] Therefore, before proceeding to the film characterization, the reference spectra of the bulk powder samples are required.

Figure 3.37 shows the spectra of the QA polymorph powders in the low wavenumber region. The region shown in the Figure is extended towards higher energies, to include a pair of bands in the 200 - 250 cm^{-1} window. These must have mostly the character of molecular vibrations rather than of lattice phonons, as they appear only slightly broadened in the powder spectra compared to the single crystals. Indeed, intra-molecular modes are expected to be nearly dispersionless, with the disorder and/or lattice defects and molecules at the surfaces/interfaces not affecting strongly their

bandwidth. [152] Notably, their intramolecular character has been confirmed by DFT simulations of the QA vibrational spectrum.

Even so, these bands have been useful during the QA characterization, since the band at 216 cm^{-1} is much broader in α'-QA than that in β-QA, and it is not detected in γ-QA, while the peak around 230 cm^{-1} occurs at higher frequency in γ-QA with respect to the other two polymorphs.

As expected, the spectra of the α'-QA is somehow similar to that of β-QA, due to their very similar structures, with the same hydrogen-bonding pattern even if the α'-QA has only one molecule per unit cell. [139] Accordingly, in the α' form three modes are Raman active lattice phonons, but only one broad band is clearly identified around 98 cm^{-1}. Its frequency is quite different from the main features of β- and γ-QA in the same spectral region. Therefore, the frequency differences among the three phases, evidenced in the Figure, show that polymorph discrimination by Raman spectroscopy is possible in all cases.
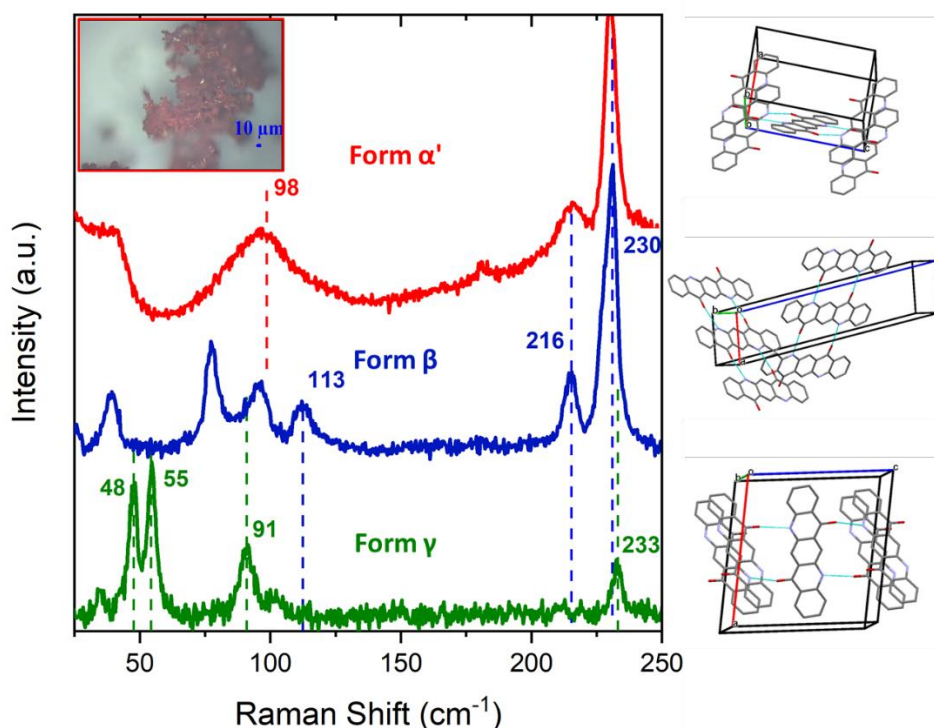

Figure 3.37: Raman spectra of the QA polymorphs in the low-frequency spectral region, with their corresponding crystal structure (right side) and the image of the α' powder inset. The red trace was performed on the α'-powder, while the blue and green one on the β and γ-crystals respectively.

Figure 3.38 presents the IR spectra of perfluorocarbon mulls of α'-, β- and γ-QA (recorded at the University of Parma). Similarly to what observed for the single crystals, the CH stretching region (right side of the Figure 3.38) allows for an easy discrimination of β- and γ-QA, whereas the α' phase just displays a broader pattern compared to the β form. Another useful window to discriminate the three polymorphs is between 1300–1650 cm^{-1}, where small but significant frequency differences are present (highlighted in the Figure). Therefore, also the IR spectra can be used to discriminate between α'-, β- and γ-polymorphs.
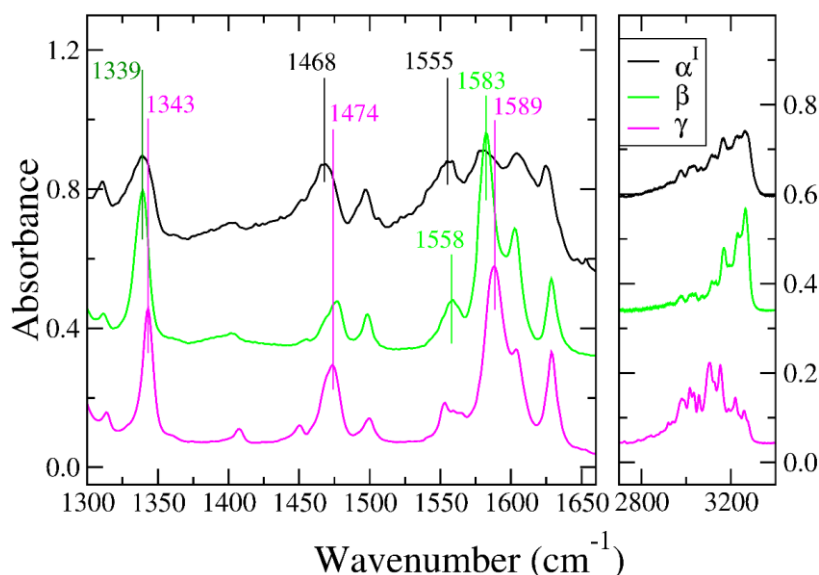

Figure 3.38: IR spectra performed on the α', β and γ powders.

The colour difference between the powders has suggested the electronic absorption spectrum as the most direct method to identify these polymorphs. Nevertheless, obtaining the relevant reference spectra is very cumbersome. Our samples yield in all cases saturation, due to the huge transition intensity and the powders give too much scattering. Moreover, grinding the powders so to reduce the particle size resulted in a colour change, signalling the transformation of all the samples to the β-form. The available literature is not very helpful in this matter, as the measurement conditions are not reported and there are disagreements among different papers. [151], [153] However, the

previously reported evidences recorded during the Raman clearly indicated that the luminescence spectra of the three QA polymorphs are different.

Emission carries the advantage of sensitivity, even though it may be affected by impurities, self-absorption and scattering. For this reason, we decided to extensively test it anyway, both with Bologna and Parma instruments. We thus verified that, despite small differences in the peak maxima frequencies, the overall band-shape is reproducible for each given polymorph, regardless of its being single crystal, powder or polycrystalline. Figure 3.39 evidences what explained above. The α' phase shows a very broad luminescence located between 600-800 nm with a weak but visible shoulder around 620 nm; the β form has a neat spectrum, with a maximum around 620 nm a relevant vibronic progression. Finally, the γ emission has a strange shape with a maximum around 650 nm and a shoulder around 600 nm, with a slow and structureless decay down to 800 nm. This suggests that the study of the photophysics of the QA must be a complex but worthwhile task, especially in view of the application in photovoltaics [143]). For the aim of our work, this kind of study is not needed, as we mean to prove that the sample emission can be conveniently used as an alternative to Raman and IR techniques for QA polymorphs identification in thin films.
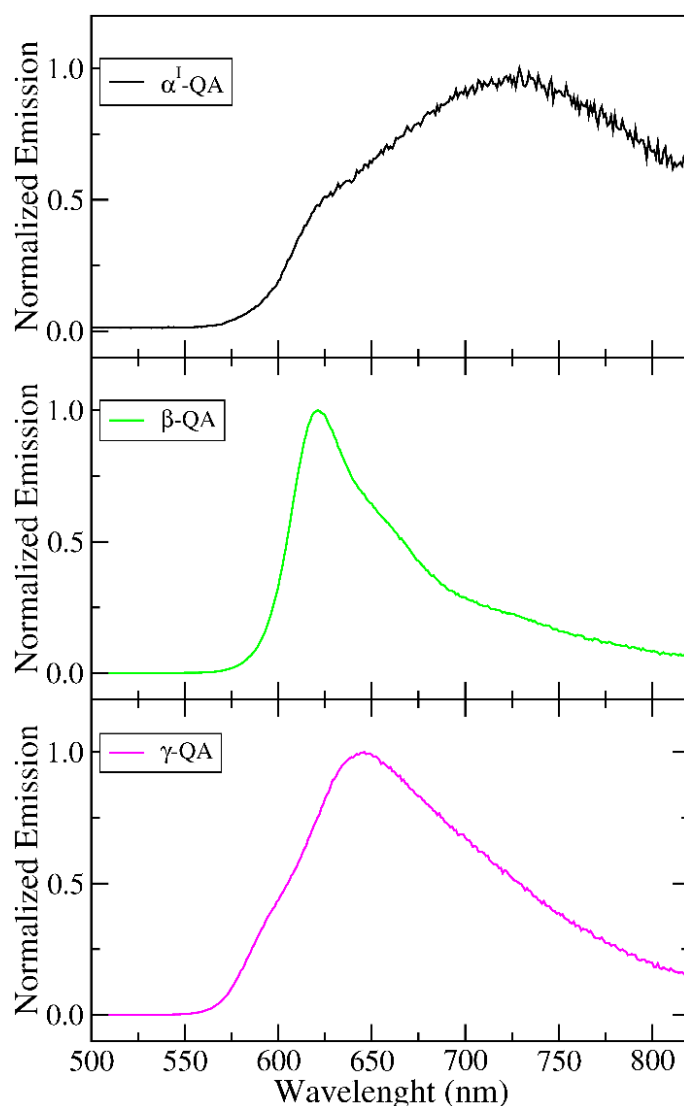
Figure 3.39: Emission spectra performed on the α', β and γ powders.

3.3.5. Characterization of sublimed QA films

After the study of the bulk, the proposed spectroscopic methods were tested to identify QA polymorphs grown in films. In particular, the results below are performed on a couple of films grown on a glass slide (film labelled #1 and #2), and a couple (#3 and #4, thin and thick respectively) grown on a KBr window.

We begin with the Raman spectra recorded in the lattice phonon region. Regrettably, the method has shown some limitations on films due, firstly, to the strong luminescence (higher than in the bulk), which we could elude with a quite heavy

background subtraction to extract the Raman bands. Secondly, the presence of orientational disorder in the films is probably the cause of the considerable broadening of the bands related to the lattice modes. Moreover, in the films a coexistence of different polymorphs is present at the submicrometric scale.

The comparison between the Raman results on bulk and on films clearly displays that film #2 on glass (grey trace in the left panel) corresponds to the β form, as evidenced by the bands around 112, 216 and 230 cm^{-1}. Instead, the analysis of the film #1 on glass (orange trace in the left panel) suggests that the sample contains a mixture of the γ and β polymorph, as highlighted in Figure 3.40 by the presence of significant peaks from both phases. The broad band 88 cm^{-1}, for example, is an indication of the presence of the γ phase, whereas the absence of the doublet around 50 cm^{-1}, which is a marker of the same phase, can be explained as due to a large broadening or polarization effects. The most intense band occurs at 233 cm^{-1}, typical of the γ phase, but a weaker shoulder around 229 cm^{-1} is our diagnostic of β-QA, which therefore likely coexists with γ-QA.

The right panel in Figure 3.40 clearly shows that the in thick film on KBr the β phase is dominant, possibly with some contamination of γ-QA. The Raman spectrum of the thin film on KBr has too low intensity to be disentangled from the emission background, hence nothing can be said about the phase.
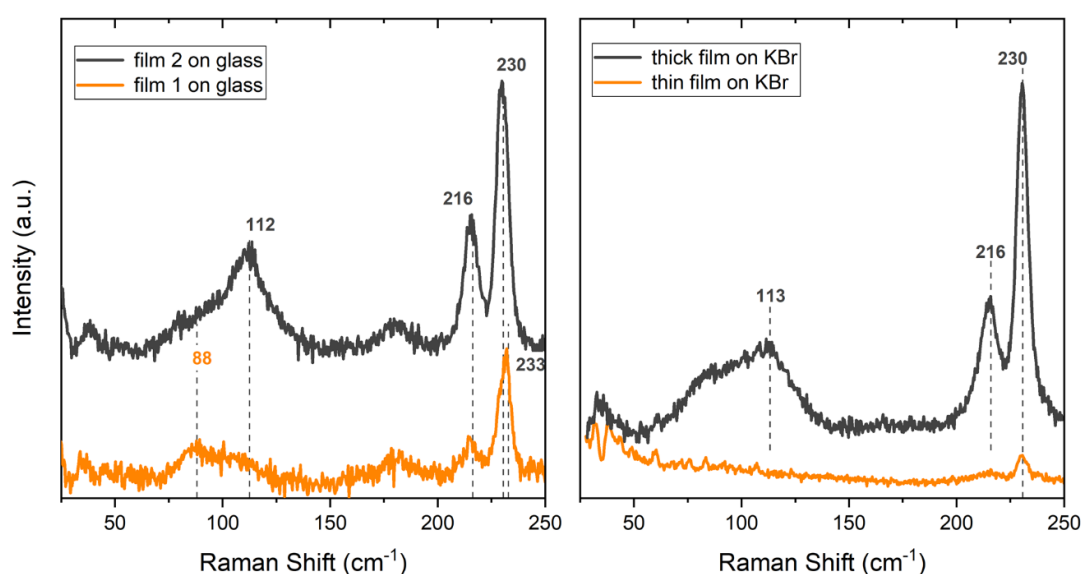

Figure 3.40: Low-frequency Raman spectra performed on QA films. The left panel shows the samples on glass substrate, while the right panel the ones on KBr.

IR absorption spectra cannot be applied to films on glass, so only the results collected on KBr are shown in Figure 3.41, along with the IR spectrum of β-QA powder for comparison. This measurement confirms that on both films on KBr the β form is present, whereas the co-existence with other polymorphs, suggested by Raman, cannot be confirmed.
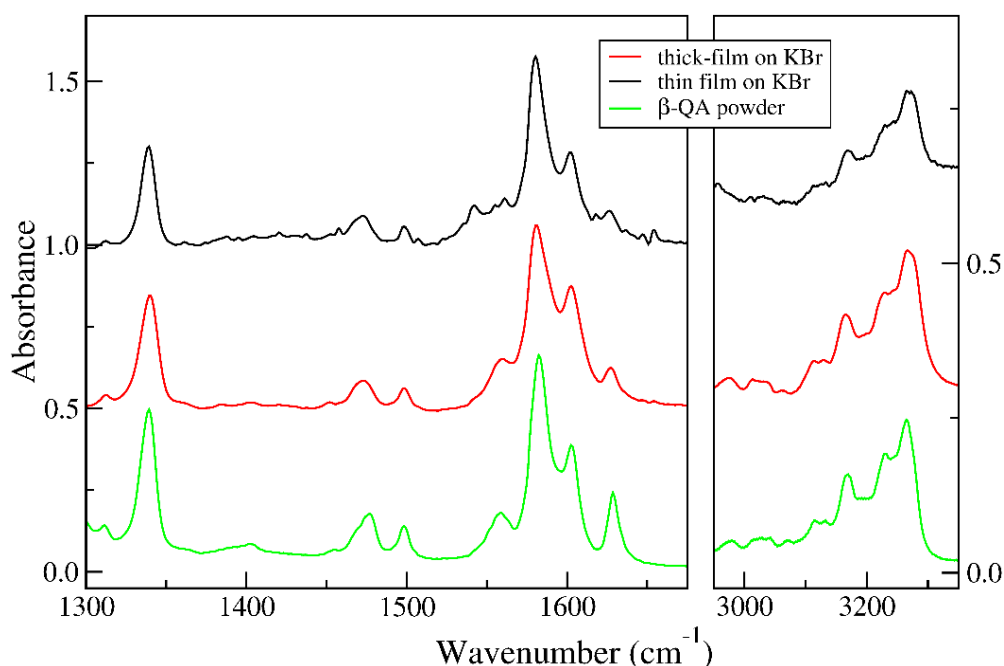
Figure 3.41: IR spectra of QA films on KBr. The green trace shows the spectrum of the β powder for comparison.

Luminescence spectra performed on QA film samples are shown in Figure 3.42, where top and bottom panels display the results on glass and KBr, respectively. By comparison with the spectra of bulk phase, we can confirm that both the films grown on KBr belong to the β phase. In addition, as suggested from the Raman spectra presented above, the thick film also contains some γ-QA, revealed by the shoulder around 670 nm and absent in the thin film. The two films grown on glass display clearly different luminescence spectra, which can be associated to two different polymorphs, film#1 to γ-QA, and film #2 to β-QA. The broadness of the film#1 luminescence band does not exclude the presence of the β-polymorph suggested by Raman. We did not record any

clear evidence of contamination by α-QA, even though this cannot be completely dismissed from the present data.

The few examples reported here allow us to deduce that the sublimation temperature is certainly not the only parameter driving the growth towards one or the other polymorph, but that subtle changes of the sublimation conditions are also of relevance. [154]
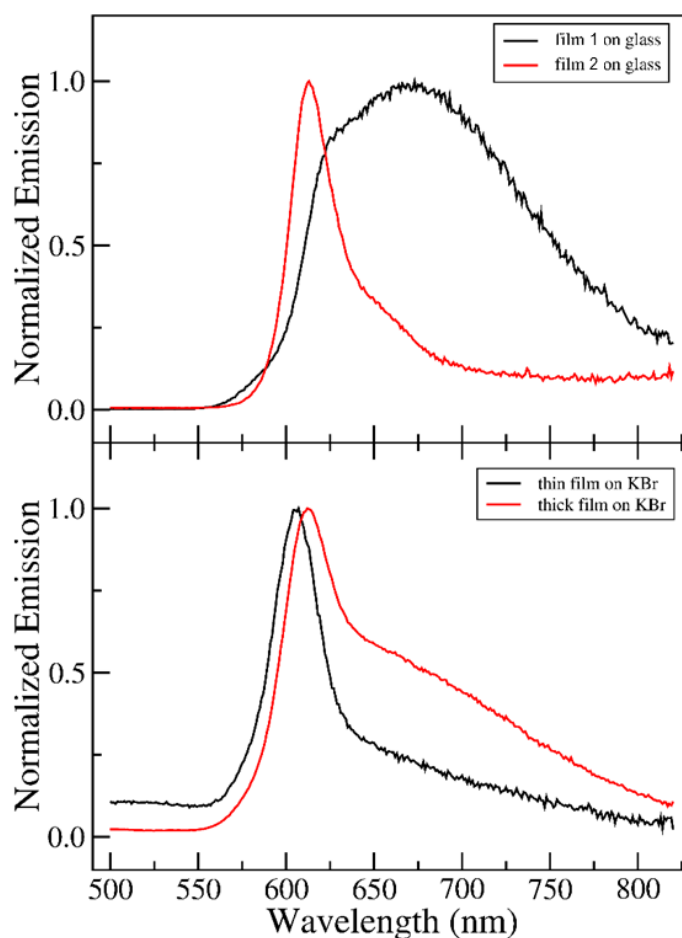

Figure 3.42: Emission spectra of QA films on glass (top panel) and on KBr substrates (bottom panel).

3.3.6. Conclusions

In this chapter we have shown how the combination of spectroscopic techniques, namely IR, Raman and luminescence can concur to achieve a better understanding of the

polymorphism in a complicated case such as QA, which we were able to analyse both in bulk and film samples.

The older literature reports that the γ polymorph grows by sublimation at high temperature (≈600 K) and should be considered as the most heat-stable form. [155], [156] The growth of β-QA should instead take place at the lower sublimation temperature of 500 K. [157] Finally, a more recent work [77], [143] has detected only the β phase in sublimed QA films.

Our experiments have demonstrated that in some cases a coexistence of β- and γ-QA occurs, which might be due to similar cohesive energies. In fact, also small changes in the sublimation conditions can induce the growth either form. The simultaneous growth of both phases is then possible in the films. In many respects, the study presented here is not complete and further experiments should be aimed at finding the growth conditions needed for polymorph selection, so to investigate the proprieties of each form separately in device performances.

Chapter 4

4. Polymorphism in pharmaceutical molecules

Among the various areas where polymorphism plays a relevant role, pharmaceutics is certainly the one with the highest impact because of its strategic role in pharmaceutical companies and in the manufacturing processes for drug development. [158]–[161] In this field, polymorphism can lead to modifications of the biopharmaceutical behaviour of a drug. In addition, a structure obtained for marketing can be metastable and transform in another thermodynamically favoured depending on environmental variables such as temperature, pressure and humidity, all factors on which relative phase stability is dependent. The interconversion between a compound forms influences its shelf life, affecting the maintenance of the desired characteristics, such as the drug therapeutic efficacy, with the transformed crystalline form displaying dramatically different properties.

Obtaining a specific polymorph in controlled and reproducible conditions is not always an easy task, as extensive scientific literature reports. [5] Among pharmaceutics, the most emblematic example of the impact of polymorphism is probably the case of Ritonavir (Norvir), a drug used for the treatment of AIDS. Released in a crystalline form called form I, it was removed from the marked when after two years it was found to transform suddenly and with no warnings into a phase thermodynamically more stable and much less soluble (form II). [162] The new form II was of course chemically identical, but its lower solubility and the different kinetics dramatically influenced the drug bioavailability. [13] The pharmaceutical company (Abbott Laboratories) worked on identifying, isolating and characterizing form II, and only after a long investigation the role played by polymorphism in this incident was discovered. The impossibility to obtain again form I or another stable phase with the wanted solubility forced Abbott to recall the drug from the market for a long time. Finally, Norvir was released in a different formulation. [163]

After this event, the international community has fully acknowledged the importance of the polymorphism phenomenon. The Food and Drug Administration (FDA) now requires pharmaceutical companies to perform a polymorph screening, as complete

as possible, of the Active Pharmaceutical Ingredient (API) in the drugs subjected to clinical tests before marketing, and afterwards a continuous monitoring in the production process. The European Patent Office (EPO) requires the characterization by XRD for patenting a drug released in a crystalline form.

It is thus evident how polymorphism represents a problem when occurring at the end of the evaluation path of a drug, while it is a criterion of choice if analysed in the early stages, as the most suitable crystalline form for clinical tests, and then for the market, can be selected. A change of crystalline form in the course of experimentation it obviously causes costs to rise and generally requires new bioavailability tests (explained below).

Polymorphism is indeed widespread in the pharmaceutics, with the 70% of the barbiturates, 60% of sulfonamides and 23% of steroids existing in different polymorphs or solvates. We could say that the interplay between thermodynamics and kinetics governs the entire pharmaceutical industry with, after all, poor control exercised over the whole process. This is the reason why the research and characterization of the polymorphs of a compound, including its solvate structures and co-crystals with other substances, is particularly important in the pharmaceutical field.

As stated above, the drug properties which is affected by polymorphism is, ultimately, bioavailability. Bioavailability is one of the main pharmacokinetic properties of the active ingredient. In pharmacology, the term is used to describe the fraction of administered dose of drug that reaches the systemic circulation without undergoing any chemical modification. Bioavailability can also be defined as the measurement of the rate and extent to which the drug is made available to the body at the site of action, see Figure 4.1. [164] Several physiological factors can reduce the bioavailability of a drug, but also the chemical-physical properties of the API (such as solubility) and in general the medicine formulation, with their excipients and its production processes, can affect it final values.
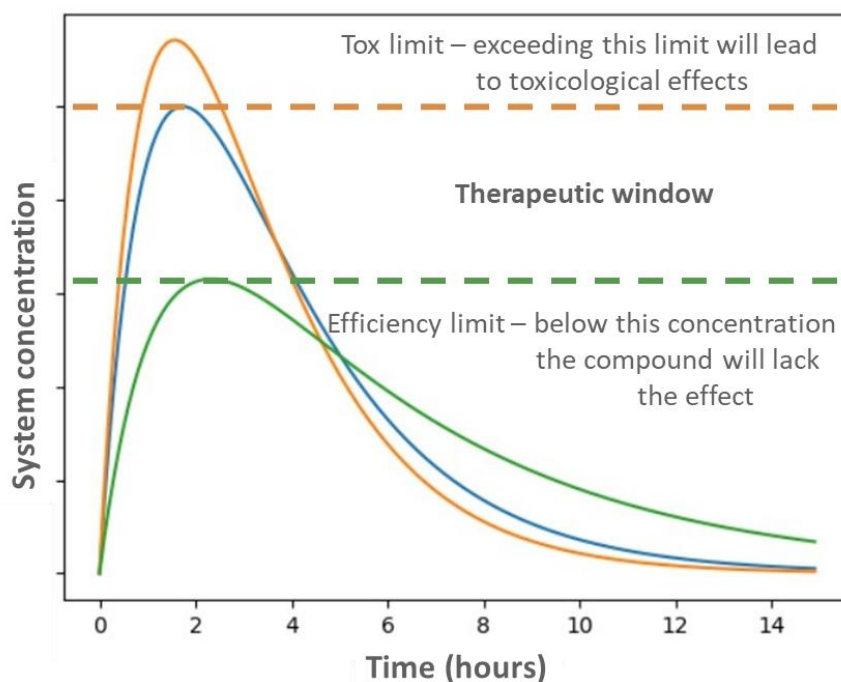
Figure 4.1: Effects of the dissolution rate on the bioavailability of the API in a generic case.

In summary, the study of polymorphism in the pharmaceutical field has multiple purposes:

- complete the knowledge of the physical-chemical properties of an API;
- avoid risks to people's health;
- avoid recalling a medicine from the market;
- patent reasons (each polymorph can be patented separately).

The crystal growth of pharmaceutical compounds is commonly carried out in solution, so to obtain specimens in the bulk form, i.e. of macroscopic dimensions. Parameters such as temperature and degree of super-saturation are set in the process. However, the applied method may fail to induce the growth of sought polymorphs; in addition, it could desirable to let the crystallization take place at a solid interface, where the solution is deposited, in which conditions new polymorphs might be kinetically stabilized by the substrate.

For applications, many formulations are already delivered from films in the form of plasters and the use of these new phases has several advantages, such as, for example,

a better solubility in water, which is a very attractive feature because several new generation drugs are characterized by a very low solubility in this solvent. Indeed, alternative metastable forms may also exhibit better processability during grinding and compression, and lower hygroscopicity. [165] In addition, crystallization processes of pharmaceutical compounds on surfaces or in confined spaces such as micro/nano-cavities, [166] are interesting for future applications in the field of the so-called personalized medicine. This involves the administration of drugs in doses selectable for each patient, supplied in films obtained by deposition techniques such as spin-coating, drop casting, and inject printing.

Until now, not many data exist on the formation of these forms in pharmaceutical science. There are numerous excellent solution-based growth studies [25], [167] showing that growth modifications occur in the proximity of a surface, but typically only large crystals of already known polymorphs were obtained. This is, however, also due to the fact that some of these studies lack the experimental tools necessary to unambiguously identify the nature of a SIP, if this is present. Hence, the necessity of optimizing the methods which promote new routes for a fast and non-destructive crystal structure recognition. The high sensitivity of lattice phonon Raman microscopy makes this technique a now recognized precious tool for SIP detection, in support to structural and computational methods.

The next paragraphs will be dealing with Raman studies of three different active pharmaceutical ingredients, the crystal state of which was analysed both in the bulk and in films. The general approach is, of course, similar to that adopted for the investigation of organic semiconductors. The molecular structures of the described systems, namely Paracetamol, Phenytoin and Nabumetone, are illustrated in Figure 4.2. In the crystal state they share the common trait that growth on surfaces clearly stabilizes a metastable form.

As shown in the following, Raman has not been the only technique employed, or the one which provided the most exhaustive information on the system. But in all cases allowed for a view from a different perspective.
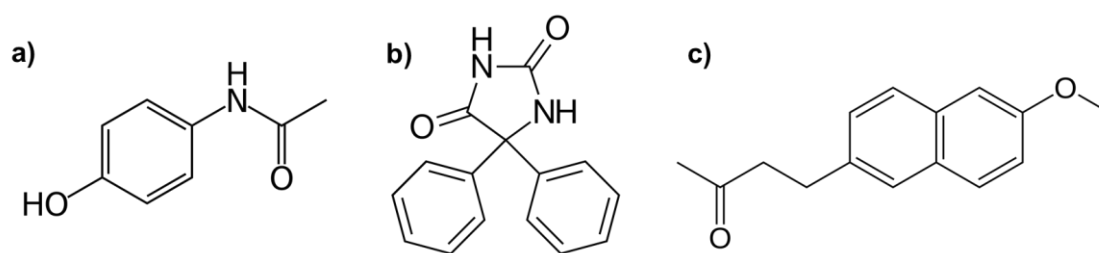
Figure 4.2: Molecular structure of a) Paracetamol, b) Phenytoin, c) Nabumetone.

4.1.   Paracetamol

4.1.1. Introduction

Paracetamol (acetaminophen or N-(4-hydroxyphenyl)acetamide) is a well known compound, largely used in medical science as an analgesic and antipyretic. It is the API of several pharmaceutical products and is also used in many formulations, in combination with other substances, for the treatment of viral forms from cooling and acute or chronic pain. [168]

The original method for production involves the nitration of phenol with sodium nitrate, yielding a mixture of two isomers, from which the wanted 4-nitrophenol can be separated by steam distillation. In this electrophilic aromatic substitution reaction, the phenol oxygen is strongly activating, and the reaction requires mild conditions compared to benzene nitration. Subsequently, the nitro group is reduced to amino, giving 4-aminophenol. Finally, the amine is acetylated with acetic anhydride. Industrially, the direct hydrogenation is preferred, while sodium borohydride is employed in the laboratory scale.

This synthetic route was discovered in 1878 by Harmon Northrop Morse, but the use of Paracetamol in the medical field began only several years later. Initially other compounds, such as Aniline Acetanilide and Phenacetin, were used as antipyretics despite their being rather toxic to humans. In fact, their beneficial effects derived precisely from the transformation into Paracetamol in the organism. Thus, Paracetamol is the so-called active metabolite of its precursors acetanilide and phenacetin. [169]

Paracetamol, which is on the market since 1949, is the most used drug after Aspirin. It has many advantages, being easy to synthesize, showing few side effects and presenting always a high bioavailability regardless of the way it is assumed.

The Paracetamol molecule consists of an amine and a hydroxyl group, both strong donors in hydrogen bonds, as well as a carbonyl group, which is considered a good acceptor. The hydroxyl group is also a weak acceptor. Also based on its chemical nature, for this API it is easy to hypothesize the formation of different polymorphs. [170]

As previously discussed, among the various areas where polymorphism plays a relevant role there is certainly pharmaceutics, and Paracetamol is not an exception in this. Currently there are three known phases called form I, II and III. The monoclinic form I, [171] is present in the commercial powder and in the market, being certainly the most thermodynamically stable phase. Form II [172] is a metastable phase which transforms into form I at ambient temperature. It holds processing advantages over form I, as it undergoes a plastic deformation upon compaction, facilitating the fabrication of tablets, with savings in time and material. [173] Notably, it is also slightly more soluble than form I. Finally comes the metastable form III. [174] Information on the relative thermodynamic stability of the three forms and on the phase transformation routes among them is provided by DSC and thermal XRD measurements given in the appendix section 4.1.5 (Figures A1–A5). All crystal structures have been resolved by single crystal XRD, and those used in the present work are listed in Table 4.1.

Table 4.1: Structural parameters at ambient conditions of the currently known Paracetamol forms.

	a (Å)	b (Å)	c (Å)	β (deg)	V (Å³)	Crystal System	Space Group	Z
Form I [175]	7.1	9.21	11.6	97.84°	750.39	monoclinic	P2$_1$/c	4
Form II [173]	17.17	11.78	7.21	90°	1458.02	orthorhombic	Pbca	8
Form III [174]	11.84	8.56	14.82	90°	1501.41	orthorhombic	Pca2$_1$	8

This chapter concerns the Paracetamol polymorphism revisited by means of the micro-Raman technique. Firstly, lattice phonon spectra have been used to clearly identify the pure phases in bulk. Secondly, we have investigated drop casted and spin coated films grown on different substrate, following the most recent findings on surface-mediated

structures. Besides confirming the selectivity of these surfaces for the metastable form III, we are able to demonstrate its stability over a time span of several months. The mechanism of transformation of form III to II has investigated by Raman, showing that the change starts on the surface with the formation of (0 0 1) layers of form II, which subsequently propagate into the bulk via a partially ordered intermediate state.

4.1.2. Sample preparation and experimental setup

Crystal Growth: Crystals of Paracetamol (Sigma-Aldrich, 98%) were grown from solutions of methanol and ethanol, from the melt, by sublimation in a glass tube and by PVT.

Films preparation: Films on glass, gold, and polystyrene surfaces were deposited by spin coating THF and ethanol solutions, following the protocol reported in the literature: 1.0 wt% solutions of Paracetamol in either ethanol or tetrahydrofuran were prepared. Substrates were cut into pieces of 1.5 x 1.5 cm^2 and were extensively rinsed with ethanol followed by sonication within ethanol and acetone bath in a v/v ratio of 1:1 for 30 min. Afterwards, the substrate was rinsed with 2-propanol and dried under a steady nitrogen stream. The spin parameters (17 rps in 3 sec for 60 sec) were the same for each coating. [176]

Raman Spectra: Raman spectra in the energy interval of the lattice phonons with excitation wavelength at 647.1 nm. Instead in the energy interval of the intramolecular vibrations was used the excitation wavelength at 514.5 nm.

DSC: DSC measurements of the Paracetamol samples were performed using a DSC 204 F1 Phoenix calorimeter (Netzsch, Selb, Germany). In the standard crucibles, a quantity of about 8 mg of Paracetamol was included. The measurements were performed under an inert nitrogen atmosphere to prevent potential oxidation.

XRD: XRD experiments were performed using an Empyrean reflectometer from PANalytical (Netherlands). The radiation was provided by a copper sealed tube and a parallel beam mirror. The beam is further defined by various slits prior entering the three-dimensional pixel solid-state detector in one-dimensional mode. For the heating of the sample, a DHS-900 (Anton-Paar GmbH, Graz, Austria) system was used. This heating device directly allowed thin-film samples to be measured at highly accurate temperatures. To prevent sample degradation due to oxygen, a dome made from PEEK was used, which was constantly flushed with helium.

4.1.3. Results and discussion

Lattice phonon Raman spectra of forms I, II, and III.

Form I was obtained by crystallization from ethanol and methanol as well as by sublimation and PVT methods, whereas form II was grown by slow cooling of the melt at 190 °C. Following consolidated procedures, the lattice phonon spectra of the corresponding physically pure polymorphs have been recorded as references (see Figure 4.4).

The growth of form III, the formerly elusive polymorph of Paracetamol, [174], [177] is more challenging. This polymorph [178], [179] can be obtained by a thermal cycle after amorphization, but minimal changes of the experimental conditions or adopting covered or uncovered conditions are sufficient to produce the other forms in the process. An exhaustive review of these methods is reported in the literature. [180] We indeed obtained form III when slowly heating up to 85 °C [181] the amorphous phase prepared by quickly cooling the melt at T ≈ 24 °C and letting the whole sample cool down overnight. As suggested by the literature and confirmed by us, the use of a coverslip on the sample was crucial to selectively produce the desired phase. The appearance of a new phonon profile in the Raman spectrum (violet trace in Figure 4.3a) demonstrated the growth of the expected form III. [180]

Quite interestingly, during the thermal treatment, we could spot the nucleation of the new phase at the centre of the topmost layer of the amorphous sample (see arrow

in Figure 4.3b). From here, the slow crystallization of form III started at 85 °C, triggering the transformation of the entire sample, which was completed overnight after returning to ambient temperature (Figure 4.3c,d).
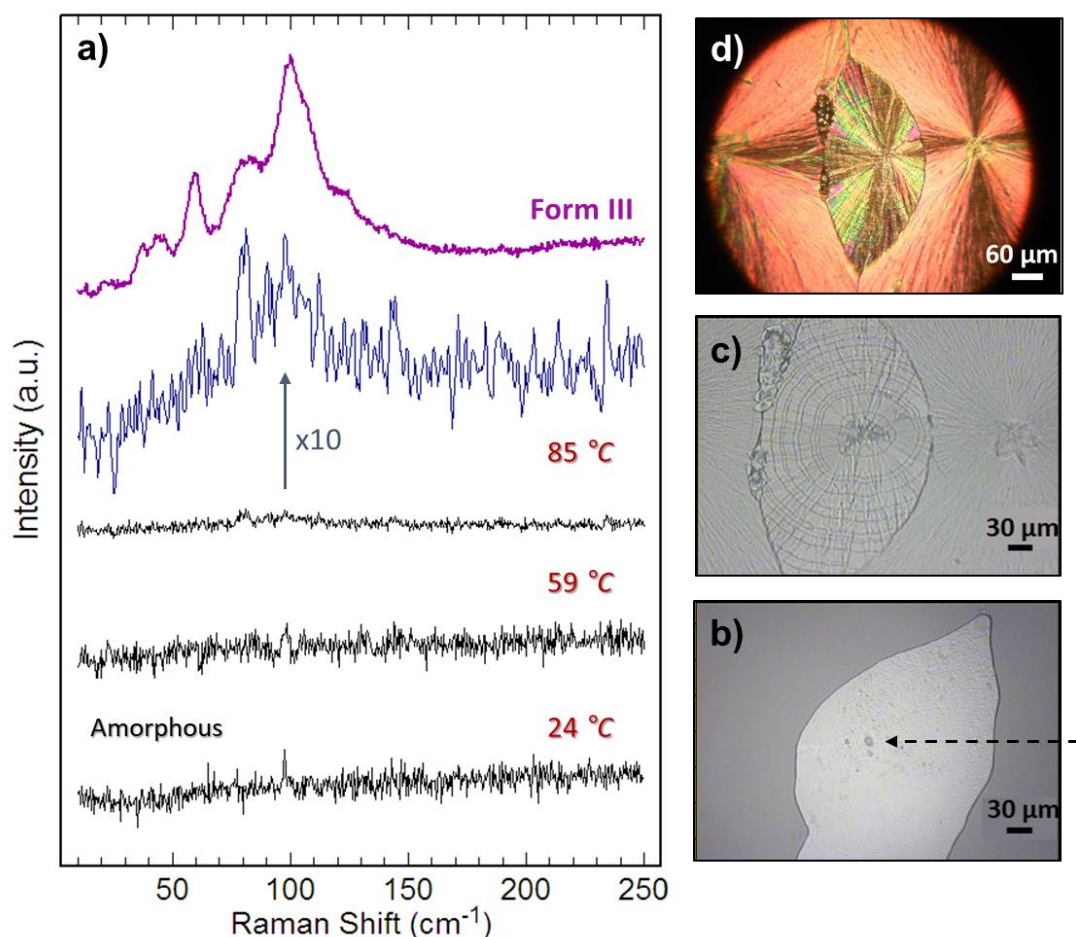
Figure 4.3: a) Raman spectra of the thermal cycle of amorphous Paracetamol to obtain form III (left side): the magnified spectrum at 85 °C highlights the appearance of the bands at ca 80 and 103 cm^{-1} of form III. Right side, images of the sample: b) Starting of the nucleation of form III in the amorphous phase (no phonon structure); c) Crystallization at 85 °C; d) Magnified view at the polarizing microscope of the transformation zone.

The amorphous sample kept at room temperature, that is, not subjected to the heating cycle, after 3 weeks instead displayed a mixing of forms II and III (*vide infra*). Notably, the Raman spectra of the polymorphs are clearly distinct in the region of the lattice phonons, thus allowing for a quick polymorph identification, whereas only slight differences in the energy interval of the intramolecular vibrations are observed,

confirming the unmodified molecular identity in all phases. In Figure 4.4 the Raman spectra of Paracetamol polymorphs in the energy interval 20-3500 cm^{-1} are reported. On the right-hand side of the Figure, the high frequency range where intramolecular modes are detected, common to all the polymorphs. Lattice phonons are shown in the zoomed in interval on the left-hand side: here different polymorphs can be identified by different spectral patterns.
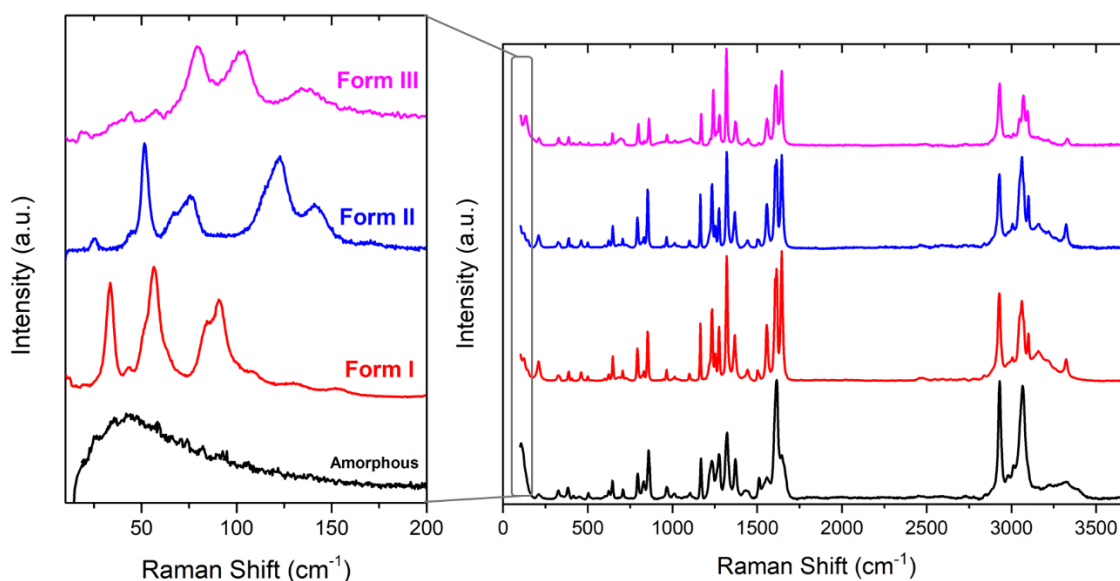

Figure 4.4: Raman spectra of Paracetamol polymorphs in the energy interval 20-3500 cm^{-1}. On the left-hand side, the lattice phonon interval is zoomed in to display the different spectral patterns of the three polymorphs.

Lattice phonon Raman spectra patterns strongly depend on sample orientation as shown in Figure A6, in which the spectra recorded in different points of the sample of Figure 4.3 are given, and all peaks reported in the literature [182] for form III can be found. Further information was gathered by exploiting the confocality of the Raman spectrometer, which enabled us to probe the phase homogeneity of crystal domains at different sample depths. [183] This was achieved by focusing the laser light with microscope objectives having different numerical apertures (NAs). Typical values of the theoretical penetration depths vary from 7.5 μm (100x) to 900 μm (6.3x), as reported in Table 2.1 (see main text in paragraph 2.1.3). The spectra of Figure 4.5 are recorded on a sample in which crystallization occurs starting from an amorphous phase. They

qualitatively account for the gradual decrease of the crystallinity on going from the surface (form III+II, 50x and 100x) to inside the bulk (amorphous, 6.3x), as a valuable demonstration of the mechanism of surface crystallization proposed literature. [184]
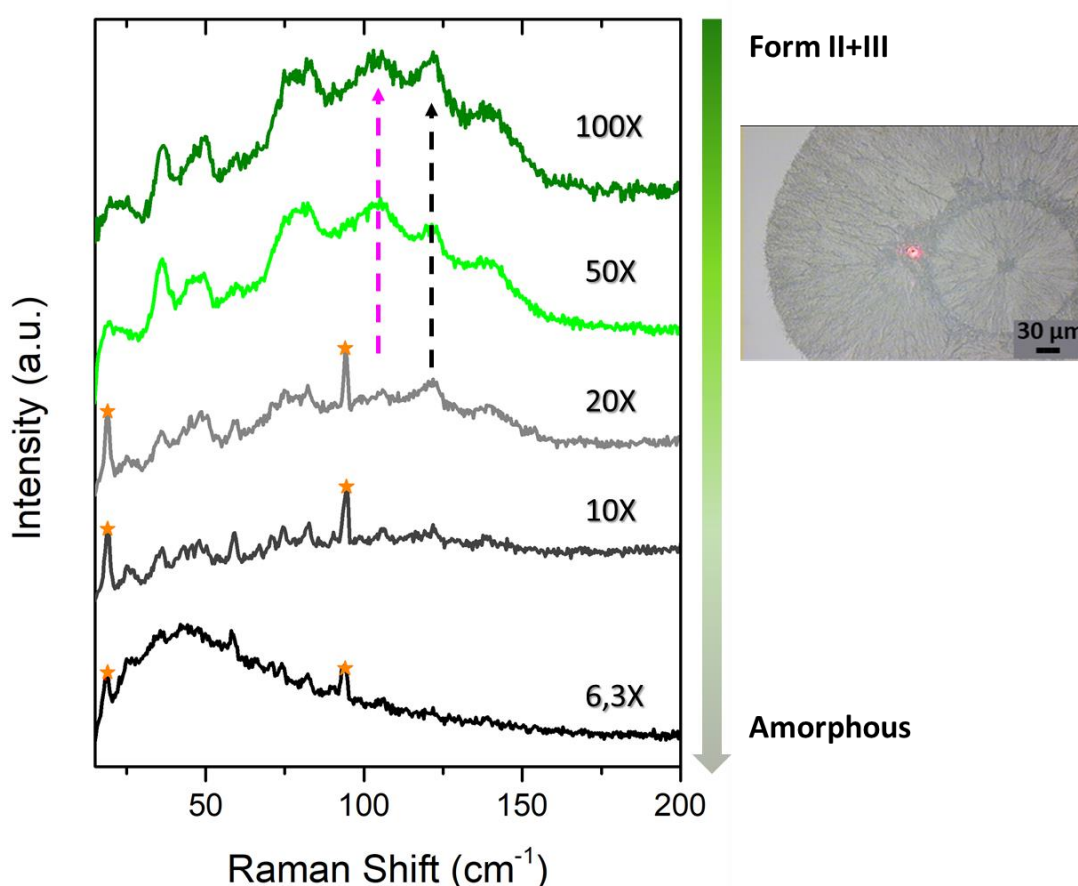
Figure 4.5: The effect of the penetration depth in the sample of forms III+II obtained from the amorphous phase. Form II is identified by the band at 122 cm^{-1} (black arrow), and form III by the band at 103 cm^{-1} (violet arrow). Orange stars indicate peaks of the substrate. The penetration depth increases from the top (100x) to the bottom (6.3x). A picture of the sample is shown at the right.

Phase Mixing

The three known pure phases of Paracetamol were also found to display extensive phase mixing, which could be analysed by Raman mapping (see paragraph 2.1.3). [183] Phase mixing is a common occurrence in polymorphism, with crystal phases that may coexist on a micrometric scale as different domains in the same crystallite, affecting the physical purity of the sample. [11] In Paracetamol, this mixing is selective because it

involves form II with either form I or III, but is never observed between forms I and III. Typically, phase mixing between forms I and II occurs during the slow cooling of the melt leading to the formation of form II (Figure A7). In a similar way, forms II and III may coexist after formation of form III from the amorphous phase (Figure A8). This situation is pictured in Figure 4.6, where a Raman map is used to show the spatial distribution of both phases in the vicinity of the nucleation centre of form III, triggered from the amorphous phase. The map results are particularly useful, demonstrating that the technique can provide a powerful and immediate visual representation of the amount of form III, which, by heating and with time, spontaneously transforms to form II.
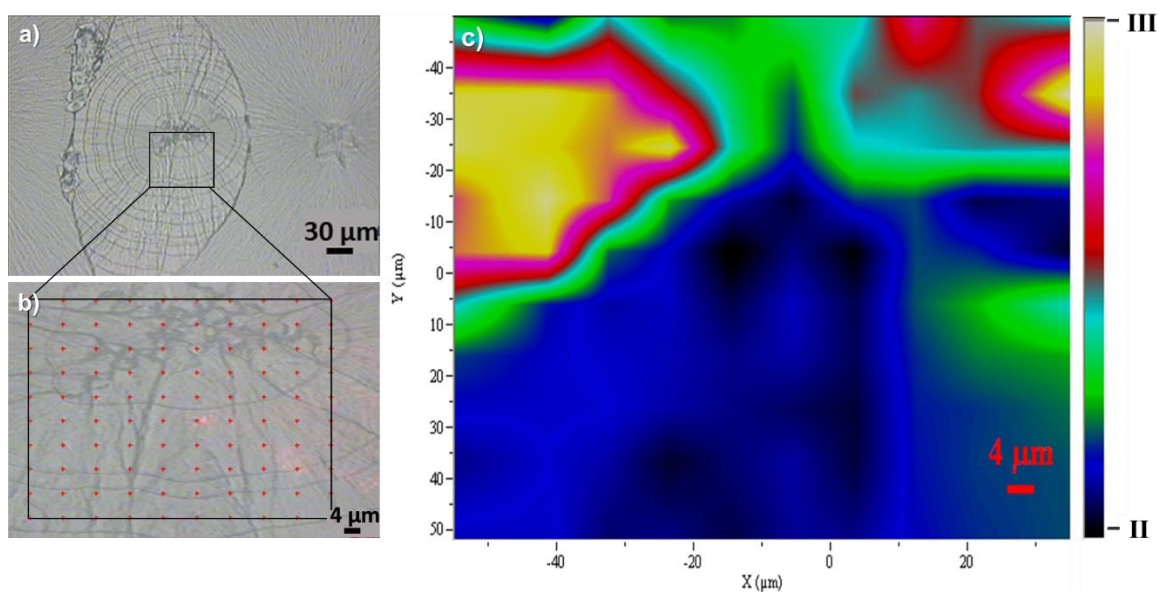
Figure 4.6: Raman mapping (c) and microscope images (a and b) of the phase mixing between forms II and III on the same sample of Figure 4.3 after a few days of heating. A false colour palette visually identifies the spatial distribution of either phase.

A final interesting point to remark is the attainment of form III by sublimation, although with the concomitant presence of form II, a result not previously reported in the literature (Figure A9).

Growth on substrates: Surface-Induced Polymorphs on glass

A few layers of a given organic material on a suitable substrate can show molecular organizations different from those found in the bulk phase. [17] Typical examples can be found among organic semiconductors such as Pentacene and Thiophene derivatives. [20], [185]–[188] These structures are often referred to as surface-induced polymorphs (SIPs). The same approach has been applied to pharmaceutical compounds, [189] successfully proving that films grown on substrates may selectively stabilize a particular crystal phase. [26], [176] In particular, Paracetamol was studied as a model API system to show that the metastable form III could be selectively stabilized in spin-coated films on glass substrates subjected to thermal treatment. [176]

Spin-coated samples of Paracetamol were prepared on glass substrates with 1 wt % solutions of either ethanol or tetrahydrofuran (THF) but without any subsequent heating. From both solutions, completely amorphous samples were consistently obtained, which, over time, crystallized with different kinetics and crystal morphologies. In detail, the samples from ethanol crystallized in 1 day, whereas the THF ones could be analysed just after 1 h and form III was found to grow over large areas of the film. Its stability as well as its spontaneous transformation to II was followed spectroscopically, detecting a progressive rise of the phonon peak at about 122 cm^{-1}, as shown by the arrow of Figure 4.7, which is the characteristic signature of form II in the film spectra, as extensively discussed in the next section. The example given in Figure 4.7 refers to a sample obtained by depositing 200 μL of THF solution, crystallized as form III from the amorphous phase and whose process of transformation under ambient conditions to form II was so slow that it was not fully completed even in a time span of months.
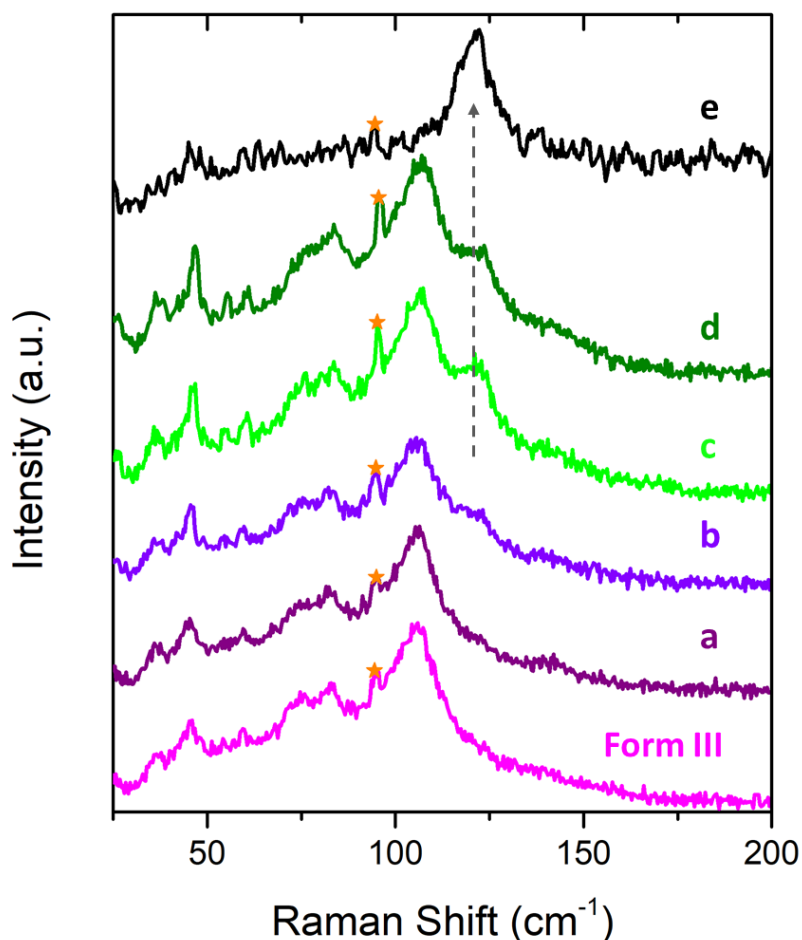
Figure 4.7: Lattice phonon spectra follow the process of the transformation of form III to II in time. Example of a film obtained by deposition of 200 µL of a solution in THF 1% wt on glass; (a): one week later; (b): after one month; (c): after 2 months; (d): after 3 months; (e): after 7 months. Red stars indicate peaks of the substrate.

This exceptional persistence in time of the metastable form III on glass represents an unprecedented record of stability. This result, besides its spectroscopic evidence, has also been confirmed by a specular XRD diffraction pattern of Paracetamol on glass, as shown in Figure 4.8, where only a single peak has been observed. Here, the conclusion is twofold. First, the peak position corresponds to Paracetamol in its form III; second, the presence of one peak only is the typical situation of a sample strongly textured, where the crystal preferably contacts the surface with one exclusive orientation, that is, the $(0\,0\,1)$ plane, like samples on silicon. [176] In $(0\,0\,1)$ texturing, the molecules lie flat on the surface, so that the molecular contact area with the underlying substrate is maximized.

Finally, we should point out that the surface-mediated arrangement so obtained is not a new polymorph, as strictly speaking a SIP would be, but rather a metastable form with an unexpected stability in time. Therefore, we would rather call it a surface-stabilized polymorph.
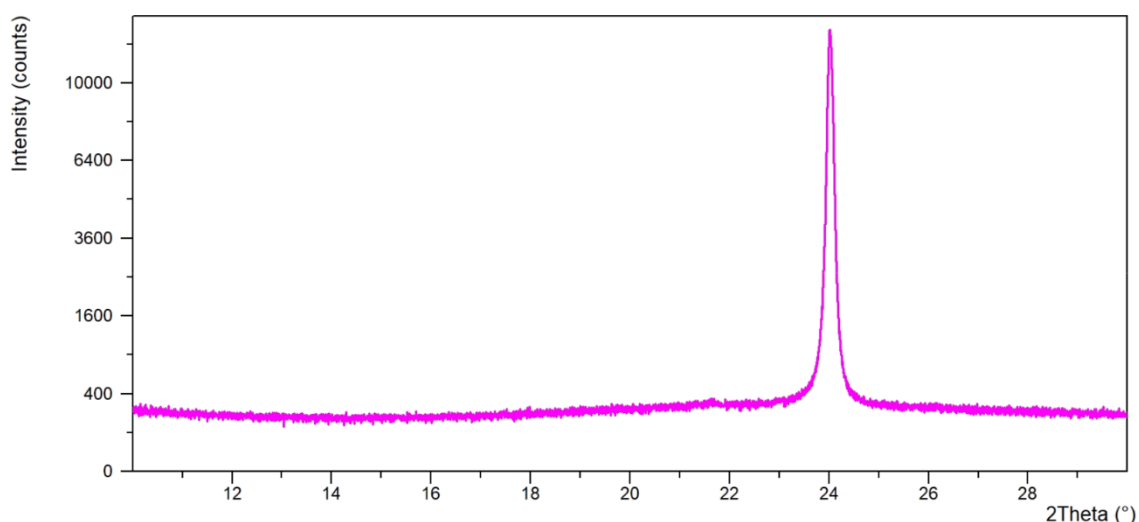

Figure 4.8: Specular XRD pattern of a film obtained by deposition of 200 μL of 1 wt% Paracetamol solution in THF on glass, showing the typical $(0\ 0\ 4)$ peak of form III.

Transformation from form III to II

Raman spectroscopy is not only capable of efficiently following the time evolution of form III to form II in Paracetamol films but also yields interesting hints about the different route taken by this transformation in the films with respect to the bulk material. When a smaller amount of THF solution (150 μL, 1wt%) is deposited on the glass substrate, the film crystallizes to form III and rapidly switches to form II after only 10 min at room temperature. Therefore, the rate of transformation depends on the quantity of material deposited on the substrate: the smaller the amount of material, the faster the process. [190] The reason for this may be that the rate of the variation in the concentration and the level of supersaturation change drastically, especially when using a fast evaporating solvent such as THF. This might result in the formation of a distinct amorphous phase or even of nuclei, which favours the formation of form II. However, as seen in the left panel of Figure 4.9, we do not detect the direct transformation of form III,

but rather a change of its spectral features, which move to a poorly defined profile with basically only one intense band located at 122 cm^{-1}. By comparison with the bulk crystal spectra (blue trace of the same Figure), even though at the very same wavenumber there exists a correspondence with one of the most intense Raman-active phonons of form II, we do notice that all other phonon bands are either fading or completely washed away.

The full spectrum of form II finally develops only at a later stage. Therefore, we are inclined to consider the poorly defined pattern indicated by an arrow in the Figure as the signature of an intermediate state, which acts as a precursor of form II before completely transforming into it.

To explain the nature of such an intermediate state is not straightforward, as it requires the knowledge of phonon response for each direction of the single crystal and then the transfer of this information to the film grown on the substrate. From a spectroscopic point of view, this implies measuring polarized Raman spectra (see paragraph 2.1.4), in which a mutual orientation between crystal axes and polarization of the exciting laser field is selected, so that a specific correspondence of each phonon band to its symmetry can be determined. Details on the machinery of this procedure go beyond the aim of this paper and can be found in a dedicated book. [30] We recall that the polarized Raman spectra of Paracetamol can be found in the literature, [191] but no data are available in the strategic lattice phonon region. Polarized phonon spectra of a single crystal of form II are shown in Figure 4.9 (right panel), the caption of which schematically clarifies the geometry of the experiment. The orientation of the single crystal under investigation must be known to extract useful information from the data. Following experimental reports [173], [190] and computational predictions, [192] the needle-like single crystals lie on the (0 0 1) or *ab* plane, which is also the crystal orientation parallel to the molecular layers [173], [176], [193], [194] with a growth direction along *a*, that is, the direction of elongation of Paracetamol molecules. [190] With this in mind, we can label all spectra following Porto's notation, that is, we can identify the matrix element (ij) of the polarizability tensor responsible for the Raman scattering in each specific experimental configuration, [30], [149] as marked in the Figure.
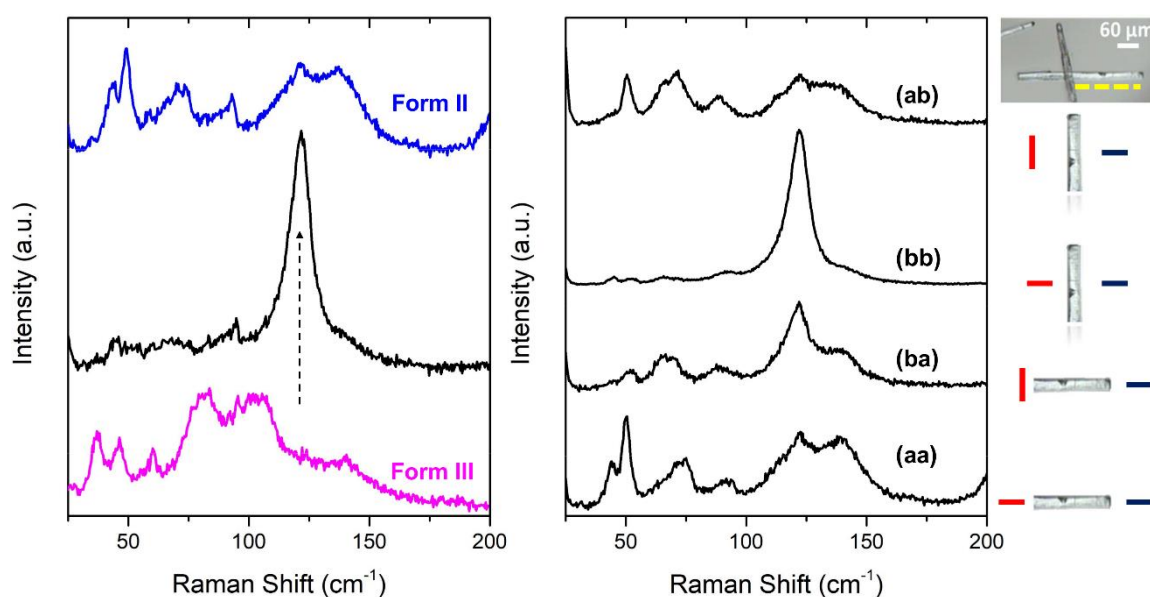
Figure 4.9: Left side: transformation of form III to II in a film obtained by deposition of 150 µL of a solution in THF 1% wt on glass. Right side: Polarized lattice phonon spectra of single crystals of Paracetamol of form II oriented as displayed. The definitions aa, bb and ab=ba indicate the directions (horizontal and vertical bars) of the polarization vector of both incident (red bars) and scattered (dark blue bars) light, with respect to the crystal axes. In the picture of the sample the crystal area analysed is indicated by the yellow dashed line.

Relating oriented single-crystal polarized phonons to the film spectral features is now achievable. The spectrum of the intermediate state, with the peak at 122 cm^{-1}, corresponds almost exactly to that indicated as (*bb*) in the single-crystal polarized spectra. It looks as though the presumably random molecular arrangement in the film of Paracetamol molecules on top of the substrate behaves as an ordered, organized structure when probed by exciting and collecting light, both polarized parallel to the b-axis. However, the film is far from being a system comparable to a single crystal. Thus, the correspondence between the two spectra must indicate that identical profiles arise from altogether different physical conditions. To explain this correspondence, precise information is needed on how Paracetamol crystal domains organize on a substrate. Ehmann and Werzer [176] report that the form II structure grows with the (0 0 1) plane parallel to the glass surface. The same orientation is found on glass, as seen in the previous section. Peterson et al. [195] suggest that there is only short-range order along the *a* axis, which is also the slow growth direction in the calculated morphology. [192] It is plausible that this situation along *a* is maintained in the early stages of form III

transformation to the intermediate state, precursor of form II, implying, because of this disorder, a loss of phonon phase correlation along *a*. Consequently, for all spectral features whose intensity depends on the polarizability matrix elements containing the a-axis, the phase matching between the incoming polarized light and the corresponding phonon mode fails. Accordingly, only those phonons marked as (*bb*) in Figure 4.9 do survive. This nicely explains why a specific polarized spectrum of the single crystal appears coincident with that of the partially disordered intermediate state of the film. In other words, the film spectrum is reminiscent of that of the polarized crystal, but the underlying physical meaning is different. We believe that the intermediate state can be described as a partially ordered structure originating on the surface and made of (0 0 1) layers of form II, which subsequently propagate into the bulk in a process similar to the so-called surface crystallization, whose mechanism proposed in literature [184] has been so convincingly demonstrated by the data in Figure 4.6.

Growth on gold and polystyrene

Spin-coated films were also prepared on gold and polystyrene substrates from THF solutions of the same concentration used for the depositions on glass. Films on gold undergo a strong dewetting, so that only 100 µL of solution could be deposited. Also in this case, form III appears to be dominant on the sample, even after warming the sample above 100 °C. Only during the cooling process, the transformation to form II was observed (see blue arrow in Figure 4.10). Lattice phonon spectra have been used to follow the process of the transformation, as shown in Figure 4.10.
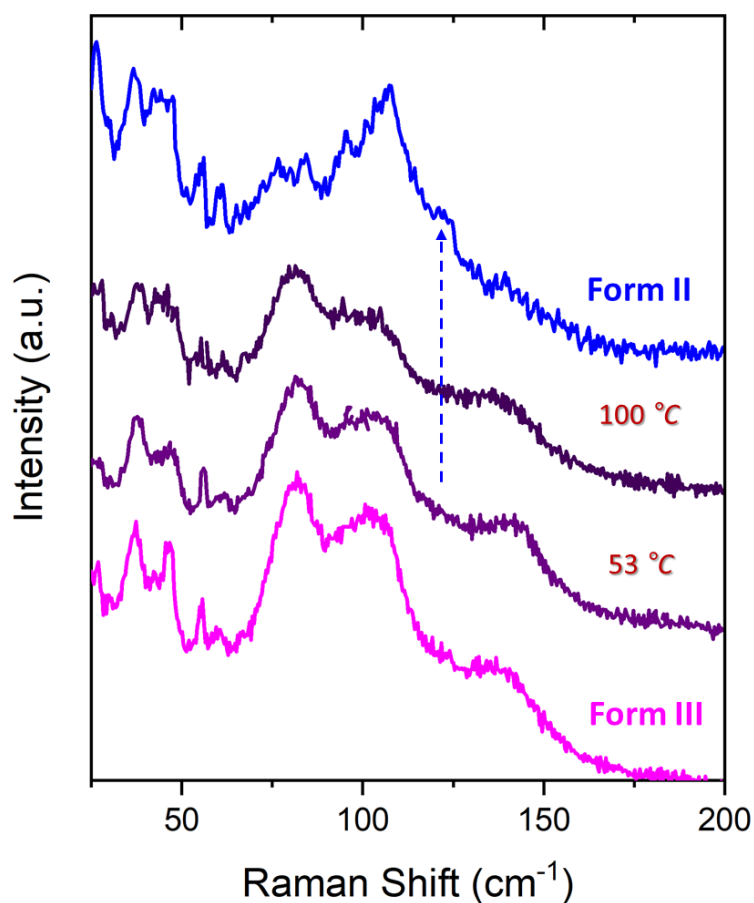
Figure 4.10: Purple trace: the spectrum of form III as recorded while heating a Paracetamol film on gold; Blue trace: the appearance of the band typical of form II during the cooling.

In the case of films on polystyrene, the identification of form III as the one obtained by deposition was performed by specular XRD reflectivity only (Figure 4.11). It is once more interesting to remark that by exploiting the complementary Raman and XRD techniques to comply with phase recognition, we could overcome the technical problems for which it was not always possible to perform both structural and spectroscopic investigations at the same time and on the very same sample.

Figure 4.11: Specular XRD reflectivity spectrum of a film obtained by deposition of 100 µL of 1% wt Paracetamol solution in THF on polystyrene, showing the typical $(0\ 0\ 4)$ peak of form III and the silicon wafer peak at higher angle.

4.1.4. Conclusions

In this chapter, we have explained our results concerning the polymorphism of Paracetamol, a model API system, obtained by employing phase recognition lattice phonon Raman microscopy. After characterizing the three pure forms of Paracetamol, we have also analysed their mixing 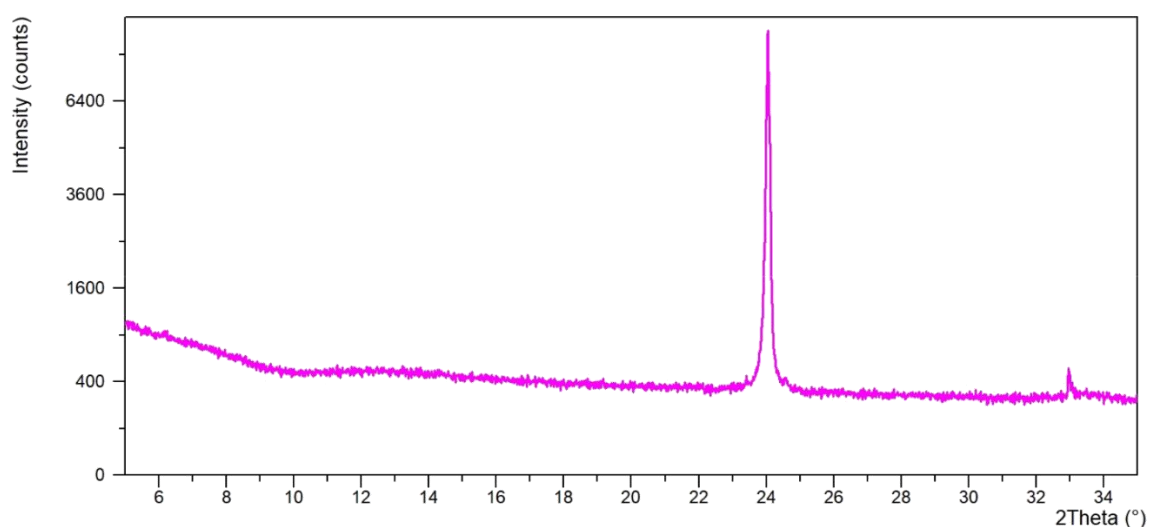as different domains in the same crystallite. We were thus able to discriminate the presence of different structures as a function of the depth within the sample by a valuable tool, which has demonstrated the mechanism of surface crystallization of the metastable form III as proposed in literature. [184]

An important task of this work has been the characterization of crystal forms of Paracetamol in spin-coated films deposited on different substrates, aiming to stabilize metastable phases. Not only did we confirm the high selectivity of Si/SiO$_x$ substrates in the growth of form III but also succeeded to have it on glass, gold, and polystyrene surfaces, finding a surprising stability in a time scale of months. Scheme 1 summarizes the outcome of drop casting and spin coating depositions of 1 wt % THF solution on glass, gold, silicon, and polystyrene.

THF solutions 1%wt

GLASS

<u>Drop</u> – 200 μL

Form III, II, II+III

<u>Spin</u> - 150 μL

III → Intermediate → II
state
(fast process)

<u>Spin</u> - 200 μL

III → II+III → II
(slow process)

POLYSTYRENE

<u>Spin</u> - 100 μL

Form III

GOLD

<u>Drop</u> - 200 μL

Form I

<u>Spin</u> - 100 μL

Form III
Even heating at 100°C

During the cooling,
form II appears
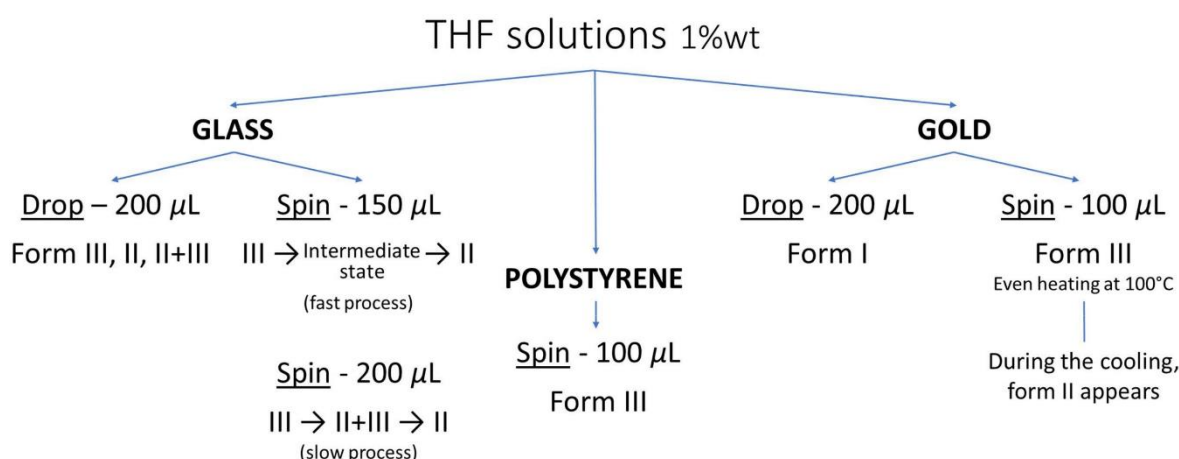
Scheme 1: Summary of non-solvated polymorphs obtained by deposition on different substrates by drop casting (Drop) and spin coating (Spin).

Notably, the measurements of accurate polarized spectra of phonon modes have clarified the mechanism underlying the transformation from form III to II. This occurs via an intermediate state consisting of a partially disordered layered structure building up on top of the film of form III grown on the glass surface. In the second step, the fully ordered structure of the bulk is eventually reached. In conclusion, micro-Raman spectroscopy has confirmed to be a sound technique to monitor crystal structures in the time scale of seconds, also scanning them for physical impurities, both for bulk crystals and thin films, offering a number of very useful applications in pharmaceutical science.

4.1.5. Appendices

Appendix I: Differential Scanning Calorimetry (DSC) and thermal X-Ray diffraction (XRD) measurements

The DSC experiment helps clarifying the relative stability of Paracetamol forms I, II and III. The heating (black trace of Figure A1) of commercial Paracetamol shows the melting point of crystal form I, at temperatures > 175 °C, while the amorphous phase is obtained on cooling from the melt (cooling trace, reported in red of Figure A1). The

crystallization process of form III can be identified by the exothermic peak in the heating process of the amorphous (green trace of Figure A1) at 82 °C and is followed by the exothermic peak of the transformation to form II at 128 °C, which finally melts at 164°C.
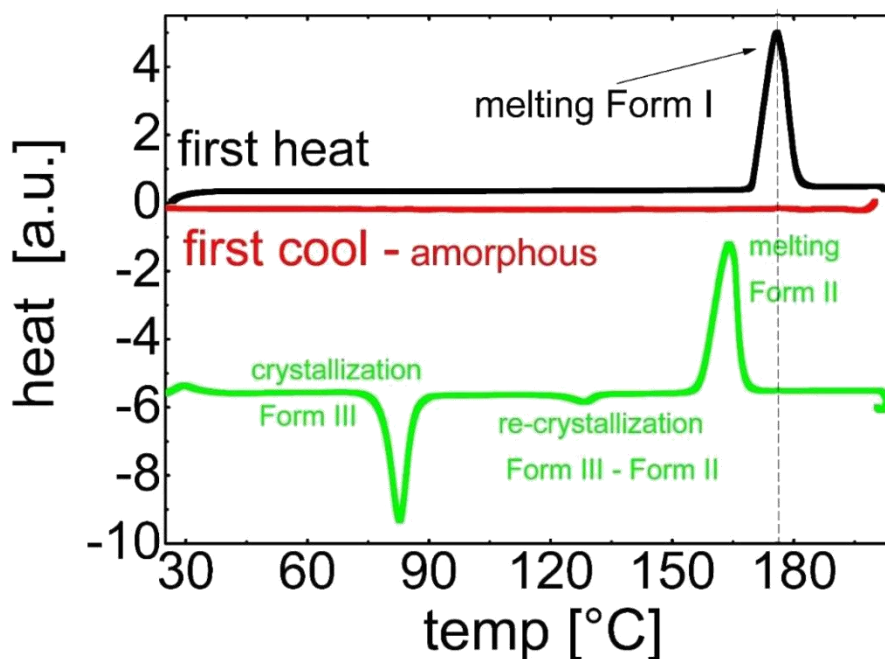
Figure A1: DSC curves of Paracetamol on heating (black curve), on cooling (red curve) and on the second heating run (green curve).

An analogous sequence of processes as those identified by the DSC technique have been detected by thermal X-ray diffraction measurements of Paracetamol. In the following, Figure A2 displays PXRD spectra simulated from the literature data for the three phases known from literature. These data are used for polymorph identification in the measurements reported and commented in Figures A3, A4 and A5.

Figure A2: Simulated X-ray diffraction powder pattern of Paracetamol from generated from CIF files downloaded from the Cambridge Structure Database: HXACAN30 for form I, [175] HXACAN08 for form II [173] and HXACAN29 for form III. [174] For the most prominent peaks the hkl values are given on top. These data are used as references for all XRD analysis.
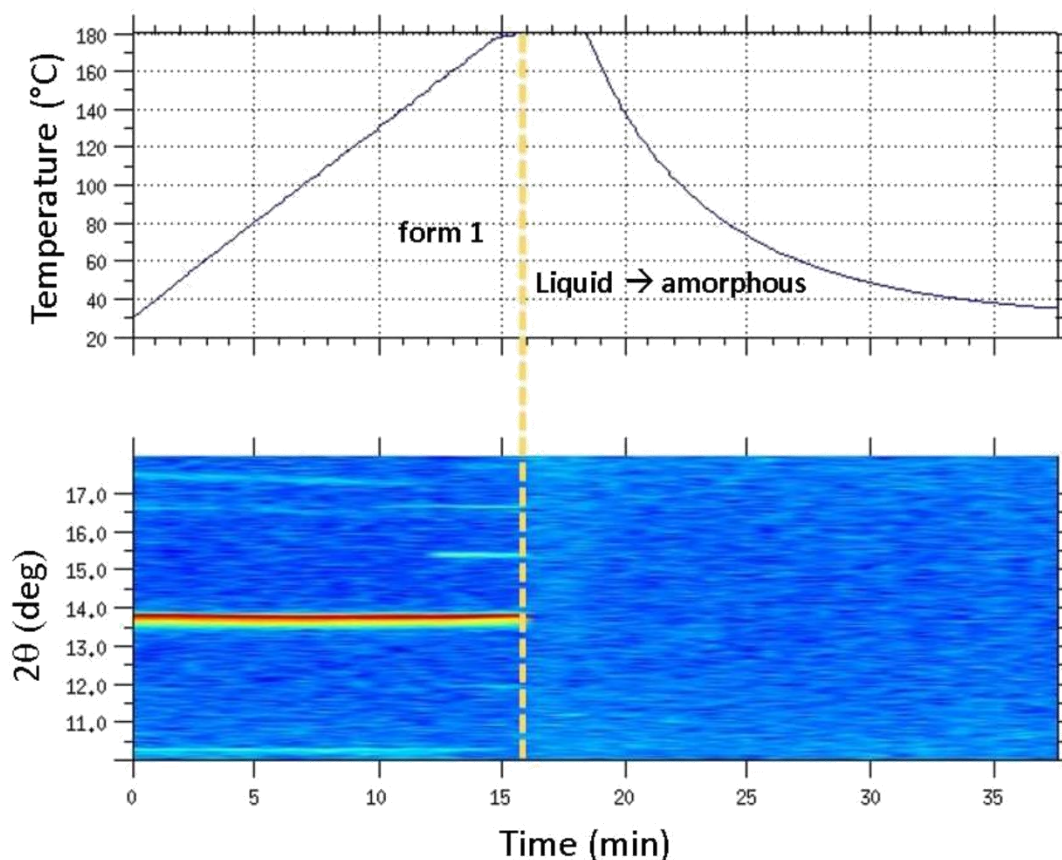
Figure A3: In-situ temperature dependent X-ray diffraction measurements of Paracetamol. Top: plot of the temperature as a function of time. Descriptions indicate the majority polymorphic fo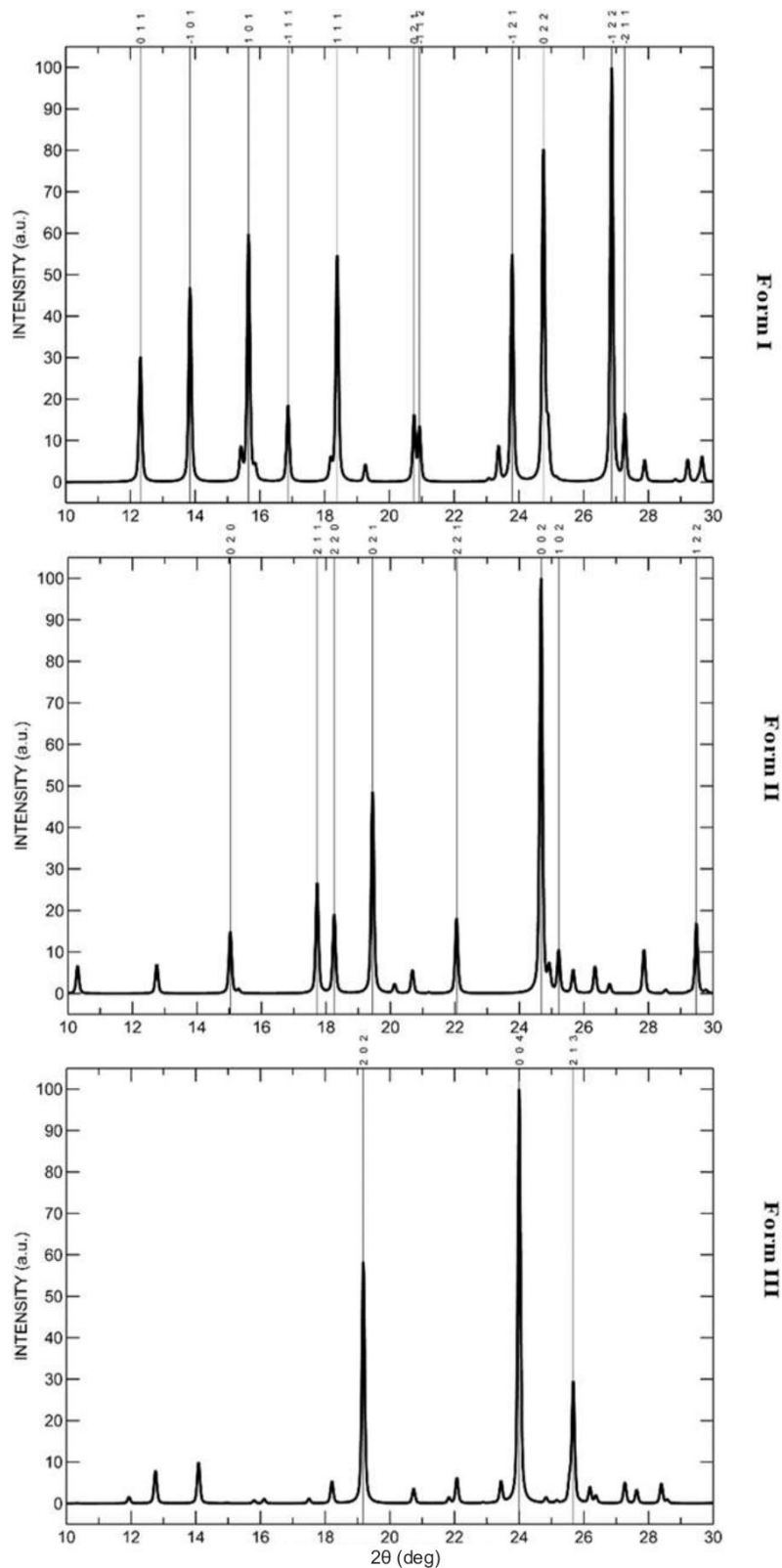rms or physical state. Bottom: record of the diffraction angle 2ϑ (along y) as a function of time. The diffracted intensity is represented by a colour code with red being high and blue being low intensity.

The dependence of the X-ray diffractograms as a function of time, during a temperature cycle, are shown in Figure A3. Starting at low temperature there are several peaks visible within this scan. As the temperature increases the peaks shift slightly due to thermal expansion. At about 180 °C the disappearing of the peaks identifies the melting point. The small shift in temperature compared to the DSC measurement is due to the fact that an individual X-ray measurement take about 3 minutes, which results in a spectrum being taken at a temperature range rather than an exact value. On cooling, there are no crystals forming suggesting that this sample remained amorphous.

Figure A4: In-situ temperature dependent X-ray diffraction measurements of Paracetamol a position slightly different to those in Fig. S3. Top: plot of the temperature as a function of time. Descriptions indicate the majority polymorphic forms or physical state. Bottom: record of the diffraction angle 2ϑ (along y) as a function of time. The diffracted intensity is represented by a colour code with red being high and blue being low intensity.

In Figure A4, the melting of form II is shown at a peak position of 21.5° at a temperature of 165 °C. It should be noted that this sample also contained some Paracetamol in form I which melts at about 180 °C. After this the sample is amorphous until the temperature drops to about 40 °C (at about 33 min). At this point the crystalline peaks form again. The peak position and the DSC measurements agree that this is form III of Paracetamol.
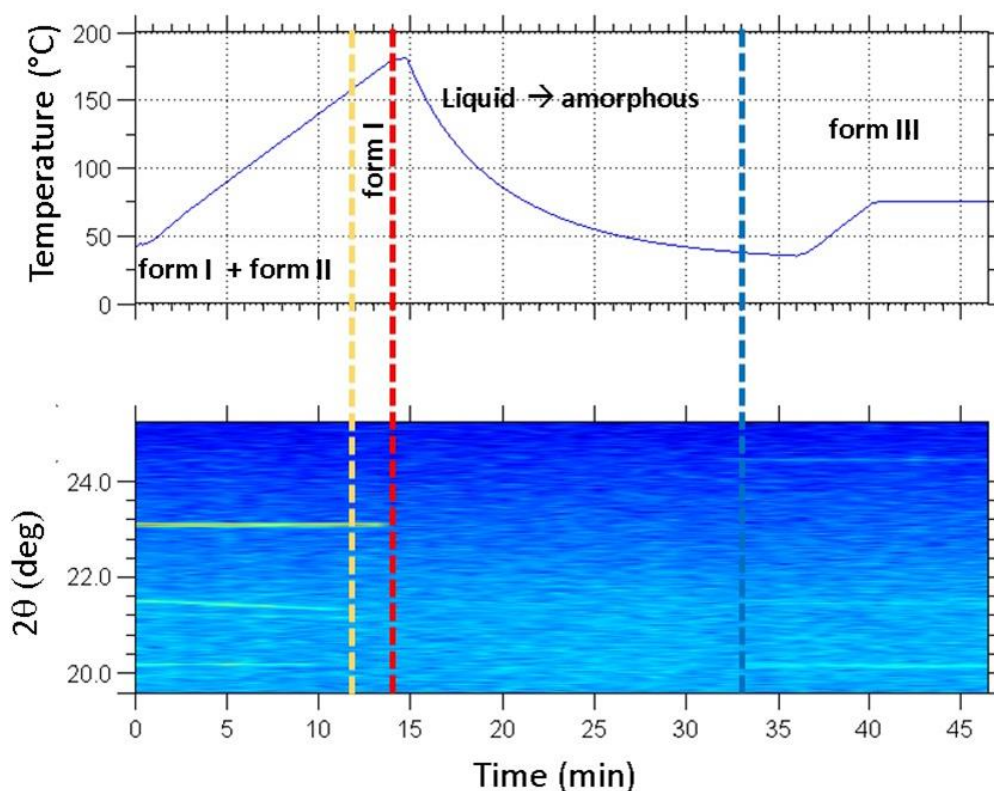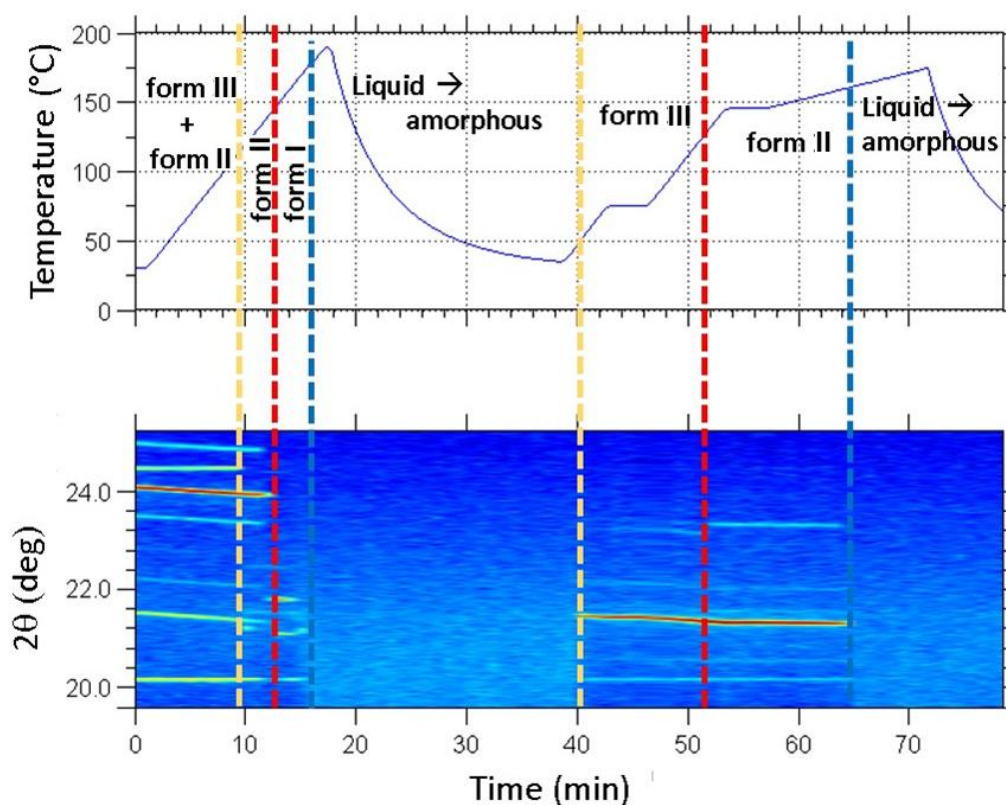
Figure A5: In-situ temperature dependent X-ray diffraction measurements of Paracetamol a position slightly different to those in Fig. S3. Top: plot of the temperature as a function of time. Descriptions indicate the majority polymorphic forms or physical state. Bottom: record of the diffraction angle 2ϑ (along y) as a function of time. The diffracted intensity is represented by a colour code with red being high and blue being low intensity.

Figure A5 show the phase behaviour of a thin film sample having initially form II and form III present. On heating then the form III disappears first at around 120 °C leaving only form II behind. On further heating some the form II transfers into form I slightly above 150 °C. The entire film is melted above 180 °C. On cooling the sample remains long in the amorphous state but then form III starts forming. At this stage other peaks are not found. At 120 °C the transfer into form II takes place which then melts at about 150 °C.

Appendix II: Orientation effects of form III
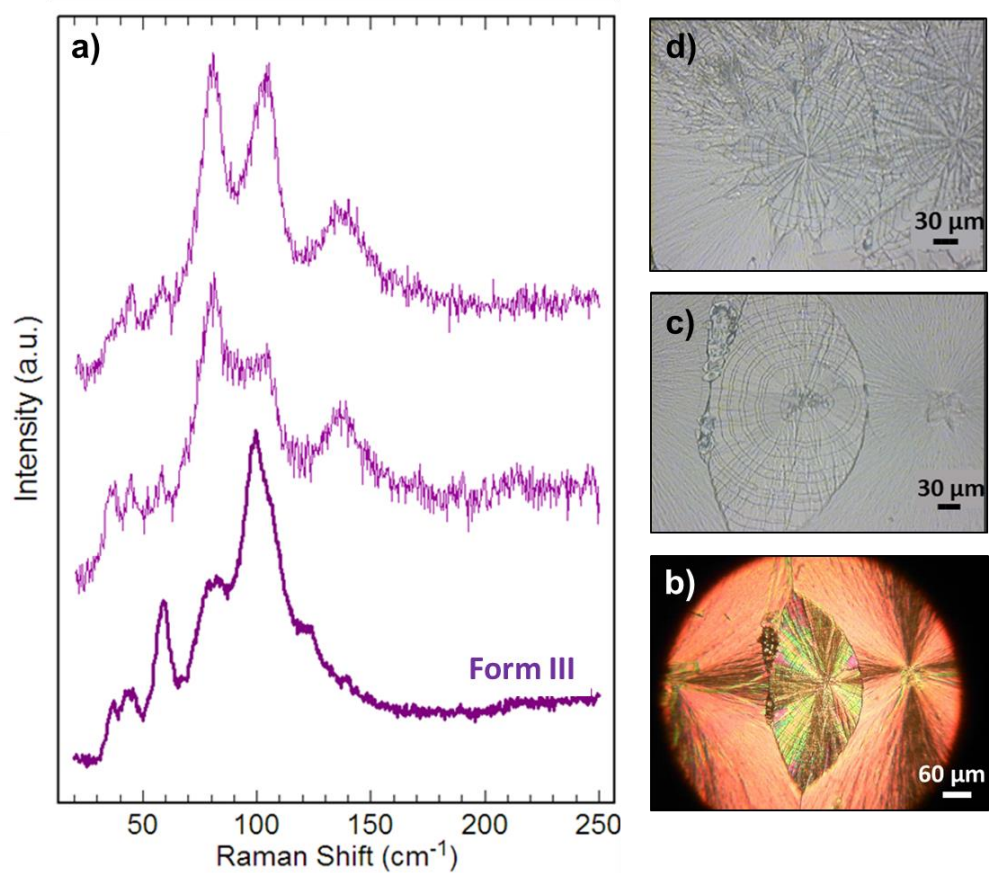
Figure A6: Lattice phonons spectra of form III performed in different micro-areas on the same sample. This picture clearly explains how much the lattice phonon spectra pattern strongly depends on sample orientation.

Appendix III: Phase Mixing
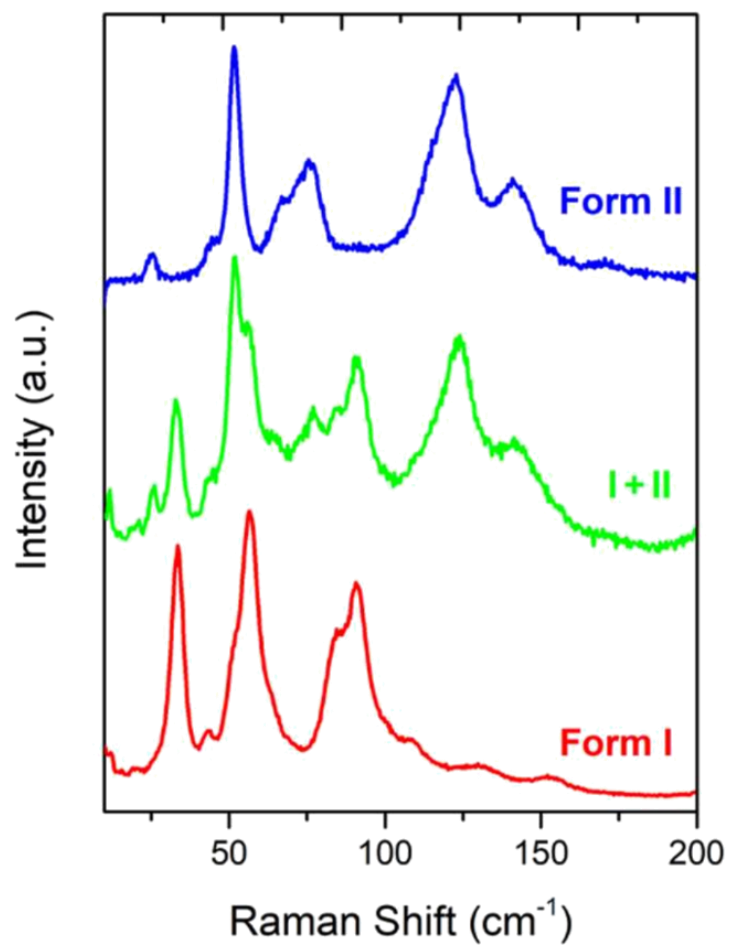
Figure A7: Lattice phonons spectra of form I, II used as references for the interpretation of the phase mixing spectrum of forms I + II (green trace), in which peaks of both forms are detected.
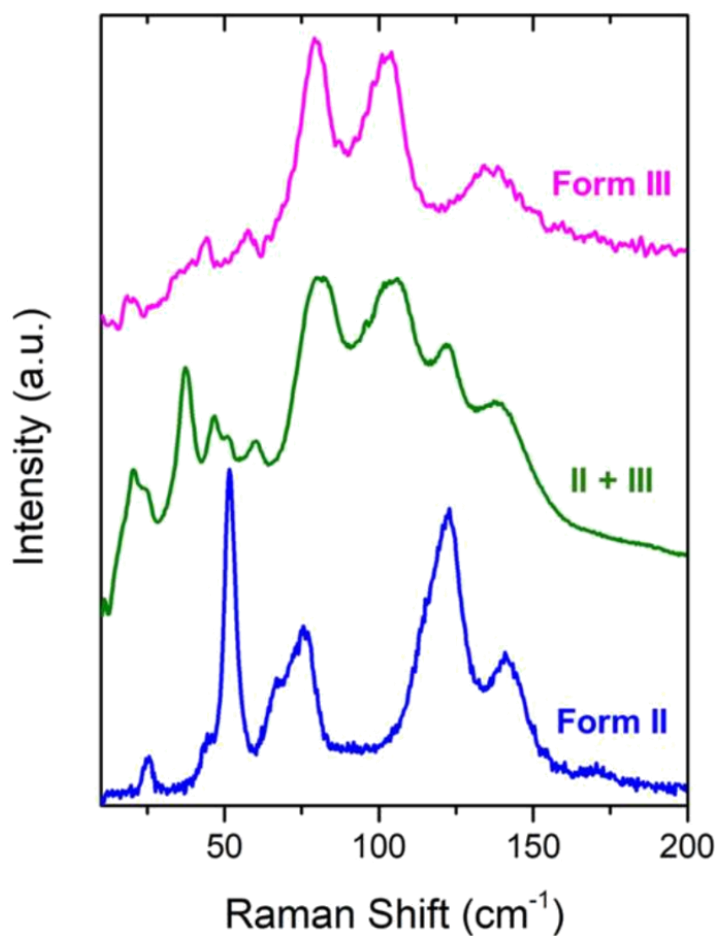
Figure A8: Lattice phonons spectra of form II and III used as references for the interpretation of the phase mixing spectrum of forms II + III (green trace), in which peaks of both forms are detected.

Figure A9 pictures the sublimation process in which crystals of forms I, II and III were obtained together, the latter ones also in extensive phase mixing, along with the spectra measured on the specimens shown in the images, collected in different areas of the cold finger and displaying distinct morphologies.
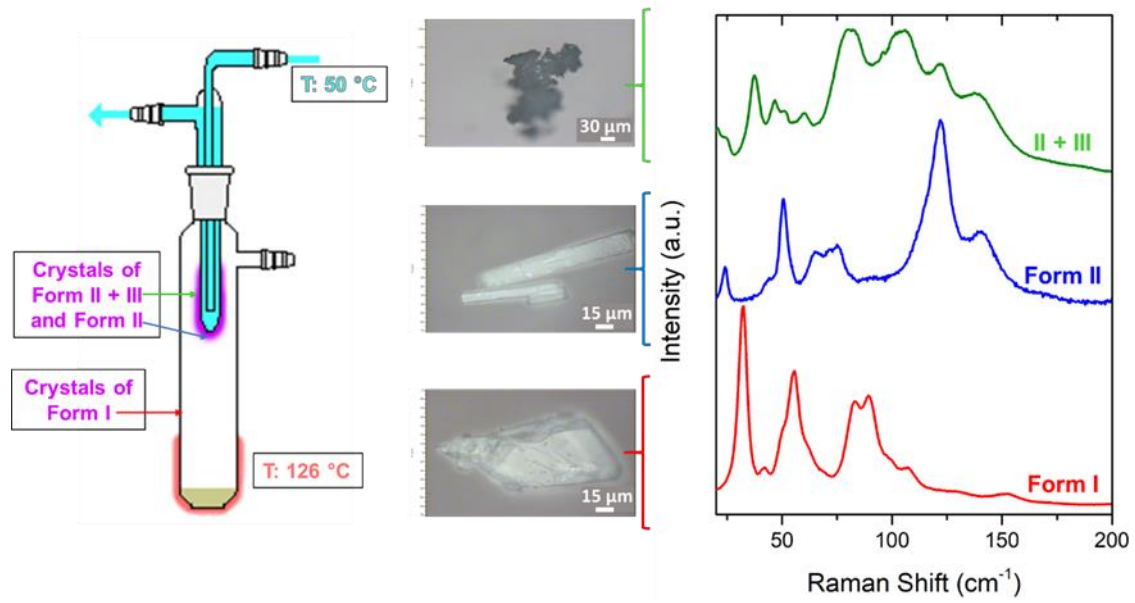
Figure A9: Phase mixing of Forms II + III as detected in crystals obtained by sublimation in the conditions shown on the left-hand side of the Figure, in the areas of the cold finger indicated by the arrows.

4.2.   Phenytoin

Paragraphs concerning the study of Phenytoin in its bulk and film state have been adapted with permission from the publication Giunchi A, Rivalta A, Bedoya-Martínez N, Schrode B, Braun DE, Werzer O, Venuti E and Della Valle RG, "*Surface Induced Phenytoin Polymorph. 2. Structure Validation by Comparing Experimental and Density Functional Theory Raman Spectra*", Cryst. Growth Des, (2019), 19, 6067. Copyright (2019) American Chemical Society. DOI: 10.1021/acs.cgd.9b00863.
In particular DFT Raman spectra simulations are comprised in the PhD work of Andrea Giunchi.

4.2.1. Introduction

Phenytoin (4,4-Diphenyl-4H-imidazole-2,5-diol) is an anticonvulsant drug, also known with the commercial name of Dilantin. It was synthesised for the first time in 1908 by the German chemist Heinrich Biltz, but its applications for seizures were discovered only in 1936. [196]

Only one crystal form of Phenytoin has been fully characterized so far in the literature (form I). This has an orthorhombic lattice, space group Pna2$_1$ (C$^9_{2v}$), with four molecules in the unit cell, all equivalent by symmetry (Z = 4, Z' = 1). [197], [198] A second phase (form II) has been recently identified by GIXD on thin samples deposited on glass substrates. It is therefore a SIP, not yet fully characterized in the literature, but which exhibits advantageous drug release performance in terms of dissolution time. [26]

As discussed in a recent work by co-workers, [199] GIXD measurements on crystalline Phenytoin films detected in all cases diffraction peaks characteristic of form I and, in some cases, additional peaks due to form II. However, the characterization of a thin solid layer grown at a solid surface is challenging, and this is especially true if the structure is unknown. GIXD is, together with electron diffraction, a good method to solve the structure of thin films. In short, diffraction from crystals gives reciprocal space information (peak positions and intensities). Peak positions allow determining the crystal unit cell, while the intensities provide structure information, i.e. the location of the atoms within the cell. Obtaining a direct solution is complicated by the problem of the lost phase information. Computers assisted construction gives access to structural information by either direct or indirect methods. The approach usually works well for most small

molecular or macromolecular crystals but, because of its statistical nature, require recording many Bragg peaks. GIXD often provides only a limited number of Bragg reflections because of a number of reasons such as weak diffraction, small scattering volume, high sample aspect ratio or defects, in addition to experimental damping resulting from temperature vibration (Debye-Waller like damping) or polarization of the X-ray beam. This makes less effective the conventional structure solving methods, which are suitable for large single crystals.

Nonetheless for Phenytoin form II, by varying and optimizing the deposition conditions, it was possible to obtain enough peaks for a successful indexing, yielding the lattice parameters of this structure, which was found to be monoclinic. Deeper analyses of the GIXD data, combined with crystal structure prediction (CSP) methods, yielded a preliminary $P2_1/c$ (C^5_{2h}) structure with four molecules in the unit cell, all equivalent by symmetry (Z = 4, Z' = 1).

The proposed $P2_1/c$ structure appeared plausible and reproduced the experimental diffraction pattern. Looking for further validation and a better identification of such a structure, we decided to measure and calculate the Raman spectra of both Phenytoin crystal forms in the low wavenumber region. Indeed, the synergy between highly accurate density functional theory calculations with dispersion corrections (DFT-d) and low frequency Raman spectroscopy is very effective [200], [201] for polymorph identification. Analysis of the spectra, and comparison between experimental and calculated spectra, may thus be used to support and validate any suggested structure.

In the present investigation, we have therefore used the micro Raman technique to map areas of Phenytoin films where the two different phases I and II appear, identifying the lattice phonon pattern typical of each of them, while polarized Raman spectra have been recorded to assist the assignment of the observed features. The good agreement between experiments and calculations for Phenytoin form I was used to validate the computational approach. For form II the analysis has instead led us to revise the previously proposed $P2_1/c$ structure, characterized by the presence of a symmetry inversion centre. In the computations, the structure is found to correspond to an energy saddle rather than a minimum and, moreover the simulated spectra display a very poor

agreement with the experiments. By perturbation of the saddle geometry, a new non-centrosymmetric Pc minimum is reached, with two non-equivalent pairs of molecules in the unit cell (Z = 4, Z' = 2). Such a minimum, although extremely close to the $P2_1/c$ structure, is characterized by a different set of Raman symmetry selection rules and thus yield very different spectra, which finally do account for the experimental results. Accordingly, the computed GIXD pattern is also very satisfactory, and actually represents an improvement over the preliminary $P2_1/c$ structure.

4.2.2. Experimental and theoretical methods

Sample preparation and Raman Spectroscopy: Various samples were investigated by Raman spectroscopy for the purposes of this work:

- Commercial Phenytoin from Sigma Aldrich, available as a crystalline powder certainly attributable to form I; [197], [198]

- Elongated needle-like single crystals obtained by slow evaporation from solutions in ethanol (EtOH);

- Films obtained by drop casting a THF solution on heated glass substrates, [26] following the procedure described elsewhere. [199]

All samples were characterized by Raman spectroscopy. A flexible molecule such as Phenytoin is expected to display over this range also intramolecular vibrations, like for instance the hindered rotations of the phenyl rings, which mix with the lattice phonons. Raman spectra were recorded in the energy interval of the lattice phonons with excitation wavelength at 647.1 nm, while in the energy interval of the intramolecular vibrations the 514.5 nm line were used.

Computational methods: Details on the computational methods are reported in Ref. [202]

4.2.3. Results and discussion

Experimental results: Form I

Unpolarized Raman spectra in the wavenumber interval 15-200 cm^{-1} of the commercial powder and of a needle-like single crystal are shown in Figure 4.12, along with the computed frequencies and intensities which will be discussed in the following. The two spectra clearly correspond to the same crystal structure, and since the powder certainly belongs to the more common form I, we deduce that the needle belongs to the same form. X-ray indexing of Phenytoin needles [203] obtained from EtOH and displaying the same morphology have shown that the needle axis lies in the direction of the crystal axis *a*. This observation is in agreement with the literature finding for orthorhombic molecular crystals, [204] for which the long side of the crystal, that is the direction of fastest growth, is usually parallel to the shortest axis (i.e. *a*).
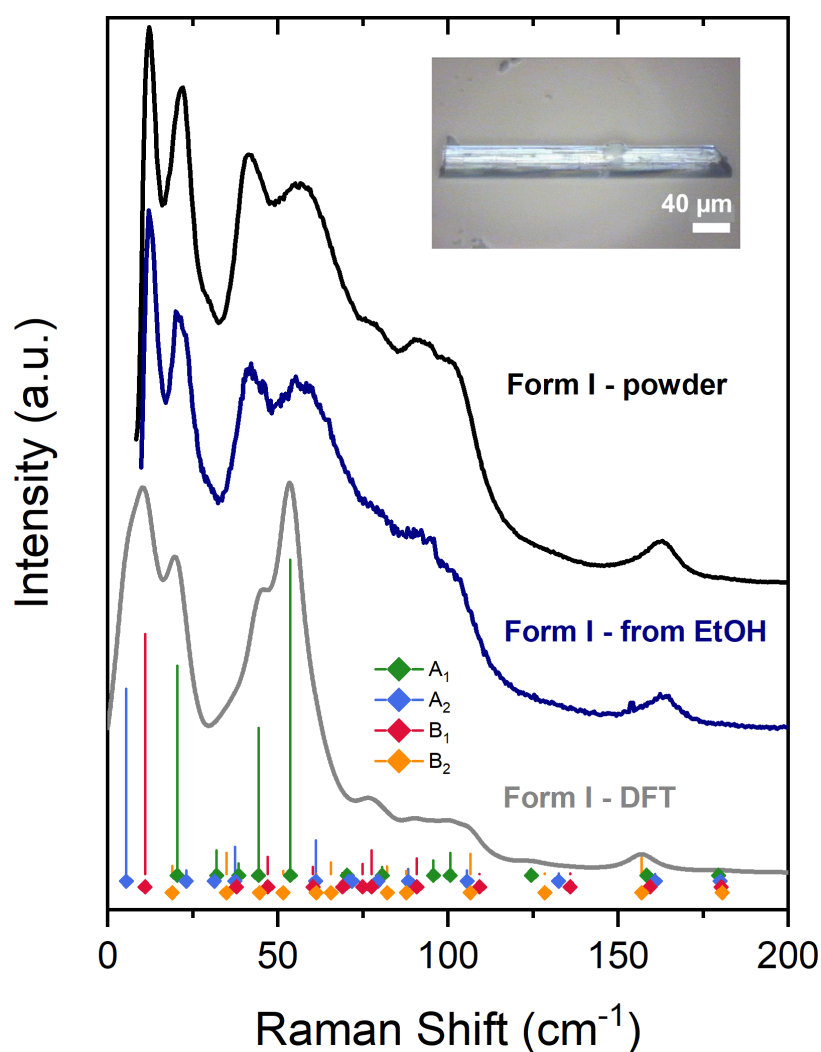
Figure 4.12: Upper traces: Unpolarized Raman spectrum of the commercial powder (form I) and of a single needle-like crystal obtained by deposition from EtOH (sample image shown in the inset) in the wavenumber range 15-200 cm^{-1}. Lower trace: computed unpolarized spectra for form I. Position and height of the vertical bars represent computed frequencies and intensities of the vibrational modes. Mode symmetries are labelled by colours, as indicated in the Figure.

Polarized Raman spectra (see paragraph 2.1.4) of the same crystal recorded in a back-scattering geometry are shown in Figure 4.13. The sample is placed on the stage with the needle axis, which corresponds to one of the extinction directions and identifies with the crystal axis a, either parallel or perpendicular to the polarization direction of the analyser (output polarizer) which, as indicated in the Figure, had a fixed orientation, while the polarization direction of the impinging radiation could be rotated. Accordingly, the polarization of exciting and scattered light beams is indicated by the labels a or a$_\perp$, depending on their orientation either parallel or perpendicular to the crystal axis a. As

expected from theory, spectra recorded in cross polarization, i.e. $aa_\perp$ or $a_\perp a$ spectra, were found to look identical and therefore only one of them is shown in Figure 4.13.

For the purposes of labelling the vibrational symmetry species [205] in the C^9_{2v} factor group, it is necessary to specify that the C_2 axis lies along b and that we have arbitrarily chosen the σ_v and σ'_v planes to be on bc and ab, respectively (the opposite choice would of course be possible). This information on the symmetry of the crystal is sufficient to interpret and assign the most important spectral features. As mentioned above, polarizations parallel to the needle are aligned to the orthorhombic axis a, while those perpendicular to it ($a_\perp$) are along some unknown combination of b and c.

Therefore, aa spectra probe modes of A_1 symmetry and derive their intensities from the α_{aa} component of the polarizability tensor. The bands observed in $a_\perp a_\perp$ spectra arise from the α_{bb}, α_{cc} and α_{bc} polarizability components, and correspond to modes of symmetry A_1 and B_1. Finally, $aa_\perp$ (or $a_\perp a$) spectra involve α_{ab} and α_{ac} polarizability components, thus probing modes of symmetries B_2 and A_2, respectively.
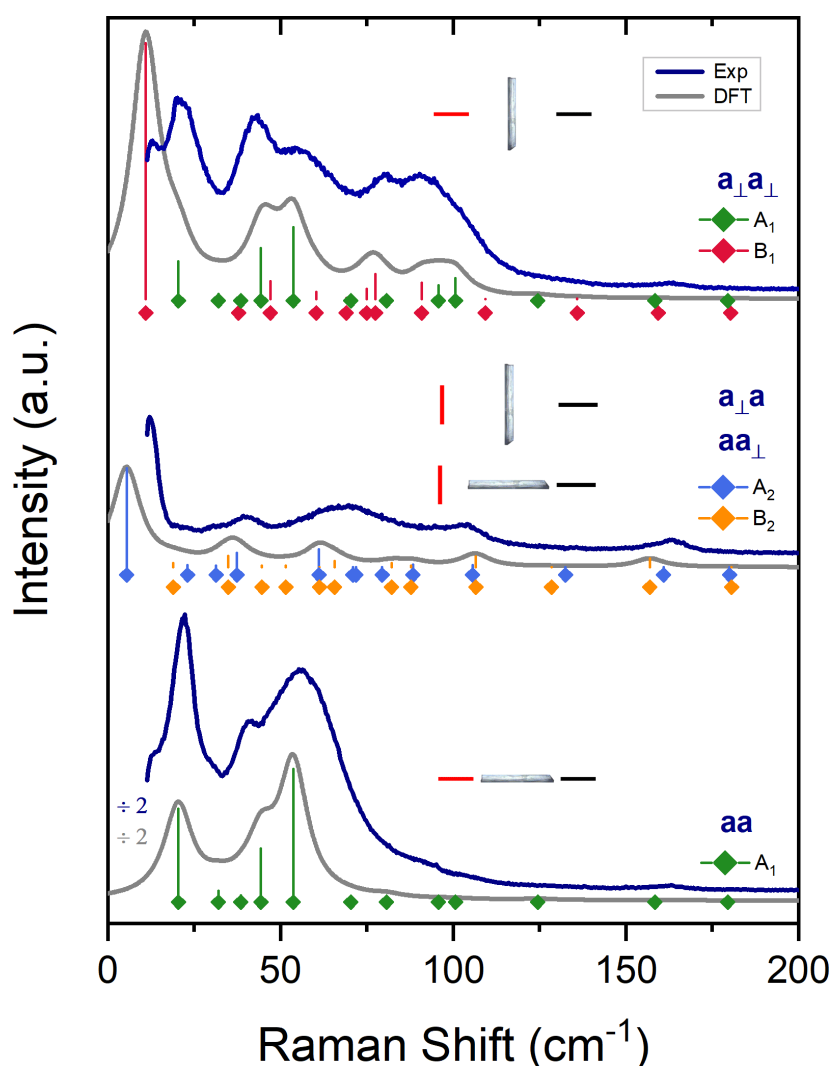
Figure 4.13: Coloured traces: Polarized Raman spectra for a single needle-like crystal of form I in the wavenumber range 15-200 cm^{-1}. Horizontal or vertical bars in the insets indicate the direction of the polarization vector of incident and scattered light with respect to the needle axis. The notation a or $a_\perp$ indicate a direction parallel or perpendicular to the needle, which grows along the crystal axis a. Grey traces: Calculated spectra evaluated as discussed in the text, for clarity all shown with the a downward intensity shift. Position and height of the vertical bars represent computed frequencies and intensities of the vibrational modes. Mode symmetries are labelled by colours, as indicated in the Figure.

Experimental results: Form II

Films prepared by drop casting adopt very nonuniform morphologies, as shown by the optical image of a typical sample in Figure 4.14. For this sample we have used the confocal microscope to acquire Raman spectra at all points of the grid superimposed over the image and found different spectral patterns, as illustrated in Figure 4.15, where the spectrum of the commercial powder, which belongs to form I, is also shown. Spectra with

lattice peaks precisely matching those of the commercial powder are found at some grid points, where only form I is therefore present. At other grid points we record spectra where none of the characteristic peaks of form I are visible. It is therefore possible to infer that only the different form II (pure SIP), is present at these areas. At yet other points we find combinations of the two detected spectra, which clearly correspond to mixtures of the two forms (phase coexistence or mixing). Analogous behaviour is found for other samples.
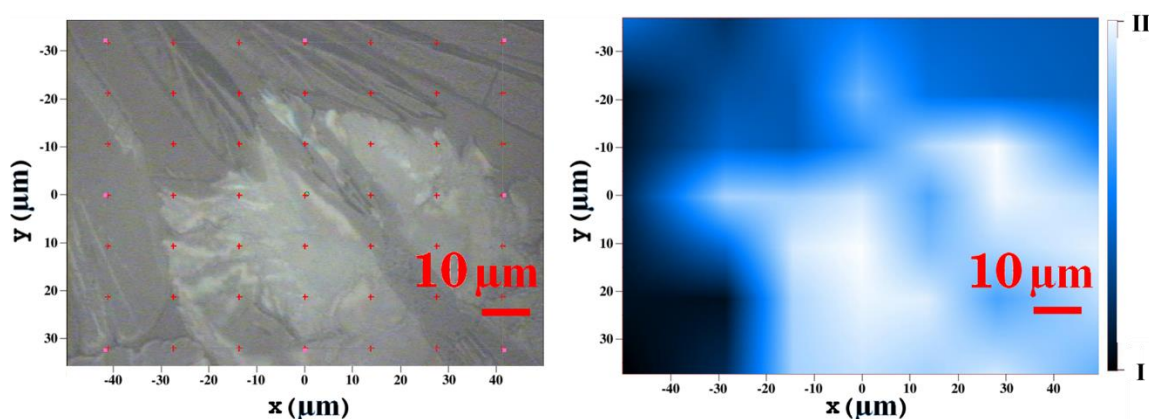
Figure 4.14: Optical image (left) and Raman map (right) of a selected film sample. The Raman map refers to the XY grid of points drawn over the optical image, with a colour scaling from extremely dark (form I) to extremely light blue (form II).

A full map (described in paragraph 2.1.3) of the relative proportions of the two forms at the various grid points has thus been deduced from the relative intensity of appropriate spectral windows typical of the two forms. We have used the window 53-59 cm^{-1} for form I and 30-36 cm^{-1} for form II, as indicated by the shaded areas in Figure 4.15, resulting the concentration map shown in Figure 4.14 (right panel). As expected, we observe a close correspondence between the Raman map and the optical image (i.e. between spectrum and morphology), with form II corresponding to whitish powder-like portions of the sample and form I to darker fibrous portions.
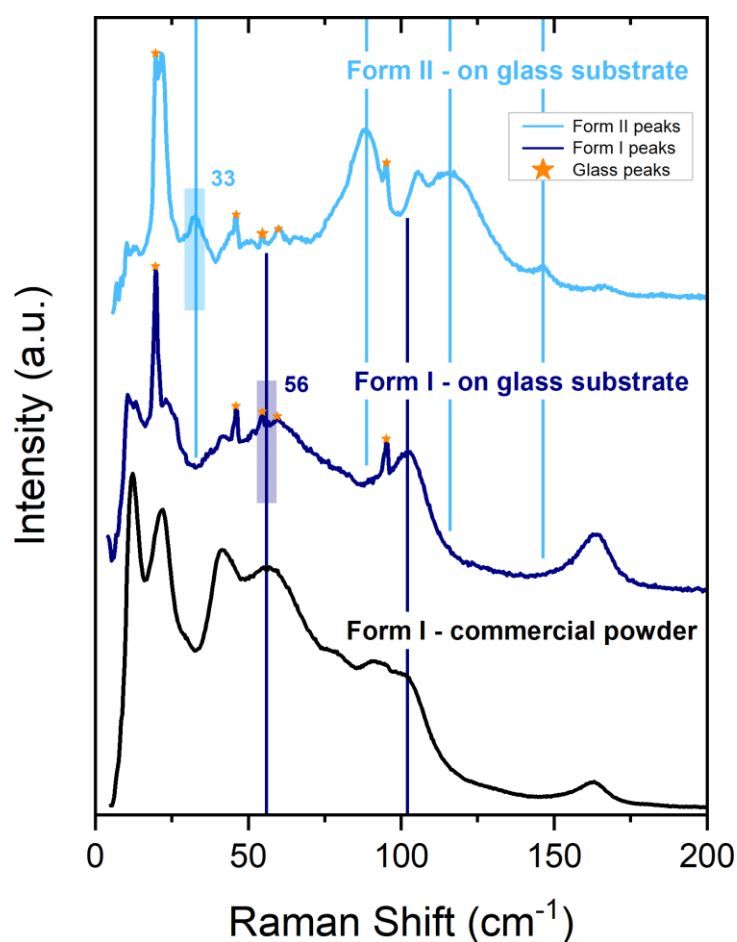
Figure 4.15: Low wavenumber Raman spectra of Phenytoin commercial powder, and at two different points of a selected film prepared by drop casting. Peaks indicated with stars are due to the glass substrate. Shaded areas indicate spectral windows chosen to quantify the proportion of the two phases.

To check for the chemical identity of the sample we have recorded the Raman spectra on the intramolecular vibration region (500-1250 cm^{-1}), reported in Figure 4.16, where the few spectral differences detected between the two forms in this range are indicated. The intramolecular Raman spectra of Phenytoin form I and form II appear very similar and this confirms that the molecules assume virtually the same conformation in both polymorphs. Slightly different spectral features are observed in the energy range 950-1050 cm^{-1}, corresponding to CC and CH bending vibrations, which could be ascribed to the different H-bonding patterns of the two structures. Also, the so-called fingerprint range below 700 cm^{-1}, were mostly torsional modes are detected, displays some band shifts.
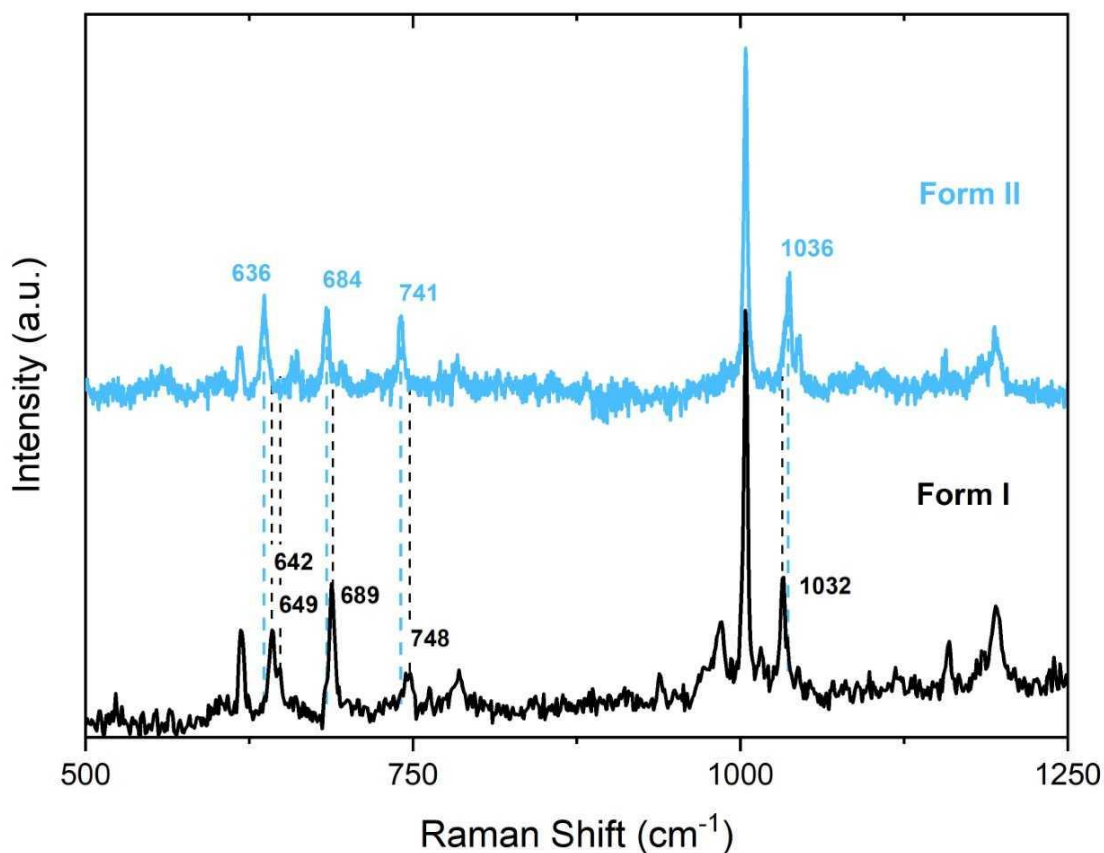
Figure 4.16: Raman spectra of Phenytoin forms I and II in the wavenumber interval 500-1250 cm^{-1}, where the intramolecular vibrations are detected. The vertical bars identify the bands which fall at different wavenumbers in the two polymorphs.

Computational results: Form I

Starting from the experimental structure, [198] we relaxed it to the equilibrium structure with VASP and then computed vibrational frequencies, eigenvectors and Raman intensities. All frequencies were computed to be positive, proving that the found structure is indeed a stable minimum. Experimental and calculated unpolarized Raman spectra of form I are shown in Figure 4.12. The calculated spectra were obtained at 293 K (i.e. using the experimental lattice parameter corresponding to this temperature), for an exciting laser line at 647.1 nm. They are the sum of Lorentzian bands with the computed frequencies and intensities, and full widths at half maximum (FWHM) chosen to match the experimental widths and fixed at 5 cm^{-1}. The agreement between calculated and experimental spectra is fair, with the exception of the lowest peak around 10 cm^{-1},

for which the calculated intensity exceeds the measured peak height. We consider such a discrepancy as an artefact due to the subtractive monochromator configuration of the experimental setting, which is designed to cut intensities in the vicinity of the laser exciting line.

Experimental and calculated polarized Raman spectra for form I are shown in Figure 4.13. As already mentioned, about the $a_\perp$ orientation we only know that it must lie in the *bc* plane, not necessarily corresponding to a crystal axis. In the calculation of the spectra we have therefore averaged the intensity contributions over the unknown rotation around the *a* axis, obtaining intensities for the polarized spectra, in which each term involves the expected α_{ij} polarizability components. An almost perfect agreement between calculations and experiments is found for the *aa* spectrum. This spectroscopic result confirms the deduction that the long side of the crystal is parallel to *a* axis. The good match between calculated and experimental spectra, both unpolarized and polarized, validates the computational method.

Computational results: Form II

As already discussed, previous GIXD measurements and CSP calculations gave a $P2_1/c$ (C_{2h}^5) crystal structure which reproduced quite well the experimental diffractogram. [199] By relaxing this structure to the nearest stationary point in our calculations, and then computing the vibrational modes, we discovered that the experimental spectrum was not properly reproduced, as it can be seen when comparing the experimental and computed unpolarized Raman spectra shown in Figure 4.18. More importantly, we found an imaginary frequency for an intramolecular mode of Bu symmetry, i.e. with atomic displacements which are antisymmetric with respect to both the inversion and C_2 operations, indicating that the preliminary $P2_1/c$ packing corresponds to a saddle point in the potential energy surface rather than to a genuine minimum. A graphical representation of this mode is shown in Figure 4.17.
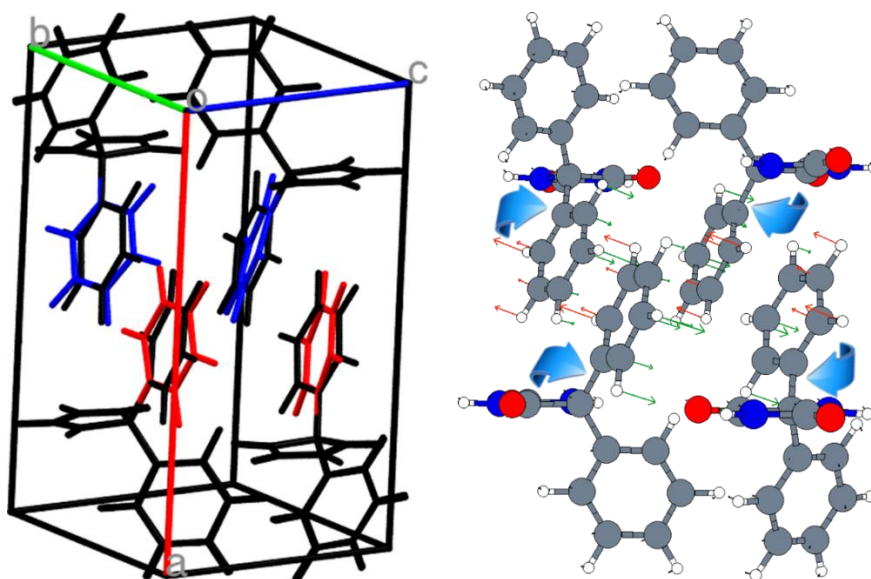
Figure 4.17: Left panel: Overlapped structures of the two DFT-d stationary points of form II. P2₁/c (black) and Pc (coloured) structures are respectively an energy saddle and a minimum and differ for the rotation of the phenyl groups. Molecules with the same colour are equivalent by symmetry. Right panel: Atomic displacements (eigenvectors) of the B_u mode with imaginary frequency.

By perturbing the system along the eigenvector of the imaginary frequency, all symmetry operations of P2₁/c group except the glide plane are lost and a new Pc (C^2_s) minimum energy structure is obtained.

The Pc minimum is only slightly more stable than the original P2₁/c saddle point (ΔE =0.067 kcal per mole of Phenytoin) and is geometrically similar to it. So similar, in fact, that the standard crystallographic tool PLATON, [199], [206] converts to Pc structure back to the P2₁/c one if the default distance tolerance for the identification of atoms equivalent by symmetry (0.25 Å) is set.

Despite their close structural and dynamical similarities, the two structures can be promptly distinguished on the bases of their vibrational properties, because in the Pc packing all the modes become Raman active, as a result of the symmetry lowering with loss of inversion. For this reason, the calculated Pc spectrum displays more bands and, as shown in Figure 4.18, agrees much better with the experiment.

By analysing the structures in detail, [202] we find that the transformation leading from the P2₁/c (C^5_{2h}) to the Pc (C^2_s) structure involves a slight rotation of the phenyl groups in two opposite directions (see Figure 4.17). As a consequence, the inversion and C_2 screw axis symmetries of C^5_{2h} are lost, while the glide plane symmetry is preserved.

Depending on their parity with respect to the latter symmetry operation, the four irreducible representations of the C_{2h}^5 group merge into the two C_s^2 representations, with the correlation scheme $A_g + B_u \rightarrow A'$, $A_u + B_g \rightarrow A''$. By examining the calculated intensities in Figure 4.18, in fact, we find that A_g or B_g bands computed for the P2_1/c structure usually have corresponding A' or A'' bands for the Pc structure which, however, display many additional bands, which are those arising from the A_u or B_u Raman inactive P2_1/c modes.
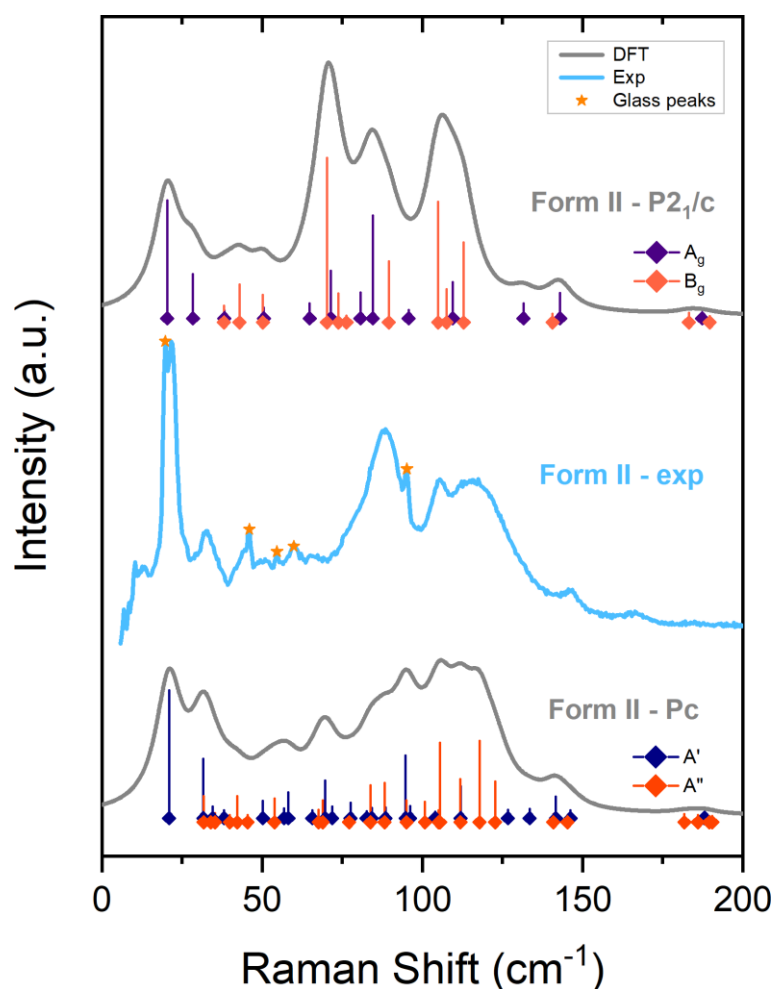
Figure 4.18: Experimental unpolarized Raman spectra for form II of Phenytoin (coloured trace), and computed powder spectra for the P2₁/c and Pc computed structures (grey traces). Position and height of the vertical bars represent computed frequencies and intensities of the vibrational modes. Mode symmetries are labelled by colours, as indicated in the figure. As discussed in the text, the Aₒ and Bₒ modes of P2₁/c are two strict subset of A' and A'' of Pc, respectively.

4.2.4. Conclusions

A previous work of the present collaboration group [199] reported the solution of the crystallographic structure of the surface induced phase II of Phenytoin determined by combining GIXD experiments with CSP calculations.

In our studies, with the aim to validate the candidate structure for form II, [202] we have investigated the experimental and calculated Raman spectra of the two known crystal forms in the low wavenumber region. The comparison between experimental and calculated spectra may thus be used to validate any proposed structure, while the computed frequencies can be compared to their experimental equivalents, and also be used to check the stability of the stationary point.

Form I was confirmed to correspond to a stable minimum and gave computed Raman spectra in excellent agreement with the experiments.

For form II the best CSP structure, although able to reproduce the GIXD measurements, instead gave computed Raman spectra which did not match the experiments and furthermore corresponded to a centrosymmetric saddle point structure with an imaginary frequency.

Descent from the saddle yielded a non-centrosymmetric minimum, also with the correct GIXD pattern. The saddle and the minimum, although very close, are however characterized by different Raman symmetry selection rules and the spectra computed for the minimum are therefore very different and in excellent agreement with the experimental pattern, thus confirming that the structure is correct.

Convergence to saddle structures of too high symmetry could occur in many CSP searches. The identification of these saddles is often not attempted at a DFT-d level for hundreds of structures, although with increasing computer power it could be systematically performed by computing the vibrational spectrum and checking for imaginary frequencies. A related problem, in the opposite direction, was often noticed in the past, when it became clear that many published X-ray studies gave erroneous structures with too low crystallographic symmetry. [207] This problem was eventually solved when software tools like PLATON [206] were developed to routinely check the

crystallographic coordinates for missing symmetries. [208] By far the most common case is precisely the missing of an inversion centre, which is also the most serious case because it leads to incorrect crystal property predictions. Reliable detection of the inversion in borderline situations presents problems even now, [207] since PLATON, for instance, needs to allow for noise in the atomic coordinates. Fortunately, as we have demonstrated in practice, an analysis of the Raman and/or infrared spectra may easily reveal the presence (or absence) of the inversion and thus conclusively validate a structure.

4.3.   Nabumetone

Film fabrication and Raman measure*ment*s presented in this section were obtained by Isotta Bonvicini under the supervision of the author, or by the author herself.

4.3.1. Introduction

Nabumetone (4-(6-methoxynaphthalen-2-yl)butan-2-one) is a Nonsteroidal Anti-Inflammatory Drug (NSAID), which is known on the market with different brand names such as Gambaran, Relafen and Relifex. It is produced starting from the 1-naphthaleneacetic acid and is used in the treatment of osteoarthritis, rheumatoid arthritis and soft tissue injuries. It is rapidly metabolized in the liver to a major active metabolite, 6-methoxy-2-naphthyl acetic acid, which is thought to be the compound primarily responsible for therapeutic effect. Nabumetone is sold in crystalline form, but unfortunately, is characterized by a low solubility in water and low bioavailability, and shows many side effects.

In the literature [209] two polymorphs of Nabumetone have been reported and their cell parameters are given in Table 4.2.

Table 4.2: Crystallographic data of Nabumetone form I and II, measured at 158 K.

Form	a (Å)	b (Å)	c (Å)	β (deg)	Volume (Å³)	Crystal System	Space group	Z	Z'	morphology
I [209]	21.87	5.33	22.23	111.93	2403.3	monoclinic	P2$_1$/c	8	2	Needles
II [209]	26.9	5.88	7.9	91.86	1249.4	monoclinic	P2$_1$/c	4	1	Plates

Both structures are monoclinic (space group P2$_1$/c). Form I has 8 molecules per cell and the asymmetric unit (Z') consists of two molecules which are not equivalent to each other by symmetry. Form II, instead, has four molecules per unit cell and Z' = 1. It is interesting to note that, in this case, the polymorphs can also be distinguished by their morphology. Molecular geometry is the same for both phases, meaning that they are

classified as packing polymorphs, and so no remarkable differences are expected between their spectra in the intramolecular mode ranges.

The theory predicts 24 Raman active lattice vibrations for form I and 12 for form II, but, since Nabumetone cannot be considered a rigid molecule, modes at low wavenumbers will be a mixture of inter- and intra-molecular vibrations.

Thermodynamic data indicate form I as the thermodynamically stable one up to the melting point of the compound. Form II, instead, grows only with difficulty and once obtained it quickly transforms into phase I, even by simple mechanical solicitation. At room temperature form I is denser than form II by approximately 4%. In a molecular crystal a higher density is generally a good indicator of the greater thermodynamic stability at the given temperature and pressure conditions. In fact, the higher the density, the better the molecular packing through which the interactions, that allow the formation of the crystal itself, are established. DSC measurements [209] showed that form I is characterized by a melting point at 80 °C, while form II melts at about 65 °C with a melting enthalpy that is clearly smaller than that of form I, suggesting a greater solubility and a clear indication of lower packing energy.

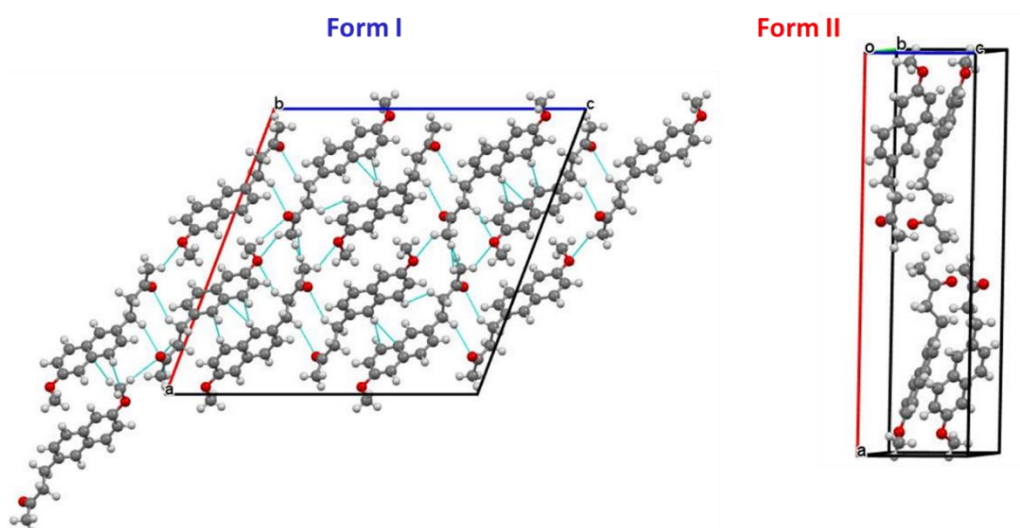*Figure 4.19: Left-side) Arrangement of the Nabumetone molecules on the ac plane of the form I. The image shows the short-range interactions involving the oxygens of the carbonyl and methoxy groups. Right side) Herringbone arrangement of the naphthalene units of the Nabumetone molecules in form II: the hydrogens of the aromatic ring of a molecule point towards the aromatic ring of a neighbour one.*

The energy difference between the two forms is due to different packing geometries. In form I the molecules are arranged head-to-tail with respect to each other, while in form II the head-to-head type is present. [210] In Form I there are C-H $\cdots$ O bonds which involve both the carbonyl oxygen, which bonds two molecules, and the methoxy group, for a total of three interactions that combine pairs of adjacent molecules, giving rise to a layer organization. The *ac* plane of this structure is shown in Figure 4.19. In form II the structure has a herringbone arrangement which involves the naphthalene units. Therefore, the CH $\cdots$ π interactions between the hydrogens of a molecule and the electron density of the ring of the adjacent one, predominate. The packing of the form I is more efficient, and this translates into greater stability. The thermodynamic data available for the two forms (enthalpies and melting points) [209] indicate that this is a case of a monotropic polymorphism, in which form I is thermodynamically more stable in any temperature condition, so that only the transformation of form II to form I is possible. A clearer representation of the packing differences in the two forms is given in Figure 4.20.
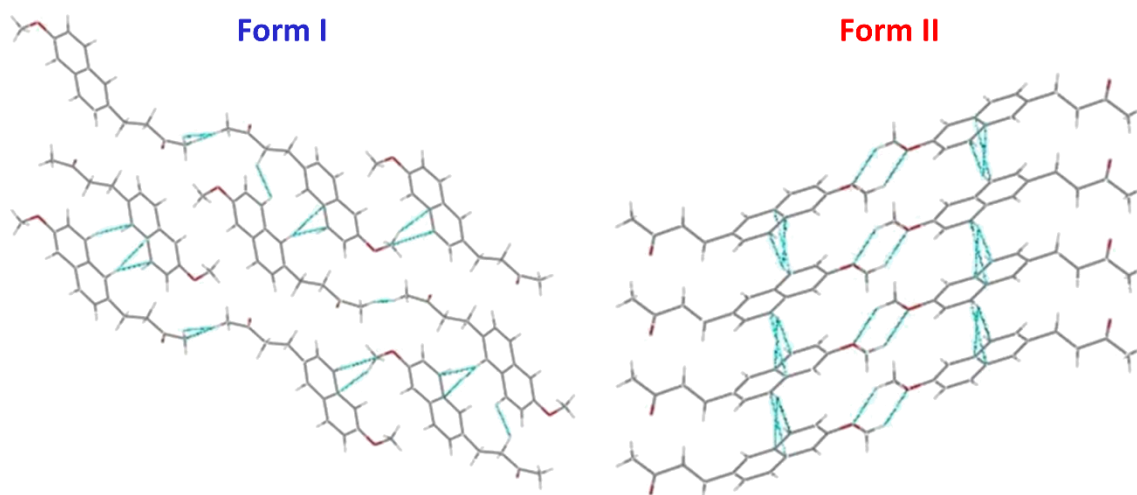
Figure 4.20: Comparison of the molecular packings of the two polymorphs of Nabumetone. Blue bonds between atoms identify intermolecular interactions.

The research group working at the Department of Pharmaceutical Technologies of the University of Graz (Austria) was interested in the study of crystallization processes of Nabumetone in films obtained by spin coating, which they first analysed by GIXD. The aim was to verify whether the presence of predominantly isotropic surfaces, such as glass

and silicon oxide, could induce the growth of metastable forms, including the so-called "Surface Stabilized Polymorphs". Structural X-ray measurements showed the stabilization of form II in the films, although often in coexistence with form I. They also suggested the existence of a third phase (form III), the growth of which could be mediated by the surface. In fact, this latter appears to differ from form II only for a different netplane distance.

Considering their results, we decided to combine the GIXD measurements with our micro Raman studies in order to confirm the X-ray analysis. Furthermore, the best spatial resolution of our technique was useful to determine whether the coexistence of the various polymorphs occurs through a real mixing of the phases on a micrometric scale or through a segregated growth.

4.3.2. Sample preparation

Crystal Growth: Crystals of suitable dimensions of Nabumetone (Sigma-Aldrich, 98%) were grown by recrystallization from solution. The solution obtained by dissolving 15 mg/mL of powder in ethanol, sonicated until complete dissolution, was introduced in 5 mL graduated flasks or in 2 mL vials, each containing 0.3 mL of the starting solution. The containers were covered with PARAFILM®, on which holes were made to allow slow evaporation of the solvent at room temperature. The formation of the metastable form II [210] occurs under very slow evaporation conditions and in the presence of high surface contact of the solution with the container, effects that we have tried to reproduce by varying the number of holes on the PARAFILM® and the dimensions of the container. The crystal growth required a period varying from 10 to 16 days, but samples of both forms were obtained, distinguishable by the different morphology: well-formed needles for the form I in most of the cases and irregular-shape platelets for the form II only inside the vials.

Other thicker crystals were obtained from the melt. The commercial powder was liquefied on a glass slide and keep at the melting point for 30 minutes, in order to be certain that the compound was completely melted. For the cooling, two procedures were

followed: the sample was quenched at RT or slowly cooled on the hot plate which had been turned off.

Films preparation: Films on glass substrates were deposited by spin coating 70 µL of ethanol solutions. Substrates were cut into pieces of 1.5 x 1.5 cm^2 and were extensively rinsed with ethanol followed by sonication within ethanol and acetone bath in a 1:1 (v/v) ratio for 30 min. Afterwards, the wafer was rinsed with 2-propanol and dried under a steady nitrogen stream. The spin parameters used are reported in Table 4.3.

Table 4.3: Parameters used for Nabumetone films deposited by spin coating.

Program Name	Rate (rpm)	Acceleration (s)	Deceleration (s)	Time (min)
R1	800	3	0.2	1
R2	900	3	0.2	1
R3	1000	3	0.2	1
R4	1200	3	0.2	1
R5	1400	3	0.2	1

4.3.3. Experimental setup

Raman Spectroscopy: All samples were characterized by Raman spectroscopy: in the energy interval of the lattice phonons with excitation wavelength at 647.1 nm, while in the energy interval of the intramolecular vibrations the 514.5 and 785 nm lines were used.

4.3.4. Results and discussion on bulk

The commercial Nabumetone powder is microcrystalline. The measurement of its Raman spectrum at low wavenumbers allows us to identify a high number of peaks of the form I, highlighted in Figure 4.21. Because of the complexity of the system, it is impossible to distinguish all the 24 expected bands in the lattice phonon energy region. This

suggested that we should not proceed with an analysis of peaks by deconvolution. In fact, given their high number, those bands certainly consist of many peaks under the experimental trace and the fitting process might strongly depend on the choice of the initial parameters. In the commercial powder spectrum we were able to identify the characteristic bands of the form I, at 33 and 101 cm^{-1}, [211] that have been used as diagnostics throughout the study. Their choice is not only dictated by the intensity of these two vibrational modes, but also by the fact that they fall outside the range of wavenumbers in which the characteristic bands of form II are observed.

Figure 4.21 shows the spectrum of a small needle of form I, together with its optical microscope image. It coincides, except for the relative intensity variations of the bands, with the commercial powder spectrum and this allowed its identification.
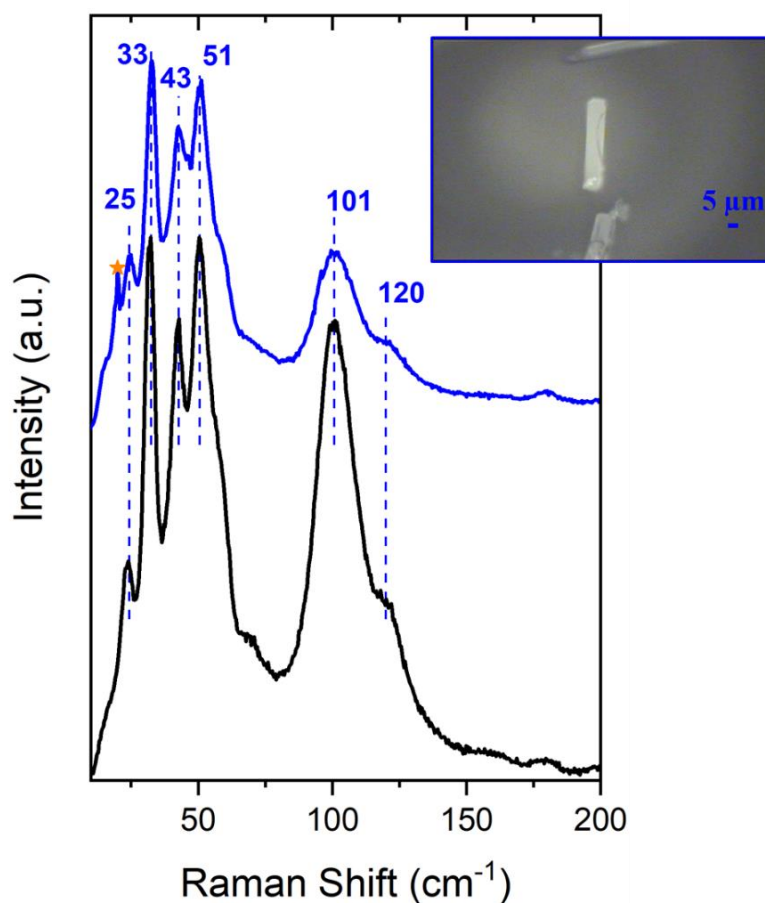

Figure 4.21: Raman spectra performed in lattice phonon energy region on the commercial powder (black trace) and on a single needle-like crystal of form I (blue trace), the inset shows the image of the sample. The main peaks of this form are highlighted. The peaks indicated with a star is duo to the substrate.

In order to observe new peaks not visible in the commercial powder, polarized spectra (explained on paragraph 2.1.4) were performed on a crystal of form I. A needle of form I displayed extinction in cross-polarized illumination when its long axis was aligned with the exciting light polarization. Face indexing by XRD was not available. However, on the bases of its morphology, we assumed that the direction of the crystal fastest growth was coincident with the *b* axis, which corresponds to an extinction direction of the monoclinic structure. This makes the interpretation of experiment in polarized light straightforward.

In Figure 4.22 the results for a needle-crystal oriented along the axis *b* or perpendicular to it are shown. In detail, Raman spectra were collected in backscattering geometry with the polarization of the incoming and scattered light parallel to each other (labelled as parallel polarizers in Figure 4.22) and in the sample extinction direction they reveal modes of A_g symmetry. This allows us to assign an A_g symmetry to the intense band taken as a diagnostic at 101 cm^{-1}. Among the remaining bands identified in the powder, those at 51 and 120 cm^{-1} are also certainly of A_g symmetry. The shoulder of the band at 51 cm^{-1}, which is located at 60 cm^{-1}, is resolved as an A_g mode.

Modes of B_g symmetry can instead be detected by rotating by 90° the polarization direction of the incoming light (spectra labelled as crossed polarizers in Figure 4.22). The analysis allows us to identify the 33 cm^{-1} diagnostic mode as of B_g symmetry, together with the bands at 25 and 43 cm^{-1}.
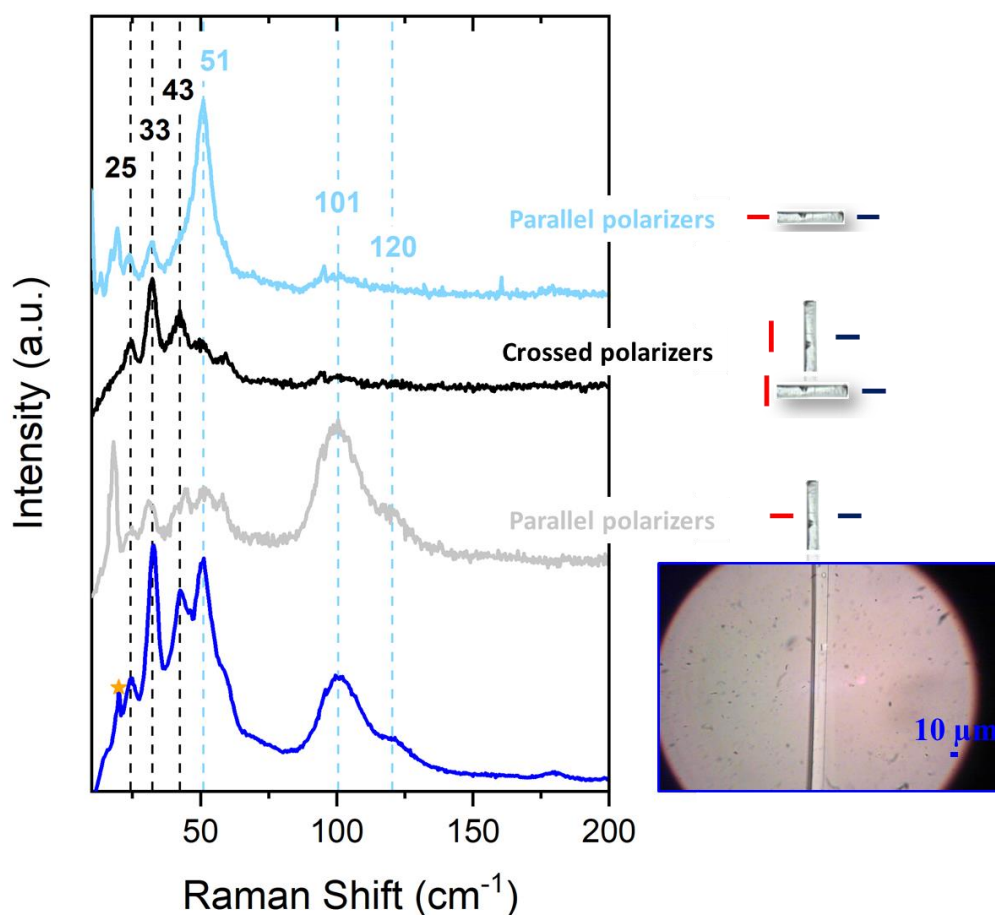
Figure 4.22: Polarized Raman spectra for a single needle-like crystal of form I in the low wavenumber energy range. Horizontal or vertical bars in the insets indicate the direction of the polarization vector of incident and scattered light with respect to the needle axis. The peaks indicated with a star is duo to the substrate.

The measurement of platelets shape crystals, qualitatively identified as form II because of their morphology, was difficult due to the instability of this phase in bulk. Indeed, it easily transforms into form I by mechanical stress (e.g. just by handling the platelets with tweezers) or by simple exposure to laser light. The phase transition appears through a colour change of the sample, which from transparent becomes white, due to the formation of many microdomains of form I.

Lattice phonon spectra were recorded on those crystals of form II and they are shown in Figure 4.23 (left hand side). For this phase, 12 Raman active vibrations are expected but in the spectrum there are many peaks of the substrate due to the thinness

of the sample. Only two broad bands at 131 and 143 cm^{-1} can be clearly distinguished and these will be used for the identification of the phase.

Most of these platelets are not single crystals and show distinct domains which extinguish at different orientations under the polarized light microscope. Polarized spectra were performed by isolating a single crystal domain (the analysed area is indicated with an arrow in Figure 4.23, right hand side) and revealed the presence of other bands at 18, 31, 59, 72 and 149 cm^{-1}. However, the high instability of this polymorph made impossible to bring these measurements to completion.
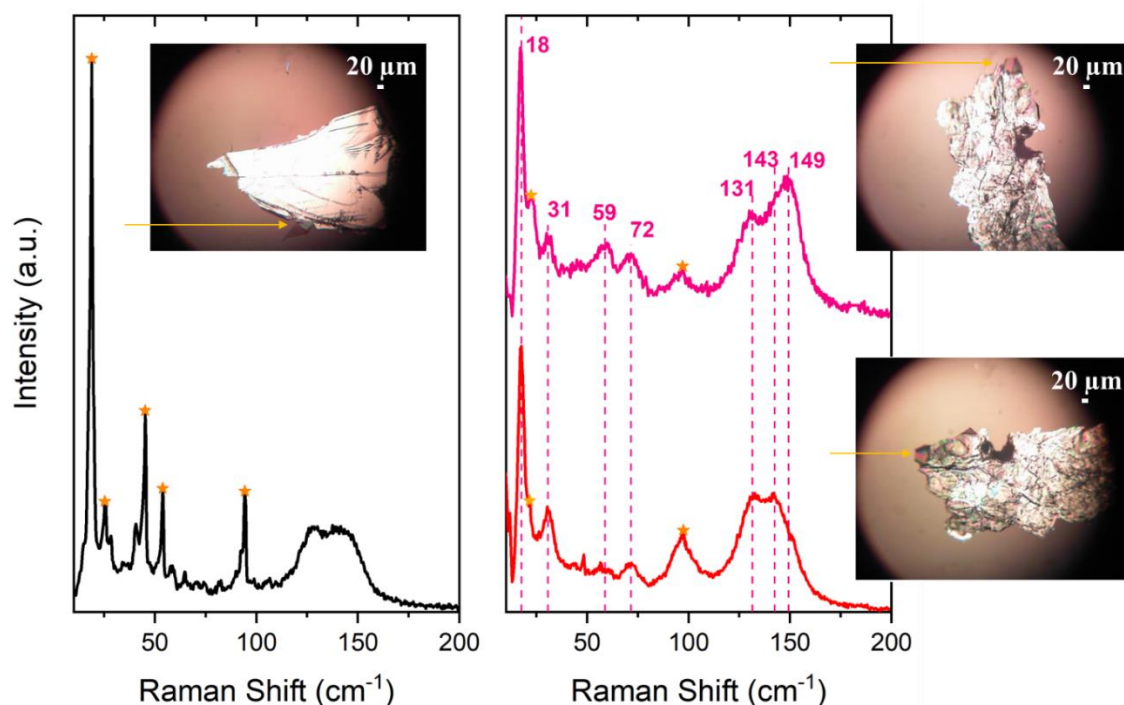
Figure 4.23: Raman spectra performed in lattice phonon energy region on a platelet-like crystal of form II (the analysed area is indicated with an arrow in the inset). Left-side: unpolarized spectra. Right-side: spectra were performed by orienting the sample and the exciting light, but without analyser. The orange stars indicate the main peaks of the substrate.

As an example of the instability of form II, Figure 4.24 shows the spectra recorded on a platelet that, in a very short time (about 30 minutes), is transforming into form I. The change of the pattern in the lattice phonon energy range is very evident.
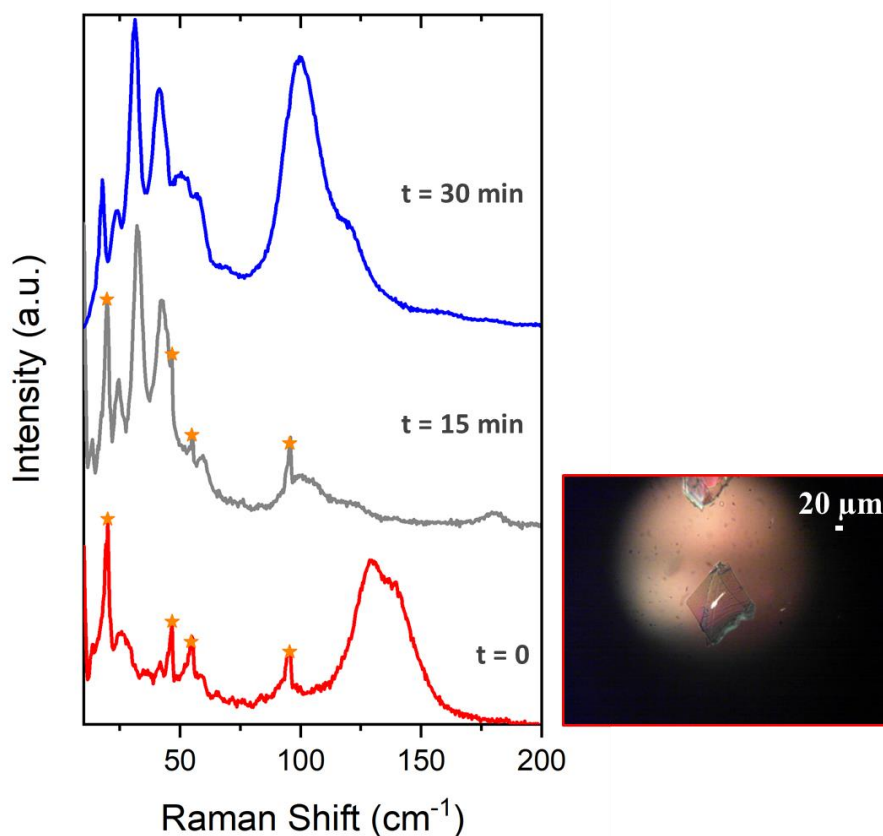
Figure 4.24: Transformation of a platelet-like crystal from form II (red trace) to form I (blue trace), followed by Raman measurements in lattice phonon energy region, for about 30 minutes. The orange stars indicate the main peaks of the substrate. The image shows a typical crystal of form II.

To obtain thicker crystals of form II (presumably more stable over time), melt crystallization was performed. Unexpectedly, the behaviour of Nabumetone seems to contradict Ostwald's rule: fast cooling produced form I, while slow cooling processes gave an amorphous substance that partly became form I and partly form II. It often happens that the growth of a metastable form passes through the formation of an amorphous phase (in accordance with the Ostwald's rule), but to obtain it by slow cooling of the melt, as in this case, is quite unusual.

The form II crystals obtained from the amorphous phase displayed irregular shapes and were found to be segregated from those of form I. The Raman spectra are shown in Figure 4.25 and are characterized by a good signal-to-noise ratio with respect to the previous ones. It was then possible to identify a good number of bands and provide

a useful spectrum for the identification of this polymorph, undoubtedly better than the only one reported in the literature. [211]
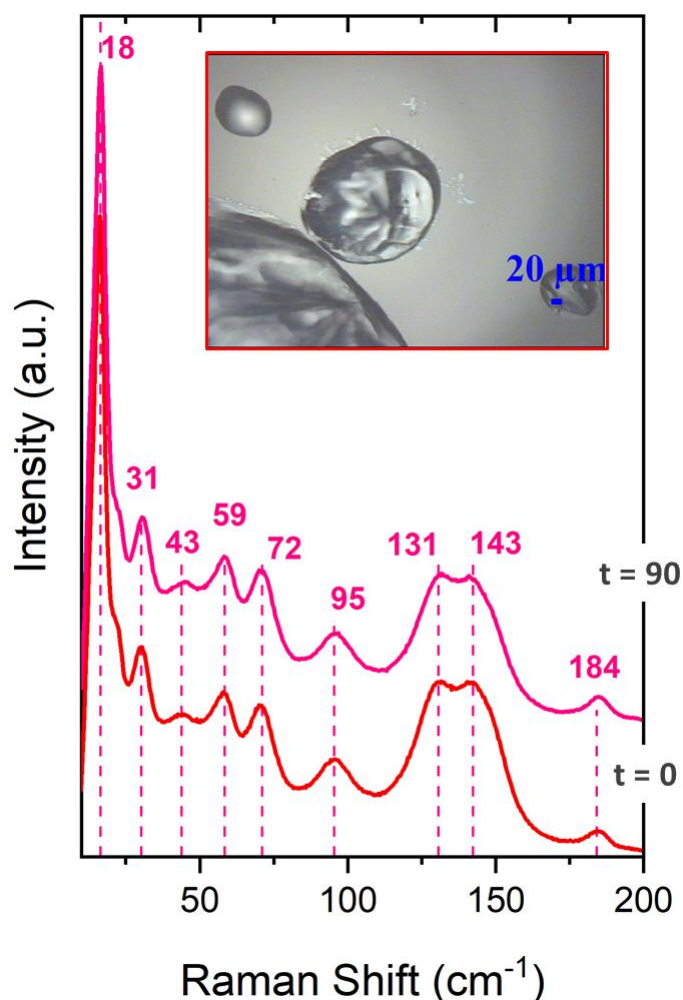
Figure 4.25: Raman spectra of form II recorded in lattice phonon energy region on a sample obtained from the melt (shown in the inset). The two spectra were recorded at different times to verify the stability of the polymorph.

The red trace in Figure 4.25 was recorded as soon as the transformation of the sample from amorphous to crystalline was observed (t = 0), while the pink one was after ≈ 90 min. It was found that, despite all the manipulations and the irradiation with the laser light, the phase transformation had not yet taken place. The samples obtained from melt are effectively stable for a few hours, even if their morphological characteristics do not allow their study in polarized Raman spectroscopy.

4.3.5. Result and discussion on films

As described in the introduction (see paragraph 4.3.1), according to the X-ray diffraction data, Nabumetone metastable forms were found to grow preferentially in the film phase. In particular, many of the structurally characterized films had diffraction peaks of both forms I and II, accompanied in some cases by two peaks not attributable to either of them. The Raman microscopy study aimed to: i) verify whether the growth of the two polymorphs occurs in a segregated way on the micrometric scale that the technique allows us to investigate; ii) identify/confirm the presence of a third polymorph, the growth of which is assumed to be determined by the presence of the substrate. In fact, the only two reflections observed at XRD constitute a clue, but not the certainty of the existence of such a form.

The characterization of the bulk phases has provided the Raman spectra of reference for the spectroscopic analysis of a series of films obtained by the spin coating technique, for which several parameters influencing the crystalline growth have been varied. In particular, the effects of the concentration of the deposited solution, of the solvent and of the deposition rate were studied.

Study of the different effects that can influence the growth on film

The first step was to test the effect of the concentration in the solutions. Starting from the initial solution, another three were prepared:

<u>Solution 1</u>: Concentration 15 mg/mL (ca 7 x 10^{-2} M), stock solution;

<u>Solution 2</u>: Dilution 1:2 (ca 3.5 x 10^{-2} M);

<u>Solution 3</u>: Dilution 1: 3 (ca 2 x 10^{-2} M);

<u>Solution 4</u>: Dilution 1: 4 (ca 1.5 x 10^{-2} M).

These dilutions were necessary because the analysis of a film obtained from the stock solution led to the exclusive formation of form I. To select the dependence on the

concentration, all the depositions (70 μL) were made on glass substrates with only the R4 program (having the characteristics described in Table 4.3).

In the film obtained from solution 2, both forms were present, often in contiguous areas but clearly segregated and no spectra of phase-mixing were observed in any of these films. A typical example of a film spectrum from this solution is shown in Figure 4.26. The inset shows the image of the sample in which the measurement areas are highlighted.

The metastable form II is instead the only one present in the films obtained from solution 3, even if the corresponding spectra are very noisy due to the low concentration. This effect is even more marked in samples obtained from solution 4, which was too thin to give an appreciable Raman signal. In conclusion, we can say that a lower concentration favours the formation of form II. The lifetime of this phase is also very long, compared to the bulk, since the transformation in form I began only after two weeks.
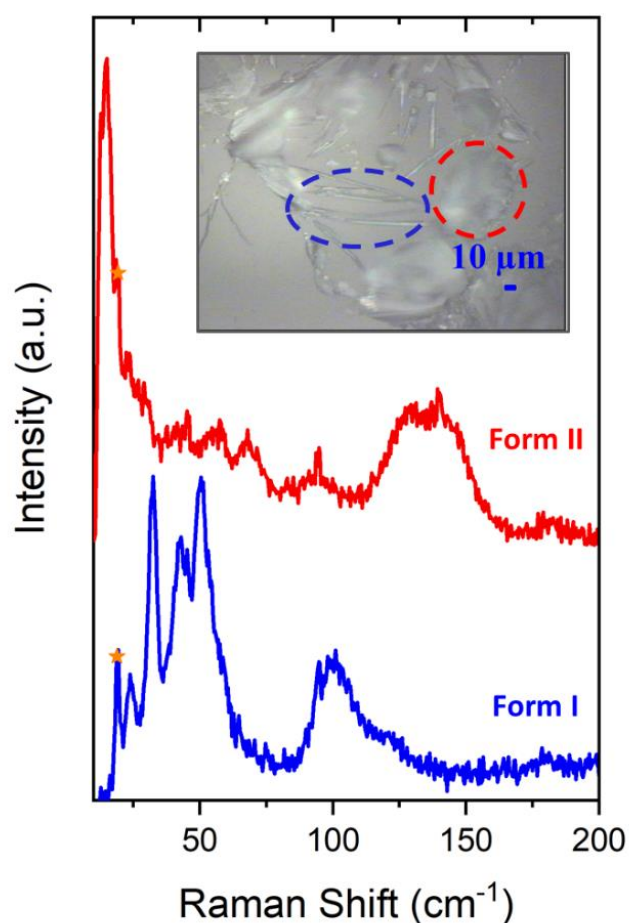
Figure 4.26: Raman spectra performed on a spin coated film obtained by using solution #2 and R4 program, see main text for details (the analysed area are highlighted in the inset with the colour code used for the spectra). The orange stars indicate the main peaks of the substrate.

Secondly, the effect of the rate was tested. After finding that the concentration is able to select the metastable form, the solution 3 was chosen to study the effect of the spin coating speed. The test was also done because the X-ray measurements suggested that the third polymorph (form III) grew together with form II in depositions at low rates. Films with solution 3 (70 µL per sample) were prepared using all the programs reported in Table 4.3 (R1 to R5). The results are shown in Figure 4.27. At the lowest speed (800 rpm) the formation of forms I and II is observed, while the growth of the pure form II begins from 900 rpm. At 1400 rpm, the low intensity of the lattice bands suggests a lower crystallinity of the sample, meaning that when the speed increases the film assumes the characteristics of an amorphous. No peaks belonging to a hypothetical new form could be identified in any of the deposition.
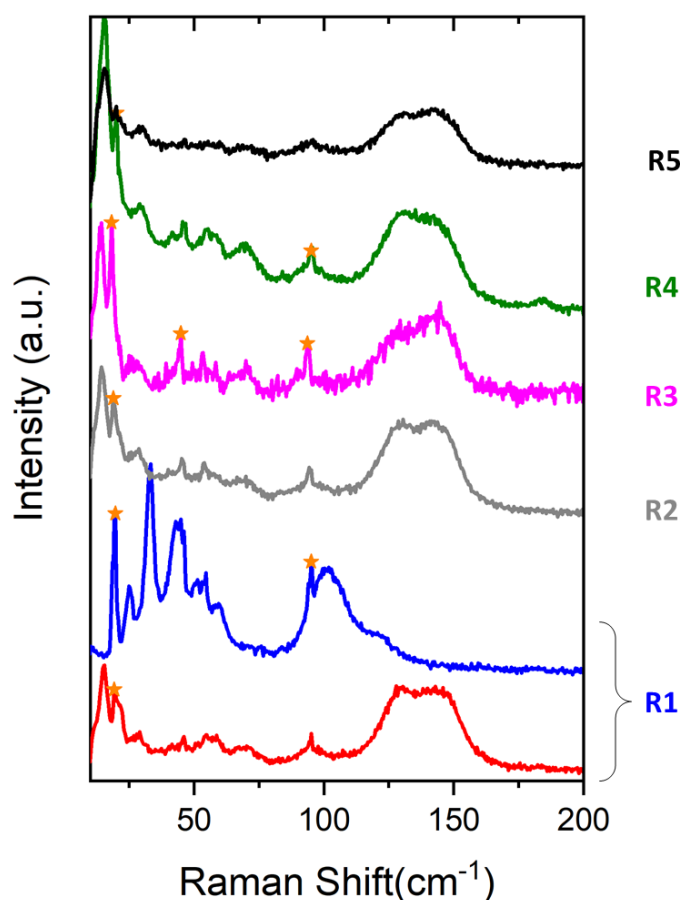
Figure 4.27: Raman spectra performed on a spin coated film obtained by using solution #3 and programs from the slowest (R1) to the highest rate (R5), see main text for details. The orange stars indicate the main peaks of the substrate. Except for the blue trace (corresponding to form I), all the spectra belong to form II.

The effect of the solvent was also checked, since the nature of the recrystallization solvent can influence the characteristics of the crystalline phase that is formed. Nabumetone is soluble in many solvents, both polar and protic, but X-ray experiments seemed to indicate that, among many, protic solvents are best able to induce the growth and stabilization of metastable forms. Maintaining ethanol as a reference solvent, since on films prepared from this solvent the metastable form II was obtained in a reproducible way, methanol depositions were performed with the same concentrations used for ethanolic solutions and the same deposited amount and the program R3 (1000 rpm). This latter parameter represented a compromise to investigate the possible formation of form III, since at too low speeds we saw pure form I, while high speeds selected form II.

Spectroscopically, films prepared in MeOH displayed both similarities and differences with respect to those in EtOH. In the range of concentrations from 6 to 3.5 x 10^{-2} M only form I is obtained but, at lower concentrations, form I and form II coexist, again as segregated. However, not even from methanol a new phase was observed. The X-ray data suggest that the new form III is structurally similar to form II and grows in the same conditions - indeed it was never observed as pure in diffraction measurements. This set of measurements, with the failure in detecting a new phase, convinced us to drop the search for form III by Raman.

Finally, the effect of the thickness was checked. The deposition of multiple layers of Nabumetone in the film phase was used for a dual purpose. First, all the methods employed for obtaining form II (including the capillary growth reported in the literature [210]) suggest a strong influence of the solid interface. We therefore wanted to test whether in conditions where this influence fails, due to an increased thickness of the film, the II form disappears. Secondly, we were also after thicker samples of form II that could provide good Raman spectra.

For this reason, samples were prepared using the R2 program with ethanolic solution 3, which was repeatedly deposited in 70 μL volumes on a glass substrate. Up to three depositions the phase obtained is pure form II, but with successive additions form I appears (thus the sample contains II + I). After six depositions, form I is the only one present. This confirms what we expected: by increasing the thickness, the system loses memory of the substrate effect, and the structure growing is the one thermodynamically stable.

The quality of the Raman signal of form II on the film obtained after three depositions, and shown in Figure 4.28, is excellent with respect to the thin samples of Figure 4.26 and comparable to that of crystals obtained from the melt.
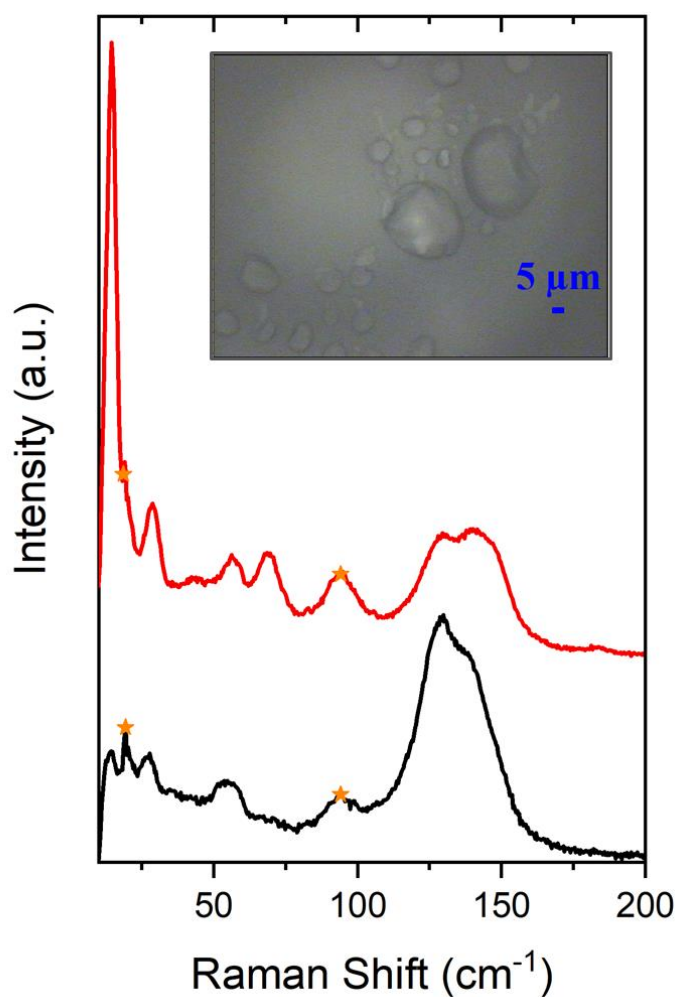
Figure 4.28: Raman spectra performed on a spin coated film obtained by using solution #3 and the program at 900rpm, deposited three times (three layers). The inset shows the image of the investigated sample. The orange stars indicate the main peaks of the substrate.

Raman mapping on a Nabumetone film sample

In Figure 4.29, the optical image of a mixed film (forms I + II) is shown at the top left (Figure 4.29a). The red box identifies the area of the sample that has been analysed, and the points in inset are those of the measurement grid. The collection of the recorded spectra is shown in the bottom left of the same Figure, where the wavenumber intervals assumed as diagnostic for each form are also indicated (92-115 cm^{-1} and 127-160 cm^{-1} for form I and II, respectively). The relative concentrations of the two forms in each point can be calculated as the ratio between the spectral intensities integrated in each interval (form I/form II). In this case, shades of blue were chosen as colour code, with the darkest

shade corresponding to pure phase II. The resulting map (Figure 4.29c) shows the spatial distribution of the phases in the analysed area and allows us to confirm the absence of an extensive phase mixing : the two forms grow essentially as segregated.
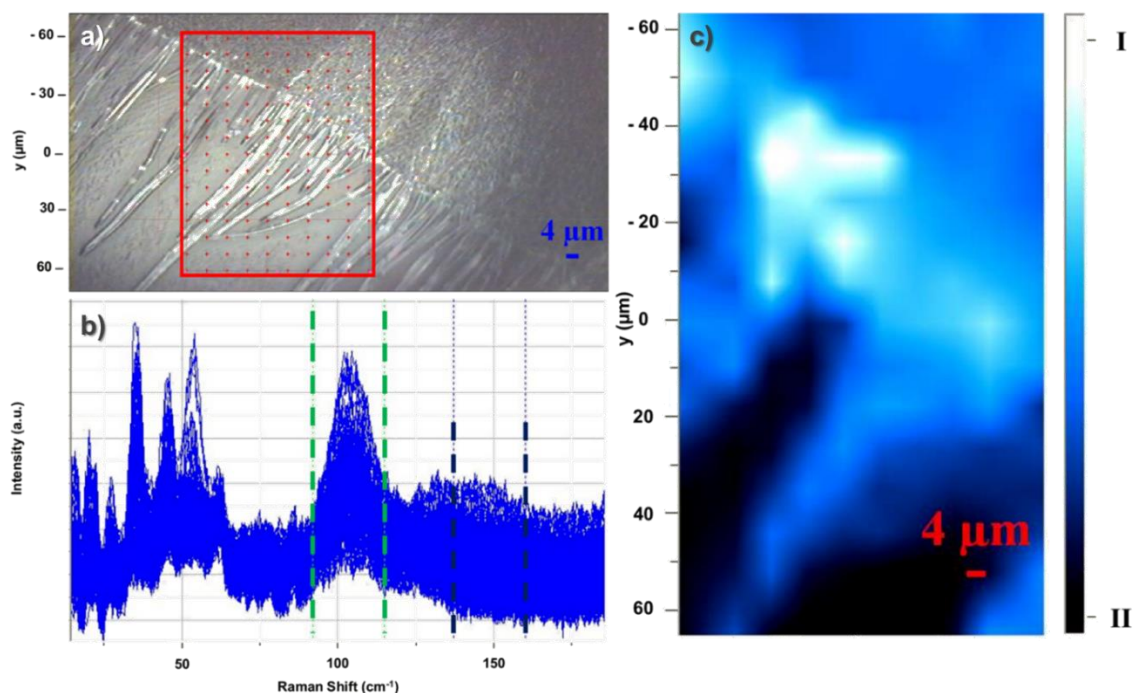
Figure 4.29: Raman mapping of a Nabumetone film containing both form I and II. a) microscope image of the analysed sample. b) collection of all the recorded spectra: the dotted green lines identify the frequency range of the diagnostic bands of form I (92-115 cm⁻¹), while the blue one is the interval for the form II (127-160 cm⁻¹). c) the Raman map refers to the XY grid of points drawn over the optical image, with a colour scaling from extremely dark (form II) to extremely light blue (form I) to map the distribution of the two phases.

Investigation in the intramolecular modes

As described in the introduction (see paragraph 4.3.1), polymorphs of Nabumetone are of the "packing" type, and the molecular conformation is the same in the two structures. In this case the spectra of intramolecular vibrations should be the same, except for the different splittings that originate from the different number of molecules per unit cell. However, different patterns of intermolecular interactions, such as those described for Nabumetone in Figure 4.19 and in Figure 4.20, might produce difference in the frequencies of modes related to groups of atoms involved in the interaction itself.

In order to investigate this effect, intramolecular spectra of both forms were recorded, even though a detailed vibrational analysis was not carried out.

For form I, recording of the Raman spectrum did not present any particular problems. Form II unfortunately is too unstable in the bulk for an extended spectral scan, while in film, where it is stabilized, the signal is always very weak due to the low amount of compound. A compromised turned out to be the multilayer deposition film, and the spectra obtained for the two phases are compared in Figure 4.30.

They appear very similar, confirming that, although the molecule is rather flexible, it tends to assume the same conformation even in two very different crystal structures. Some differences are found in the so-called fingerprint region, but these are mainly relative intensity variations. A small variation was found for the frequency of the carbonyl group C = O, which falls in form I at 1704 cm^{-1} and at higher values in form II. The datum is in agreement with the presence, in the former structure, of stronger intermolecular interactions of the type C-H $\cdots$ O, which weaken the C=O double bond. Unfortunately, the result remains uncertain, mostly because of the poor quality of the form II spectrum.
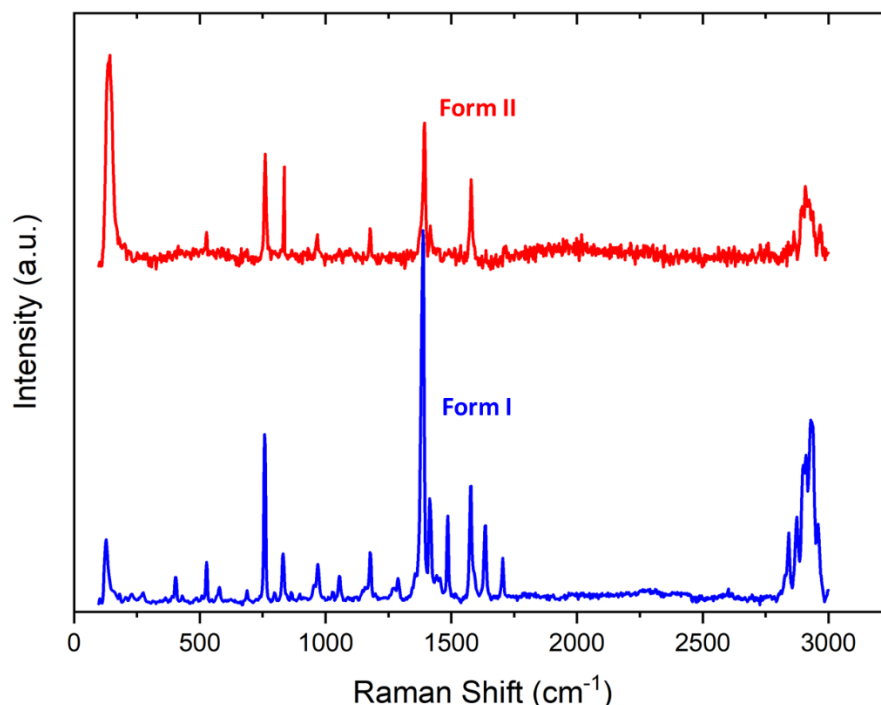

Figure 4.30: Raman spectra of Nabumetone forms I and II in the highest wavenumber interval, where the intramolecular vibrations are detected.

4.3.6. Conclusions

The Raman investigation performed on crystalline samples of Nabumetone allowed for a much more accurate characterization of its polymorphs compared to what already reported literature. [211] As expected, form II is rather difficult to obtain in the bulk and the melt crystallization process, through a preliminary amorphization of the sample, appears to be the best method. Probably, the presence of interfaces drives a growth of the "kinetic" type also in the bulk, selecting the metastable polymorph. This in fact is what happens in the crystallization in capillary or vial, with little volume of solution compared to the area of the container, or in an amorphous obtained on a surface (such as a glass slide). It is however quite evident how difficult is the control of all the external parameters that determine the formation of a crystalline structure rather than another.

Also in the case of films, the presence of the solid surface plays an important role both in the growth process and in the increased kinetic inertia of form II, significantly delaying its transformation to the thermodynamically stable phase. Form II "survives" in the film for a long time but to get it pure it is necessary to act empirically on parameters such as concentration, solvent and rotation speed of the support during spin coating deposition. The ability of the solvent to drive the growth of a polymorph is known and depends on the nature of the solute/solvent interaction and solubility. Furthermore, an increase in the rotation speed facilitates the spreading of the solution on the support and the achievement of a high surface/volume ratio in a short time, favouring kinetic rather than thermodynamic processes. The role of concentration seems to be more complex in the case of Nabumetone, because it is by decreasing it that the metastable form is obtained.

Spectroscopic measurements were not able to confirm the growth of a third form (form III), even on samples in which X-ray measurements suggested its presence. A possible explanation can be found in the structural data. The reflexes that identify the third X-ray form are related to the crystallographic planes (h00), parallel to the plane of contact *bc* of the crystalline film with the surface. The structural data indicates that the main difference between forms II and III consists in an increased interplanar distance. As

form II films are found to grow with the (1 0 0) face contacting the surface, in the backscattering geometry of our setup, the detectable Raman allowed modes can gain their intensity only from the *bb*, *cc*, and *bc* components of the polarizability tensor. Thus, they mostly correspond to translations and rotations which change the intermolecular distances/orientations on the crystallographic directions *b* and *c* (along which the shortest intermolecular contacts are present), coupled to low frequency molecular vibrations. This set of modes is expected to fall and is indeed observed on the high energy side of the lattice phonon spectrum, giving rise to the broad band system characterizing form II (between 110 and 170 cm^{-1}). Unfortunately, these modes are the least sensitive to the increase of netplane distance which marks the difference between form II and form III. This makes, in the present measurements, Raman spectroscopy in fact unsuited to discriminate between the two polymorphs.

Chapter 5

5. General conclusions

The study of the phenomenon of polymorphism in organic systems is a very topical subject and, together with selection and control, is part of an emerging design strategy for obtaining materials, as it allows modulating their functional properties. X-ray diffraction and electron microscopy methods still are the techniques of choice for the identification of the crystal structure of a compound, also for growths on surfaces and in confined environments. However, much effort has been devoted in past years in the search of additional experimental and computational methods to identify and predict the crystal phases.

In the present thesis, while selecting lattice phonon Raman spectroscopy as the main technique for the solid state investigation, we have demonstrated how it is actually the synergy provided by the combination of different experimental and computational approaches that allows one to obtain a clearer picture of the polymorph landscape of a system. In addition, the knowledge on a certain structure, which arises from many different sources, constitutes a sort of "database" or information repository which can be used whenever needed for structure identification.

The compounds covered here belong either to the large class of the organics with semiconducting properties or to the even larger class of the pharmaceuticals. They were in fact chosen as model systems, because each of them was characterized by polymorphism in a non-trivial way and could profit by the application of a multi-methodological approach.

In the case of **Indigo**, X-ray provided the "structure database" for the spectroscopic investigation. However, the phase assignment in the film phase was made possible by the Raman measurements, thus demonstrating the interface selectivity for the B form, despite the fact that the two known polymorphs of this compound constitute in the bulk an exemplary case of concomitant growth. DFT was used to assist the Raman investigation, assigning the vibrational modes to the observed peaks. The information

that Raman could not provide about the film molecular organization, also because of the intrinsic poor crystallinity which characterizes the Indigo growths on films, was supplied by the application of the AFM and TEM techniques.

Thioindigo is also a system which displays two polymorphs, but we have found that one of them, namely the metastable α form, can be only obtained, even in its bulk form, when crystals are grown from solution on substrates. Polarized Raman spectroscopy combined with the DFT simulations of the polarized spectra enabled us to determine the phase and the molecular orientation in the highly homogenous films obtained by a shearing deposition technique. In fact, we were able to detect the alignment of the *a* crystallographic axis of the α form along the shearing direction, with an angular spread which was found to be the same both by the spectroscopic and GIXD methods. We were also looking for a possible new phase, whose existence was checked by AFM and TEM measurements.

A fully spectroscopic approach has been employed in the polymorph characterization of **Quinacridone**, where the different molecular packing of the known forms, together with their different hydrogen bond patterns result into distinct vibrational (IR and Raman) and electronic spectra. For this system, we believe we were able to provide information that can be readily exploited to study Quinacridone films grown in various ways.

Coming to the pharmaceutical, in the case of **Paracetamol** Raman mapping measurements have shown how the metastable phase III can be found (and get stabilized) in the films. A DSC experiment clarified the relative stability of Paracetamol forms I, II and III. More importantly, we believe that polarized Raman spectra have shed some light on the mechanism of transformation of phase III into phase II, thus yielding information also on the alignment of the phases at the interface, in combination with the GIXD investigation.

Also for **Nabumetone**, Raman mapping has evidenced that the two known polymorph grow as segregated domains. Furthermore, it was possible to follow the fast transformation of the metastable phase as a function of time, thanks to the efficiency of the Raman technique. This method was also used to investigate the possible existence of a third phase, the existence of which was hinted by the GIXD measurements.

Finally, **Phenytoin** is the exemplary case in which experimental structural data (GIXD), albeit incomplete, can be fed into a computational approach such as crystal structure prediction to yield a structure that can be at once validated both by further calculations (DFT) and by experiments (Raman). The final result is really interesting, as it has been the simple application of the Raman selection rules that has enabled us to choose between two slightly different structures, which differed only by the presence (or the absence) of the inversion centre.

From the point of view of the various techniques, besides XRD and Raman used in all cases, Raman mapping was particularly helpful for a micrometre investigation of all pharmaceutics. AFM and TEM measurements provided information on the morphology and crystallinity of Indigoids. For these latter and for Phenytoin (where it was crucial), DFT calculations were performed. IR for Quinacridone and DSC for Paracetamol were also useful. In this way we have clarified many open issues and obtained new results, vindicating the fruitfulness of the multi-methodological approach for polymorphism.

Bibliography

[1]   J. Bernstein, *Polymorphism in molecular crystals*. Oxford: Oxford Science Publications, 2002.

[2]   W. C. McCrone, *Polymorphism in Physics and Chemistry of the Organic Solid State*. New York: Wiley Interscience, 1965.

[3]   W. Ostwald, *Lehrbuch der allgemeinen Chemie*. Leipzig: Engelmann, 1885.

[4]   J. Bernstein, R. J. Davey, and J. Henck, "Concomitant Polymorphs," *Angew. Chemie Int. Ed.*, vol. 38, pp. 3440–3461, 1999.

[5]   J. D. Dunitz and J. Bernstein, "Disappearing Polymorphs," *Acc. Chem. Res.*, vol. 28, no. 4, pp. 193–200, Apr. 1995.

[6]   K. R. Seddon, "Pseudo polymorph: A Polemic," *Cryst. Growth Des.*, vol. 4, no. 6, pp. 1087–1087, Nov. 2004.

[7]   S. Aitipamula *et al.*, "Polymorphs, salts, and cocrystals: What's in a name?," *Cryst. Growth Des.*, vol. 12, no. 5, pp. 2147–2152, 2012.

[8]   J. Hulliger, "Chemistry and Crystal Growth," *Angew. Chemie Int. Ed. English*, vol. 33, no. 2, pp. 143–162, Feb. 1994.

[9]   K. Sato and R. Boistelle, "Stability and occurrence of polymorphic modifications of the stearic acid in polar and nonpolar solutions," *J. Cryst. Growth*, vol. 66, no. 2, pp. 441–450, Mar. 1984.

[10]   E. H. Lee, "A practical guide to pharmaceutical polymorph screening & selection," *Asian J. Pharm. Sci.*, vol. 9, no. 4, pp. 163–175, 2014.

[11]   A. Brillante, I. Bilotti, R. G. Della Valle, E. Venuti, and A. Girlando, "Probing polymorphs of organic semiconductors by lattice phonon Raman microscopy," *CrystEngComm*, vol. 10, no. 8, pp. 923–1092, 2008.

[12]   G. R. Desiraju, *Crystal Engineering: The design of Organic Solids*. Amsterdam: Elsevier, 1989.

[13]   R. E. Notari, *Biofarmaceutica e farmacocinetica*. Piccin-Nuova Libraria, 1981.

[14]   C. D. Dimitrakopoulos and P. R. L. Malenfant, "Organic Thin Film Transistors for Large Area Electronics," *Adv. Mater.*, vol. 14, no. 2, pp. 99–117, Jan. 2002.

[15] N. Karl, "Charge carrier transport in organic semiconductors," *Synth. Met.*, vol. 133–134, pp. 649–657, Mar. 2003.

[16] H. Yoshida, K. Inaba, and N. Sato, "X-ray diffraction reciprocal space mapping study of the thin film phase of pentacene," *Appl. Phys. Lett.*, vol. 90, no. 18, p. 181930, Apr. 2007.

[17] A. O. F. Jones, B. Chattopadhyay, Y. H. Geerts, and R. Resel, "Substrate-induced and thin-film phases: Polymorphism of organic materials on surfaces," *Adv. Funct. Mater.*, vol. 26, no. 14, pp. 2233–2255, 2016.

[18] S. Schiefer, M. Huth, A. Dobrinevski, and B. Nickel, "Determination of the Crystal Structure of Substrate-Induced Pentacene Polymorphs in Fiber Structured Thin Films," *J. Am. Chem. Soc.*, vol. 129, no. 34, pp. 10316–10317, Aug. 2007.

[19] A. Moser *et al.*, "A disordered layered phase in thin films of sexithiophene," *Chem. Phys. Lett.*, vol. 574, pp. 51–55, Jun. 2013.

[20] I. Salzmann *et al.*, "Epitaxial growth of π-stacked perfluoropentacene on graphene-coated quartz," *ACS Nano*, vol. 6, no. 12, pp. 10874–10883, 2012.

[21] B. Schrode *et al.*, "Substrate-Induced Phase of a Benzothiophene Derivative Detected by Mid-Infrared and Lattice Phonon Raman Spectroscopy," *ChemPhysChem*, vol. 19, no. 8, pp. 993–1000, Apr. 2018.

[22] D. Nabok, P. Puschnig, C. Ambrosch-Draxl, O. Werzer, R. Resel, and D.-M. Smilgies, "Crystal and electronic structures of pentacene thin films from grazing-incidence x-ray diffraction and first-principles calculations," *Phys. Rev. B*, vol. 76, no. 23, p. 235322, Dec. 2007.

[23] B. Wedl *et al.*, "Crystallisation kinetics in thin films of dihexyl-terthiophene: the appearance of polymorphic phases," *RSC Adv.*, vol. 2, no. 10, p. 4404, 2012.

[24] A. C. Mayer, A. Kazimirov, and G. G. Malliaras, "Dynamics of Bimodal Growth in Pentacene Thin Films," *Phys. Rev. Lett.*, vol. 97, no. 10, p. 105503, Sep. 2006.

[25] Y. Diao, A. S. Myerson, T. A. Hatton, and B. L. Trout, "Surface Design for Controlled Crystallization: The Role of Surface Chemistry and Nanoscale Pores in Heterogeneous Nucleation," *Langmuir*, vol. 27, no. 9, pp. 5324–5334, May 2011.

[26] D. Reischl *et al.*, "Surface-Induced Polymorphism as a Tool for Enhanced

Dissolution: The Example of Phenytoin," *Cryst. Growth Des.*, vol. 15, no. 9, pp. 4687–4693, 2015.

[27]   A. Brillante *et al.*, "Confocal Raman Spectroscopy of α-Sexithiophene: From Bulk Crystals to Field-Effect Transistors," *Adv. Funct. Mater.*, vol. 17, no. 16, pp. 3119–3127, 2007.

[28]   S. Price, "The computational prediction of pharmaceutical crystal structures and polymorphism," *Adv. Drug Deliv. Rev.*, vol. 56, no. 3, pp. 301–319, Feb. 2004.

[29]   R. L. McCreery, *Raman spectroscopy for chemical analysis.* New York: John Wiley & Sons, 2000.

[30]   D. A. Long, *Raman spectroscopy*. New York: McGraw-Hill International Book Company, 1977.

[31]   I. R. Lewis and H. Edwards, *Handbook of Raman Spectroscopy*. New York: Marcel Dekker Inc., 2001.

[32]   M. Born and K. Huang, *Dynamical Theory of Crystal Lattices*. New York: Oxford University Press, 1954.

[33]   C.-Y. Chen *et al.*, "Understanding the Interplay between Molecule Orientation and Graphene Using Polarized Raman Spectroscopy," *ACS Photonics*, vol. 3, no. 6, pp. 985–991, Jun. 2016.

[34]   E. Venuti, R. G. Della Valle, L. Farina, A. Brillante, M. Masino, and A. Girlando, "Phonons and structures of tetracene polymorphs at low temperature and high pressure," *Phys. Rev. B*, vol. 70, no. 10, p. 104106, Sep. 2004.

[35]   G. Turrell and J. Corset, *Raman Microscopy: Developments and Applications*. Elsevier Academic Press, 1996.

[36]   T. C. Damen, S. P. S. Porto, and B. Tell, "Raman Effect in Zinc Oxide," *Phys. Rev.*, vol. 142, no. 2, pp. 570–574, Feb. 1966.

[37]   R. Loudon, "The Raman effect in crystals," *Adv. Phys.*, vol. 13, no. 52, pp. 423–482, Oct. 1964.

[38]   H. Jiang and C. Kloc, "Single-crystal growth of organic semiconductors," *MRS Bull.*, vol. 38, no. 1, pp. 28–33, Jan. 2013.

[39]   R. . Laudise, C. Kloc, P. . Simpkins, and T. Siegrist, "Physical vapor growth of organic

semiconductors," *J. Cryst. Growth*, vol. 187, no. 3–4, pp. 449–454, May 1998.

[40] P. G. Simpkins and K. S. Chen, "Convection in horizontal cavities," *J. Fluid Mech.*, vol. 166, pp. 21–39, May 1986.

[41] "https://www.ossila.com/pages/spin-coating#spin-coating-general-theory." .

[42] Y. Diao, L. Shaw, Z. Bao, and S. C. B. Mannsfeld, "Morphology control strategies for solution-processed organic semiconductor thin films," *Energy Environ. Sci.*, vol. 7, no. 7, pp. 2145–2159, 2014.

[43] I. Temiño, F. G. Del Pozo, M. R. Ajayakumar, S. Galindo, J. Puigdollers, and M. Mas-Torrent, "A Rapid, Low-Cost, and Scalable Technique for Printing State-of-the-Art Organic Field-Effect Transistors," *Adv. Mater. Technol.*, vol. 1, no. 5, p. 1600090, Aug. 2016.

[44] J. Xu *et al.*, "Probing the interfacial molecular packing in TIPS-pentacene organic semiconductors by surface enhanced Raman scattering," *J. Mater. Chem. C*, vol. 2, no. 16, pp. 2985–2991, 2014.

[45] S. R. Forrest, "Ultrathin Organic Films Grown by Organic Molecular Beam Deposition and Related Techniques," *Chem. Rev.*, vol. 97, no. 6, pp. 1793–1896, Oct. 1997.

[46] S. Kowarik, A. Gerlach, and F. Schreiber, "Organic molecular beam deposition: fundamentals, growth dynamics, and in situ studies," *J. Phys. Condens. Matter*, vol. 20, no. 18, p. 184005, May 2008.

[47] A. Köhler and H. Bässler, *Electronic Processes in Organic Semiconductors*. Weinheim, Germany: Wiley-VCH Verlag GmbH & Co. KGaA, 2015.

[48] M. Schwoerer and H. C. Wolf, *Organic Molecular Solids*. Wiley, 2006.

[49] A. J. Heeger, "Semiconducting and Metallic Polymers: The Fourth Generation of Polymeric Materials (Nobel Lecture)," *Angew. Chemie Int. Ed.*, vol. 40, no. 14, pp. 2591–2611, Jul. 2001.

[50] X. Zhao, S. T. Chaudhry, and J. Mei, "Heterocyclic Building Blocks for Organic Semiconductors," *Adv. Heterocycl. Chem.*, vol. 120, pp. 133–171, 2017.

[51] X. Guo, M. Baumgarten, and K. Müllen, "Progress in Polymer Science Designing ⬚ -conjugated polymers for organic electronics," *Prog. Polym. Sci.*, vol. 38, no. 12, pp.

1832–1908, 2013.

[52] G. J. Hedley, A. Ruseckas, and I. D. W. Samuel, "Light Harvesting for Organic Photovoltaics," *Chem. Rev.*, vol. 117, no. 2, pp. 796–837, Jan. 2017.

[53] K. Leo, "Organic photovoltaics," *Nat. Rev. Mater.*, vol. 1, no. 8, p. 16056, Aug. 2016.

[54] H. Sirringhaus, "25th anniversary article: Organic field-effect transistors: The path beyond amorphous silicon," *Adv. Mater.*, vol. 26, no. 9, pp. 1319–1335, 2014.

[55] J. T. E. Quinn, J. Zhu, X. Li, J. Wang, and Y. Li, "Recent progress in the development of n-type organic semiconductors for organic field effect transistors," *J. Mater. Chem. C*, vol. 5, no. 34, pp. 8654–8681, 2017.

[56] F. Garnier, "Organic-Based Electronics à la Carte," *Acc. Chem. Res.*, vol. 32, no. 3, pp. 209–215, Mar. 1999.

[57] D. J. Mascaro, "Organic thin- film transistors : A review of recent advances," vol. 45, no. 1, pp. 11–27, 2001.

[58] G. Horowitz, "Organic thin film transistors: From theory to real devices," *J. Mater. Res.*, vol. 19, no. 7, pp. 1946–1962, Jul. 2004.

[59] J. Fraxedas, *Molecular Organic Materials - From Molecules to Crystalline Solids*. Cambridge: Cambridge University Press, 2006.

[60] H. Dong, X. Fu, J. Liu, Z. Wang, and W. Hu, "25th Anniversary Article: Key Points for High-Mobility Organic Field-Effect Transistors," *Adv. Mater.*, vol. 25, no. 43, pp. 6158–6183, 2013.

[61] J. Bernstein, "Polymorphism – A Perspective," *Cryst. Growth Des.*, vol. 11, no. 3, pp. 632–650, Mar. 2011.

[62] J. Nyman and G. M. Day, "Static and lattice vibrational energy differences between polymorphs," *CrystEngComm*, vol. 17, no. 28, pp. 5154–5165, 2015.

[63] F. Cicoira and C. Santato, Eds., *Organic Electronics*. Weinheim, Germany: Wiley-VCH Verlag GmbH & Co. KGaA, 2013.

[64] H. Chung and Y. Diao, "Polymorphism as an emerging design strategy for high performance organic electronics," *J. Mater. Chem. C*, vol. 4, no. 18, pp. 3915–3933, 2016.

[65] M. Irimia-Vladu, "'Green' electronics: biodegradable and biocompatible materials

and devices for sustainable future," *Chem. Soc. Rev.*, vol. 43, no. 2, pp. 588–610, 2014.

[66] B. R. Bakshi, T. G. Gutowski, and D. P. Sekulić, *Thermodynamics and the Destruction of Resources*, 1st ed. Cambridge University Press, 2011.

[67] M. Irimia-Vladu, E. D. Glowacki, N. S. Sariciftci, and S. Bauer, *Green Materials for Electronics*. Wiley-VCH, 2017.

[68] H. Tao, D. L. Kaplan, and F. G. Omenetto, "Silk Materials - A Road to Sustainable High Technology," *Adv. Mater.*, vol. 24, no. 21, pp. 2824–2837, Jun. 2012.

[69] M. Irimia-vladu *et al.*, "Environmentally sustainable organic field effect transistors," *Org. Electron.*, vol. 11, no. 12, pp. 1974–1990, 2010.

[70] M. Irimia-Vladu *et al.*, "Biocompatible and biodegradable materials for organic field-effect transistors," *Adv. Funct. Mater.*, vol. 20, no. 23, pp. 4069–4076, 2010.

[71] M. Irimia-Vladu *et al.*, "Vacuum-processed polyaniline-C60 organic field effect transistors," *Adv. Mater.*, vol. 20, no. 20, pp. 3887–3892, 2008.

[72] T. Lei *et al.*, "Biocompatible and totally disintegrable semiconducting polymer for ultrathin and ultralightweight transient electronics," *Proc. Natl. Acad. Sci.*, vol. 114, no. 20, pp. 5107–5112, May 2017.

[73] H. Liu *et al.*, "Application of Biodegradable and Biocompatible Nanocomposites in Electronics: Current Status and Future Directions," *Nanomaterials*, vol. 9, no. 7, p. 950, Jun. 2019.

[74] E. D. Głowacki, G. Voss, and N. S. Sariciftci, "25th Anniversary Article: Progress in Chemistry and Applications of Functional Indigos for Organic Electronics," *Adv. Mater.*, vol. 25, no. 47, pp. 6783–6800, Dec. 2013.

[75] M. Truger *et al.*, "Surface-Induced Phase of Tyrian Purple (6,6'-Dibromoindigo): Thin Film Formation and Stability," *Cryst. Growth Des.*, vol. 16, no. 7, pp. 3647–3655, Jul. 2016.

[76] E. D. Głowacki, G. Voss, L. Leonat, M. Irimia-Vladu, S. Bauer, and N. S. Sariciftci, "Indigo and Tyrian Purple - From Ancient Natural Dyes to Modern Organic Semiconductors," *Isr. J. Chem.*, vol. 52, no. 6, pp. 540–551, Jun. 2012.

[77] E. D. Głowacki *et al.*, "Hydrogen-Bonded Semiconducting Pigments for Air-Stable

Field-Effect Transistors," *Adv. Mater.*, vol. 25, no. 11, pp. 1563–1569, Mar. 2013.

[78] M. Irimia-Vladu *et al.*, "Stability of Selected Hydrogen Bonded Semiconductors in Organic Electronic Devices," *Chem. Mater.*, vol. 31, no. 17, pp. 6315–6346, Sep. 2019.

[79] M. Seefelder, *Indigo in Culture, Science and Technology*. Landsberg: ecomed, 1994.

[80] P.-F. Gordon and P. Gregory, *Organic Chemistry in Colour*. Berlin: Springer-Verlag, 1987.

[81] H. Zollinger, *Color Chemistry*, 2nd editio. Weinheim: Wiley-VCH, 1991.

[82] C. J. Cooksey, "Tyrian purple: 6,6'-Dibromoindigo and related compounds," *Molecules*, vol. 6, no. 9, pp. 736–769, 2001.

[83] M. Irimia-Vladu *et al.*, "Indigo - A Natural Pigment for High Performance Ambipolar Organic Field Effect Transistors and Circuits," *Adv. Mater.*, vol. 24, no. 3, pp. 375–380, Jan. 2012.

[84] E. D. Głowacki, M. Irimia-Vladu, S. Bauer, and N. S. Sariciftci, "Hydrogen-bonds in molecular solids – from biological systems to organic electronics," *J. Mater. Chem. B*, vol. 1, no. 31, p. 3742, 2013.

[85] B. Scherwitzl, R. Resel, and A. Winkler, "Film growth, adsorption and desorption kinetics of indigo on SiO 2," *J. Chem. Phys.*, vol. 140, no. 18, p. 184705, May 2014.

[86] D. V. Anokhin *et al.*, "Towards understanding the behavior of indigo thin films in organic field-effect transistors: a template effect of the aliphatic hydrocarbon dielectric on the crystal structure and electrical performance of the semiconductor," *Chem. Commun.*, vol. 50, no. 57, p. 7639, 2014.

[87] P. Susse and A. Wolf, "A New Crystalline Phase of Indigo Enantiomer Resolution of Spiroketals," *Naturwissenschaften*, vol. 67, p. 453, 1980.

[88] F. Kettner, L. Hüter, J. Schäfer, K. Röder, U. Purgahn, and H. Krautscheid, "Selective crystallization of indigo B by a modified sublimation method and its redetermined structure," *Acta Crystallogr. Sect. E Struct. Reports Online*, vol. 67, no. 11, pp. o2867–o2867, Nov. 2011.

[89] T. Salzillo *et al.*, "Structural, Spectroscopic, and Computational Characterization of the Concomitant Polymorphs of the Natural Semiconductor Indigo," *J. Phys. Chem.*

C, vol. 122, no. 32, pp. 18422–18431, 2018.

[90] P. Süsse, M. Steins, and V. Kupcik, "Indigo: Crystal structure refinement based on synchrotron data," *Zeitschrift für Krist.*, vol. 184, no. 3–4, pp. 269–273, Jan. 1988.

[91] E. A. Gribova, G. S. Zhdanov, and G. A. Golder, "X-Ray Determination of the Structure of Indigo and Thoindigo.," *Kristallografiya*, vol. 1, p. 53, 1956.

[92] H. Von Eller, "Structure de colorants indigoïdes. III-Structure cristalline de l'indigo," *Bull.Soc.Chim.Fr.*, pp. 1433–1438, 1955.

[93] W. A. MacDonald, M. K. Looney, D. Mackerron, R. Adam, K. Hashimoto, and K. Rakos, "Latest advances in substrates for flexible electronics Factors influencing film choice," *J. Soc. Inf. Disp.*, vol. 15, no. 12, pp. 1075–1083, 2007.

[94] G. M. Sheldrick, "SHELX-97: Program for Crystal Structure Determination," in *University of Gottingen: Gottingen, Germany*, 1997.

[95] C. F. Macrae *et al.*, "Mercury CSD 2.0 – new features for the visualization and investigation of crystal structures ," *J. Appl. Crystallogr.*, vol. 41, no. 2, pp. 466–470, 2008.

[96] *Oxford Diffraction Ltd (Agilent Technologies)*. Oxfordshire, UK, 2010.

[97] C. Y. Legault, "CYLview," in *Université de Sherbrooke*, 2009.

[98] C. R. Groom, I. J. Bruno, M. P. Lightfoot, and S. C. Ward, "The Cambridge Structural Database," *Acta Crystallogr. Sect. B Struct. Sci. Cryst. Eng. Mater.*, vol. 72, no. 2, pp. 171–179, Apr. 2016.

[99] A. Cohelo, "TOPAS-Academic." Coelho Software, Brisbane, Australia, 2007.

[100] A. Tkatchenko and M. Scheffler, "Accurate Molecular Van Der Waals Interactions from Ground-State Electron Density and Free-Atom Reference Data," *Phys. Rev. Lett.*, vol. 102, no. 7, p. 073005, Feb. 2009.

[101] A. Tkatchenko, R. A. Distasio, R. Car, and M. Scheffler, "Accurate and efficient method for many-body van der Waals interactions," *Phys. Rev. Lett.*, vol. 108, no. 23, pp. 1–5, 2012.

[102] R. G. Della Valle, E. Venuti, A. Brillante, and A. Girlando, "Inherent structures of crystalline pentacene," *J. Chem. Phys.*, vol. 118, no. 2, pp. 807–815, 2003.

[103] F. H. Stillinger and T. A. Weber, "Hidden structure in liquids," *Phys. Rev. A*, vol. 25,

no. 2, pp. 978–989, 1982.

[104] A. S. Davydov, *Theory of Molecular Excitons*. Springer US, 1971.

[105] W. Humphrey, A. Dalke, and K. Schulten, "VMD: molecular dynamics," *J. Mol. Graph.*, vol. 14, no. 1, pp. 33–38, 1996.

[106] W. Lüttke, H. Hermann, and M. Klessinger, "Theoretically and Experimentally Determined Properties of the Fundamental Indigo Chromophore," *Angew. Chemie Int. Ed. English*, vol. 5, no. 6, pp. 598–598, 1966.

[107] E. Tatsch and B. Schrader, "Near-infrared fourier transform Raman spectroscopy of indigoids," *J. Raman Spectrosc.*, vol. 26, no. 6, pp. 467–473, Jun. 1995.

[108] A. Amat, F. Rosi, C. Miliani, A. Sgamellotti, and S. Fantacci, "Theoretical and experimental investigation on the spectroscopic properties of indigo dye," *J. Mol. Struct.*, vol. 993, no. 1–3, pp. 43–51, May 2011.

[109] J. G. Amar, F. Family, and P.-M. Lam, "Dynamic scaling of the island-size distribution and percolation in a model of submonolayer molecular-beam epitaxy," *Phys. Rev. B*, vol. 50, no. 12, pp. 8781–8797, Sep. 1994.

[110] X. Liu, S. H. Mohamed, J. M. Ngaruiya, M. Wuttig, and T. Michely, "Modifying the growth of organic thin films by a self-assembled monolayer," *J. Appl. Phys.*, vol. 93, no. 8, pp. 4852–4855, Apr. 2003.

[111] K. Reichelt, "Nucleation and growth of thin films," *Vacuum*, vol. 38, no. 12, pp. 1083–1099, 1988.

[112] T. Yoshinobu, A. Iwamoto, K. Sudoh, and H. Iwasaki, "Scaling Analysis of a - and poly -Si Surface Roughness by Atomic Force Microscopy," *MRS Proc.*, vol. 367, no. 1, pp. 329–334, Sep. 1994.

[113] I. Levine, A. Yoffe, A. Salomon, W. Li, Y. Feldman, and A. Vilan, "Epitaxial two dimensional aluminum films on silicon (111) by ultra-fast thermal deposition," *J. Appl. Phys.*, vol. 111, no. 12, p. 124320, Jun. 2012.

[114] A. B. Hamouda, A. Pimpinelli, and R. J. Phaneuf, "Surface Science Anomalous scaling in epitaxial growth on vicinal surfaces : meandering and mounding instabilities in a linear growth equation with spatiotemporally correlated noise," *Surf. Sci.*, vol. 602, pp. 2819–2827, 2008.

[115] A. Brillante *et al.*, "Structure and dynamics of pentacene on SiO2: From monolayer to bulk structure," *Phys. Rev. B*, vol. 85, no. 19, p. 195308, May 2012.

[116] A. Patterson, "The Scherrer Formula for X-Ray Particle Size Determination," *Phys. Rev.*, vol. 56, no. 10, pp. 978–982, 1939.

[117] C. Liu, D.-Y. Khim, and Y.-Y. Noh, "Organic Field-Effect Transistors by a Solvent Vapor Annealing Process," *J. Nanosci. Nanotechnol.*, vol. 14, no. 2, pp. 1476–1493, 2014.

[118] H. Uno, K. Moriyama, T. Ishikawa, N. Ono, and H. Yahiro, "Thioindigo precursor: control of polymorph of thioindigo," *Tetrahedron Lett.*, vol. 45, no. 49, pp. 9083–9086, Nov. 2004.

[119] E. Steingruber, "Indigo and Indigo Colorants," in *Ullmann's Encyclopedia of Industrial Chemistry*, Weinheim, Germany: Wiley-VCH Verlag GmbH & Co. KGaA, 2004.

[120] N. M. Khusayfan, E. F. M. El-Zaidia, and M. M. El-Nahass, "Fabrication and Electrical Characteristics of Thioindigo/Silicon Heterojunction," *Silicon*, vol. 10, no. 6, pp. 2519–2526, 2018.

[121] K. Fukushima, K. Nakatsu, R. Takahashi, H. Yamamoto, K. Gohda, and S. Homma, "Crystal Structures and Photocarrier Generation of Thioindigo Derivatives," *J. Phys. Chem. B*, vol. 102, no. 31, pp. 5985–5990, 2002.

[122] W. Haase-Wessel, M. Ohmasa, and P. Siisse, "Thioindigo: Crystal Structural Data for Modification II," *Naturwissenschaften*, vol. 64, p. 435, 1977.

[123] R. Pfattner, S. T. Bromley, C. Rovira, and M. Mas-Torrent, "Tuning crystal ordering, electronic structure, and morphology in organic semiconductors: Tetrathiafulvalenes as a model case," *Adv. Funct. Mater.*, vol. 26, no. 14, pp. 2256–2275, 2016.

[124] A. Rivalta *et al.*, "Crystal alignment of surface stabilized polymorph in thioindigo films," *Dye. Pigment.*, vol. 172, no. August 2019, p. 107847, Jan. 2020.

[125] N. Marom *et al.*, "Many-Body Dispersion Interactions in Molecular Crystal Polymorphism," *Angew. Chemie Int. Ed.*, vol. 52, no. 26, pp. 6629–6632, Jun. 2013.

[126] J. A. Chisholm and S. Motherwell, "COMPACK : a program for identifying crystal

structure similarity using distances," *J. Appl. Crystallogr.*, vol. 38, no. 1, pp. 228–231, Feb. 2005.

[127] F. G. Del Pozo *et al.*, "Single crystal-like performance in solution-coated thin-film organic field-effect transistors," *Adv. Funct. Mater.*, vol. 26, no. 14, pp. 2379–2386, 2015.

[128] M. R. Niazi *et al.*, "Contact-induced nucleation in high-performance bottom-contact organic thin film transistors manufactured by large-area compatible solution processing," *Adv. Funct. Mater.*, vol. 26, no. 14, pp. 2371–2378, 2016.

[129] A. Lausi *et al.*, "Status of the crystallography beamlines at Elettra," *Eur. Phys. J. Plus*, vol. 130, no. 3, p. 43, Mar. 2015.

[130] W. Kabsch, "XDS," *Acta Crystallogr. Sect. D Biol. Crystallogr.*, vol. 66, no. 2, pp. 125–132, Feb. 2010.

[131] G. M. Sheldrick, "SHELXT – Integrated space-group and crystal-structure determination," *Acta Crystallogr. Sect. A Found. Adv.*, vol. 71, no. 1, pp. 3–8, Jan. 2015.

[132] G. M. Sheldrick, "Crystal structure refinement with SHELXL," *Acta Crystallogr. Sect. C Struct. Chem.*, vol. 71, no. 1, pp. 3–8, Jan. 2015.

[133] P. Emsley and K. Cowtan, "Coot : model-building tools for molecular graphics," *Acta Crystallogr. Sect. D Biol. Crystallogr.*, vol. 60, no. 12, pp. 2126–2132, Dec. 2004.

[134] A. L. Spek, "Structure validation in chemical crystallography," *Acta Crystallogr. Sect. D Biol. Crystallogr.*, vol. 65, no. 2, pp. 148–155, Feb. 2009.

[135] B. Schrode *et al.*, "GIDVis : a comprehensive software tool for geometry-independent grazing-incidence X-ray diffraction data analysis and pole-figure calculations," *J. Appl. Crystallogr.*, vol. 52, no. 3, pp. 683–689, Jun. 2019.

[136] I. Salzmann and R. Resel, "STEREOPOLE : software for the analysis of X-ray diffraction pole figures with IDL," *J. Appl. Crystallogr.*, vol. 37, no. 6, pp. 1029–1033, Dec. 2004.

[137] M. R. Niazi *et al.*, "Solution-printed organic semiconductor blends exhibiting transport properties on par with single crystals," *Nat. Commun.*, vol. 6, 2015.

[138] A. Rivalta *et al.*, "Bulk and Surface-Stabilized Structures of Paracetamol Revisited by Raman Confocal Microscopy," *ACS Omega*, vol. 3, no. 8, pp. 9564–9571, 2018.

[139] E. F. Paulus, F. J. J. Leusen, and M. U. Schmidt, "Crystal structures of quinacridones," *CrystEngComm*, vol. 9, no. 2, pp. 131–143, 2007.

[140] H. Liebermann *et al.*, "Über die Bildung von Chinakridonen aus p-Di-arylamino-terephtalsäuren. 6. Mitteilung über Umwandlungsprodukte des Succinylobernsteinsäureesters," *Justus Liebig's Ann. der Chemie*, vol. 518, no. 1, pp. 245–259, 1935.

[141] T. B. Reeve and E. C. Botti, "Du Pont Official Digest," vol. 31, pp. 991–1002, 1958.

[142] W. Herbst and K. Hunger, *Industrial Organic Pigments*, 3rd editio. Weinheim: Wiley-VCH, 2004.

[143] S. Dunst, E. Karner, M. E. Coppola, G. Trimmel, and M. Irimia-Vladu, "Comparison of the solution and vacuum-processed quinacridones in homojunction photovoltaics," *Monatshefte für Chemie - Chem. Mon.*, vol. 148, no. 5, pp. 863–870, May 2017.

[144] A. D. Squires, R. A. Lewis, A. J. Zaczek, and T. M. Korter, "Distinguishing Quinacridone Pigments via Terahertz Spectroscopy: Absorption Experiments and Solid-State Density Functional Theory Simulations," *J. Phys. Chem. A*, vol. 121, no. 18, pp. 3423–3429, May 2017.

[145] T. E. Gorelik, C. Czech, S. M. Hammer, and M. U. Schmidt, "Crystal structure of disordered nanocrystalline α II -quinacridone determined by electron diffraction," *CrystEngComm*, vol. 18, no. 4, pp. 529–535, 2016.

[146] D. Berg, C. Nielinger, W. Mader, and M. Sokolowski, "Quinacridone organic field effect transistors with significant stability by vacuum sublimation," *Synth. Met.*, vol. 159, no. 23–24, pp. 2599–2602, Dec. 2009.

[147] E. Daniel Głowacki *et al.*, "Intermolecular hydrogen-bonded organic semiconductors—Quinacridone versus pentacene," *Appl. Phys. Lett.*, vol. 101, no. 2, p. 023305, Jul. 2012.

[148] G. Lincke and H.-U. Finzel, "Studies on the Structure of alpha-Quinacridone," *Cryst. Res. Technol.*, vol. 31, no. 4, pp. 441–452, 1996.

[149] G. Turrell, *Infrared and Raman Spectra of Crystals*. Academic Press, 1972.

[150] S. De Feyter, A. Gesquière, F. C. De Schryver, U. Keller, and K. Müllen, "Aggregation properties of soluble quinacridones in two and three dimensions," *Chem. Mater.*, vol. 14, no. 3, pp. 989–997, 2002.

[151] C. Binant, B. Guineau, and A. Lautié, "The application of electronic and vibrational spectroscopic techniques to the identification of quinacridone pigments in vehicle paint systems," *J. Soc. Dye. Colour.*, vol. 106, no. 5–6, pp. 187–191, Oct. 2008.

[152] A. Girlando, M. Masino, A. Brillante, T. Toccoli, and S. Iannotta, "Raman identification of polymorphs in pentacene films," *Crystals*, vol. 6, no. 4, pp. 1–10, 2016.

[153] P. Erk, H. Hengelsberg, M. F. Haddow, and R. Van Gelder, "The innovative momentum of crystal engineering," *CrystEngComm*, vol. 6, no. 78, pp. 474–483, 2004.

[154] T. Salzillo *et al.*, "Spectroscopic identification of quinacridone polymorphs for organic electronics," *CrystEngComm*, vol. 21, no. 24, pp. 3702–3708, 2019.

[155] F. H. Chung and R. W. Scott, "Vacuum sublimation and crystallography of quinacridones," *J. Appl. Crystallogr.*, vol. 4, no. 6, pp. 506–511, Dec. 1971.

[156] J. Kalinowski, W. Stampor, P. Di Marco, and V. Fattori, "Electroabsorption study of excited states in hydrogen-bonding solids: epindolidione and linear trans-quinacridone," *Chem. Phys.*, vol. 182, no. 2–3, pp. 341–352, May 1994.

[157] N. Nishimura, T. Senju, and J. Mizuguchi, "5,7,12,14-Tetrahydro[2,3- b]quinolinoacridine (β form)," *Acta Crystallogr. Sect. E Struct. Reports Online*, vol. 62, no. 10, pp. o4683–o4685, Oct. 2006.

[158] J. Bernstein, "Polymorphism of pharmaceuticals," in *Polymorphism in molecular crystals*, New York: Oxford University Press, 2002, pp. 240–255.

[159] H. G. Brittain, *Polymorphism in Pharmaceutical Solids, Second Edition*. Taylor & Francis, 2009.

[160] A. J. Cruz-Cabeza, S. M. Reutzel-Edens, and J. Bernstein, "Facts and fictions about polymorphism," *Chem. Soc. Rev.*, vol. 44, no. 23, pp. 8619–8635, 2015.

[161] T. D. Turner, P. J. Halfpenny, and K. J. Roberts, "Pharmaceutical Solid-State

Characterisation Techniques," Springer, 2017, pp. 367–393.

[162] J. Bernstein, "DIVERSITY AMIDST SIMILARITY: A Multidisciplinary Approach to Polymorphs, Solvates and Phase Relationships," in *Erice, Sicily June 19*, 2004.

[163] S. R. Chemburkar *et al.*, "Dealing with the Impact of Ritonavir Polymorphs on the Late Stages of Bulk Drug Process Development," *Org. Process Res. Dev.*, vol. 4, no. 5, pp. 413–417, Sep. 2000.

[164] L. Shargel and A. B. Yu, *Applied Biopharmaceutics & Pharmacokinetics*, 4th editio. New York: McGraw-Hill, 1999.

[165] S. Domingos, V. André, S. Quaresma, I. C. B. Martins, M. F. Minas da Piedade, and M. T. Duarte, "New forms of old drugs: improving without changing," *J. Pharm. Pharmacol.*, vol. 67, no. 6, pp. 830–846, Jun. 2015.

[166] M. Preis, J. Breitkreutz, and N. Sandler, "Perspective: Concepts of printing technologies for oral film formulations," *Int. J. Pharm.*, vol. 494, no. 2, pp. 578–584, Oct. 2015.

[167] J. Aizenberg, A. J. Black, G. M. Whitesides, and X. Sam, "Control of crystal nucleation by patterned self-assembled monolayers," vol. 1720, no. 1971, pp. 1997–2000, 1999.

[168] R. Botting, "Paracetamol-inhibitable COX-2," *J. Physiol. Pharmacol.*, vol. 51, pp. 609–618, 2000.

[169] G. G. Graham and K. F. Scott, "Mechanism of action of paracetamol," *Am. J. Ther.*, vol. 12, pp. 46–55, 2005.

[170] V. André, M. F. M. da Piedade, and M. T. Duarte, "Revisiting paracetamol in a quest for new co-crystals," *CrystEngComm*, vol. 14, no. 15, p. 5005, 2012.

[171] B. Y. M. Haisa, S. Kashino, R. Kawai, and H. Maeda, "The Monoclinic Form of p-Hydroxyacetanilide," *Acta Crystallogr. Sect. B Struct. Sci.*, vol. 32, pp. 1283–1285, 1976.

[172] T. N. Drebushchak and E. V. Boldyreva, "Variable temperature (100-360 K) single-crystal X-ray diffraction study of the orthorhombic polymorph of paracetamol (p-hydroxyacetanilide)," *Zeitschrift fur Krist.*, vol. 219, no. 8, pp. 506–512, 2004.

[173] G. Nichols and C. S. Frampton, "Physicochemical characterization of the

orthorhombic polymorph of paracetamol crystallized from solution," *J. Pharm. Sci.*, vol. 87, no. 6, pp. 684–693, 1998.

[174] M.-A. Perrin, M. A. Neumann, H. Elmaleh, and L. Zaske, "Crystal structure determination of the elusive paracetamol Form III," *Chem. Commun.*, no. 22, pp. 3181–3183, 2009.

[175] Y. V. Nelyubina, I. V. Glukhov, M. Y. Antipin, and K. A. Lyssenko, "'Higher density does not mean higher stability' mystery of paracetamol finally unraveled," *Chem. Commun.*, vol. 46, no. 20, pp. 3469–3471, 2010.

[176] H. M. A. Ehmann and O. Werzer, "Surface mediated structures: Stabilization of metastable polymorphs on the example of paracetamol," *Cryst. Growth Des.*, vol. 14, no. 8, pp. 3680–3684, 2014.

[177] R. Telford *et al.*, "Stabilisation of metastable polymorphs: the case of paracetamol form III," *Chem. Commun.*, vol. 52, no. 81, pp. 12028–12031, 2016.

[178] S. Qi, P. Avalle, R. Saklatvala, and D. Q. M. Craig, "An investigation into the effects of thermal history on the crystallisation behaviour of amorphous paracetamol," *Eur. J. Pharm. Biopharm.*, vol. 69, no. 1, pp. 364–371, 2008.

[179] P. Di Martino, P. Conflant, M. Drache, J.-P. Huvenne, and A.-M. Guyot-Hermann, "Preparation and Physical Characterization of Forms H and Hi of Paracetamol," *J. Therm. Anal.*, vol. 48, pp. 447–458, 1997.

[180] J. B. Nanubolu and J. C. Burley, "Investigating the Recrystallization Behavior of Amorphous Paracetamol by Variable Temperature Raman Studies and Surface Raman Mapping," *Mol. Pharm.*, vol. 9, no. 6, pp. 1544–1558, Jun. 2012.

[181] J. C. Burley, M. J. Duer, R. S. Stein, and R. M. Vrcelj, "Enforcing Ostwald's rule of stages: Isolation of paracetamol forms III and II," *Eur. J. Pharm. Sci.*, vol. 31, no. 5, pp. 271–276, 2007.

[182] J. B. Nanubolu and J. C. Burley, "In situ Raman mapping for identifying transient solid forms," *CrystEngComm*, vol. 17, no. 28, pp. 5280–5287, 2015.

[183] A. Brillante, I. Bilotti, R. G. Della Valle, E. Venuti, M. Masino, and A. Girlando, "Characterization of Phase Purity in Organic Semiconductors by Lattice-Phonon Confocal Raman Mapping: Application to Pentacene.," *Adv. Mater.*, vol. 17, p.

2549–2553, 2005.

[184] T. Wu and L. Yu, "Surface crystallization of indomethacin below Tg," *Pharm. Res.*, vol. 23, no. 10, pp. 2350–2355, 2006.

[185] A. Brillante *et al.*, "Phase recognition by lattice phonon Raman spectra: The triclinic structure of the organic semiconductor dibenzo-tetrathiafulvalene," *Chem. Phys. Lett.*, vol. 523, pp. 74–77, 2012.

[186] A. O. F. Jones *et al.*, "Substrate-induced phase of a [1]benzothieno[3,2- b]benzothiophene derivative and phase evolution by aging and solvent vapor annealing," *ACS Appl. Mater. Interfaces*, vol. 7, no. 3, pp. 1868–1873, 2015.

[187] S. T. Salammal *et al.*, "Polymorphism in bulk and thin films: The curious case of dithiophene-DPP(Boc)-dithiophene," *J. Phys. Chem. C*, vol. 118, no. 1, pp. 657–669, 2014.

[188] I. Salzmann *et al.*, "Structure solution of the 6, 13-pentacenequinone surface-induced polymorph by combining X-ray diffraction reciprocal-space mapping and theoretical structure modeling," *Cryst. Growth Des.*, vol. 11, no. 2, pp. 600–606, 2011.

[189] B. Chattopadhyay, L. Jacobs, P. Panini, I. Salzmann, R. Resel, and Y. Geerts, "Accessing Phase-Pure and Stable Acetaminophen Polymorphs by Thermal Gradient Crystallization," *Cryst. Growth Des.*, vol. 18, no. 3, pp. 1272–1277, 2018.

[190] G. Bolla and A. S. Myerson, "SURMOF induced polymorphism and crystal morphological engineering of acetaminophen polymorphs: advantage of heterogeneous nucleation," *CrystEngComm*, vol. 20, pp. 2084–2088, 2018.

[191] B. A. Kolesov, M. A. Mikhailenko, and E. V. Boldyreva, "Dynamics of the intermolecular hydrogen bonds in the polymorphs of paracetamol in relation to crystal packing and conformational transitions: a variable-temperature polarized Raman spectroscopy study," *Phys. Chem. Chem. Phys.*, vol. 13, no. 31, pp. 14243–14253, 2011.

[192] T. Beyer, G. M. Day, and S. L. Price, "The prediction, morphology, and mechanical properties of the polymorphs of paracetamol," *J. Am. Chem. Soc.*, vol. 123, no. 21, pp. 5086–5094, 2001.

[193] M. A. Mikhailenko, T. N. Drebushchak, T. P. Shakhtsneider, and V. V Boldyrev, "Etching patterns on the monoclinic and orthorhombic paracetamol," *Arkivoc*, vol. 2004, no. 12, pp. 156–169, Mar. 2005.

[194] Y. Nguyen Thi, K. Rademann, and F. Emmerling, "Direct evidence of polyamorphism in paracetamol," *CrystEngComm*, vol. 17, no. 47, pp. 9029–9036, 2015.

[195] M. L. Peterson *et al.*, "Iterative high-throughput polymorphism studies on acetaminophen and an experimentally derived structure for form III," *J. Am. Chem. Soc.*, vol. 124, no. 37, pp. 10958–10959, 2002.

[196] J. Aicardi, *Epilepsy : a comprehensive textbook*, 2nd ed. Philadelphia: Wolters Kluwer Health/Lippincott Williams & Wilkins, 2008.

[197] A. Camerman and N. Camerman, "The stereochemical basis of anticonvulsant drug action. I. The crystal and molecular structure of diphenylhydantoin, a noncentrosymmetric structure solved by centric symbolic addition," *Acta Crystallogr. Sect. B Struct. Crystallogr. Cryst. Chem.*, vol. 27, no. 11, pp. 2205–2211, 1971.

[198] T. K. Chattopadhyay, R. A. Palmer, and J. N. Lisgarten, "X-ray structural and potential energy studies on zentropil (5,5-diphenyl-2,4-imidazoli dine dione)," *J. Crystallogr. Spectrosc. Res.*, vol. 23, no. 2, pp. 149–152, 1993.

[199] D. E. Braun *et al.*, "Surface Induced Phenytoin Polymorph. 1. Full Structure Solution by Combining Grazing Incidence X-ray Diffraction and Crystal Structure Prediction," *Cryst. Growth Des.*, vol. 19, no. 11, pp. 6058–6066, Nov. 2019.

[200] N. Bedoya-Martínez *et al.*, "DFT-Assisted Polymorph Identification from Lattice Raman Fingerprinting," *J. Phys. Chem. Lett.*, vol. 8, no. 15, pp. 3690–3695, Aug. 2017.

[201] N. Bedoya-Martínez, A. Giunchi, T. Salzillo, E. Venuti, R. G. Della Valle, and E. Zojer, "Toward a Reliable Description of the Lattice Vibrations in Organic Molecular Crystals: The Impact of van der Waals Interactions," *J. Chem. Theory Comput.*, vol. 14, no. 8, pp. 4380–4390, Aug. 2018.

[202] A. Giunchi *et al.*, "Surface Induced Phenytoin Polymorph. 2. Structure Validation by Comparing Experimental and Density Functional Theory Raman Spectra," *Cryst.*

Growth Des., vol. 19, no. 11, pp. 6067–6073, Nov. 2019.

[203] K. Moriyama, N. Furuno, and N. Yamakawa, "Crystal face identification by Raman microscopy for assessment of crystal habit of a drug," *Int. J. Pharm.*, vol. 480, no. 1–2, pp. 101–106, 2015.

[204] E. Menard, A. Marchenko, V. Podzorov, M. E. Gershenson, D. Fichou, and J. A. Rogers, "Nanoscale Surface Morphology and Rectifying Behavior of a Bulk Single-Crystal Organic Semiconductor," *Adv. Mater.*, vol. 18, no. 12, pp. 1552–1556, Jun. 2006.

[205] E. B. Wilson, J. C. Decius, and P. C. Cross, *Molecular Vibrations*. New York: McGraw-Hill International Book Company, 1955.

[206] A. L. Spek, "Single-crystal structure validation with the program PLATON," *J. Appl. Crystallogr.*, vol. 36, no. 1, pp. 7–13, Feb. 2003.

[207] R. E. Marsh, M. Kapon, S. Hu, and F. H. Herbstein, "Some 60 new space-group corrections," *Acta Crystallogr. Sect. B Struct. Sci.*, vol. 58, no. 1, pp. 62–77, Feb. 2002.

[208] Y. Le Page, "MISSYM 1.1 – a flexible new release," *J. Appl. Crystallogr.*, vol. 21, no. 6, pp. 983–984, Dec. 1988.

[209] C. P. Price, A. L. Grzesiak, M. Lang, and A. J. Matzger, "Polymorphism of Nabumetone," *Cryst. Growth Des.*, vol. 2, no. 6, pp. 501–503, 2002.

[210] L. J. Chyall, J. M. Tower, D. A. Coates, T. L. Houston, and S. L. Childs, "Polymorph Generation in Capillary Spaces : The Preparation and Structural Analysis of a Metastable Polymorph of Nabumetone," *Cryst. Growth Des.*, vol. 2, no. 6, pp. 505–510, 2002.

[211] S. Roy, B. Chamberlin, and A. J. Matzger, "Polymorph Discrimination using Low Wavenumber Raman Spectroscopy," vol. 17, no. 7, pp. 976–980, 2013.